

DEFORMATION AND PHYSICAL AGING OF RUBBER-MODIFIED
POLYLACTIDE GRAFT COPOLYMERS

A Dissertation
SUBMITTED TO THE FACULTY OF
UNIVERSITY OF MINNESOTA
BY

Grayce Christina Thereyo

IN PARTIAL FULFILLMENT OF THE REQUIREMENTS
FOR THE DEGREE OF
DOCTOR OF PHILOSOPHY

Marc A. Hillmyer, Adviser

December 2014

© Grayce Christina Theryo 2014

Acknowledgements

My completion of this dissertation would not have been possible without the help and support of many people. I would like to thank my adviser, Marc Hillmyer, not only for his valuable advice and guidance which has helped me to become a research scientist, but also for always having complete confidence in my abilities. I owe many thanks to the former post-doctoral associates, graduate students and staff that I worked with including: Dr. Feng Jing, Prof. Megan Robertson, Dr. Louis Pitet, Prof. William Gramlich, all of whom helped me get started with this project, Dr. Marc Rodwogin, Dr. Jennifer Lowe, Dr. Ameara Mansour, Dr. Paula Delgado and Dr. Henry Martinez– for helpful discussions and general research advice, Dr. Robert Hafner– for assistance with using the transmission electron microscope; Dr. Steven Weigand and Dr. Mike Guise at the Advanced Photon Source for assistance with setting-up and operating the 5ID-D synchrotron beam line and tensile tester, and Dr. Carmelo Declet-Perez for assistance with collecting the in-situ SAXS data. I'd like to thank Maureen Ulbee for helping me overcome many of the non-technical challenges I encountered while writing my dissertation. I am forever grateful to Christy and Dennis Huberty for taking me in and patiently supporting me while I was writing my dissertation. I also owe a debt of gratitude to my parents, Teddy and Maria Theryo, and my brothers, Peter for their unwavering love and support. And finally, I must thank the one person I turn to during all the good and bad times, my best friend and kindred spirit, Mark Huberty, for always loving me no matter what...

Abstract

With the goal of rubber-toughening polylactide (PLA), high PLA content graft copolymers containing a rubbery-backbone and randomly spaced polylactide arms were synthesized using a two-step “grafting from” approach to give poly(1,5-cyclooctadiene-co-5-norbornene-2-methanol-*graft*-lactide) [PCNL]. The reaction scheme allowed for independent control of the total backbone molar mass, the backbone molar mass between graft points ($M_{n,eff}$) and the weight fraction of PLA (w_{PLA}). A series of graft copolymers, containing 80 to 99 wt.% PLA, were synthesized with $M_{n,eff}$ ranging from 0.7 – 5.6 kg/mol. For an expected PLA graft molar mass of ~60 kg/mol, adventitious initiation of lactide was competitive with initiation by the macroinitiator, resulting in blends of PCNL and PLA. Graft copolymers where $w_{PLA} = 0.89$ to 0.96, exhibited liquid-like packing of rubber domains in a matrix of PLA. The rubber domain radius (R_c) ranged from ~ 4 nm to 9 nm, and increased as a function of $M_{n,eff}$. In-situ small-angle x-ray scattering and tensile testing studies identified a new deformation phenomenon occurring prior to the yield point in both PLA and PCNL, independent of physical aging. We attribute the scattering evidence to micro-shear band and shear craze formation. Furthermore, while PLA deforms primarily by homogeneous crazing, rubber domain cavitation induced crazing was observed in PCNLs ($w_{PLA} = 0.95$) with two different R_c (4 and 7 nm). Overall, the graft copolymer architecture seemed to have little to no effect on the physical aging kinetics of PLA. However, hetero-phase cavitation induced crazing was more prevalent for $R_c = 7$ nm, resulting in a more stable craze morphology that was not seen in PLA.

Table of Contents

Acknowledgements.....	i
Abstract.....	ii
List of Tables.....	vi
List of Figures.....	vii
List of Abbreviations.....	xii
Chapter 1: Introduction.....	1
1.1 Motivation.....	1
1.2 Strategy.....	5
1.3 Overview of dissertation.....	10
1.4 References.....	10
Chapter 2: Synthesis of poly(1,5-cyclooctadiene-co-5-norbornene-2- methanol-graft-DL-lactide).....	14
2.1 Background.....	14
2.2 Experimental.....	16
2.2.1 Materials.....	16
2.2.2 General characterization methods.....	17
2.2.3 General synthetic procedure for polylactide.....	18
2.2.4 General synthetic procedure for poly(1,5-cyclooctadiene-co-5-norbornene-2- methanol) [PCN].....	19
2.2.5 Procedure for time-resolved synthesis of PCN.....	20
2.2.6 General synthetic procedure for poly(1,5-cyclooctadiene-co-5-norbornene-2- methanol)- <i>graft</i> -poly(lactide) [PCNL].....	20
2.2.7 Procedure for time-resolved synthesis of PCNL.....	21
2.3 Results.....	22
2.3.1 Poly(1,5-cyclooctadiene-co-5-norbornene-2-methanol).....	22
2.3.2 Poly(1,5-cyclooctadiene-co-5-norbornene-2-methanol)- <i>graft</i> -poly(lactide).....	26
2.3.2.1 Molar mass characterization.....	26
2.3.2.2 Thermal properties.....	36
2.3.2.3 Library of graft copolymers.....	39
2.4 Summary.....	40
2.5 Acknowledgements.....	41

Table of Contents	iv
2.6 References.....	41
Chapter 3: Morphology of polylactide graft copolymers	43
3.1 Background.....	43
3.2 Experimental.....	50
3.2.1 Sample preparation	50
3.2.2 Transmission electron microscopy methods.....	51
3.2.3 Small-angle x-ray scattering methods.....	52
3.3 Results.....	52
3.3.1 Morphology predictions for PCNL.....	52
3.3.2 Morphology of PCNLs, 99 wt.% PLA.....	56
3.3.3 Morphology of PCNLs, 89 – 95 wt.% PLA	57
3.3.4 Morphology of PCNLs, 80 wt.% PLA.....	62
3.3.5 Discussion.....	63
3.4 Summary	65
3.5 References.....	67
Chapter 4: Tensile deformation and physical aging of poly(DL-lactide).....	70
4.1 Background.....	70
4.2 Experimental.....	79
4.2.1 Materials	79
4.2.2 Compression molding of tensile bars.....	79
4.2.3 Ambient conditioning of compression molded tensile bars per ASTM D882. 80	
4.2.4 Controlled physical aging of compression molded tensile bars.....	81
4.2.5 Quantitative tensile testing.....	81
4.2.6 In-situ small-angle x-ray scattering and tensile testing.....	82
4.3 Results.....	84
4.3.1 Quantitative tensile properties	84
4.3.2 Simultaneous small-angle x-ray scattering and tensile testing	91
4.3.2.1 Results for aged PDLLA-58k	93
4.3.2.2 Results for unaged PDLLA-58k	100
4.3.3 Analysis of pre-yield streaks.....	107
4.4 Summary	117
4.5 Acknowledgements.....	118

4.6 References.....	118
Chapter 5: Tensile deformation and physical aging of poly(1,5-cyclooctadiene-co-5-norbornene-2- methanol-graft-DL -lactide)s	123
5.1 Background.....	123
5.2 Experimental.....	126
5.2.1 Materials	126
5.2.2 Compression molding of tensile bars.....	126
5.2.3 Conditioning of compression molded tensile bars.....	127
5.2.4 Quantitative tensile testing.....	127
5.2.5 In-situ small-angle x-ray scattering and tensile testing.....	127
5.3 Results.....	128
5.3.1 The effect of physical aging on tensile properties of PCNLs	128
5.3.2 Simultaneous small-angle x-ray scattering and tensile testing	133
5.3.2.1 Results for aged PCNL-594-90-95, $M_{n,eff} = 0.7$ kg/mol.....	134
5.3.2.2 Results for unaged PCNL-594-90-95	140
5.3.2.3 Results for PCNL-495-19-95, $M_{n,eff} = 2.8$ kg/mol.....	147
5.4 Summary.....	155
5.5 References.....	157
Chapter 6: Physical aging kinetics of polylactide graft copolymers.....	159
6.1 Background.....	159
6.2 Experimental.....	162
6.2.1 Materials	162
6.2.1 Physical aging calorimetry procedure.....	163
6.2.2 Modeling of physical aging kinetics	165
6.3 Results.....	168
6.4 Summary and Discussion.....	174
6.5 Final Conclusions.....	175
6.6 Acknowledgements.....	177
6.7 References.....	177
Bibliography	179
Appendix A.....	189

List of Tables

Table 2-1 Poly(1,5-cyclooctadiene-co-5-norbornene-2-methanol) [PCN] macroinitiators	26
Table 2-2 Library of poly(1,5-cyclooctadiene-co-5-norbornene-2-methanol)- <i>graft</i> -poly(DL-lactide) characteristics.....	39
Table 3-1 The morphological characteristics of the polylactide graft copolymers	55
Table 3-2 Results from the fit of the PCNL graft copolymer SAXS data to the Percus-Yevick model	60
Table 4-1 Physical properties of poly(D,L-lactide) [PDLLA] studied	79
Table 4-2 Physical aging conditions	85
Table 5-1 Physical aging conditions	127
Table 5-2 Characteristics of materials in physical aging study	128
Table 6-1 Molecular characteristics of the graft copolymers studied.....	162
Table 6-2 The enthalpic aging rate and time to equilibrium measured for $T_g - T_a = 7$ °C.	171
Table 6-3 Apparent activation energy used in the Tool-Narayanaswamy-Moynihan fit and the resulting fitted parameters.....	172
Table 6-4 Enthalpic aging rate and time to equilibrium of simulated data where $T_a = 25$ °C (standard errors are listed in parentheses)	174

List of Figures

Scheme 1-1.....	4
Figure 1-1 The chemical structure of a graft copolymer	7
Figure 1-2 The chemical structure of Norbornene-spiro-lactide	8
Scheme 1-2.....	9
Figure 2-1 ¹ H NMR spectrum of poly(1,5-cyclooctadiene-co-5-norbornene-2-methanol)	24
Figure 2-2 SEC chromatograms of poly(1,5-cyclooctadiene-co-5-norbornene-2-methanol) quenched after various reaction times.....	25
Figure 2-3 The DSC traces of poly(1,5-cyclooctadiene-co-5-norbornene-2-methanol). .	25
Figure 2-4 ¹ H NMR spectrum of poly(1,5-cyclooctadiene-co-5-norbornene-2-methanol)- <i>graft</i> -poly(DL-lactide)	28
Figure 2-5 Measured $M_{n,PLA}$ compared to the expected $M_{n,PLA}$	30
Figure 2-6 Size-exclusion chromatograms for a series of graft copolymers	31
Figure 2-7 The SEC traces of the synthesis of PCNL-332-19-95	33
Figure 2-8 The ¹ H NMR spectrum of a control polymerization.....	33
Figure 2-9 The SEC traces of the synthesis of PCNL-495-19-99	35
Figure 2-10 Differential scanning calorimetry traces of the PCN-78-12 macroinitiator and its respective graft copolymers	37
Figure 2-11 Thermal transitions as a function of molar mass.	38
Figure 3-1 Schematic representation of chain distribution of a mikto-arm star polymer forming a spherical morphology	44
Figure 3-2 Strong segregation phase diagram predicted for block copolymers with various architectures	45

Figure 3-3 Illustration of a mikto-arm star polymer as the constituting block copolymer for a graft copolymer.	47
Figure 3-4 Matsen phase diagram for AB ₂ mikto arm stars.....	49
Figure 3-5 Schematic representation of the YZ and XY-planes of the compression molded dogbone sample	51
Figure 3-6 SAXS curve and transmission electron micrograph for PCNL-78-12-99	57
Figure 3-7 Schematic illustration of the parameters used in the Percus-Yevick model ...	59
Figure 3-8 Small-angle x-ray scattering curves for PCNL-495-19-95 in the compression molded state and after annealing.....	62
Figure 3-9 Small-angle x-ray scattering curves for PCNL-495-19-80 in the compression molded state	63
Figure 4-1 Photograph of diffuse shear bands in polycarbonate.	71
Figure 4-2 Schematics and transmission electron micrograph of crazes in polymers	72
Figure 4-3 Characteristic small-angle x-ray scattering pattern from a craze.....	75
Figure 4-4 Plot of entanglement density versus normalized draw ratio	76
Figure 4-5 Tensile bar geometry and a representative plot of engineering stress versus displacement	84
Figure 4-6 Representative engineering tensile stress-strain curves of poly(D,L-lactide)..	87
Figure 4-7 Young's modulus, yield strength, strain at break, and post-yield stress drop for PDLLA-75k.	89
Figure 4-8 Scanning electron micrographs of PDLLA-59k after tensile fracture	91
Figure 4-9 Schematic illustration of the general viewpoints of the sample shown by camera 3 and camera 4.....	92
Figure 4-10 In-situ tensile data for PDLLA-58k in the aged condition (~25 °C for 66 h).	94

List of Figures	ix
Figure 4-11 Optical photos of aged PDLLA-58k probed with an x-ray beam of 9 keV ..	96
Figure 4-12 In-situ SAXS data for PDLLA-58k in the aged condition.....	98
Figure 4-13 The azimuthal ranges used for integration of the 2D scattered intensity patterns are schematically illustrated.	98
Figure 4-14 Curves of scattered intensity (I) versus wavevector (q) for aged PDLLA-58k.	99
Figure 4-15 In-situ tensile data for PDLLA-58k in the aged condition.....	102
Figure 4-16 In-situ SAXS data for PDLLA-58k in the unaged condition.....	103
Figure 4-17 The 1D SAXS curves for unaged PDLLA-58k in the equatorial range.....	104
Figure 4-18 The 1D SAXS curves for unaged PDLLA-58k in the meridional range. ..	105
Figure 4-19 Plots of intensity vs. azimuthal angle for PDLLA-58k	108
Figure 4-20 Schematic illustration of pre-yield SAXS streaks	109
Figure 4-21 Schematic illustration of shear crazes	110
Figure 4-22 The SAXS curves in the equatorial direction for PDLLA-58k.....	114
Figure 5-1 Schematic illustration of crazing in block copolymers	125
Figure 5-2 Average (a) Young's modulus and (b) yield strength of tensile samples	129
Figure 5-3 Average strain at break for tensile samples.....	131
Figure 5-4 Representative engineering stress-strain curves.....	132
Figure 5-5 Average neck initiation strain for tensile samples	133
Figure 5-6 In-situ tensile data for PCNL-594-90-95 aged at 25 °C for 66 h.....	134
Figure 5-7 In-situ 2D SAXS patterns for PCNL-594-90-95 aged at 25 °C for 66 h.	135
Figure 5-8 The azimuthal ranges used to obtain curves of intensity vs. wavevector.	136

Figure 5-9 The SAXS curves of integrated scattering intensity (I) versus wavevector (q) for aged PCNL-594-90-95	138
Figure 5-10 In-situ tensile stress vs. displacement for unaged PCNL-594-90-95.....	141
Figure 5-11 The 1D SAXS curves of scattered intensity (I) versus wavevector (q) for unaged PCNL-594-90-95 near the equatorial range.	143
Figure 5-12 The 1D SAXS curves of scattered intensity (I) versus wavevector (q) for unaged PCNL-594-90-95 near the meridian.....	145
Figure 5-13 Domain spacing plotted as a function of displacement and schematic of possible resulting morphology	147
Figure 5-14 In-situ tensile data for unaged PCNL-495-19-95	148
Figure 5-15 In-situ 2D SAXS patterns for unaged PCNL-495-19-95.	149
Figure 5-16 1D SAXS curves of scattered intensity (I) versus wavevector (q) for unaged PCNL-495-19-95 near the equatorial range.....	151
Figure 5-17 The 1D SAXS curves of scattered intensity (I) versus wavevector (q) for unaged PCNL-495-19-95 near the meridian.....	153
Figure 5-18 Domain spacing plotted as a function of displacement for unaged PCNL-495-19-95.	155
Figure 6-1 Schematic of the enthalpy change of a glassy polymer.	160
Figure 6-2 Differential scanning calorimetry (DSC) curves	161
Figure 6-3 Heating/cooling protocol.....	163
Figure 6-4 A schematic of excess enthalpy due to physical aging	166
Figure 6-5 Enthalpy change due to physical aging at various degrees of ΔT	170
Figure 6-6 The apparent activation energy, Δh^*	171
Figure 6-7 The average and standard deviation of the non-exponentiality (β) and non-linearity (x) parameters	173

List of Figures	xi
Figure A-1 In-situ tensile data for PCNL-594-90-95 aged at 25 °C for 66 h.	189
Figure A-2 Intensity versus azimuthal angle for aged PCNL-594-90-95.....	189
Figure A-3 In-situ tensile data for unaged PCNL-594-90-95 (-10 °C for 66 h).....	190
Figure A-4 Intensity versus azimuthal angle for unaged PCNL-594-19-95.....	190
Figure A-5 In-situ tensile stress vs. displacement for aged PCNL-495-19-95.....	191
Figure A-6 The in-situ 2D SAXS patterns for aged PCNL-495-19-95	191
Figure A-7 Intensity versus azimuthal angle for aged PCNL-495-19-95.....	192
Figure A-8 The 1D SAXS curves of scattered intensity (I) versus wavevector (q) for aged PCNL-495-19-95 near the equator.....	193
Figure A-9 The 1D SAXS curves of scattered intensity (I) versus wavevector (q) for aged PCNL-495-19-95 near the meridian	194
Figure A-10 Domain spacing plotted as a function of displacement for (i) aged PCNL-495-19-95 and (ii) unaged PCNL-495-19-95.	195

List of Abbreviations

a.u.	arbitrary units
ASTM	American Society for Testing and Materials
COD	1,5-cyclooctadiene
C_p	heat capacity
CTA	chain transfer agent
d^*	average interparticle spacing
DAB	1,4-cis-diacetoxy butene
DSC	differential scanning calorimetry
\bar{D}	molar mass dispersity
E	Young's modulus
G2	2 nd generation Grubbs' catalyst
H_∞	enthalpy at equilibrium
I	integrated intensity
L	lactide
l_A	packing length of species A
M_c	critical molar mass for entanglement
M_e	molar mass between entanglements
M_n	number-average molar mass
MW	molecular weight
n.a.	not applicable
n.d.	not determined
n.o.	not observed
NM	5-norbornene-2-methanol
N_n	number-average degree of polymerization
NOX	nitrogen oxides
NsL	norbornene-spiro-lactide
PB	polybutadiene
PC	polycarbonate
PCL	poly(ϵ -caprolactone)
PCN	poly(1,5-cyclooctadiene-co-5-norbornene-2-methanol)
PCNL	poly(1,5-cyclooctadiene-co-5-norbornene-2-methanol-graft-lactide)
PDLLA	poly(DL-lactide)
PLA	polylactide
PMMA	poly(methyl methacrylate)
PS	polystyrene
PTMC	poly(trimethylene carbonate)
PY	Percus-Yevick model
PYSD	post-yield stress drop
q^*	wavevector value of primary scattering peak
R_c	core radius in Percus-Yevick model

R_{g0}	unperturbed radius of gyration
R_{HS}	hard sphere radius in Percus-Yevick model
ROMP	ring-opening metathesis polymerization
ROP	ring-opening polymerization
ROTEP	ring-opening transesterification polymerization
RT	room temperature
SAXS	small-angle x-ray scattering
SEC	size-exclusion chromatography
SOX	sulphur oxides
T_a	aging temperature
TBD	1,5,7-triazabicyclo[4.4.0]dec-5-ene
TEM	transmission electron microscopy
T_f	Tool fictive temperature
T_g	glass transition temperature
T_m	melting point
TNM	Tool-Narayanaswamy-Moynihan model
T_{ODT}	order-disorder transition temperature
TOM	transmission optical microscopy
VCH	4-vinyl cyclohexene
vol. %	volume percent
wt. %	weight percent
x	non-linearity parameter
β	non-exponentiality parameter
Δh^*	apparent activation energy
ΔH_t	change in enthalpy at time t due to physical aging
ΔL	tensile displacement
ΔR	corona thickness in Percus-Yevick model
ΔT	level of undercooling, $T_g - T_A$
ϵ	engineering strain
ϵ_b	tensile strain at break
η	volume fraction of effective hard spheres in the Percus-Yevick model
λ	draw ratio
ν	effective entanglement density
σ	engineering stress
σ_y	tensile yield stress
τ_0	characteristic relaxation time
Φ_c	volume fraction of cores in the Percus-Yevick model
χ	effective Flory-Huggins interaction parameter

Chapter 1: Introduction

1.1 Motivation

Polymers have become indispensable to modern life, ranging in application from medical devices to packaging and even clothing. Yet, it has only been 100 years since the first fully synthetic polymer, Bakelite, was invented by Leo Baekeland.¹ It would take an additional 50 years from the synthesis of Bakelite to recognize that the basic structure of a polymer is a long molecule made up of covalently bonded atoms.¹ But now, the polymer industry is the 3rd largest manufacturing sector in the United States.² The utility and necessity of polymers stem from their unique combination of properties afforded by their intrinsic structure. How these long chains of atoms behave is quite different from that of other solid materials such as metals and ceramics. In general, polymers have relatively low density, yet high specific strength.³ They can be formed into useful objects easily at relatively low temperatures. Polymers may be amorphous, semi-crystalline or networked (cross-linked). The mechanical properties of polymers range broadly due to the variety of possible structures resulting in the application of polymers to every aspect of life. In 2008, 72.9 billion pounds of plastic was produced in the United States with high-density polyethylene, polystyrene and polypropylene comprising 54% of the total.⁴ These commodity polymers, like most of the polymers currently produced, are derived from crude oil and natural gas.

Decades of industrialization and consumption of natural resources has taken its toll on the Earth affecting not only the environment, but also the economy. The prolonged

and continual release of greenhouse gases (carbon dioxide, methane, NOX, SOX) into the Earth's atmosphere has triggered a global climate change. Scientific indicators include an upward trend of overall global temperature as well as record changes in rainfall patterns, sea level, and snow and ice coverage.⁵ Production of polymers contributes to the emission of greenhouse gases in the use of fossil fuels as manufacturing and transportation energy sources. Additionally, incineration of polymers as a disposal method also produces greenhouse gases. Other current polymer end-of-life options are recycling and solid waste disposal. While recycling may be more environmentally friendly, only 6.8% by weight of all plastics generated in 2007 were recycled.⁶ Discarded polymers that are not recycled or incinerated end up as litter or in a landfill where they remain useless for centuries.

As mentioned above, most polymers are derived from mined resources such as crude oil or natural gas. A number of factors have caused the price of these raw materials to increase. An increasing global demand for energy due to population growth, competition for crude oil with the transportation sector and the finite nature of these resources have and will continue to escalate the price. Data from the Energy Information Administration reveal that the production of crude oil in the U.S. peaked 20-30 years ago and is currently declining.⁷ Although the 3rd largest producer of oil, the U.S. imported 58% of the petroleum products it used in 2007.⁸ Eventually, the world's supply of crude oil and natural gas will be exhausted and another source of hydrocarbons will be

required. Global climate change and exorbitant increase in oil prices are but symptoms of an underlying systemic problem.

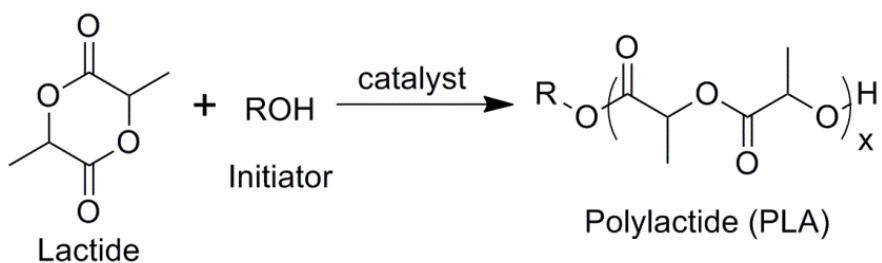
Many believe a new paradigm of sustainability is the solution. Sustainability is *“meeting the needs of the present without compromising the ability of future generations to meet their own needs.”*⁹ The idea of sustainability also became the national policy of the U.S. Environmental Protection Agency in 1969 as a commitment to *“create and maintain conditions under which [humans] and nature can exist in productive harmony, and fulfill the social, economic and other requirements of present and future generations of Americans.”*¹⁰ For polymers, sustainability entails using a raw material that can be responsibly replenished, utilizing alternative energy sources for manufacture, and reducing the contribution to the solid waste stream. Renewable resource polymers have the potential to meet these requirements. The starting material is derived from an annually renewable resource such as plants. Use of agriculture in this way may develop a new economic industry of biorefining which could utilize alternative energy sources such as solar and wind power.¹¹ Finally, new disposal options may be accessible as a result of the biologically derived starting material.

Poly lactide (PLA) is a renewable resource polymer already in commercial production. In addition to renewability, polylactide is biocompatible and hydro- and biodegradable. PLA products may be industrially composted within a reasonable time scale.¹² Polylactide has a low glass transition temperature ($T_g = 50 - 56$ °C) and an apparent lack of ductility. Thus, its application has primarily been limited to resorbable

medical devices, disposable food packaging and textile fiber. The overall goal of this work is to improve the utility of renewable resource polymers by increasing the toughness of polylactide. Enhancing the ductility of polylactide would enable its use in additional applications and offer a more sustainable alternative to petroleum-based polymers.

Lactic acid is a chiral carboxylic acid which can be naturally present in the human body.¹³ Currently, lactic acid is produced from the fermentation of dextrose. Dextrose can be obtained renewably from carbohydrate rich plants such as corn or sugar beets.¹⁴ Lactic acid may be a monomer for polylactide through condensation polymerization. The more commonly employed synthetic route is catalytic ring-opening polymerization¹⁵ (ROP) of lactide, a six-membered cyclic dimer of lactic acid (Scheme 1-1). Due to the chirality of lactic acid, lactide exists as three stereoisomers: L-lactide, D-lactide and meso-lactide. The stereoisomeric composition of the lactide feed and the stereoselectivity of the ROP catalyst will determine the stereoregularity of the resulting polymer.¹⁵ Stereoregular PLA is semi-crystalline, but this work will focus on poly(DL-lactide) [PDLLA] which is non-crystallizable due to the lack of stereoregularity. The remainder of this dissertation will use the abbreviations PLA and PDLLA interchangeably to refer to poly(DL-lactide).

Scheme 1-1



1.2 Strategy

Rubber toughening of brittle, glassy polymers is a well-studied approach that has been commercially successful for polymers such as polystyrene and poly(methylmethacrylate).¹⁶⁻¹⁸ Adding a rubbery phase to the glassy matrix allows for additional energy dissipating mechanisms during deformation. However, the apparent lack of ductility in PLA stems from its susceptibility to physical aging. Since the T_g of PLA is above room temperature, at normal use temperatures PLA is a kinetically-trapped metastable glass. Physical aging is a relaxation phenomenon that occurs in amorphous glasses as the system tries to approach thermodynamic equilibrium through local segmental motion of the polymer chains.¹⁶ A number of material properties change as a result of physical aging, including ductility. Experimental evidence has shown that the tensile strain at break of homopolymer polylactide can decrease from 300% strain to only ~ 15% strain after annealing at 25°C for 24 hours.¹⁹ Thus, the strategies utilized to toughen PLA may include altering the physical aging kinetics in addition to changing the brittle deformation mechanisms of physically aged PLA.

Of the possible methods to create a rubber-toughened material (plasticization²⁰, melt blending²⁰, reactive blending²¹), block copolymerization offers a large degree of synthetic control over block molecular weight and chain architecture, which in turn, can directly control phase morphology.²² Block copolymers containing polylactide and a rubbery polymer have been synthesized previously. Grijpma et al. synthesized linear ABA triblocks with the goal of increasing the toughness of polylactide.²³ The amorphous

polylactide blocks were synthesized from a monomer feed containing 15 mol% D-Lactide and 85 mol% L-lactide while the rubbery block was composed of either poly(trimethylene carbonate) (PTMC) or a random 50/50 copolymer of poly(trimethylene carbonate) and poly(ϵ -caprolactone) (PCL). For a composition of 80 wt% PLA, the researchers reported tensile yield stresses ranging from 36 – 41 MPa and strains at break from 120 – 210%. Differential scanning calorimetry and dynamic mechanical analysis were used to confirm microphase separation; however, no additional identification of morphology or deformation mechanism was performed.

Both chain architecture²⁴ and block copolymer morphology^{25,26} have been shown to significantly influence mechanical behavior, with lamellar structures exhibiting a desirable balance of strength and ductility. Utilizing a linear polymer architecture, the lamellar morphology is usually only attainable at glassy polymer compositions near 50 vol. %. However, by using a mikto-arm star architecture, where the simplest case consists of one arm of the glassy polymer (A) connected to two arms of the rubbery polymer (B) at a central point to form an AB₂ star, the lamellar morphology could be achieved at higher compositions of glassy polymer resulting in higher tensile strength and modulus.^{25,27} Further enhancement to strength and modulus could be achieved by tethering the chain ends of the rubbery block to prevent chain disentanglement.²⁸ In the case of a star polymer, joining multiple AB₂ stars together by the rubbery B arms will form a comb or graft copolymer. The B-blocks comprise the rubbery backbone with

glassy A blocks as the “teeth” of the comb. The phase diagram for the graft copolymer is only slightly altered with respect to its star counterpart.²⁹

Syntheses of polylactide containing block copolymers with graft architectures and star architectures have been reported. However, more often than not, the mechanical properties were not investigated or the block copolymer was simply used as a compatibilizer for physical blends.^{30–34} The synthetic methods employed to make polylactide grafted block copolymers often employ the “change of mechanism” strategy where the backbone is first polymerized by one technique followed by ring-opening polymerization of polylactide. Jha and coworkers synthesized a series of “ultralarge molecular weight bottlebrush polymers” which consisted of a poly(norbornene) backbone and poly(L-lactide) grafts (Figure 1-1).³⁵

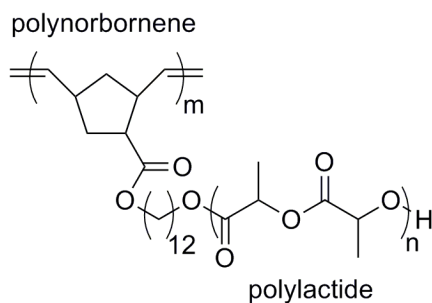
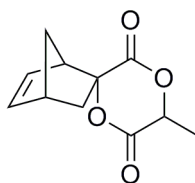


Figure 1-1 The chemical structure of a graft copolymer consisting of a polynorbornene backbone with polylactide grafts.³⁵

One of the approaches the researchers employed to construct these graft copolymers began with synthesis of the poly(norbornene) backbone by ring-opening metathesis polymerization³⁶ (ROMP) with Grubbs’ second generation catalyst to create a macroinitiator. The backbone was then used to initiate the ROP of poly(L-lactide)

catalyzed by tin(II) ethylhexanoate. High conversions and total molecular weights in excess of 1 million g/mol were obtained.

Relevant to this work, a new bifunctional monomer derived from lactide was synthesized and polymerized by Jing and Hillmyer.³⁷ The bifunctional monomer, shown in Figure 1-2, contains a lactide-like cyclic ester bonded to a norbornene-like moiety termed Norbornene-spiro-lactide (NsL).

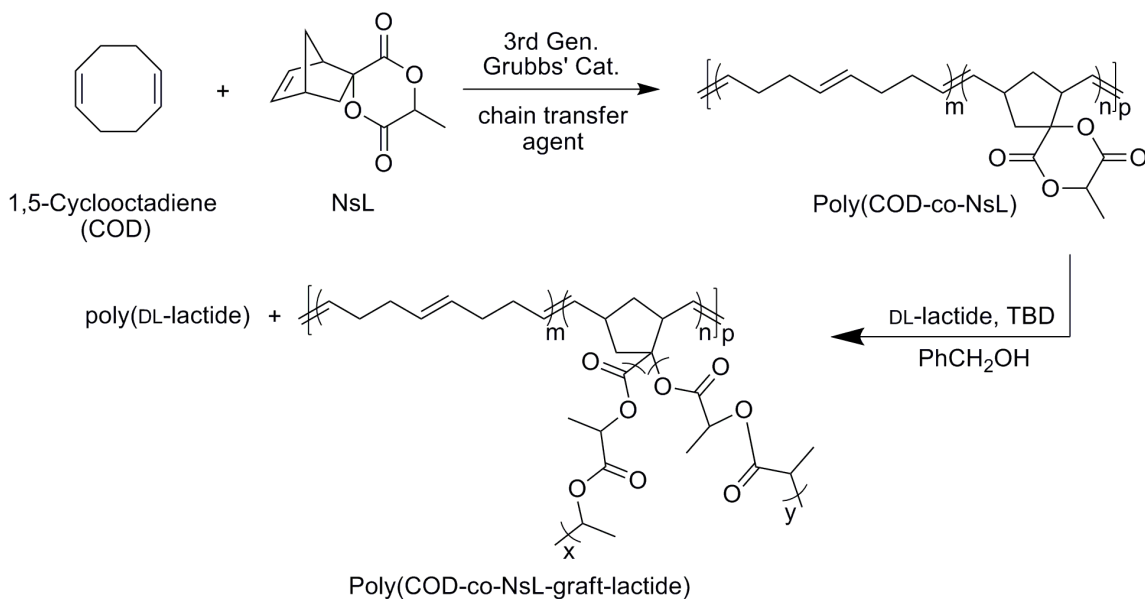


Norbornene-spiro-Lactide

Figure 1-2 The chemical structure of a bifunctional monomer, Norbornene-spiro-lactide, that can be polymerized by ring-opening metathesis polymerization or ring-opening polymerization.³⁷

As a result, the monomer could be polymerized by two different techniques: ROMP of the norbornene moiety yielding a functionalized poly(norbornene), or ROP of the cyclic ester yielding a polyester with pendant norbornene groups. A polylactide containing graft copolymer was synthesized using the bifunctional monomer as shown in Scheme 1-2. ROMP of 1,5-cyclooctadiene (COD) results in a polymer that is structurally identical to 1,4-polybutadiene. Thus, when the bifunctional monomer was copolymerized with COD through ROMP (using the 3rd generation Grubbs' catalyst), a poly(cyclooctadiene) backbone with interspersed lactide functionalized poly(norbornene) units [poly(COD-co-NsL)] was produced.

Scheme 1-2



ROP of the pendant lactide groups required external initiation by benzyl alcohol. Therefore, the ROP of the pendant lactide groups with D,L-lactide simultaneously produced homopolymer polylactide and poly(cyclooctadiene-graft-lactide). The ROP was catalyzed by 1,5,7-triazabicyclo[4.4.0]dec-5-ene (TBD), an organo catalyst that is active in solution at 25°C.³⁸ Polymerization of lactide by an organometallic catalyst, such as tin(II) 2-ethylhexanoate, requires much higher temperatures (>90°C) which could have resulted in oxidative degradation and cross-linking of the poly(cyclooctadiene) copolymer. The polymer “alloy” consisted of 20 wt% rubbery backbone and 80 wt% lactide, but the molecular weights of the homopolymer polylactide and the grafts were not characterized. Simplification and refinement of the previous synthetic scheme led to the two-step “grafting from” approach that is utilized in this work to create polylactide graft copolymers.

1.3 Overview of Dissertation

In summary, with the goal of rubber-toughening polylactide, high PLA content graft copolymers were synthesized using a two-step change-of-mechanism synthetic scheme (Chapter 2). The morphology of the graft copolymers were characterized by small-angle x-ray scattering (SAXS) and transmission electron microscopy (TEM). The observed morphologies were compared with the theoretical predictions for block copolymers possessing complex architectures (Chapter 3). The deformation mechanisms and effect of physical aging for homopolymer PDLA was then investigated by simultaneous SAXS and tensile testing experiments (Chapter 4). Then, the tensile deformation mechanisms and physical aging effects for a select number of graft copolymers was also explored by the same techniques for PDLA (Chapter 5). Finally, the influence of graft copolymerization on the kinetics of physical aging was monitored using differential scanning calorimetry (Chapter 6).

1.4 References

¹ Osswald, T. A.; Mengers, G., *Materials Science of Polymer for Engineers*; Hanser Publishers 2003.

² The Society of the Plastics Industry Plastics Fact Sheet. www.plasticsdatasource.org (accessed 03/23, 2009).

³ Callister, W. D. In *Materials Science and Engineering An Introduction*; John Wiley & Sons, Inc.: Hoboken, NJ, 2003.

⁴ American Chemistry Council December 2008 Resin Production and Sales Stats. http://www.americanchemistry.com/s_acc/sec_news_article.asp?CID=206&DID=9277 (accessed 03/23, 2009).

-
- ⁵ U.S. Environmental Protection Agency Basic Information Climate Change. <http://www.epa.gov/climatechange/basicinfo.html> (accessed 03/10, 2009).
- ⁶ U.S. Environmental Protection Agency Plastics Common Wastes and Materials. <http://www.epa.gov/epawaste/conserva/materials/plastics.htm> (accessed 03/10, 2009).
- ⁷ Energy Information Administration U.S. Crude Oil Field Production. <http://tonto.eia.doe.gov/dnav/pet/hist/mcrfpus1m.htm> (accessed 03/10, 2009).
- ⁸ Energy Information Administration EIA's Energy in Brief: How dependent are we on foreign oil? http://tonto.eia.doe.gov/energy_in_brief/foreign_oil_dependence.cfm (accessed 03/10, 2009).
- ⁹ World Commission on Environment and Development **1987**, *Annex to General Assembly document A/42/427*
- ¹⁰ U.S. Environmental Protection Agency Basic Information Sustainability. <http://www.epa.gov/sustainability/basicinfo.htm#sustainability> (accessed 03/10, 2009).
- ¹¹ Williams, C. K.; Hillmyer, M. A. *Polymer Reviews* **2008**, *48*, 1-10.
- ¹² Drumright, R. E.; Gruber, P. R.; Henton, D. E. *Adv Mater* **2000**, *12*, 1841-1846.
- ¹³ PURAC Lactic Acid- safe and natural. <http://www.lactic-acid.com/index.html> (accessed 03/02, 2009).
- ¹⁴ Vink, E. T. H.; Rabago, K. R.; Glassner, D. A.; Springs, B.; O'Connor, R. P.; Kolstad, J.; Gruber, P. R. *Macromol. Biosci.* **2004**, *4*, 551-564.
- ¹⁵ Dechy-Cabaret, O.; Martin-Vaca, B.; Bourissou, D. *Chem. Rev.* **2004**, *12*, 6147-6176.
- ¹⁶ Haward, R. N.; Young, R. J. In *The Physics of Glassy Polymers*. Chapman & Hall: London, 1997; pp 508.
- ¹⁷ Collyer, A. A. In *Rubber Toughened Engineering Plastics*. Chapman and Hall: London, UK, 1994; pp 366.
- ¹⁸ Arends, C. B. In *Polymer Toughening*. Hudgin, D. E., Ed.; *Plastics Engineering*; Marcel Dekker, Inc.: New York, NY, 1996; Vol. 30, pp 415.
- ¹⁹ Pan, P.; Zhu, B.; Inoue, Y. *Macromolecules* **2007**, *40*, 9664-9671.

-
- ²⁰ Anderson, K. S.; Schreck, K. M.; Hillmyer, M. A. *Polymer Reviews* **2008**, *48*, 85-108.
- ²¹ Liu, H.; Zhang, J. *Journal of Polymer Science Part B-Polymer Physics* **2011**, *15*, 1051-1083.
- ²² Bates, F. S.; Fredrickson, G. H. *Phys Today* **1999**, *2*, 32.
- ²³ Grijpma, D. W.; Van Hofslot, R. D. A.; Super, H.; Nijenhuis, A. J.; Pennings, A. J. *Polymer Engineering & Science* **1994**, *34*, 1674-1684
- ²⁴ Mori, Y.; Lim, L. S.; Bates, F. S. *Macromolecules* **2003**, *26*, 9879-9888.
- ²⁵ Adhikari, R.; Michler, G. H. *Progress in Polymer Science* **2004**, *9*, 949-986.
- ²⁶ Weidisch, R.; Ensslen, M.; Michler, G.; Fischer, H. *Macromolecules* **1999**, *32*, 5375-5382.
- ²⁷ Milner, S. T. *Macromolecules* **1994**, *8*, 2333-2335.
- ²⁸ Qiao, L.; Leibig, C.; Hahn, S. F.; Winey, K. I. *Ind Eng Chem Res* **2006**, *16*, 5598-5602.
- ²⁹ Matsen, M. W. *Macromolecules* **2012**, *4*, 2161-2165.
- ³⁰ Czelusniak, I.; Khosravi, E.; Kenwright, A. M.; Ansell, C. W. G. *Macromolecules* **2007**, *5*, 1444-1452.
- ³¹ Lemmouchi, Y.; Perry, M. C.; Amass, A. J.; Chakraborty, K.; Schacht, E. *Journal of Polymer Science Part A: Polymer Chemistry* **2007**, *45*, 3966-3974.
- ³² Wang, J.; Dong, C. *Macromolecular Chemistry and Physics* **2006**, *207*, 554-562.
- ³³ Chen, L.; Qiu, X.; Deng, M.; Hong, Z.; Luo, R.; Chen, X.; Jing, X. *Polymer* **2005**, *46*, 5723-5729.
- ³⁴ Joziassse, C. A. P.; Veenstra, H.; Topp, M. D. C.; Grijpma, D. W.; Pennings, A. J. *Polymer* **1998**, *39*, 467-473.
- ³⁵ Jha, S.; Dutta, S.; Bowden, N. B. *Macromolecules* **2004**, *37*, 4365-4374.
- ³⁶ Alonso-Villanueva, J.; Vilas, J. L.; Moreno, I.; Laza, J. M.; Rodriguez, M.; Leon, L. M. *Journal of Macromolecular Science Part A-Pure and Applied Chemistry* **2011**, *3*, 211-218.

³⁷Jing, F.; Hillmyer, M. A. *J. Am. Chem. Soc.* **2008**, *42*, 13826-13827.

³⁸Lohmeijer, B. G. G.; Pratt, R. C.; Leibfarth, F.; Logan, J. W.; Long, D. A.; Dove, A. P.; Nederberg, F.; Choi, J.; Wade, C.; Waymouth, R. M.; Hedrick, J. L. *Macromolecules* **2006**, *25*, 8574-8583.

Chapter 2: Synthesis of poly(1,5-cyclooctadiene-co-5-norbornene-2-methanol-graft-DL-lactide)

2.1 Background

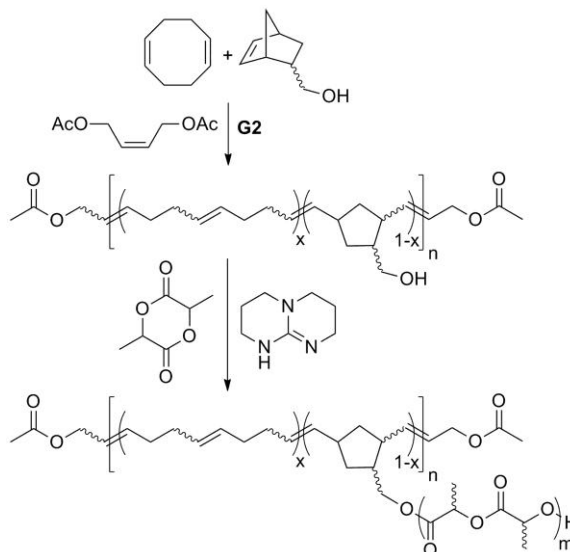
Syntheses of block copolymers containing PLA for modified mechanical behavior have been reported in the literature, and most typically employ a linear architecture with less than about 50 wt % PLA.¹⁻³ In the few reported cases of PLA block copolymers containing predominantly PLA, compositions of greater than 90 wt % PLA have rarely been explored.⁴ Twenty years ago, Grijpma and coworkers synthesized star-block copolymers of poly(trimethylene carbonate) [PTMC] and polylactide and found ductile behavior at a composition of 89 wt% PLA.⁵

Motivated by previous reports, we hypothesize that the synthesis and development of PLA graft copolymers may well provide materials with enhanced toughness.⁶⁻¹⁰ Recently, Jing and Hillmyer described the synthesis of a bifunctional monomer consisting of a lactone substituted with a norbornene moiety.¹¹ Ring-opening metathesis polymerization (ROMP) of the bifunctional monomer and 1,5-cyclooctadiene yielded a rubbery macromolecule with pendant lactones. Subsequent ring-opening transesterification polymerization (ROTEP) of D,L-lactide in the presence of the rubbery “backbone” provided mixtures composed of polylactide graft copolymer and homopolymer poly(D,L-lactide) [PLA]. At 20 wt % rubber, the composite material exhibited significantly enhanced tensile toughness (8×) as compared to a model PLA homopolymer.

Inspired by that study, we now introduce a simplified synthetic approach for the facile synthesis of polylactide graft copolymers utilizing both ROMP and ROTEP as shown in Scheme 2-1.¹²⁻¹⁵ First, a rubbery backbone is synthesized by ring-opening metathesis copolymerization of commercially available 1,5-cyclooctadiene (COD) and 5-norbornene-2-methanol (NM) catalyzed by the second-generation Grubbs' catalyst (G2).^{4,16} A chain transfer agent (CTA), cis-1,4-diacetoxy-2-butene, is used to control the degree of polymerization of the copolymer.¹⁷ The average number of grafts sites per chain and the average spacing between grafts can be controlled through the comonomer ratio and CTA concentration. ROP of D,L-lactide (**L**) from the **PCN** macroinitiator catalyzed by 1,5,7-triazabicyclo[4.4.0]dec-5-ene (TBD)^{18,19} provides the desired graft copolymer, poly(1,5-cyclooctadiene-co-5-norbornene-2-methanol-*graft*-D,L-lactide) [**PCNL**].

This chapter describes the two step synthetic route utilized to obtain asymmetric block copolymers composed of polylactide grafts emanating from a rubbery, olefinic linear backbone. Ring-opening metathesis polymerization proved to be a versatile and forgiving method for creating a low T_g copolymer which could serve as a macroinitiator for lactide polymerization. Following the description of the macroinitiators, the ring-opening polymerization of lactide initiated by the macroinitiators is detailed. Graft copolymers containing majority polylactide were targeted and characterized. The molecular weights and thermal properties of the graft copolymers discussed in this thesis are summarized in Table 2-2.

Scheme 2-1 Synthesis of polylactide graft copolymers



2.2 Experimental

2.2.1 Materials

ACS reagent grade starting materials and solvents were used as received from commercial suppliers without further purification unless otherwise stated. Degassed dichloromethane was purified by a commercial solvent purification system (MBraun). Degassed toluene was purified by a custom-made solvent purification line equipped with an activated alumina catalyst and a supported copper catalyst. Benzyl alcohol, 1,5-cyclooctadiene, cis-2-butene-1,4-diol diacetate, 5-norbornene-2-methanol and the Second Generation Grubbs (G2) catalyst were purchased from Aldrich. The 5-norbornene-2-methanol used contained 0.75 mol % dicyclopentadiene. 1,5-cyclooctadiene and cis-2-butene-1,4-diol diacetate were distilled over CaH_2 before use. After distillation, the 1,5-cyclooctadiene contained approximately 0.12 mol % vinyl cyclohexene. DL-lactide and L-

lactide (Purac) was recrystallized from toluene or ethyl acetate, dried under vacuum at room temperature for >24 h and stored under nitrogen.

2.2.2 General characterization methods

Proton nuclear magnetic spectroscopy (^1H NMR) was performed on a Varian Inova 500 at 500 MHz at room temperature. Samples were prepared in CDCl_3 (Cambridge Isotope Laboratories) to concentrations of approximately 18 mg per mL with subsequent filtering through glass wool to remove any dust. Chemical shifts are reported in ppm with respect to the residual chloroform proton signals assigned to 7.26 ppm. NMR data processing was performed using Varian software VNMR.

Size-exclusion chromatography (SEC) was performed at 35 °C on a Hewlett-Packard 1100 series liquid chromatograph equipped with three Plgel 5 μm Mixed-C columns in series and a Hewlett-Packard 1047A differential refractometer and will be denoted as “SEC CHCl_3 ”. Chloroform was used as the mobile phase with an elution rate of 1 mL/min. Samples were prepared by dissolving 1 to 2 mg of polymer in chloroform and filtering the solution through a 0.2 μm Teflon filter. Polystyrene standards (Polymer Laboratories) were used for calibration of molar mass. SEC also performed at 25 °C on an Agilent 1260 Infinity liquid chromatograph equipped with three Waters Styragel columns (HR6, HR4, HR1) and will be denoted as “SEC THF”. The system utilizes an Agilent 1260 Infinity Variable Wavelength detector, a Wyatt DAWN Heleos II light-scattering detector, and a Wyatt OPTILAB T-rex refractive index detector.

Tetrahydrofuran was used as the mobile phase with an elution rate of 1 mL min⁻¹. Samples were prepared by dissolving 1-2 mg of polymer in tetrahydrofuran and filtering the solution through a 0.2 µm Teflon filter. Polystyrene standards (Polymer Laboratories) were used for calibration of molar mass.

Differential scanning calorimetry (DSC) was performed on a TA DSC Q1000 utilizing an indium standard for temperature calibration. At least 4 mg of sample contained in hermetically sealed aluminum pans were analyzed under N₂ with a 10 °C/min heating rate. DSC was also performed on a TA Discovery DSC utilizing an indium standard for temperature calibration and a sapphire standard for heat capacity calibration. 3 to 5 mg of sample contained in a crimped T-zero aluminum pan was analyzed under N₂. Thermal transition temperatures were determined from the second heating after annealing above the glass transition or melting point for at least 1 min to erase thermal history. The glass transition temperature (T_g) was determined as the half-height midpoint of the transition.

2.2.3 General synthetic procedure for polylactide

In a dry box, DL-lactide [15 g, 0.104 mol], dichloromethane (120 mL) and benzyl alcohol (0.0298 g, 0.276 mmol) dissolved in dichloromethane (2 mL) were added to a 480 mL pressure vessel equipped with a stir bar. The vessel was sealed and the lactide was allowed to dissolve. A catalyst stock solution was made by dissolving 1,5,7-triazabicyclo[4.4.0]dec-5-ene (TBD) [27.8 mg, 0.199 mmol,] in dichloromethane (1 mL) in a 1-dram vial and sealed with a Teflon septum cap. After the lactide dissolved, 0.5 mL

of the catalyst stock solution was added to the vessel (target $[M]_0:[TBD]=1000$). The pressure vessel was sealed and removed from the dry box. The polymerization solution was allowed to stir for 60 min at RT before quenching with excess benzoic acid (> 10 equivalents) dissolved in dichloromethane (10 mL). The polymer was precipitated into hexanes one and methanol once before drying in a vacuum oven at 80–90 °C for four days.

2.2.4 General synthetic procedure for poly(1,5-cyclooctadiene-co-5-norbornene-2-methanol) [PCN]

In the dry box, a catalyst/CTA solution was prepared by adding cis-2-butene-1,4-diol diacetate (301 μ L, 1.91 mmol), 2nd generation Grubbs' catalyst (32.4 mg, 38.2 μ mol), and dichloromethane (40 mL) to a vial. To a 150 mL pressure vessel were added 5-norbornene-2-methanol (346 μ L, 2.86 mmol), 1,5-cyclooctadiene (10.0 g, 92.4 mmol), dichloromethane (30 mL), and a stir bar. 10 mL of the freshly prepared stock solution was added to the pressure vessel to initiate the polymerization at room temperature. After at least 20 h, the sealed vessel was removed from the dry box and the polymerization was quenched by adding an excess amount (>20 equivalents) of ethyl vinyl ether. The polymer solution was precipitated from methanol at least twice to remove catalyst residues and ethyl vinyl ether. The purified polymer was dissolved in 30 mL of CH_2Cl_2 . Butylated-hydroxy toluene (0.1 g) was added to the solution. A majority of the solvent was allowed to evaporated before the sample was vacuum dried at 30-40°C until all residual solvent was removed. Purified samples were stored at -20°C.

2.2.5 Procedure for time-resolved synthesis of PCN

In the dry box, G2 (0.006 g) was massed into a 20 mL scintillation vial and dissolved in 5 mL CH₂Cl₂. 5-norbornene-2-methanol (2.454 g) was added to a 150 mL pressure vessel by mass using glass pipette. 1,5-cyclooctadiene (14.997 g) was added to the pressure vessel using a 1 mL plastic syringe equipped with an 18 gage needle. A magnetic stirbar and CH₂Cl₂ (42 mL) were added to the pressure vessel. The G2 solution was added to the stirring pressure vessel and rinsed with CH₂Cl₂ (5 mL). Small aliquots (~1 mL) of the reaction mixture were pipetted into 1 dram vials and sealed with PTFE lined septa caps. The reaction was quenched after various reactions times ranging from 40 min to 48 h with excess ethyl vinyl ether ([ethyl vinyl ether]: [G2] > 10). ¹H NMR was performed on the crude aliquots as well as on samples precipitated in MeOH 1x. SEC was performed on the precipitated polymers.

2.2.6 General synthetic procedure for poly(1,5-cyclooctadiene-co-5-norbornene-2-methanol)-*graft*-poly(lactide) [PCNL]

Poly(1,5-cyclooctadiene-co-5-norbornene-2-methanol) was removed from the freezer and allowed to warm to RT (~15 min). The desired amount (0.71 g) was added to a 250 mL pressure vessel and brought into the dry box. In the dry box, dichloromethane (118 mL) and a magnetic stir bar were added to the pressure vessel which was then sealed. After PCN had dissolved (~30 min), DL-lactide (14.2 g, 98.6 mmol) was added and the pressure vessel sealed. The lactide was allowed to dissolve with stirring. A catalyst stock solution was made by dissolving 1,5,7-triazabicyclo[4.4.0]dec-5-ene (TBD)

[27.8 mg, 0.199 mmol] in dichloromethane (1 mL) in a 1 dram vial and sealed with a Teflon septum cap. The catalyst solution (0.5 mL) was added to the vessel and sealed. The polymerization was allowed to proceed for 30 to 60 min (depending on targeted molar mass) before removing the sealed vessel from the dry box. The reaction was then quenched with benzoic acid (>10 equivalents relative to TBD) dissolved in CH₂Cl₂ (10-20 ml). The polymer was precipitated into hexanes once and methanol once before dissolution in dichloromethane (180 mL). Butylated hydroxyl toluene (0.15 g, 0.7 mmol) was added to the polymer solution and dissolved. The mixture was then poured into a Teflon dish and allowed to dry under ambient pressures and temperatures for 3 days before drying in a vacuum oven at 80°C for four days.

2.2.7 Procedure for time-resolved synthesis of PCNL

In the dry box, a quench solution was made by dissolving benzoic acid (0.013 g) and butylated hydroxyl toluene (0.016 g) in CH₂Cl₂ (3.15 mL) in a glass scintillation vial. In a separate scintillation vial, PCN (0.007g) and DL-lactide (0.7 g, recrystallized from ethyl acetate) were dissolved in CH₂Cl₂ (5.6 mL). A catalyst stock solution of TBD (0.68 mg/mL) in CH₂Cl₂ made. 1 mL of the catalyst solution was added to the scintillation vial containing the dissolved macroinitiator and monomer and stirred on a magnetic stir plate. After various reaction times, an aliquot of the reaction mixture was removed using a fresh pipette and dispensed into a 1 dram vial containing 0.5 mL of the quench solution and a stir bar.

For comparison, a control reaction consisting of only monomer and catalyst (no initiator) was performed. In a dry box, DL-lactide (0.7 g) in a scintillation vial was dissolved with CH_2Cl_2 (5.6 mL) and stirring. A TBD stock solution (0.68 mg/mL) and benzoic acid solution (0.2 mg/mL) were made in CH_2Cl_2 . 1 mL of the TBD solution was added to the monomer solution. After various reaction times, aliquots (~ 1mL) were taken from the reaction mixture using a fresh pipette and dispensed into a 1 dram vial containing benzoic acid solution (0.5 mL).

2.3 Results

2.3.1 Poly(1,5-cyclooctadiene-co-5-norbornene-2-methanol)

Poly(1,5-cyclooctadiene-co-5-norbornene-2-methanol) [PCN] was successfully synthesized using ring-opening metathesis polymerization. The nomenclature used in this study is PCN-X-Y where X is the average degree of polymerization of 1,5-cyclooctadiene (COD) and the Y is the average number of 5-norbornene-2-methanol (NM) units per chain. Molar mass control was obtained through the use of chain transfer agents. A small amount of 4-vinyl cyclohexene (VCH), an isomer of COD was found in the monomer and acted as an adventitious chain transfer agent limiting the maximum possible degree of polymerization to ~600.²⁰ The further addition of 1,4-cis-diacetoxy butene (DAB) as a chain transfer agent allowed for smaller molar masses.²¹ The molar mass and NM content was monitored by ^1H NMR as shown in Figure 2-1. The degree of polymerization of COD was calculated by Equation 2-1 using the integrations of the ^1H NMR signals (Figure 2-1) from the olefinic protons (H_a), one of the two methylene

protons of the VCH endgroup (H_c), and the methylene protons of the acetoxy end group ($H_{d, trans}$ and $H_{d, cis}$).

$$N_n COD = \frac{H_a/4}{H_c + (H_{d,trans} + H_{d,cis})/4} \quad \text{Equation 2-1}$$

The NM content was determined using Equation 2-2 and the integration of the NMR signals from the methylene protons (H_e , H_f) on NM adjacent to the hydroxyl group and the olefinic protons of polymerized COD (H_a).

$$\text{mol \% Norbornene Methanol} = \frac{(H_e + H_f)/2}{H_a/4 + (H_e + H_f)/2} \quad \text{Equation 2-2}$$

Macroinitiators with a variety of parameters were synthesized. The degree of polymerization of COD ranged from 78 to 592 while the amount of NM ranged from 2 to 13 mol% (Table 2-1). A statistical distribution of NM in the copolymer was promoted by: the addition of DAB chain transfer agent, a low relative amount of NM, and long reaction times (~20h) to allow for many cross-metathesis reactions. Additionally, NMR analysis of crude aliquots of the synthesis of PCN-594-90 after various reaction times (40 min – 24 h) revealed that the conversion of COD and NM were the same at each time point and the polymer present in the crude mixture possessed a monomodal molecular weight distribution observed by SEC (Figure 2-2). Additionally, the relative amount of reacted NM to reacted COD in the reaction mixture remained constant at 13 mol% for every time point. Finally, DSC of the macroinitiator revealed only one T_g and multiple broad melting transitions (Figure 2-3). Although copolymerization reactivity ratios were not calculated,

the combined evidence suggests that the distribution of NM is likely close to statistical.

Table 2-1 summarizes the characteristics of the macroinitiators used to make graft copolymers for this study.

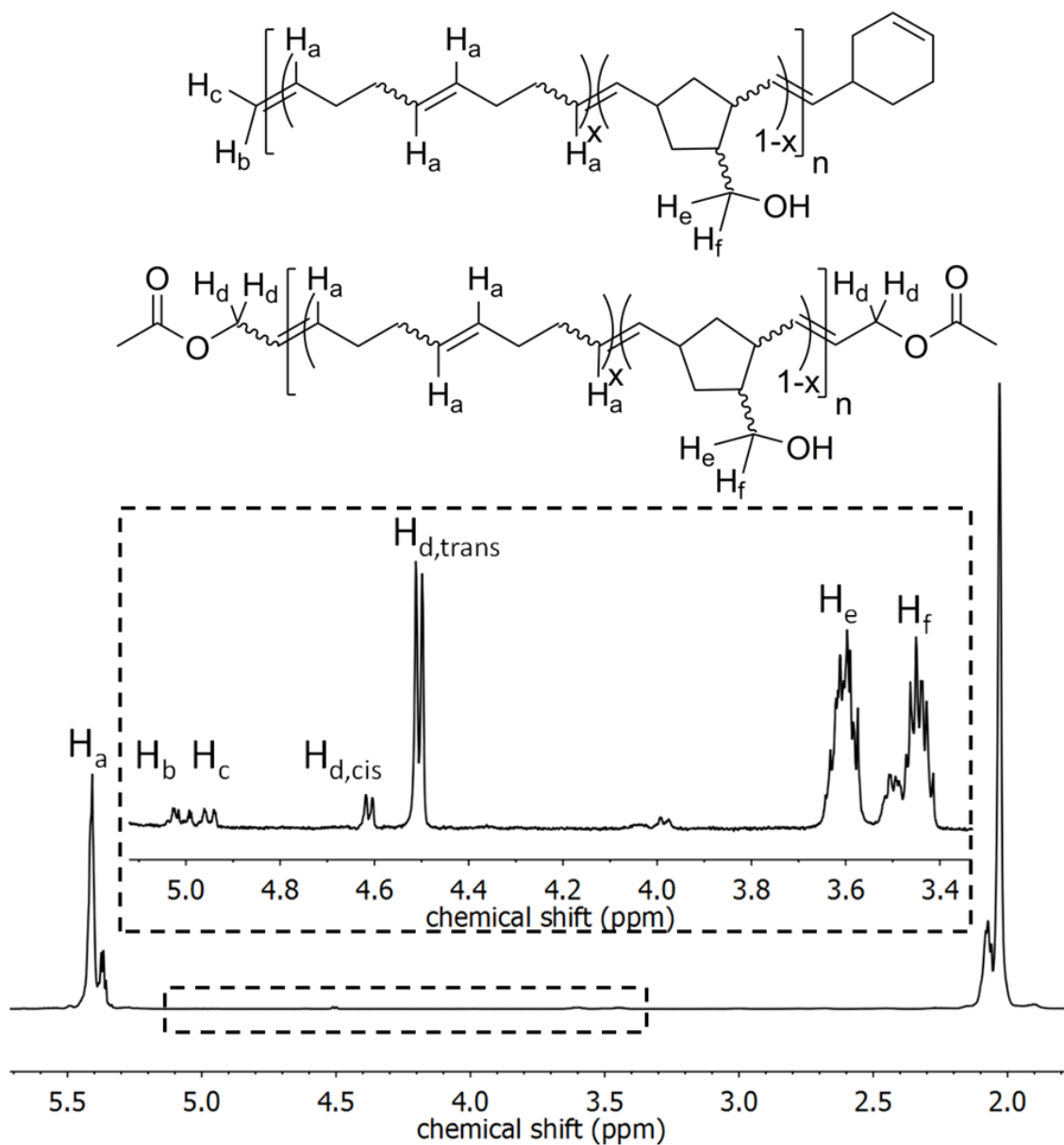


Figure 2-1 ^1H NMR spectrum of poly(1,5-cyclooctadiene-co-5-norbornene-2-methanol) in the chemical shift range of 1.8–5.7 ppm. The inset highlights the NMR signals of the macroinitiator end groups (H_b , H_c , H_d) and from the norbornene methanol (H_e , H_f).

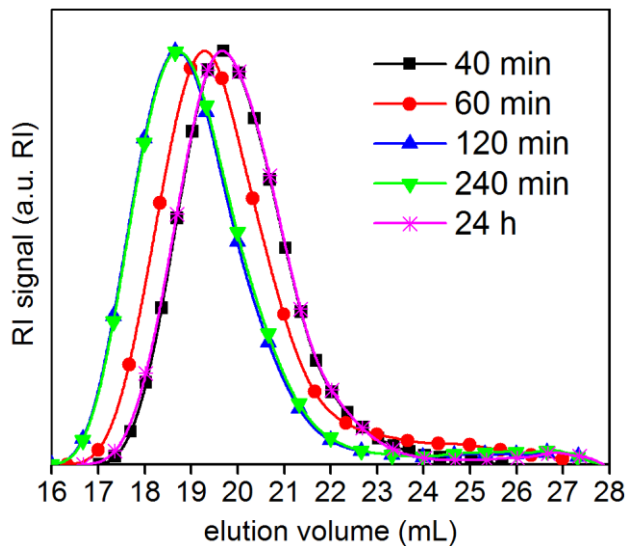


Figure 2-2 The molecular weight distribution of poly(1,5-cyclooctadiene-co-5-norbornene-2-methanol) quenched after various reaction times as determined by size-exclusion chromatography.

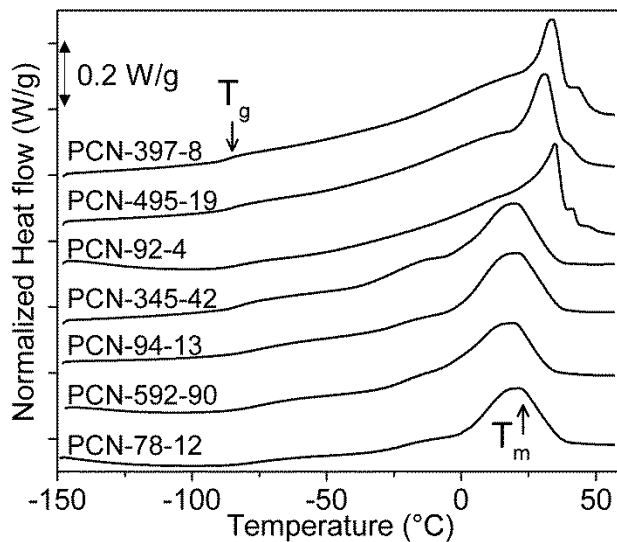


Figure 2-3 The DSC traces of the synthesized poly(1,5-cyclooctadiene-co-5-norbornene-2-methanol) [PCN] macroinitiators show a T_g near -80°C and broad melting transitions near room temperature.

Table 2-1 Poly(1,5-cyclooctadiene-co-5-norbornene-2-methanol) [PCN] macroinitiators

Nomenclature	N _n COD ^a	grafts /chain ^a	M _n eff (kg/mol) ^b	T _g (°C) ^c	T _m (°C) ^c	ΔH _m (J/g) ^c	% xtal ^d	Đ ^e
PCN-92-4	92	4	2.5	-81	34	54	63	
PCN-345-42	345	42	0.9	-81	18	39	46	2.5
PCN-397-8	397	8	5.4	-87	34	58	69	1.9
PCN-495-19	495	19	2.8	-85	31	50	59	2.0
PCN-594-90	594	90	0.7	-75	18	33	38	1.9
PCN-78-12[†]	78	12	0.7	-75	21	32	38	2.0
PCN-94-13[†]	94	13	0.8	-76	19	36	42	2.2
PCN-332-11[‡]	332	11	3.3	-81	33	16	18	1.7

^a Determined by ¹H NMR of as-dried sample

^b M_{n,eff} = N_n COD * 108/(grafts/chain)

^c Determined from 2nd heating after erasing thermal history

^d % crystallinity calculated assuming heat of fusion of trans-1,4-polybutadiene (85.2 J/g)²²

^e Determined by SEC in CHCl₃ at 35°C, calibrated with polystyrene standards

[†]Synthesized by Dr. Megan L. Robertson. [‡] Synthesized by Dr. Feng Jing.

2.3.2 Poly(1,5-cyclooctadiene-co-5-norbornene-2-methanol)-*graft*-poly(lactide)

2.3.2.1 Molar Mass Characterization

Polymerization of lactide grafts was achieved using PCN as a macroinitiator. An organic catalyst, 1,5,7-Triazabicyclo[4.4.0]dec-4-ene (TBD), was chosen due to its high functional group tolerance and relatively fast and controlled polymerization of lactide at room temperature^{18,19}. Polymerizations were allowed to reach ~99% conversion and thus, PLA content was controlled by the initial monomer feed. Graft copolymers with compositions ranging from 80 to 99 wt.% PLA were synthesized from the macroinitiators discussed in section 2.3.1 with reaction times ranging from 30 to 90 min at room temperature. The nomenclature used to describe the graft copolymers is PCNL-X-Y-Z, where the first two numbers pertain to the macroinitiator as explained above in section

2.3.1, and the last number denotes the weight percent of lactide in the graft copolymer. ^1H NMR of the graft copolymer (Figure 2-4) allowed for characterization of the composition and PLA graft M_n using Equations 2-3 and 2-4 respectively. After initiation, the ^1H NMR signals from the methylene protons adjacent to the hydroxyls in the macroinitiator shift from around 3.45 and 3.6 ppm (Figure 2-4, H_e and H_f) to centered around 3.95 and 4.15 ppm (Figure 2-4, H_d and H_c). The ^1H NMR signals from uninitiated hydroxyls were not observed in the spectra for the graft copolymers indicative of complete initiation of the macroinitiator hydroxyls. Additionally, the methine proton of the PLA end group was also observed at ~ 4.35 ppm (Figure 2-4, H_c). For some graft copolymers, an additional signal at ~ 3.75 ppm was observed (denoted by the asterisk in Figure 2-4). The origin of this signal will be discussed below.

$$wt\% \text{ PLA} = \frac{\left(\frac{H_b}{2}\right) 144 \frac{g}{mol}}{\left(\frac{H_b}{2}\right) 144 \frac{g}{mol} + \left(\frac{H_a}{4}\right) 108 \frac{g}{mol}} \times 100\% \quad \text{Equation 2-3}$$

$$M_n \text{ PLA graft} = \left(\frac{H_b/2}{H_c/2}\right) \times 144 \frac{g}{mol} \quad \text{or} \quad \left(\frac{H_b/2}{H_d + H_e/2}\right) \times 144 \frac{g}{mol} \quad \text{Equation 2-4}$$

$$\begin{aligned} & \text{Expected } M_{n,PLA} \\ & = \frac{w_{PLA} \left[\left(108 \frac{g}{mol} \times N_{n,COD}\right) + \left(124 \frac{g}{mol} \times \frac{\text{avg. \# hydroxyls}}{PCN \text{ chain}}\right) \right]}{(1 - w_{PLA}) \left[\frac{\text{avg. \# hydroxyls}}{PCN \text{ chain}} \right]} \quad \text{Equation 2-5} \end{aligned}$$

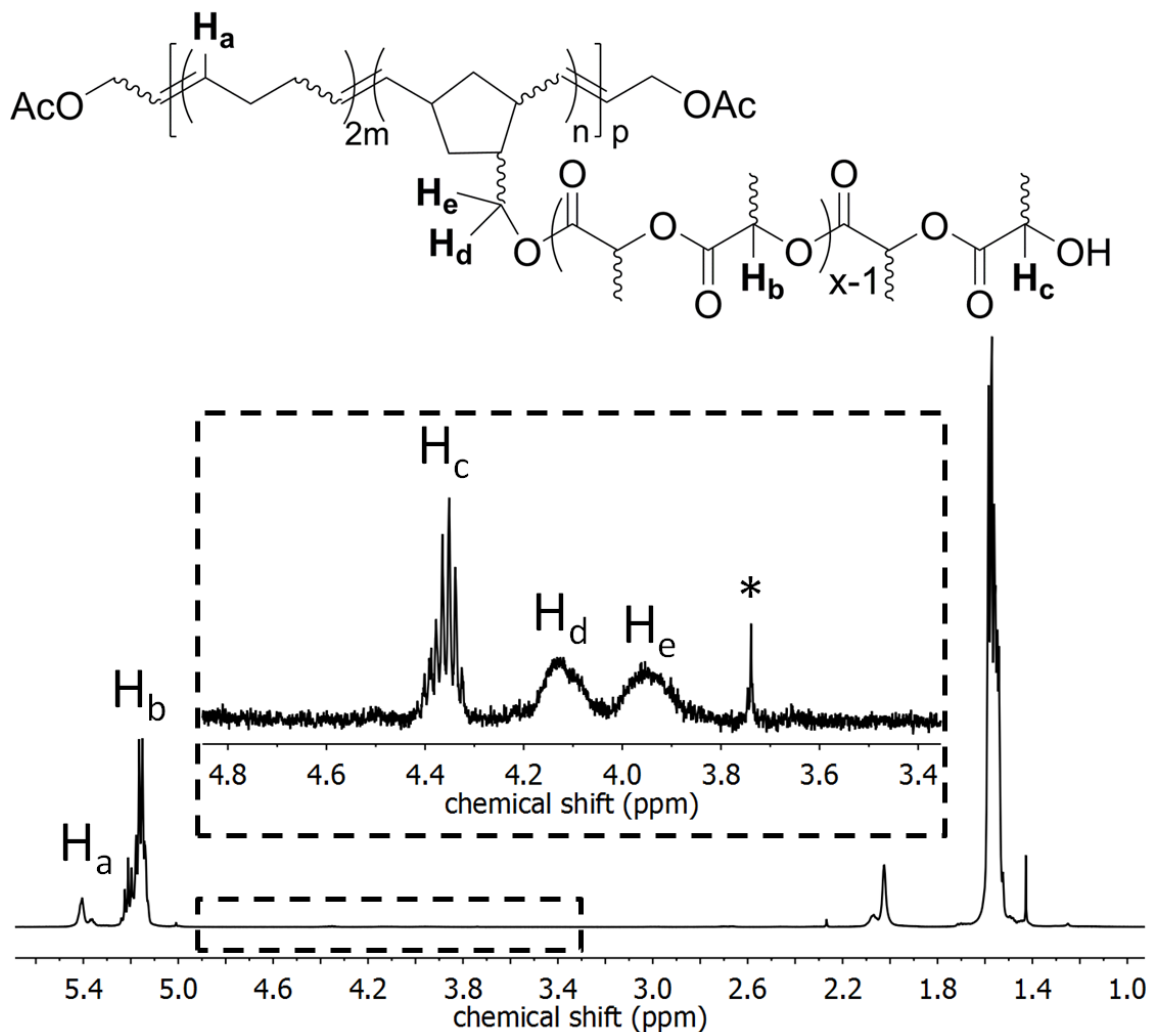


Figure 2-4 ¹H NMR spectrum of poly(1,5-cyclooctadiene-co-5-norbornene-2-methanol)-graft-poly(DL-lactide) [PCNL] in the chemical shift range of 0.9–5.7 ppm. The signals from the olefinic methine protons of the macroinitiator (H_a) and the methine protons of the polylactide main chain (H_b) are utilized to determine the composition of PCNL. The inset highlights the NMR signals from the methine proton of the PLA end group (H_c) and from the methylene protons adjacent to the reacted hydroxyl groups of the norbornene methanol in the macroinitiator (H_d, H_e). The asterisk (*) highlights a set of peaks (~3.75 ppm) that was observed in some of the graft copolymers and is likely an end group of adventitiously initiated homopolymer polylactide chains.

Using the M_n of the macroinitiator and the average number of hydroxyls per chain of the macroinitiator as determined by ¹H NMR of the macroinitiator, and the

composition as determined by ^1H NMR of the purified graft copolymer, an expected PLA M_n was calculated (Equation 2-5) and compared with the measured PLA M_n calculated by end-group analysis using the PLA end group methine proton (H_c) and the methylene protons (H_d , H_e) adjacent to the hydroxyl of the initiator. As seen in Figure 2-5, fairly good agreement between the expected and both measured values of PLA M_n is found until an expected M_n of ~ 60 kg/mol regardless of composition. The PLA M_n measured from the methine proton is consistently less than expected for graft copolymers with expected $M_n \geq 60$ kg/mol. On the other hand, the PLA M_n measured from the methylene protons originally from the initiator agrees with the expected PLA M_n within the error of NMR measurement for high molar mass polymers. The lack of agreement between the two end groups suggests that the ring-opening polymerization of lactide catalyzed by TBD and initiated by PCN is not well controlled for reactions where $[\text{M}]_0 : [\text{OH}] > 400$.

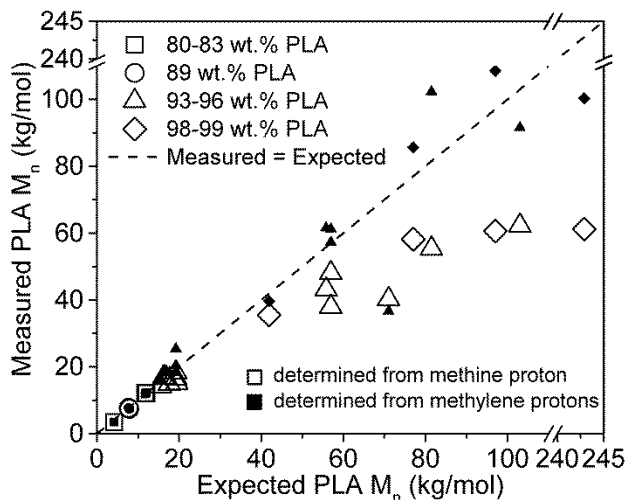


Figure 2-5 End group analysis from ^1H NMR data of graft copolymers was used to measure the M_n of PLA based on the methine proton (open symbols) and the methylene protons (solid symbols) adjacent to the hydroxyl group of the initiator for a range of PLA compositions. The measured values are compared to the expected PLA M_n that is calculated knowing the M_n of the macroinitiator, the average number of hydroxyls per macroinitiator chain and the graft copolymer composition.

This is further illustrated by comparison of the molecular weight distributions of a series of graft copolymers initiated from the same macroinitiator but varying in PLA composition resulting in various values of $[M]_0 : [\text{OH}]$ as shown in Figure 2-6. The molecular weight distribution, as characterized by SEC, is monomodal for both the 80 and 90 wt.% PLA polymers where the $[M]_0 : [\text{OH}]$ was 82 and 176 respectively. In contrast, the 95 wt.% PLA graft copolymer has both a high molecular weight shoulder and a low molecular weight tail. The 99 wt.% PLA graft copolymer has a high molecular weight minor shoulder adjacent to a very broad major peak which has a peak maximum occurring at a lower molecular weight than all the other graft copolymers.

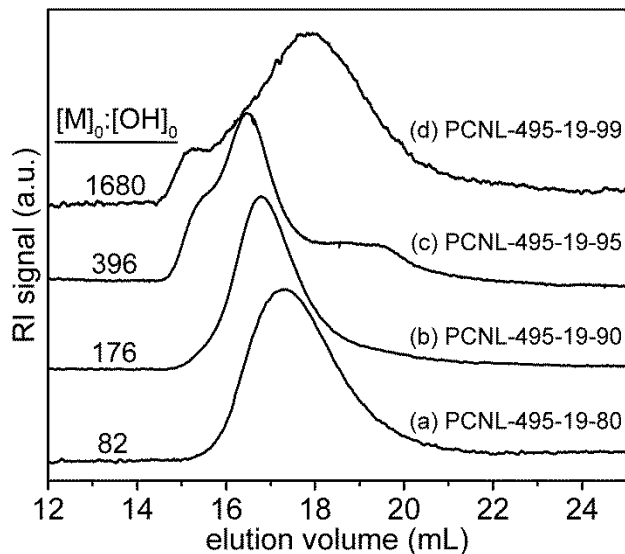


Figure 2-6 The size-exclusion chromatograms for a series of graft copolymers synthesized from the same macroinitiator are compared to illustrate the loss of polymerization control when $[M]_0:[OH]$ exceeds approximately 400.

To elucidate the origin of the shape of the molecular weight distributions, syntheses of PCNL-332-11-95 (Figure 2-7) and PCNL-495-19-99 (Figure 2-9) and the respective control reactions were quenched at various times and characterized by SEC. The control reactions consisted of lactide and TBD without added initiator in the same concentrations as their respective graft copolymer polymerization reactions. In the case of PCNL-332-11-95 (Figure 2-7), after 1 minute of reaction time, the SEC trace shows a high MW peak with a lower MW peak/tail. Unexpectedly, the control reaction, devoid of added initiator, also shows a peak in SEC after 1 minute of reaction, which corresponds to low MW polylactide initiated adventitiously as confirmed by ^1H NMR (Figure 2-8). The signal observed previously in the representative ^1H NMR spectrum of purified graft copolymer at ~ 3.75 ppm (Figure 2-4, denoted by an asterisk) is also seen in the spectrum of the control reaction mixture before purification starting at 15 minutes of reaction time

confirming the origin of the signal. Furthermore, the peak in the control reaction possesses a similar peak elution volume as the low MW peak/tail in the graft copolymer reaction after 1 minute. As the reaction progresses in time, the molecular weight distribution of the graft copolymer shifts to lower elution volume while mostly retaining the multimodal shape previously observed at 1 minute indicating that both the graft copolymer and adventitiously initiated PLA are increasing in MW. Likewise, in the control, as the reaction time increases, the SEC peak shifts to higher MW with little change to the shape of the peak and similar peak elution volume as in the graft copolymer. Thus, the lower MW tail observed in the SEC trace of PCNL-332-11-95 is attributed to adventitiously initiated homopolymer PLA. ^1H NMR end group analysis of the control reaction after 60 minutes a number-average degree of polymerization of 362. Assuming that the adventitiously initiated homopolymer in the graft polymerization has the same degree of polymerization as the control, the actual composition of the graft copolymer is found to be 93.9 wt. % polylactide with a PLA M_n of 45.5 kg/mol. The homopolymer PLA comprises 14 wt.% of the graft copolymer/homopolymer blend and has an M_n of 52.1 kg/mol.

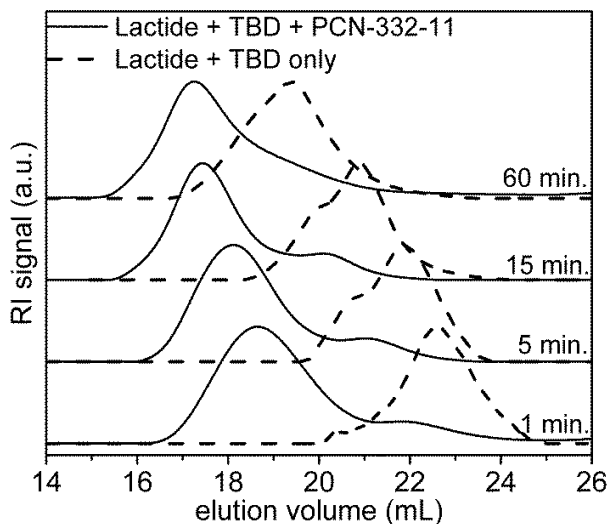


Figure 2-7 The SEC traces of the synthesis of PCNL-332-19-95 (—) and a control (---) devoid of macroinitiator are compared at various times during the reaction revealing that the low molecular tail present in the final graft copolymer (—) is adventitiously initiated PLA.

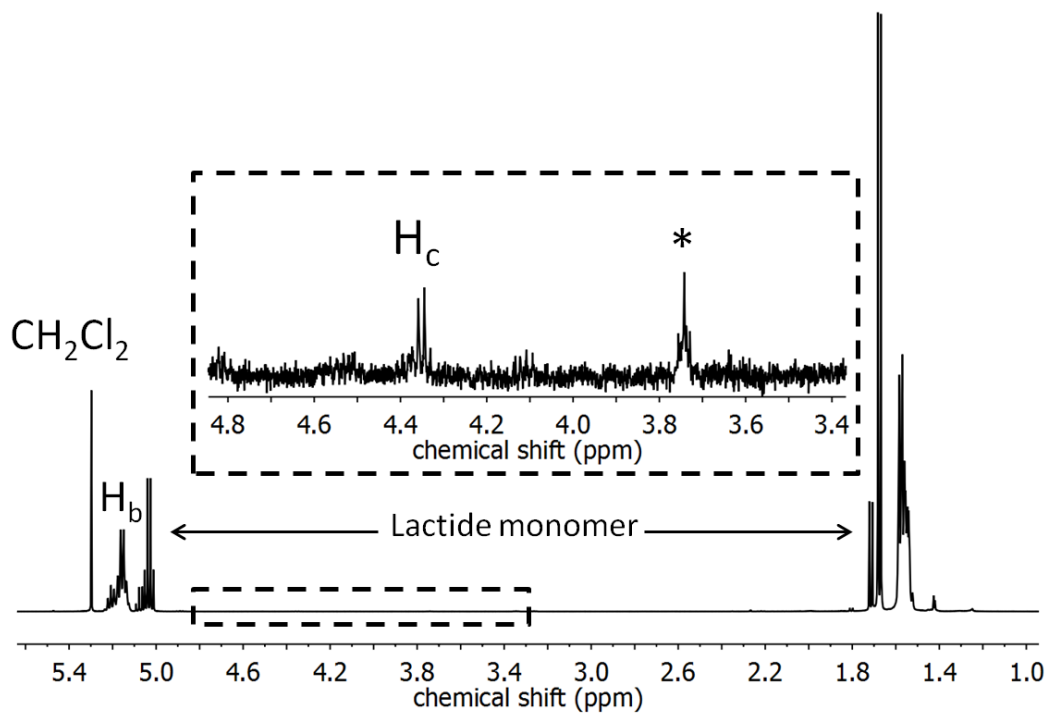


Figure 2-8 The ^1H NMR spectrum of a control reaction, before purification, containing only lactide and catalyst (1,5,7-triazabicyclo[4.4.0]dec-5-ene) in the same concentrations as in the polymerization of PCNL-332-11-95. Signals corresponding to polylactide (H_b) and the methine end group proton (H_c) are observed in addition to the unknown signal (*) observed previously in the spectrum for the graft copolymer.

In the case of PCNL-495-19-99 (Figure 2-9), after 5 minutes of reaction, the product has a bimodal distribution with similar intensity in both of the peaks. As before, the control reaction in which no initiator was added, also exhibited a polymer product after only a few minutes of reaction. In fact, the product from the control reaction has the same shape and nearly the same peak elution volume as the lower MW peak observed in the graft copolymer after 5 minutes. After 15 minutes both peaks in the graft copolymerization shift to lower elution volume and a high MW shoulder develops on the higher MW peak due to the MW limitation of the SEC columns. Additionally, the intensity of the peak from adventitiously initiated PLA increases relative to the higher MW graft copolymer peak. Finally, after 60 minutes, the high MW peak shifts into the position where the high MW shoulder was observed previously while the peak from the adventitiously initiated PLA increases in dispersity, MW and relative intensity. ^1H NMR end group analysis of the crude product of the control reaction after 30 minutes revealed 70% conversion of lactide monomer to polymer and a degree of polymerization of 415. Thus, at full conversion, N_n is expected to be ~ 595 . Using this value and the ^1H NMR data of the graft copolymerization product after 60 minutes, the actual composition of the graft copolymer was found to be 97.7% polylactide with a PLA M_n of 126.1 kg/mol. The adventitiously initiated homopolymer PLA is estimated to comprise 44 wt.% of the product and have an M_n of 85.7 kg/mol. The high MW shoulder observed in the SEC trace of the graft copolymer, first observed after 15 minutes in Figure 2-9, is believed to result from some of the graft copolymer chains exceeding the MW range of the SEC

separation columns. Thus, the highest MW chains are all eluted at the same time without separation resulting in the high MW shoulder.

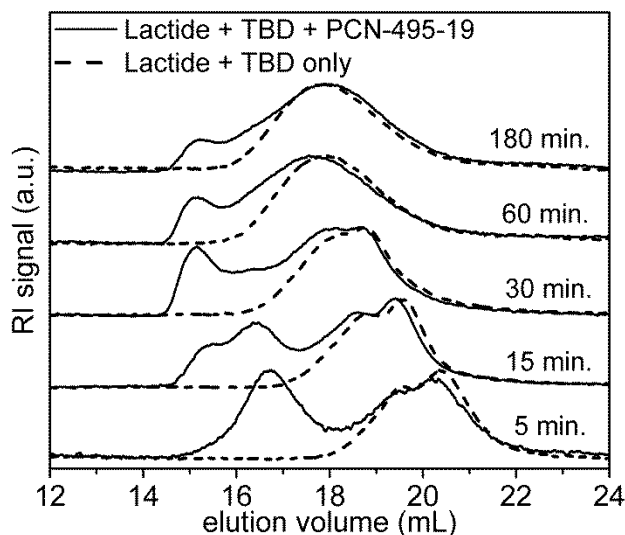


Figure 2-9 The SEC traces of the synthesis of PCNL-495-19-99 (—) and a control (---) devoid of macroinitiator are compared at various times during the reaction revealing that the lower molecular weight peak present in the graft copolymer is adventitiously initiated polylactide.

Complete molecular weight characterization of the graft copolymers with $[M]_0:[I]_0 > \sim 400$ requires isolation of the adventitiously initiated homopolymer PLA either by fractionation or time-resolved synthesis in order to independently determine the N_n of the homopolymer PLA. Solvent/non-solvent fraction with acetone and hexanes was attempted with PCNL-495-19-95 and PCNL-19-99. In both cases, all of the adventitiously initiated homopolymer PLA could not be isolated completely and without contamination from small amounts of graft copolymer. The time-consuming nature of time-resolved syntheses prevented the complete characterization of all the graft copolymers which contain adventitiously initiated PLA. Therefore, it is assumed that graft copolymers with $[M]_0:[I]_0 > \sim 400$ are blends of graft copolymer and homopolymer

PLA and that the relative amount of homopolymer increases in proportion to the $[M]_0:[I]_0$ value. The molecular weight and dispersity of the graft copolymers discussed in this thesis are summarized in Table 2-2.

2.3.2.2 Thermal properties

Differential scanning calorimetry of the graft copolymers revealed PLA T_g 's in the typical range of 50-60°C for poly(DL-lactide)²³ as seen in Figure 2-10 which compares PCNLs initiated from the same macroinitiator (also shown in Figure 2-10) but, varying in PLA content. However, even at the lowest PLA content (89 wt. %), the T_g of the PCN backbone was not observed, likely due to the small relative amount of PCN in the copolymers. For most of the graft copolymers, a weak endotherm corresponding to the T_m of PCN was observed. However, the intensity of the melting transition (and thus, the crystallinity) appeared to decrease with increasing PLA content. In some cases, the T_m of PCN was not observed at all. The T_m of PCN was found to correlate with the graft spacing as characterized by $M_{n,eff}$ (molar mass of COD in the backbone divided by average number of grafts) regardless of PLA composition (Figure 2-11, bottom and left axes). Additionally, the T_g of PLA generally correlated with the measured PLA M_n (Figure 2-11, top and right axes). The scatter in the data may result from an inaccurately measured $M_{n,PLA}$ for those graft copolymers which contain adventitiously initiated homopolymer PLA. The lack of $T_{g,PLA}$ depression is consistent with microphase separation of the PCN and PLA components. Using the heat of fusion for all trans poly(1,4-butadiene), 85.2 J/g²², the percent crystallinity of the rubbery backbone in the

entire polymer was calculated and found to be rather low (~1%) on average. Ultimately, the thermal characterization indicates that the graft copolymer is microphase separated. The PCN in the graft copolymer is likely amorphous at room temperature due to the small amount of crystallinity in addition to a value of T_m at or below room temperature. The thermal characteristics of the graft copolymers discussed in this thesis are summarized in Table 2-2.

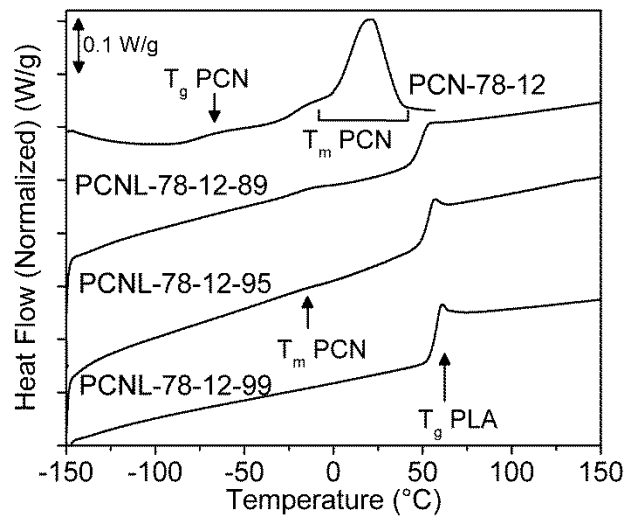


Figure 2-10 The differential scanning calorimetry traces of the PCN-78-12 macroinitiator and its respective graft copolymers containing various relative amounts of PLA are compared. The data was collected upon heating at 10°C/min after erasing thermal history.

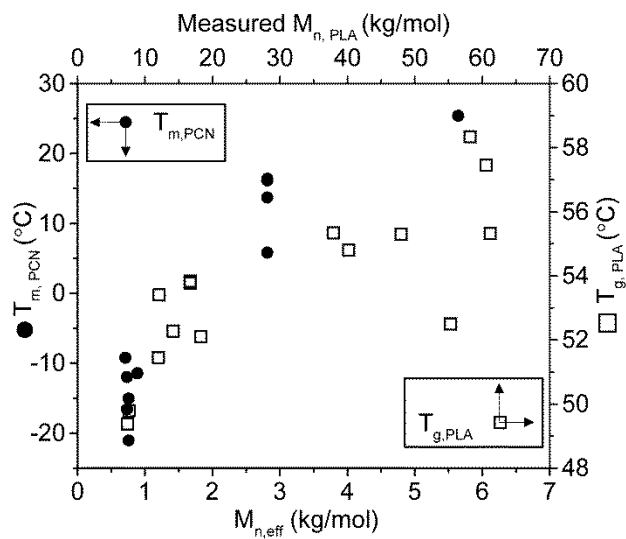


Figure 2-11 The peak melting point of the PCN backbone in the graft copolymer ($T_{m,PCN}$, ●) is found to increase with increasing graft spacing characterized by $M_{n,eff}$ (left and bottom axes). The T_g of PLA (□) in the graft copolymer appears to trend with the PLA M_n as calculated by the methine proton in 1H NMR (right and top axes).

2.3.2.3 Library of graft copolymers

Table 2-2 Library of poly(1,5-cyclooctadiene-co-5-norbornene-2-methanol)-*graft*-poly(DL-lactide) characteristics

Nomenclature	wt.% PLA ²	N _n COD ¹	Grafts/chain ¹	M _{n,eff} COD ¹ (kg/mol)	M _{n,PLA} methine proton ² (kg/mol)	M _{n,PLA} methylene protons ² (kg/mol)	Đ ³	Homopolymer PLA ³		PCN		PLA T _g ⁴ (°C)
								wt.%	M _n (kg/mol)	T _m ⁴ (°C)	% xtal	
PCNL-495-19-80	80	495	19	2.8	12.1	11.8	1.8	n/a	n/a	16.4	4.2	53.4
PCNL-495-19-81	81	495	19	2.8	12.0	12.2		n/a	n/a	16.2	5.2	53.1
PCNL-78-12-89	89	78	12	0.7	7.7	7.7	1.5	n/a	n/a	-12.0	1.1	49.8
PCNL-94-13-89	89	94	13	0.8	7.4	7.4	1.6	n/a	n/a	-15.1	0.8	49.4
PCNL-594-90-95	95	594	90	0.7	14.2	15.7		n/a	n/a	-9.2	0.4	52.3
PCNL-78-12-95	95	78	12	0.7	16.8	18.4	1.5	n/a	n/a	-16.6	0.1	53.8
PCNL-94-13-95	95	94	13	0.8	16.7	18.1	1.4	n/a	n/a	-21.0	0.3	53.8
PCNL-345-42-95	95	345	42	0.9	18.3	20.4	2.0	n/a	n/a	-11.4	0.7	52.1
PCNL-92-4-96	96	92	4	2.8	40.2	36.6	2.8	n/a	n/a	n/o	n/o	54.4
PCNL-397-8-93	93	397	7.6	5.6	46.9	56.5	2.4	n/d	n/d	25.4	1.1	52.5
PCNL-495-19-95	95	495	19	2.8	48.0	57.2	2.3	n/d	n/d	13.7	0.9	55.3
PCNL-495-19-95	95	495	19	2.8	37.9	61.2		n/d	n/d	n/o	n/o	54.7
PCNL-332-11-95	95	332	11	3.3	46.2	54.6	2.9	14	52	n/d	n/d	n/d
PCNL-332-11-95	95	332	11	3.3	62.2	69.9	2.3	n/d	n/d	19.5	0.8	57.0
PCNL-397-8-95	95	397	8	5.6	62.2	91.5	2.5	n/d	n/d	n/d	n/d	n/d
PCNL-78-12-99	99	78	12	0.7	58.2	85.7	4.3	n/d	n/d	n/o	n/o	58.3
PCNL-94-13-99	99	94	13	0.8	60.6	108.5	4.7	n/d	n/d	n/o	n/o	57.5
PCNL-495-19-99	99	495	19	2.8	61.2	100.3	4.0	44.4	85.7	5.8	0.2	55.3

¹ Determined from ¹H NMR of macroinitiator, ² Determined from ¹H NMR of graft copolymer, ³ Determined by SEC in CHCl₃ at 35°C calibrated with polystyrene standards, ⁴ Determined by DSC upon heating at 10 °C/min after erasing thermal history, n/a- not applicable, n/d-not determined., n/o- not observed.

2.4 Summary

In general, the two step synthetic route of ROMP of 1,5-cyclooctadiene and 5-norbornene-2-methanol followed by ROP of lactide was successful for yielding graft copolymers with a rubbery backbone and statistically spaced polylactide grafts. Low T_g (around $-80\text{ }^\circ\text{C}$) PCN macroinitiators with a range of molar masses and hydroxyl content were synthesized in quantitative yield. The comonomer content, as determined by ^1H NMR, reflected the initial comonomer feed. Prolong reaction times and a chain transfer agent was used to promote a statistical distribution of the hydroxyl-functionalized comonomer. Ring-opening polymerization of lactide initiated from the macroinitiators and catalyzed by TBD appeared to well-controlled for graft copolymers where $[\text{M}]_0 : [\text{I}] < \sim 400$. Complete initiation of the pendant hydroxyl groups was confirmed by ^1H NMR. However, adventitious initiation of PLA by TBD became kinetically competitive with propagation from the macroinitiator for graft copolymers where $[\text{M}]_0 : [\text{I}] > \sim 400$, resulting in a blend of graft copolymer and homopolymer PLA. Complete characterization of the mixture required isolation of the adventitiously initiated homopolymer. Solvent/non-solvent fractionation did not successfully isolate the homopolymer; however, time-resolved synthesis of the graft copolymers and the control reaction (no added initiator) allowed for estimation of the molar mass of the homopolymer. Thermal characterization of the PCNL graft copolymers ultimately indicated the backbone to be likely amorphous and microphase separated from the PLA matrix.

2.5 Acknowledgements

Thanks to Dr. Feng Jing, Dr. Louis M. Pitet and Dr. Megan L. Robertson for assisting with the synthesis of the graft copolymers in the early stages of the project.

This work was supported by the USDA and the U.S. DOE through Grant DE-PS36-06GO96002P. This work was also supported by the Center for Sustainable Polymers, an NSF-funded Center for Chemical Innovation at the University of Minnesota. Parts of this work were carried out in the Institute of Technology Characterization Facility, University of Minnesota, a member of the NSF-funded Materials Research Facilities Network.

2.6 References

- ¹ Frick, E. M.; Zalusky, A. S.; Hillmyer, M. A. *Biomacromolecules* **2003**, *4*, 216–223.
- ² Cohn, D.; Hotovely-Salomon, A. *Polymer* **2005**, *46*, 2068–2075.
- ³ Wanamaker, C. L.; O'Leary, L. E.; Lynd, N. A.; Hillmyer, M. A.; Tolman, W. B. *Biomacromolecules* **2007**, *8*, 3634–3640.
- ⁴ Pitet, L. M.; Hillmyer, M. A. *Macromolecules* **2009**, *42*, 3674–3680.
- ⁵ Grijpma, D. W.; Joziase, C. A. P.; Pennings, A. J. *Makromol. Chem.-Rapid* **1993**, *14*, 155–161.
- ⁶ Pae, Y. *J. Appl. Polym. Sci.* **2006**, *99*, 300–308.
- ⁷ Milner, S. T. *Macromolecules* **1994**, *27*, 2333–2335.
- ⁸ Xenidou, M.; Beyer, F. L.; Hadjichristidis, N.; Gido, S. P.; Tan, N. B. *Macromolecules* **1998**, *39*, 7659–7667.
- ⁹ Zhu, Y.; Burgaz, E.; Gido, S. P.; Staudinger, U.; Weidisch, R.; Uhrig, D.; Mays, J. W. *Macromolecules* **2006**, *39*, 4428–4436.
- ¹⁰ Adhikari, R.; Michler, G. H. *Prog. Polym. Sci.* **2004**, *29*, 949–986.

-
- ¹¹ Jing, F.; Hillmyer, M. A. *J. Am. Chem. Soc.* **2008**, *130*, 13826–13827.
- ¹² Czelusniak, I.; Khosravi, E.; Kenwright, A. M.; Ansell, C. W. G. *Macromolecules* **2007**, *40*, 1444–1452.
- ¹³ Oh, S.; Lee, J.; Theato, P.; Char, K. *Chem. Mater.* **2008**, *20*, 6974–6984.
- ¹⁴ Wang, Y.; Noga, D. E.; Yoon, K.; Wojtowicz, A. M.; Lin, A. S. P.; Garcia, A. J.; Collard, D. M.; Weck, M. *Adv. Func. Mater.* **2008**, *18*, 3638–3644.
- ¹⁵ Runge, M. B.; Dutta, S.; Bowden, N. B. *Macromolecules* **2006**, *39*, 498–508.
- ¹⁶ Bielawski, C. W.; Grubbs, R. H. *Angew. Chem. Int. Ed.* **2000**, *39*, 2903–2906.
- ¹⁷ Hillmyer, M. A.; Nguyen, S. T.; Grubbs, R. H. *Macromolecules* **1997**, *30*, 718–721.
- ¹⁸ Lohmeijer, B. G. G.; Pratt, R. C.; Leibfarth, F.; Logan, J. W.; Long, D. A.; Dove, A. P.; Nederberg, F.; Choi, J.; Wade, C.; Waymouth, R. M.; Hedrick, J. L. *Macromolecules* **2006**, *39*, 8574–8583.
- ¹⁹ Kiesewetter, M. K.; Shin, E. J.; Hedrick, J. L.; Waymouth, R. M. *Macromolecules* **2010**, *43*, 2093–2107.
- ²⁰ Ji, S.; Hoye, T.; Macosko, C. *Macromolecules* **2004**, *37*, 5485–5489.
- ²¹ Hillmyer, M. A.; Nguyen, S. T.; Grubbs, R. H. *Macromolecules* **1997**, *30*, 718–721.
- ²² Mark, J. E. In *Physical properties of polymers handbook*; Springer: 2007;
- ²³ Anderson, K. S.; Schreck, K. M.; Hillmyer, M. A. *Polymer Reviews* **2008**, *48*, 85–108.

Chapter 3: Morphology of polylactide graft copolymers

3.1 Background

The mechanical properties of block copolymers are dictated not only by their composition, but also by their block sequences,¹ architecture² and morphology.³ For example, Adhikari *et al.* synthesized a series of polystyrene (PS) and polybutadiene (PB) block copolymers with approximately the same composition (~ 70 vol% PS), for every material with total M_n ranging between 82 – 116 kg/mol.⁴ By varying architecture and width of the interface (through copolymer composition gradients), different equilibrium morphologies were accessed, specifically, cylindrical domains of PS in a PB matrix, cylindrical domains of PB in a PS matrix, lamella and a gyroid-like structure in order to decouple the effect of composition and morphology. The researchers found that the type of mechanical (elastomeric, ductile, brittle) behavior observed correlated well with the specific morphology. The material that consisted of cylindrical PS domains in a PB matrix behaved as a thermoplastic elastomer while the inverse morphology exhibited brittle behavior with relatively high strength and modulus. The materials with lamellar morphologies, whether from an asymmetric linear triblock or star block copolymer, exhibited ductile behavior as did the lone gyroid-like morphology with intermediate values of strength and modulus. The range in tensile behavior is astounding considering that the volume fraction of PS was essentially the same for every material tested. The works of Adhikari and many others illustrate the variety of deformation mechanisms that can occur in block copolymers as a direct result of variation in morphology.^{3,4}

Altering the topology or chain architecture of a block copolymer has been shown to influence the resulting phase behavior.^{5,6} In 1994, Milner considered the influence of architecture on block copolymer phase morphology starting with a Y-shape or mikto-arm star strongly segregated diblock copolymer having two A arms and one B arm.⁷ Such a graft copolymer is of the A_2B form. The A arms were considered equal in length and the volumes of A and B monomers were assumed equal. Thus, at $f_B = 0.5$, the length of each A arm was half the length of the A arm. Milner reasoned that if the Y block copolymer formed the classic lamellar phase at $f_B=0.5$, the A arms would be required to stretch more than the B arm to maintain constant density across all the domains, which would be entropically unfavorable due to the loss of possible conformations. Instead, the interface would curve at such a composition to allow the A arms more volume on the convex side of the curvature (Figure 3-1).

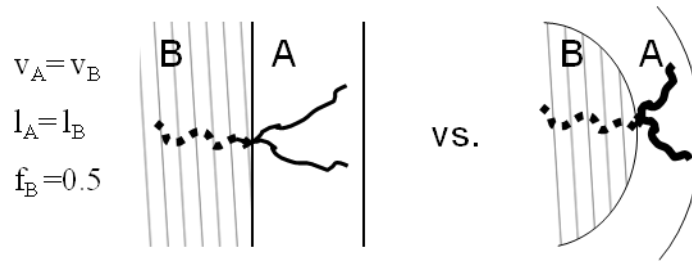


Figure 3-1 A schematic representation of chain distribution of a mikto-arm star polymer forming a spherical morphology as a result of its complex architecture.

Generalizing the situation and considering only one interface at which the junction point was located, a phase diagram, shown in Figure 3-2, for strongly segregated diblock copolymers ($\chi N \geq 100$) with variable architecture was predicted.¹ Only the free energies for the spherical (sph), cylindrical (cyl), gyroid (bic) and lamellar (lam) morphologies

were compared in the prediction. Strong segregation was assumed, thus allowing the phase boundaries to be a function only of composition (volume fraction of B, ϕ_B) and conformational symmetry quantified by an asymmetry parameter (ε). As shown in Equation 3-1, the asymmetry parameter is a ratio of the effect of architecture (parameterized by number of arms, n) and inherent chain flexibility (parameterized by packing length, l)² of each block on the overall conformation of each type of chain.

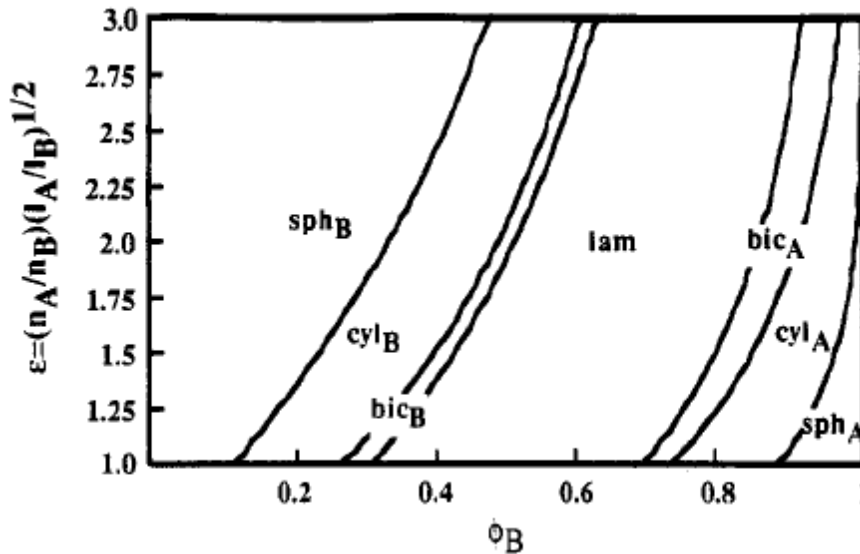


Figure 3-2 Strong segregation phase diagram predicted for block copolymers with various architectures as a function of an asymmetry parameter, ε , and composition in volume fraction of component B, ϕ_B . The only morphologies considered were spherical (sph), cylindrical (cyl), gyroid (bic) and lamellar (lam).¹ Reprinted with permission from Chain Architecture and Asymmetry in Copolymer Microphases, Milner, S. T. *Macromolecules* **1994**, 27, 2333-2335. Copyright ©1994 American Chemical Society.

$$\varepsilon \equiv \left(\frac{n_A}{n_B}\right) \left(\frac{l_A}{l_B}\right)^{\frac{1}{2}} \quad \text{Equation 3-1}$$

Relative to the phase diagram for a linear AB diblock, the effect of multiple arms skews the phase boundaries resulting in the loss of symmetry about $\phi = 0.5$ and a different dependence on ϕ . To illustrate the drastic change, consider a strongly segregated, diblock

copolymer ($n_A=n_B$) with $\phi_B=0.8$ and equal packing lengths ($l_A=l_B$) so that $\varepsilon = 1$. At equilibrium, the specified diblock is predicted to form cylinders of A in a matrix of B.⁸ However, if the same two blocks ($l_A=l_B$) are joined to form an A_2B star ($n_A=2n_B$), then $\varepsilon = 2$ and the equilibrium morphology is lamellae. A number of experimental groups qualitatively confirmed Milner's predicted phase diagram by synthesizing A_2B and A_3B mikto-arm star copolymers and characterizing morphology by small-angle x-ray scattering (SAXS) and transmission electron microscopy (TEM).⁹⁻¹³ From these studies, it was concluded that the Milner phase diagram slightly overestimates the phase boundaries towards higher values of ϕ_B when compared to the observed morphologies.

Especially relevant to this work, the same research groups synthesized and characterized more complex block copolymer architectures including pi-shaped and graft copolymers.¹⁴⁻²³ They hypothesized that the morphology of these complex systems would be similar to their respective "constituting block copolymers" and dependent on the degree of segregation (χN) of the constituting block copolymer. The theory was originally proposed by Gido and co-workers and is similar to the morphological relationship between an ABA triblock and AB diblock.¹⁴ The constituting block copolymer can be thought of as a repeat unit containing both blocks that would re-create the original block copolymer if replicated in series. For example, the constituting block copolymer of a regularly spaced graft copolymer with trifunctional junction points, is an AB_2 mikto-arm star copolymer where the length of the B arms is half the length between the A-B junction point and the length of the A arm is the length of the A graft as illustrated in Figure 3-3.

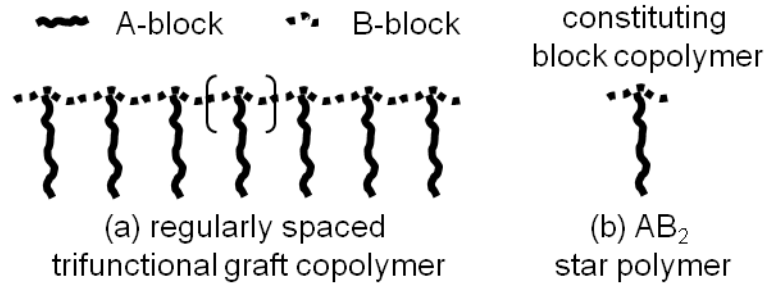


Figure 3-3 A (a) regularly spaced trifunctional graft copolymer can be considered a series of (b) constituting block copolymers which in this case is an AB_2 star polymer.

Utilizing this theory, the morphology of a regularly-spaced graft copolymer could be predicted with a phase diagram for a mikto-arm star (such as the Milner phase diagram). The researchers further determined that graft copolymers with both randomly²⁰ and regularly²² spaced junction points appear to obey the constituting block copolymer hypothesis, generally forming the morphologies observed for their respective constituting block copolymers including spherical, cylindrical and lamellar. However, the morphologies became less ordered for randomly placed junctions and for graft copolymers with increasing number of junctions per chain.

In 2012, Matsen utilized self-consistent field theory to predict the phase diagram for a conformationally symmetric ($l_A=l_B$) AB_2 mikto-arm star copolymer ($\epsilon=2$) as a function of χN and ϕ_A (Figure 3-4a) in the intermediate and weak segregation regimes ($\chi N \leq 50$).²⁴ The morphologies considered included: closed-packed spheres (S_{cp}), body-centered spheres (S), spheres with $Pm\bar{3}n$ symmetry (S_{A15})²⁵⁻²⁸ hexagonally packed cylinders (C), gyroid (G), $Fddd$ morphology (O^{70})²⁹, lamellae (L) and perforated lamellae (PL). As seen in Figure 3-4a, simply changing the block connectivity significantly alters the dependence on ϕ , which was also observed previously by Milner in the strong

segregation limit. However, Matsen's phase diagram also predicts the stability of additional phases that were not considered by Milner. Matsen further probed the constituting block copolymer theory by predicting the phase diagram for a regularly-spaced trifunctional graft copolymer composed of an infinite number of AB_2 constituting block copolymers. As before, the A and B blocks were assumed to be conformationally symmetric ($\epsilon=2$). The result, shown in Figure 3-4b, is somewhat similar to Figure 3-4a as expected, with the significant differences being the loss of the S_{cp} phase on the right side, increases in the size of the S_{A15} , O_{70} , and PL regions, and changes to the order-disorder transitions (ODT). Matsen attributes the change in ODT to the relative decrease in free-chain end density in the graft copolymer as compared to the mikto-arm star. Free-chain ends promote disorder due to the ability of end segments to easily pull-out from a domain. The other morphological changes are ascribed to the change in architecture which increases the thickness of the majority domain in the higher f side of the phase diagram, thereby reducing packing frustration and stabilizing the more complex morphologies (e.g. PL).

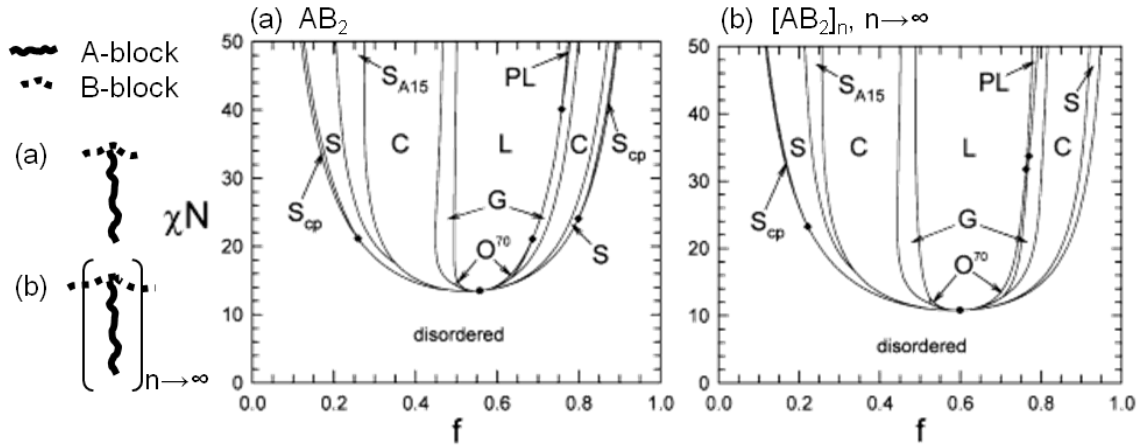


Figure 3-4 (a) Matsen phase diagram²⁴ for AB_2 mikto-arm star polymer as a function of the volume fraction of A, where A and B are conformationally symmetric [$l_A=l_B$, $\epsilon=2$]. The morphologies considered included: closed-packed spheres [S_{cp}], body-centered spheres [S], spheres with $Pm\bar{3}n$ symmetry [S_{A15}], hexagonally packed cylinders [C], gyroid [G], $Fddd$ morphology [O^{70}], lamellae [L] and perforated lamellae [PL]. (b) Phase diagram for a graft copolymer composed of infinite AB_2 units connected by the B-blocks resulting in regularly spaced, pendant A-blocks. As before, A and B are conformationally symmetric [$\epsilon=2$]. Reprinted with permission from Effect of Architecture on the Phase Behavior of AB-Type Block Copolymer Melts, Matsen, M. W. *Macromolecules* **2012**, *45*, 2161-2165. Copyright © 2012 American Chemical Society.

Overall, a graft copolymer with a finite number of junction points is expected to have phase behavior intermediate between the two cases predicted by Matsen.

The morphologies of the graft copolymers synthesized in Chapter 2 are investigated in this chapter by small-angle x-ray scattering and transmission electron microscopy. The majority of the samples come from as-molded tensile samples since the overall focus is the influence of morphology on tensile behavior. However, samples prepared from additional techniques (solvent casting, annealing) will be examined to help clarify the phase behavior. Due to the disperse nature of the backbone and graft molar mass, as well as the irregular placement of the junction points, we expect microphase

separated, but poorly ordered morphologies. The Matsen and Milner phase diagrams will be utilized to predict the equilibrium morphologies of the graft copolymers.

3.2 Experimental

3.2.1 Sample preparation

After synthesis, the graft copolymers were precipitated into hexanes once and methanol once before dissolution in dichloromethane (~10g polymer/mL). Butylated hydroxyl toluene (~ 1 mol %) was added to the polymer solution and dissolved. The mixture was then poured into a Teflon dish and allowed to dry under ambient pressures and temperatures for 3 days before drying in a vacuum oven at 80 °C for four days. Approximately 4 g of as dried polymer pieces was compression molded into a film of nominally 0.55 mm thickness at 150 °C for 5 minutes, with a maximum pressure of 0.7 MPa and subsequently quenched to room temperature in 5–8 minutes. Heating the graft copolymers to 160°C resulted in discoloration and cross-linking of the sample due to the unsaturated backbone. From this film, small dogbone shapes were scored on the film with a stencil and diamond scribe. The shapes were cut out with scissors. The preforms were then compression molded using a custom, stainless steel, dogbone tensile bar mold and the same conditions as listed above for the film. The flash from all tensile bar samples was removed using an Exacto knife. Using a light box and circular polarizers (one polarizer, one analyzer), the bars were examined for dust, defects, and crystallinity in the gage section.

3.2.2 Transmission electron microscopy methods

Pieces of as-compression molded tensile bars were cut with a razor blade and encapsulated in epoxy (EMbed-812, Electron Microscopy Sciences) to give samples representative of the YZ and XY-planes as illustrated in Figure 3-5. The epoxy mixture was made using the provided instructions and then pipetted into high-density polyethylene embedding capsules (BEEM embedding capsules, Electron Microscopy Sciences). The epoxy filled capsules were pre-cured without samples at 40°C for 2-3 hours in a convection oven before the samples were carefully inserted into the epoxy with tweezers. The epoxy was then allowed to fully harden at room temperature overnight.

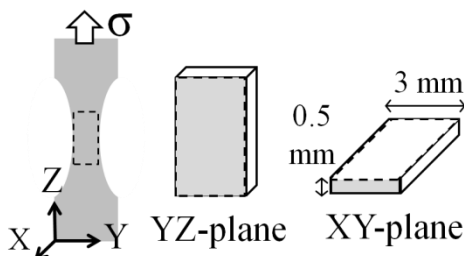


Figure 3-5 Schematic representation of the YZ and XY-planes of the compression molded dogbone sample investigated by transmission electron microscopy and small-angle x-ray scattering.

The samples were microtomed at 25 °C on a Leica EM UC6 Ultramicrotome with a diamond knife to a thickness of approximately 70 nm and floated on water onto 400 mesh copper grids. The samples were subsequently reactively stained by exposing the grids to OsO_4 vapor from a 4% aqueous solution for at least 20 minutes. TEM was performed on a FEI Tecnai Spirit BioTWIN electron microscope with an operating voltage of 120 kV.

3.2.3 Small-angle x-ray scattering methods

Small-angle x-ray scattering data was obtained at the Advanced Photon Source at Argonne National Laboratory. Specifically, data was collected at the Dupont-Northwestern-Dow Collaborative Access Team 5ID-D beamline. The x-ray wavelength was 0.72932 Å with a sample-to-detector-distance ranging from 4.04 to 5.54 meters. Two-dimensional scattering patterns were recorded on a Mar 165 mm diameter CCD detector possessing a resolution of 2048 × 2048 and azimuthally integrated to a one dimensional plot of intensity versus wavevector, q , where $q = 4\pi(\lambda \sin\{\theta/2\})^{-1}$ and θ and λ are the scattering angle and x-ray wavelength, respectively.

The azimuthally integrated SAXS data for some of the graft copolymers were modeled with the Percus-Yevick (PY) theory^{30,31} for x-ray scattering from a disordered, liquid-like packing of hard spheres. Molar mass dispersity and interfacial thickness were not taken into consideration. The fit was performed manually by first adjusting the core radius (R_c) so that the 1st minimum due to the spherical form factor was in alignment with that of the experimental data. The effective hard sphere radius was then adjusted manually to fit the lower- q peaks that resulted from interparticle scattering.

3.3 Results

3.3.1 Morphology predictions for PCNL

As described in the introduction above, the equilibrium morphology of graft copolymers can be determined by the value χN and composition of its constituting block copolymer.³ The constituting block copolymer for PCNL is a mikto-arm star of the AB_2 form (two arms of B connected to one arm of A) where B represents the PCN backbone

and A is a single PLA graft. As the grafts of PLA are likely to be statistically spaced and not regularly spaced, the total molar mass of both B arms (i.e., twice the molar mass of one B arm) in the constituting block copolymer is set equal to $M_{n,eff}$, the total PCN molar mass divided by the average number of graft points per chain (defined in Chapter 2), consistent with the work of Xenidou²⁰ and Beyer²² for randomly spaced graft copolymers. The Flory-Huggins interaction parameter, χ , between PLA and PCN has not been measured. However, the majority of the PCN backbone is ring-opened poly (1,5-cyclooctadiene) which is structurally identical to poly(1,4-butadiene) so a comparison can be made between polylactide and poly(1,4-butadiene) [PB] for simplicity. Lee et al. recently reported $\chi(T[K])$ for polylactide and polybutadiene (containing both 1,4- and 1,2- units) as³²:

$$\chi(T)_{PLA-PB} = \frac{161.6}{T} - 0.223 \quad \text{Equation 3-3}$$

A 118 \AA^3 reference volume was used in Lee's calculation. Based on this equation, the Flory-Huggins interaction parameter between PLA and PB at 298K was calculated to be 0.32. The degree of polymerization for the PLA graft will be calculated from $M_{n,PLA}$ as determined by ^1H NMR from the methine end group proton. Thus, N of the constituting block copolymer is the sum of the degree of polymerization of the two B arms and the A arm, both with respect to a 118 \AA^3 reference volume as shown in Equation 3-2 and Equation 3-3 where M_n is the number average molar mass, ρ is the mass density, v_{ref} is the reference volume and N_A is Avogadro's number.

$$N = N_{ref,PLA} + N_{ref,PCN\ eff} \quad \text{Equation 3-2}$$

$$N_{ref,i} = \frac{M_{n,i}}{m_{ref}} = \frac{M_{n,i}}{\rho_i v_{ref} N_A} \quad \text{Equation 3-3}$$

As seen in Table 3-1, χN of the constituting block copolymer was calculated for each graft copolymer resulting in values ranging from 16 to 249. Furthermore, the equilibrium morphology expected for each graft copolymer was predicted using the Matsen phase diagram²⁴ (Figure 3-3b, first discussed in Ch.3 Background) for a AB_2 graft copolymer of infinite molar mass, χN of each constituting block copolymer and the composition in terms of volume percent of PLA (ϕ_{PLA}). The asymmetry parameter at 30°C, ϵ , was calculated to be 1.90 using Equation 3-1 and the following parameters: A= PCN, B = PLA $n_A = 2$, $n_B = 1$, $l_A = b_A^2/v_{ref} = 0.48\text{\AA}$, $l_B = b_B^2/v_{ref} = 0.53\text{\AA}$, where b is the statistical segment length with respect to a reference volume of 108\AA^3 obtained from reference 33 using the value for poly(1,4-butadiene) for PCN. The graft copolymers are separated into two categories depending on their respective values of χN where $\chi N > 50$ is considered to be strongly segregated in this study and the remaining polymers are in the intermediate or weak segregation regime.

Table 3-1 The morphological characteristics of the polylactide graft copolymers

Graft Copolymer	vol % PLA ^a	χ^N ^b	Predicted morphology ^c	Observed morphology ^d	Interparticle spacing ^d , d* (nm)
Strongly Segregated					
PCNL-94-13-99	99	218	disordered	micellar	no q*
PCNL-78-12-99	98	210	disordered	micellar	no q*
PCNL-495-19-99	98	231	disordered	micellar	no q*
PCNL-78-12-98	97	129	disordered	PY sph	19.3
PCNL-92-4-96	94	157	PCN sph	PY sph	25.6
PCNL-332-11-95	93	237	PCN sph	PY sph	30.1
PCNL-495-19-95	93	184	PCN sph	PY sph	26.5
PCNL-495-19-95	93	148	PCN sph	PY sph	25.6
PCNL-345-42-95	93	69	PCN sph	PY sph	17.0
PCNL-94-13-95	93	63	PCN sph	PY sph	16.3
PCNL-78-12-95	93	63	PCN sph	PY sph	16.4
PCNL-592-90-95	93	54	PCN sph	PY sph	15.9
PCNL-397-8-95	92	249	PCN sph or cyl	PY sph	36.2
PCNL-397-8-93	90	194	PCN cyl	PY sph	34.2
PCNL-497-13-81 ^e	67	78	lamellar	PCN cyl	28.7
PCNL-495-19-81	66	57	lamellar	PCN cyl	26.1
PCNL-495-19-80	65	57	lamellar	PCN cyl	25.2
Intermediate and weakly segregated					
PCNL-78-12-89	84	31	PCN cyl	PCN sph	14.4
PCNL-94-13-89	84	30	PCN cyl	PCN sph	14.4
PCNL-78-12-83	71	16	lam/O70	PCN cyl	13.1
PCNL-354-22-82 ^e	68	35	lamellar	PCN cyl	18.5
PCNL-206-15-82 ^e	69	29	lamellar	PCN cyl	17.3

^a Determined from ¹H NMR determined composition, density of PLA³⁴ (1.26 g/mL) and density of 1,4-polybutadiene³⁵ (0.9 g/mL) at 298K

^b Segregation strength of the constituting block copolymer of each graft copolymer. N was calculated using a ref. volume of 118 Å³.

^c Morphologies determined from the Matsen phase diagram for a regularly spaced trifunctional graft copolymer with an infinite number of junctions²⁴

^d Morphology assignments were made from small-angle x-ray scattering data of as-molded samples. In some cases, data from annealed samples was utilized. $d^* = 2\pi/q^*$, where q^* is the primary scattering peak. PY = Percus-Yevick.

^e Synthesized by Joel Sarapas.

3.3.2 Morphology of PCNLs, 99 wt.% PLA

The morphology of the polylactide graft copolymers was investigated by small-angle x-ray scattering after various processing conditions above T_g including vacuum drying at 80 °C, compression molding (at 150°C) and vacuum annealing (80-100 °C). The as-molded samples were taken from undeformed, compression molded tensile bars that were nominally 0.5 mm thick and 3 mm wide. Two different orientations of the tensile bar were investigated, the YZ-direction and the XY-direction as illustrated in Figure 3-5. The sample for the XY-plane was obtained by cutting an as-molded tensile bar with a razor blade. Thus, in contrast to the YZ-sample, the surface of the XY-sample was not in the as-molded condition. Some samples were additionally annealed (after compression molding) in a DSC pan at elevated temperatures ($> T_g$) and then air-cooled to RT.

In general, three different morphologies were observed by SAXS as a function of composition. Graft copolymers with ~99 wt.% PLA exhibited little to no scattering in the q -range probed, while a poorly-ordered spherical morphology was observed for graft copolymers in the range of 89–96 wt.% PLA. Finally, a scattering consistent with hexagonally packed cylinders was observed for graft copolymers with ~80 wt.% PLA. The azimuthally-integrated 1D SAXS profile for a 99 wt% PLA graft copolymer is shown in Figure 3-6a as intensity versus scattering wavevector, $q = 4\pi/\lambda (\sin \theta/2)$, where θ is the scattering angle and λ is the wavelength of incident radiation. Recall from Chapter 2 that the 99 wt% PLA graft copolymers are actually blends of graft copolymer and homopolymer PLA. Thus, it is likely the morphology consists of micelles of graft

copolymer having a PCN core and PLA corona in a matrix of homopolymer PLA. The limited scattering may be due to both the small size of the micelles and a lack of spatial coherency. TEM of as-molded PCNL-78-12-99 in the XY-direction (Figure 3-6b) reveals a morphology of small PCN domains (stained dark with OsO₄) with wide size variation and no lattice ordering which is consistent with the SAXS data and synthetic analysis. Figure 3-6c shows the TEM micrograph for PCNL-495-19-99 which has a larger $M_{n,eff}$ (2.8 and 0.7 kg mol⁻¹ respectively) than PCNL-78-12-99. A similar, but larger morphology is observed in PCNL-495-19-99 which can be attributed to the larger $M_{n,eff}$ value. Notably, despite the extreme compositional asymmetry, a microphase separated morphology is still observed in both cases.

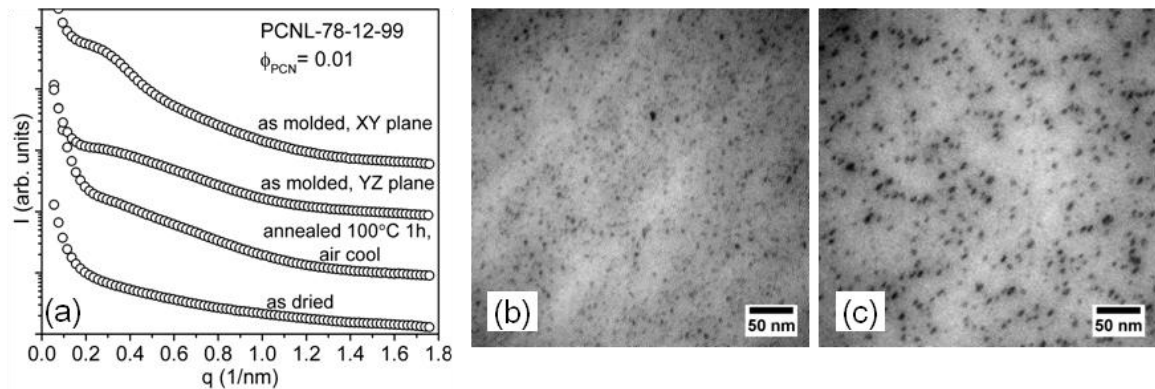


Figure 3-6 (a) Azimuthally-integrated 1D SAXS profiles, as a function of relative intensity and momentum scattering vector q , are shown for PCNL-78-12-99 after various processing conditions. Transmission electron microscopy of as-molded (b) PCNL-78-12-99 and (c) PCNL-495-19-99 in the XY-direction and stained with OsO₄ reveals a poorly ordered morphology of PCN micelles in a matrix of PLA.

3.3.3 Morphology of PCNLs, 89 – 95 wt.% PLA

The azimuthally-integrated SAXS curves for PCNL-495-19-95, shown in Figure 3-8, are representative of most of the graft copolymers studied. PCNL-495-19-95 was predicted to be strongly segregated with a morphology of PCN spheres in a matrix of

PLA. In the as-molded condition, the SAXS curves in both the YZ and XY-direction are rather similar with two interparticle interference peaks at the lower q -values (primary peak and shoulder) and one or more peaks at the higher q -values. After annealing the material at 100 °C for one hour, followed by slow cooling to room temperature, the interparticle interference peaks that were observed in the as-molded state became more defined indicating that the morphology became more ordered. The as-annealed data modeled with the Percus-Yevick (PY) theory, without consideration to dispersity, which simulates the scattering from a liquid-like packing of effective hard-spheres.³⁰ Each effective hard sphere consists of a rubbery core and a PLA corona as illustrated in Figure 3-7. The rubbery core radius, R_c , was determined from the first high- q form-factor minimum.^{30,31} Additionally, given the volume fraction of rubbery cores (ϕ_c), fitting the model to the low- q interparticle interference peaks allowed for determination of an effective hard-sphere radius (R_{HS}) and the volume fraction of effective hard spheres (η). Thus, the thickness of the PLA corona around the rubbery core (ΔR) is given by the difference of R_{HS} and R_c .

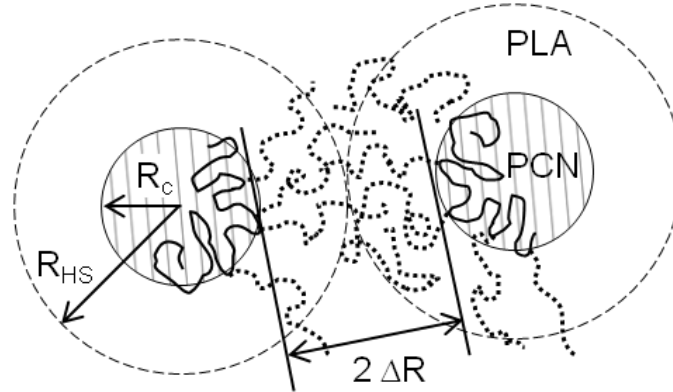


Figure 3-7 Schematic illustrating the parameters used in the Percus-Yevick model of liquid-like packing of block copolymer spherical domains with penetrable hard sphere interactions. The minority block comprises the core with a radius of R_c . The radius of the effective hard sphere, R_{HS} , includes the corona comprised of the matrix block. The corona has a thickness of ΔR .

Initially, the volume fraction of rubbery cores was set as a constant equal to the volume fraction of PCN in the graft copolymer as determined by the ^1H NMR-determined weight fraction and density of 1,4-polybutadiene at 298K. However, following the work of Kinning et al.³⁶, the volume fraction of cores was then set as an adjustable parameter. For all the relevant graft copolymers, better fits were obtained with ϕ_c as an adjustable parameter. Finally, the primary scattering peak was used to determine average the interparticle spacing, d^* . The model fit, as seen as the solid line in Figure 3-8, appears satisfactory indicating that the scattering from the graft copolymer morphology is consistent with a liquid-like packing of spherical domains. A summary of the parameters obtained from the PY fit is shown in Table 3-2.

The average interparticle spacing (d^*) was found to be $0.9 - 1.0 \times 2R_{HS}$ which is further evidence of the quality of the fit. The slight difference of the XY-scattering curve as compared to the scattering from the YZ-direction may result from the small cross-sectional area of the sample, $\sim 0.5 \text{ mm} \times 3.0 \text{ mm}$, relative to the x-ray beam size ($\sim 1 \times$

2.5 mm) and/or the SAXS sample preparation technique. Consistent with the PY-model, the morphology of as-molded PCNL-495-19-95 in the XY-direction is shown in a TEM image (Figure 3-8b) to be composed of poorly ordered spheres of rubber (stained by OsO_4) in a matrix of PLA. The values of R_c and ΔR , 7.2 and 6.1 nm respectively, from the model are qualitatively consistent with the TEM image.

Table 3-2 Results from the fit of the PCNL graft copolymer SAXS data to the Percus-Yevick model

Graft copolymer	ϕ PCN ^a	ϕ PCN best fit	η ^b	R_c (nm)	R_{HS} (nm)	ΔR (nm)
Strong Segregation						
PCNL-78-12-98	0.029	0.02	0.22	4.1	9.0	5.0
PCNL-92-4-96	0.058	0.05	0.38	6.7	13.2	6.5
PCNL-332-11-95	0.068	0.03	0.29	7.2	15.5	8.3
PCNL-495-19-95	0.072	0.07	0.42	7.2	13.3	6.1
PCNL-495-19-95	0.072	0.06	0.4	7.6	14.5	6.9
PCNL-397-8-95	0.078	0.043	0.28	9.2	17.2	8.0
PCNL-397-8-93	0.099	0.067	0.34	9.9	17.0	7.1
Intermediate and Weak Segregation						
PCNL-345-42-95	0.074	0.06	0.4	4.6	8.9	4.3
PCNL-94-13-95	0.074	0.05	0.39	4.3	8.4	4.1
PCNL-78-12-95	0.074	0.054	0.39	4.4	8.5	4.1
PCNL-594-90-95	0.069	0.062	0.41	4.6	8.6	4.0
PCNL-78-12-90	0.156	0.11	0.48	4.9	7.9	3.1
PCNL-94-13-90	0.156	0.11	0.47	4.8	7.8	3.0

^a Volume fraction of PCN in the graft copolymer as calculated from ¹H NMR determined composition and respective densities at 298K

^b Parameters obtained from the fit of the data to the Percus-Yevick model. η is the volume fraction of effective hard spheres in the samples. R_c is the radius of the core of the sphere. R_{HS} is the radius of the entire effective hard spheres. ΔR is the difference between R_{HS} and R_c .

For all the graft copolymers with spherical morphology, the fitted value of ϕ_{PCN} was found to be lower than the calculated ϕ_{PCN} . This may be due to error in the calculation of ϕ_{PCN} or more likely the existence of very small molar mass block

copolymer that becomes solubilized in the PLA matrix. R_c was found to be proportional to $M_{n,eff}$ in accord with the constituting block copolymer theory. The unperturbed radius of gyration of PCN ($R_{g0,PCN}$) was calculated from $M_{n,eff}$ and the ratio $\langle R^2 \rangle_0/M$ determined by Fetters for 1,4-polybutadiene (trans/cis/vinyl 50/40/10) at 25°C.³⁵ Overall, the ratio of $R_{g0,PCN} : R_c$ ranged from 0.7 to 1.0 with a weak proportionality to $M_{n,eff}$ indicating either that the PCN chains have a slightly extended conformation or that the rubber domain is swollen with PLA chains. Similarly, ΔR , the thickness of the PLA “shell” around the rubber core, was found to correlate linearly with $M_{n,PLA}$. The unperturbed radius of gyration for the PLA block ($R_{g0,PLA}$) was calculated from $M_{n,PLA}$ using the ratio $\langle R^2 \rangle_0/M$ as determined by Anderson and Hillmyer at 200 °C and then subsequently adjusted to 25 °C.³³ Comparison of ΔR to $R_{g0,PLA}$ revealed unusually small ratios ranging from 0.25 to 0.33 possibly indicative of an extremely collapsed conformation of the PLA chains in the block copolymer morphology and/or that the PLA chains are in a collapsed conformation and severely interpenetrating with the PLA chains of the neighboring corona. However, given the grafted nature of the PLA chains, one would expect an extended conformation so that $\Delta R > R_{g0,PLA}$.³⁰ This discrepancy may result from over interpretation of the PY model fit to the data as dispersity was not taken into consideration.

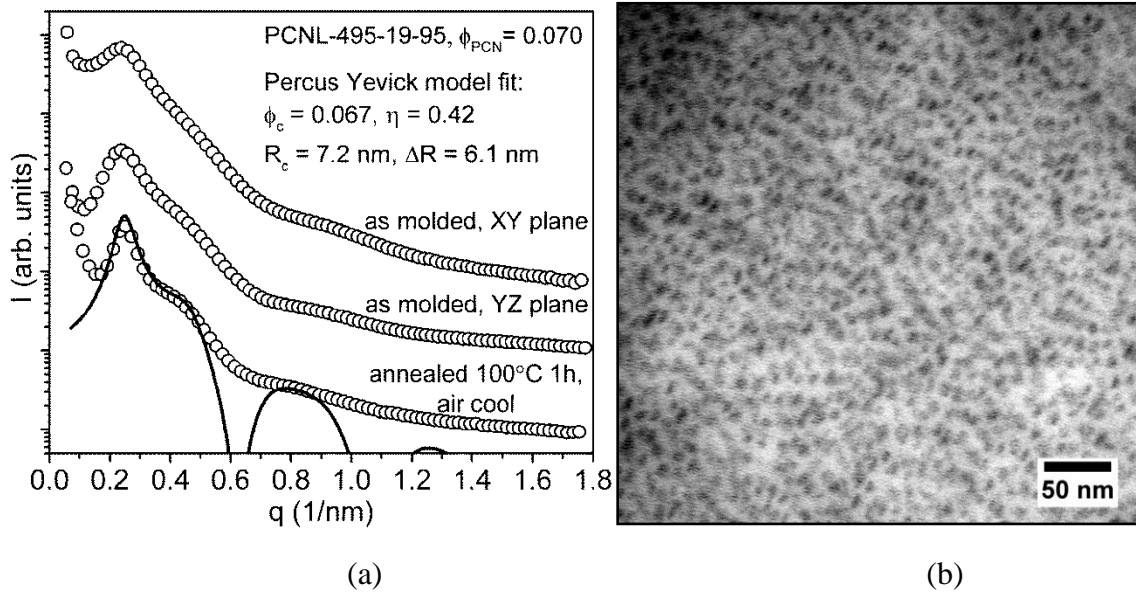


Figure 3-8 (a) Small-angle x-ray scattering curves for PCNL-495-19-95 in the compression molded state and after annealing. The solid line is a fit of the Percus-Yevick model, without accounting for molar mass dispersity, to the as-annealed data. (b) A morphology of PCN spheres (stained dark by OsO_4) with liquid-like packing in a matrix of PLA is observed in the TEM micrograph of as-molded PCNL-495-19-95 in the xy-direction. TEM of PCNL-495-19-95 in the yz-direction was not obtained.

3.3.4 Morphology of PCNLs, 80 wt.% PLA

Figure 3-9 shows the small-angle x-ray scattering curves for PCNL-495-19-80 which is fairly representative for the other graft copolymers with compositions of 83 to 80 wt% PLA. In the as-molded state, two higher order peaks ($\sqrt{4}q^*$, $\sqrt{7}q^*$) in addition to the primary scattering peak (q^*) are observed in both the XY and YZ directions. After annealing at 80 °C for 4 days, the morphology became more ordered resulting in an additional higher order peak ($\sqrt{12}q^*$) and narrowing of the primary peak. The observed scattering reflections are consistent with that expected for hexagonal packed cylinders of PCN in a matrix of PLA. The absence of the $\sqrt{3}$ reflection is likely due to destructive interference from the form factor scattering.³⁷ A TEM micrograph of the as-molded XY-

plane of PCNL-495-19-80 is shown in Figure 3-9b. Although a microphase separated morphology is observed, the cylindrical morphology is not obvious. This may be a result of the compression molding process distorting the domains.

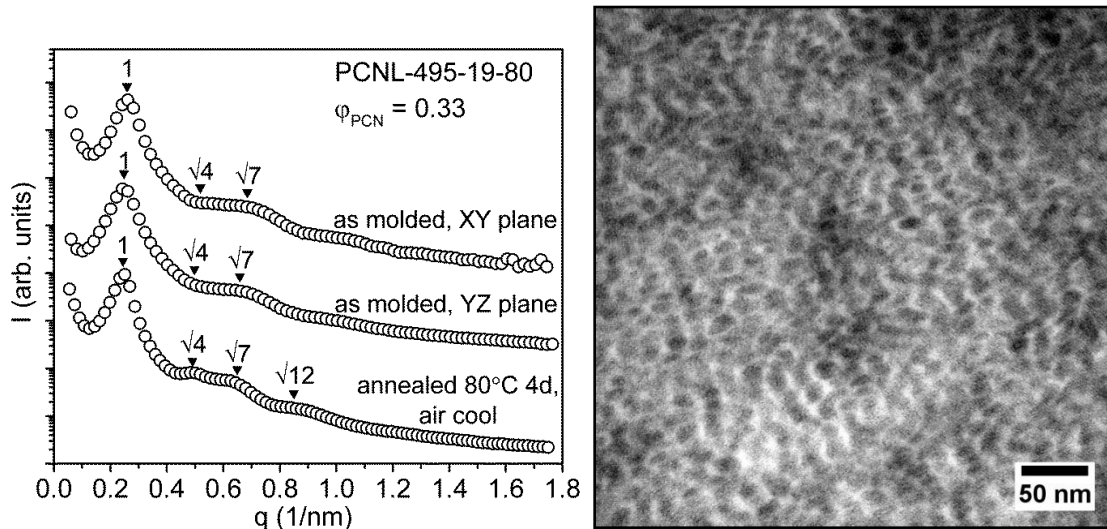


Figure 3-9 (a) Small-angle x-ray scattering curves for PCNL-495-19-80 in the compression molded state (see Figure 3-5 for explanation of orientations) and after annealing. The arrows denote the scattering peaks and their multiplicity relative to the primary peak (b) TEM micrograph of as-molded PCNL-495-19-80 in the xy-direction after staining with OsO_4 . TEM in the yz-direction was not obtained.

3.3.5 Discussion

Overall, a majority of the graft copolymers studied exhibited spherical morphologies consistent with the predictions made using the Matsen phase diagram (Figure 3-3b). Those that were expected to form lamellae exhibited cylindrical morphologies and those that were predicted to be disordered, exhibited micellar morphologies. All of the samples lacked long-range order. This is likely due to the fact that the phase diagram utilized was a prediction for an ideal case where the graft copolymer is regularly-spaced, conformationally symmetric ($\epsilon = 2$) and of infinite molecular weight. In reality, the graft copolymers are randomly spaced with molar mass

dispersity in both blocks. The asymmetry parameter calculated for PCNL was approximately 1.9 and thus, relatively close to the case of conformational symmetry ($\epsilon=2$) in accord with the Matsen phase diagram. However, the statistical nature of the junction point placement along the PCN backbone creates variability that is not easily accounted for. Since the local composition and local value of N around each junction point will vary somewhat about the average values, a more disordered structure is likely. Instead of a single constituting block copolymer, the graft copolymer may be better represented by a number of different AB_2 stars, varying in molar mass as well as composition. The molar mass dispersity of the backbone and the PLA arms may lead to the presence of very small block copolymer chains which could swell the PLA matrix around the PCN domains. The same effect would occur if homopolymer PLA was present with the graft copolymer as in the case of PCNL-495-19-99 (and others). Swelling of the PLA phase by very small block copolymer, homopolymer PLA, or solvent would effectively increase the volume fraction of PLA. Therefore, a morphology of increasing interfacial curvature, relative to the expected morphology, might be promoted possibly explaining the observation of cylindrical morphology instead of the expected lamellae. Additionally, the solubilization of small molar mass PCNL into the PLA matrix would lead to a smaller spherical domain size and larger spherical domain spacing relative to the expected dimensions calculated from the volume fraction derived from M_n and density.

It is also possible that the observed morphologies are metastable and were kinetically trapped during the polymer purification process.³⁸ After precipitation, the graft copolymers were initially cast from methylene chloride before vacuum drying in the oven

at 80-100 °C for four days. Comparison of the Hildebrand solubility parameters for methylene chloride, PLA and 1,4-PB (20.2, 19.7, 17.2 J^{1/2} cm^{3/2} respectively^{39,40,41}) indicates that methylene chloride is more selective for the PLA block. Thus, during the solvent drying process, the methylene chloride would be preferentially found in the PLA phase effectively increasing the relative volume of PLA in the material and shifting the applicable phase diagram (as discussed above). Furthermore, the order-disorder transition temperatures (T_{ODT}) of the graft copolymers were estimated using the Matsen phase diagram and the effective $\chi_{\text{PLA-PB}}$ determined by Lee et al. The majority of the T_{ODT} values were much higher than 150 °C, the compression molding temperature. Thus, the samples remained ordered during the molding process. Additionally, the vacuum drying process and any subsequent annealing (at 80-100 °C) did not allow the graft copolymer to revert to the disordered state from the potentially metastable morphology developed during solvent casting.

3.4 Summary

In summary, all of the graft copolymers synthesized in Chapter 2 appeared to have microphase separated morphologies. As a result of the homopolymer contamination, the samples containing ~99wt% PLA exhibited spherical micelles of rubber in a matrix of PLA with no interparticle interference. Samples containing 89 – 96 wt.% PLA exhibited liquid-like packing of PCN spheres in a matrix of PLA. The SAXS data was adequately modeled using the Percus-Yevick theory to determine the rubber core radius and thickness of the PLA corona. Graft copolymers having ~ 80 wt% PLA exhibited x-ray scattering consistent with hexagonally packed spheres; however, the cylindrical shape of

the domains was not seen in the as-molded TEM micrographs. Overall, the observed morphologies were not consistent with the equilibrium morphologies predicted from the Matsen phase diagram for an AB₂ graft copolymer of infinite molar mass. A number of reasons for the discrepancy were discussed. Most likely, the observed morphologies were kinetically trapped during the polymer purification process. However, the obtained information is essential for understanding structure-property relationships such as the effect of morphology on deformation mechanisms which will be examined in the next two chapters.

Acknowledgements

This work was supported by the USDA and the U.S. DOE through Grant DE-PS36-06GO96002P. This work was also supported by the Center for Sustainable Polymers, an NSF-funded Center for Chemical Innovation at the University of Minnesota. Parts of this work were carried out in the Institute of Technology Characterization Facility, University of Minnesota, a member of the NSF-funded Materials Research Facilities Network. Portions of this work were performed at the DuPont-Northwestern-Dow Collaborative Access Team (DND-CAT) located at Sector 5 of the Advanced Photon Source (APS). DND-CAT is supported by E.I. DuPont de Nemours & Co., The Dow Chemical Company and Northwestern University. Use of the APS, an Office of Science User Facility operated for the U.S. Department of Energy (DOE) Office of Science by Argonne National Laboratory, was supported by the U.S. DOE under Contract No. DE-AC02-06CH11357.

3.5 References

- ¹ Matsuo, M.; Ueno, T.; Horino, H.; Chujyo, S.; Asai, H. *Polymer* **1968**, *9*, 425-436.
- ² Staudinger, U.; Weidisch, R.; Zhu, Y.; Gido, S. P.; Uhrig, D.; Mays, J. W.; Iatrou, H.; Hadjichristidis, N. *Macromolecular Symposia* **2006**, *233*, 42-50.
- ³ Qiao, L.; Leibig, C.; Hahn, S. F.; Winey, K. I. *Ind Eng Chem Res* **2006**, *45*, 5598-5602.
- ⁴ Adhikari, R.; Lebek, W.; Godehardt, R.; Michler, G. H.; Cagiao, M. E.; Calleja, F. J. B.; Knoll, K. *J Appl Polym Sci* **2006**, *101*, 998-1006.
- ⁵ Pitsikalis, M.; Pispas, S.; Mays, J. W.; Hadjichristidis, N. In *Nonlinear block copolymer architectures; Blockcopolymers-Polyelectrolytes-Biodegradation*; Springer: 1998; pp 1-137.
- ⁶ Hadjichristidis, N.; Pispas, S.; Pitsikalis, M.; Iatrou, H.; Vlahos, C. In *Asymmetric star polymers: synthesis and properties; Branched polymers I*; Springer: 1999; pp 71-127.
- ⁷ Milner, S. T. *Macromolecules* **1994**, *27*, 2333-2335.
- ⁸ Matsen, M. W.; Bates, F. S. *Macromolecules* **1996**, *29*, 1091-1098.
- ⁹ Hadjichristidis, N.; Iatrou, H.; Behal, S. K.; Chludzinski, J. J.; Disko, M. M.; Garner, R. T.; Liang, K. S.; Lohse, D. J.; Milner, S. T. *Macromolecules* **1993**, *26*, 5812-5815.
- ¹⁰ Pochan, D. J.; Gido, S. P.; Pispas, S.; Mays, J. W. *Macromolecules* **1996**, *29*, 5099-5105.
- ¹¹ Lee, C.; Gido, S. P.; Pitsikalis, M.; Mays, J. W.; Tan, N. B.; Trevino, S. F.; Hadjichristidis, N. *Macromolecules* **1997**, *30*, 3732-3738.
- ¹² Tselikas, Y.; Iatrou, H.; Hadjichristidis, N.; Liang, K. S.; Mohanty, K.; Lohse, D. J. *J. Chem. Phys.* **1996**, *105*, 2456-2462.
- ¹³ Floudas, G.; Hadjichristidis, N.; Tselikas, Y.; Erukhimovich, I. *Macromolecules* **1997**, *30*, 3090-3096.
- ¹⁴ Gido, S. P.; Lee, C.; Pochan, D. J.; Pispas, S.; Mays, J. W.; Hadjichristidis, N. *Macromolecules* **1996**, *29*, 7022-7028.
- ¹⁵ Lee, C.; Gido, S. P.; Pitsikalis, M.; Mays, J. W.; Tan, N. B.; Trevino, S. F.; Hadjichristidis, N. *Macromolecules* **1997**, *30*, 3732-3738.

-
- ¹⁶ Sioula, S.; Tselikas, Y.; Hadjichristidis, N. *Macromolecular Symposia* **1997**, *117*, 167-174.
- ¹⁷ Gido, S. P.; Wang, Z. G. *Macromolecules* **1997**, *30*, 6771-6782.
- ¹⁸ Lee, C.; Gido, S. P.; Poulos, Y.; Hadjichristidis, N.; Tan, N. B.; Trevino, S. F.; Mays, J. W. *J. Chem. Phys.* **1997**, *107*, 6460-6469.
- ¹⁹ Lee, C.; Gido, S. P.; Poulos, Y.; Hadjichristidis, N.; Tan, N. B.; Trevino, S. F.; Mays, J. W. *Polymer* **1998**, *39*, 4631-4638.
- ²⁰ Xenidou, M.; Beyer, F. L.; Hadjichristidis, N.; Gido, S. P.; Tan, N. B. *Macromolecules* **1998**, *31*, 7659-7667.
- ²¹ Floudas, G.; Hadjichristidis, N.; Iatrou, H.; Avgeropoulos, A.; Pakula, T. *Macromolecules* **1998**, *31*, 6943-6950.
- ²² Beyer, F. L.; Gido, S. P.; Buschl, C.; Iatrou, H.; Uhrig, D.; Mays, J. W.; Chang, M. Y.; Garetz, B. A.; Balsara, N. P.; Tan, N. B.; Hadjichristidis, N. *Macromolecules* **2000**, *33*, 2039-2048.
- ²³ Mays, J. W.; Uhrig, D.; Gido, S.; Zhu, Y. Q.; Weidisch, R.; Iatrou, H.; Hadjichristidis, N.; Hong, K.; Beyer, F.; Lach, R.; Buschnakowski, M. *Macromolecular Symposia* **2004**, *215*, 111-126.
- ²⁴ Matsen, M. W. *Macromolecules* **2012**, *45*, 2161-2165.
- ²⁵ Balagurusamy, V. S. K.; Ungar, G.; Percec, V.; Johansson, G. *J. Am. Chem. Soc.* **1997**, *119*, 1539-1555.
- ²⁶ Hudson, S. D.; Jung, H. T.; Percec, V.; Cho, W. D.; Johansson, G.; Ungar, G.; Balagurusamy, V. S. K. *Science* **1997**, *278*, 449-452.
- ²⁷ Percec, V.; Cho, W. D.; Ungar, G.; Yeardeley, D. J. P. *J. Am. Chem. Soc.* **2001**, *123*, 1302-1315.
- ²⁸ Cho, B. K.; Jain, A.; Gruner, S. M.; Wiesner, U. *Science* **2004**, *305*, 1598-1601.
- ²⁹ Meuler, A. J.; Hillmyer, M. A.; Bates, F. S. *Macromolecules* **2009**, *42*, 7221-7250.
- ³⁰ Kinning, D. J.; Thomas, E. L. *Macromolecules* **1984**, *17*, 1712-1718.

-
- ³¹ Schmidt, S. C.; Hillmyer, M. A. *Journal of Polymer Science Part B: Polymer Physics* **2002**, *40*, 2364-2376.
- ³² Lee, I.; Panthani, T. R.; Bates, F. S. *Macromolecules* **2013**, *46*, 7387-7398.
- ³³ Anderson, K. S.; Hillmyer, M. A. *Macromolecules* **2004**, *5*, 1857-1862.
- ³⁴ Dorgan, J. R.; Janzen, J.; Knauss, D. M.; Hait, S. B.; Limoges, B. R.; Hutchinson, M. H. *Journal of Polymer Science Part B: Polymer Physics* **2005**, *43*, 3100-3111.
- ³⁵ Fetters, L. J.; Lohse, D. J.; Richter, D.; Witten, T. A.; Zirkel, A. *Macromolecules* **1994**, *27*, 4639-4647.
- ³⁶ Kinning, D. J.; Thomas, E. L.; Fetters, L. J. *J. Chem. Phys.* **1989**, *90*, 5806-5825.
- ³⁷ Hashimoto, T.; Kawamura, T.; Harada, M.; Tanaka, H. *Macromolecules* **1994**, *27*, 3063-3072.
- ³⁸ Pochan, D. J.; Gido, S. P.; Pispas, S.; Mays, J. W. *Macromolecules* **1996**, *29*, 5099-5105.
- ³⁹ Barton, A. F. In *CRC handbook of solubility parameters and other cohesion parameters*; CRC press: 1991;
- ⁴⁰ Schmidt, S. C.; Hillmyer, M. A. *Journal of Polymer Science Part B: Polymer Physics* **2002**, *40*, 2364-2376.
- ⁴¹ Balsamo, V.; von Gyldenfeldt, F.; Stadler, R. *Macromolecules* **1999**, *32*, 1226-1232.

Chapter 4: Tensile deformation and physical aging of poly(DL-lactide)

4.1 Background

As mentioned in Chapter 1, the overall goal of this study is to utilize a rubber-toughening strategy to enhance the mechanical robustness of polylactide. In the literature, polylactide is usually observed to be brittle in both tensile and impact tests with an average tensile strain at break of less than 10% for amorphous homopolymer poly(DL-lactide) (PDLA).¹⁻⁶ The primary plastic deformation mechanisms available to homopolymers are shear yielding and crazing. Both mechanisms are forms of strain localization with the severity increasing from shear yielding to crazing. Shear yielding is a thermally-activated displacement of polymer chains analogous to liquid flow. Studies have shown that during shear yielding, polymer chains develop higher energy conformations.⁷ In tension, when the applied stress exceeds the critical stress for shear yielding, diffuse or discrete bands (Figure 4-1a) develop in the direction of the maximum principal resolved stress, which may appear in a range from 45° to 58° relative to the tensile axis depending on stress state, pressure and sample density.^{8,9} Discrete bands, also termed “micro shear bands”, are a more localized form of deformation than diffuse bands.¹⁰ Within discrete shear bands, the deformation strain has been measured to be almost double of that in the matrix; while the strain in diffuse bands is only a few percent higher than in the rest of the polymer.¹¹ Thus, discrete bands indicate more severe strain localization than in diffuse bands. If the density of shear bands is high, sets of discrete bands may also coalesce to form a “neck” in the gage section (schematically illustrated in Figure 4-1b).^{12,13} The neck has a smaller cross-sectional area than the original,

undeformed gage. Thus, the true stress in the neck is higher than in the undeformed polymer. The polymer chains in the neck region become somewhat aligned in the tensile direction. Propagation of the neck to the undeformed polymer by cold-drawing occurs if the deformed material strain hardens sufficiently so that the local critical yield stress exceeds that of the undeformed material thereby making the delocalization of the stress more favorable. Shear yielding can also occur as homogeneous deformation due to diffuse shear bands. The alignment of the polymer chains in the shear bands renders it birefringent so that it may be visualized using transmission optical microscopy (TOM) with crossed polarizers.^{10,14}

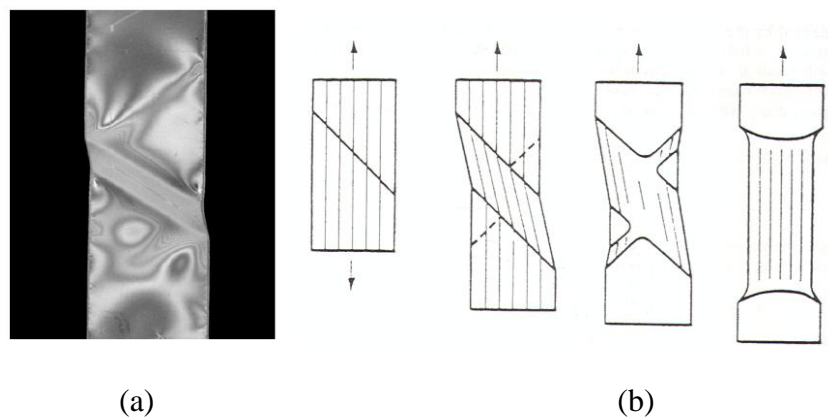


Figure 4-1 (a) Diffuse shear bands in polycarbonate can be seen in the photograph.¹⁵ Reprinted with permission from *Multi-Scale Analysis of Mechanical Properties of Amorphous Polymer Systems*, Meijer, H. E. H.; Govaert, L. E. *Macromolecular Chemistry and Physics* Vol. 204 Iss. 2 Copyright © 2003 WILEY-VCH Verlag GmbH & Co. KGaA, Weinheim. (b) The necking process with shear band formation is illustrated schematically.¹⁶ Reprinted with permission from *On the phenomenology of yield in bisphenol-A polycarbonate*, Stokes, V. k.; Bushko, W. C., *Polym. Eng. Sci. Vol. 35, Iss. 4* Copyright © 1995 Society of Plastics Engineers.

The primary deformation mechanism reported for PLA is the formation of crazes.¹⁷⁻¹⁹ Crazing, extensively studied by many researchers, is a micromechanical deformation mechanism where crack-like features are formed (illustrated schematically

in Figure 4-2a)²⁰⁻²² and grow in the direction of maximum principal strain which is perpendicular to the applied tensile stress for an isotropic material.²³ Although resembling cracks, the features, termed crazes, possess load-bearing polymer fibrils which span the newly formed faces of the craze (Figure 4-2b). The fibrils are primarily aligned parallel to the direction of stress, but can also form cross-ties that are almost perpendicular to the applied load.

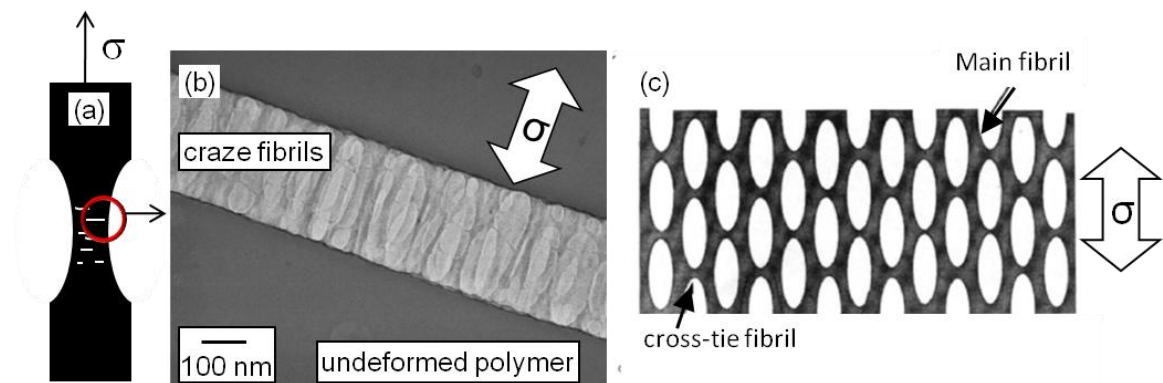


Figure 4-2 (a) The cartoon illustrates crazes which form perpendicular to the tensile direction and appear macroscopically as horizontal lines or cracks. (b) TEM of a craze reveals that the surfaces of the crack-like features are connected by polymer fibrils.²⁴ Reprinted with permission from *Crazing in glassy block copolymer thin films* Lee, J. Y.; Crosby, A. J. *Macromolecules* vol. 38 iss. 23 Copyright © 2005 American Chemical Society. The fibrils primarily align with the tensile direction, but some polymers may form cross-tie fibrils (visible in b) and schematically illustrated in (c) Reprinted with permission from *Relationship between craze microstructure and molecular entanglements in glassy polymers*. Berger, L. L. *Macromolecules* vol. 22 iss.7 Copyright © 1989 American Chemical Society.¹²

Cross-tie fibrils are essential for the transfer of stress to the craze tip and craze propagation into the undeformed material.²⁵ Macroscopically, the refractive index of the crazed polymer is locally reduced due to the fibril/void structure.²⁶ The craze features may grow large enough to scatter visible light resulting in the phenomena termed “stress whitening.”²⁷ Renouf-Glauser et al. determined craze fibril dimensions for amorphous

PLLA through model fitting of the 2D small-angle x-ray scattering (SAXS) patterns obtained during tensile deformation.¹⁷ They calculated the fibrils to be about 10 nm in diameter with a spacing of about 15 nm. The process of crazing absorbs deformation energy by lateral craze propagation which creates new surface and by craze thickening (lengthening of the fibrils) similar to the propagation of a macroscopic neck.¹² The extension of a craze fibril is governed by the intrinsic draw ratio, λ , of the polymer. The extension ratio is given by the final length of the fibril divided by the initial length of the fibril and has been found to be close to the maximum draw ratio of an entanglement segment. Thus, the critical molar mass of the polymer (M_c) must be 2–3× the molar mass between entanglements (M_e) for the craze to be stable enough to sustain a stress. A molecular weight less than M_c will result in chain pullout and unstable crack propagation instead of crazing.²⁸ The process of craze initiation is still not well understood, but is believed to develop from areas of local strain-induced plasticity and from surface defects.^{22,29,30} Furthermore, the formation of crazes has been shown to require a loss of some entanglements.³¹ Thus it follows that as the effective entanglement density (ν) increases, the craze initiation stress increases. The effective entanglement density considers both physical and chemical entanglements (e.g. cross-links). The physical entanglement density (ν_e) is the number of entangled polymer chains per unit volume as given by Equation 4-1 where ρ is the density of the polymer, N_A is Avogadro's number and M_e is the molecular weight between entanglements determined from melt rheology.³¹

$$\nu_e = \frac{\rho N_A}{M_e} \quad \text{Equation 4-1}$$

The craze fibrils lengthen by a surface drawing mechanism in which undeformed polymer directly bordering the craze interface is pulled into the craze area while maintaining a constant draw ratio. Ultimately, a craze fails by breaking of the fibrils to give way to a crack which can occur through chain scission or disentanglement depending on temperature. Crazeing stress, the stress required to propagate a craze, was found to be proportional to the yield stress of the polymer and void nucleation energy (Γ). Furthermore, the void nucleation energy is directly proportional to surface energy and entanglement density while the yield stress is known to be weakly dependent on strain rate. Crazes may be observed by SEM, TEM and small-angle x-ray scattering (SAXS) which identifies crazes by a characteristic scattering pattern^{32,33} as shown in Figure 4-3. The equatorial lobes (perpendicular to the tensile axis) are due to scattering between the craze fibrils akin to a nematic liquid crystal³⁴ while the intense meridional streak (parallel to the tensile axis) is due to scattering from the faces of the craze and reflection from the craze faces.³⁵ The streak-like nature of the scattering may be due to a distribution of domain spacings. TOM with or without crossed polarizers is less effective for the observation of crazes as they usually cannot be distinguished from cracks at the accessible length scale.³⁶

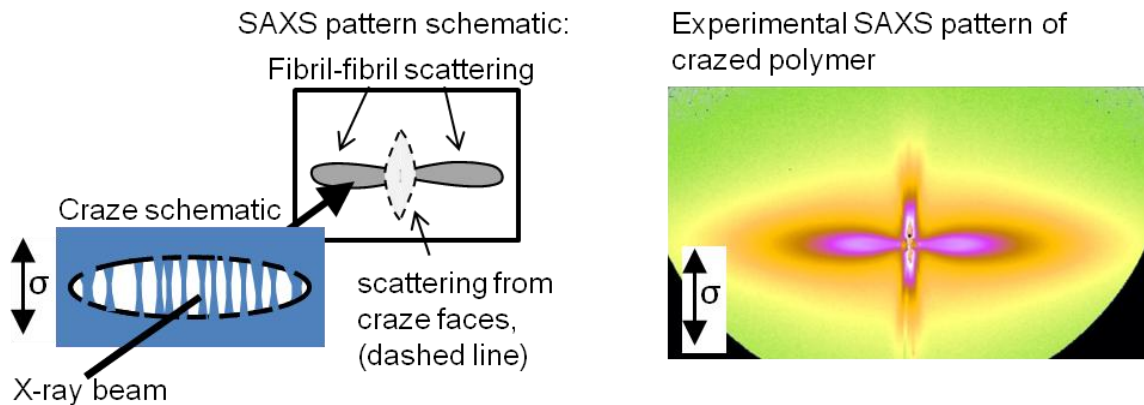


Figure 4-3 Characteristic small-angle x-ray scattering pattern from a craze.

The dominant deformation mechanism exhibited by a polymer is known to depend upon a number of variables including: effective entanglement density (ν), temperature, strain rate, thermal history and stress state.³⁷ In a seminal work, Kramer and Henke highlighted the influence of ν on dominant deformation mechanism by measuring the extension ratio (λ) of the craze or deformation zone (shear bands) observed by TEM in polystyrene films that were cross-linked to varying degrees of gel fraction by irradiation.³⁸ The effective entanglement density was calculated as the sum of the physical entanglement density of polystyrene (ν_e) and the cross-link density (ν_x). The other variables listed above were held constant. They determined that ν increases, the dominant deformation mechanism transitioned from crazing to shear yielding.³¹ As stated above, the craze stress is directly proportional to the entanglement density through the void nucleation energy term. However, the shear yield stress is unaffected by entanglement density. Thus, as the effectively entanglement density increases, shear yielding becomes energetically more favorable relative to crazing. Samples with intermediate values of ν ($\sim 5-8 \times 10^{25}$ chains/m³) exhibited both crazing and shear

banding simultaneously. In some cases, the deformation zones (DZs), areas of shear yielding, appeared to blunt the craze tip and thus, arrest further craze growth. The influence of ν on dominant deformation mechanism was also found to be true for a large variety of polymers ranging from polycarbonate to blends of polystyrene and polyphenylene oxide as shown in Figure 4-4.³⁸

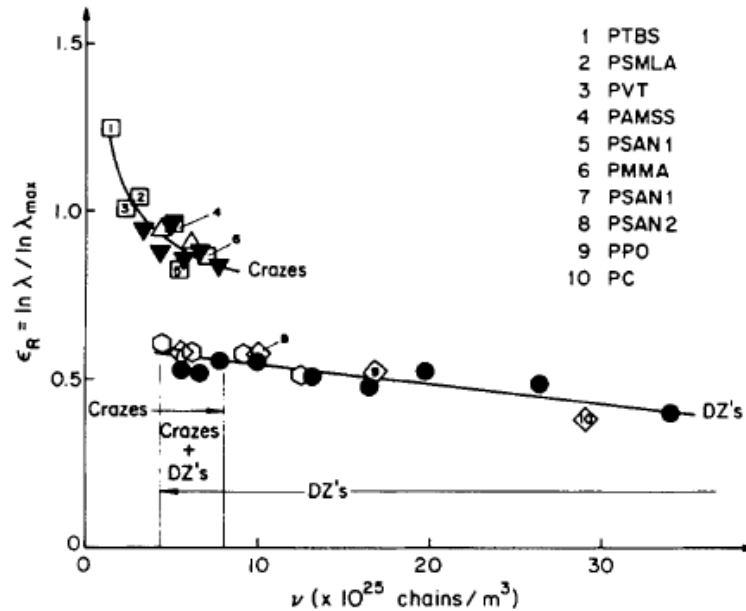


Figure 4-4 Henkee and Kramer plotted the normalized extension ratio (ϵ_R) for crazes and deformation zones (DZ's) as a function of effective entanglement density (ν) for a wide range of linear thermoplastics. Independent of polymer type, as ν increased, the dominant mechanism transitioned from crazing to shear yielding (manifested by DZ's).³⁸ Reprinted with permission from *Crazing and Shear Deformation in Crosslinked Polystyrene*. Henkee, C. S.; Kramer, E. J. *J. Polym. Sci. Polym. Phys. Ed.*, vol 22, iss 4, Copyright © 1984 John Wiley & Sons, Inc.

Although PLA is observed to be relatively brittle, the molar mass between entanglements (M_e) at 140 °C was found to be 3959 g/mol with a critical molar mass for entanglement (M_c) of 9,211 g/mol.³⁹ Using a density of 1.152 g/cm³, the ν_e for polylactide is $\sim 18 \times 10^{25}$ entangled chains/m³. Thus, Henkee and Kramer's plot (Figure 4-4) would predict relatively ductile behavior for polylactide achieved through shear

yielding along. However, polylactide, like many glassy polymers, is susceptible to physical aging and consequently, physical aging embrittlement. In fact, Henkee and Kramer specifically noted that the samples used to generate Figure 4-4 had not been physically aged.

Physical aging, also termed structural relaxation, is the phenomenon by which glassy polymers approach, often slowly, thermodynamic equilibrium when annealed below their glass transition temperature (T_g).⁴⁰ The extent of physical aging is nonlinearly dependent on the difference between the aging temperature (T_a) and T_g , the aging time (t_a), and the thermal history of the material prior to aging. The exact mechanisms responsible for physical aging are still under investigation, but it is well established that both the specific volume and enthalpy of the material decrease due to physical aging. Although large-scale chain motion is absent below T_g , sub- T_g secondary relaxations may still occur. For PLA in particular, a β relaxation attributed to a small amplitude twisting motion of the chain was identified through dielectric relaxation spectroscopy studies below the T_g .⁴¹ When a polymer glass is isothermally annealed at $T < T_g$, the structure changes through such local secondary motions to reduce its free energy and approach equilibrium. Physical aging is often discussed in terms of a potential energy landscape (PEL). The process of physical aging lowers the energy state of the material in the PEL. As a result of the structural changes that occur during physical aging, material properties are also observed to change. A general increase in yield stress and modulus due to physical aging has been noted for a variety of polymers, a phenomenon that may be related to the decrease in specific volume.⁴⁰ Additionally, physical aging has been shown

to cause embrittlement by increasing the minimum stress needed to shear yield, but not significantly affecting the critical stress for crazing.^{9,42}

Ultimately the deformation mechanism of a polymer depends upon the level of strain localization, where homogeneous shear yielding has the least amount of strain localization and crazing has the most.³⁷ Furthermore, the severity of strain localization depends upon the balance of the material's response to strain (i.e., strain hardening or softening). Strain hardening results when the true stress on the material increases with increasing strain. During strain softening, the opposite is observed, the true stress decreases with increasing strain. If strain hardening dominates, delocalized mechanisms such as stable neck propagation can occur.

By monitoring the true compressive stress-strain behavior of polycarbonate and polystyrene as a function of physical aging, van Melick and co-workers determined that strain softening, immediately after the yield point, increases with physical aging.^{37,43} Thus, as a glassy polymer is physical aged, the deformation mechanism may change from a delocalized mechanism such as homogeneous yielding to a more localized mechanism such as craze propagation due to an increase in strain softening. This ductile-to-brittle transition as a result of physical aging has been observed for a number of polymers including polycarbonate (PC),⁴⁴⁻⁴⁷ poly(hydroxy butyrate),⁴⁸ and PC/acrylic impact modified blends.^{49,50} As the T_g of polylactide is only 35 °C above room temperature at the most, physical aging may be a significant factor since an appreciable amount of physical aging can occur at room temperature. There has been recent experimental evidence to support this idea demonstrating that the ultimate elongation of polylactide

decreased from an unaged value of 300% to only 4% after 24 hours of aging at 25 °C.¹⁹ At the same time, both the modulus and yield stress increased with aging which is the expected behavior. The intrinsic mechanical behavior of polylactide, without physical aging, may be ductile; but realistically, as a commercial product, the material will physically age at room temperature before consumer use and must therefore be considered a brittle material.

In this chapter we study the tensile properties and deformation mechanisms of poly(D,L-lactide) by small-angle x-ray scattering as a function of physical aging to serve as a basis for comparison to our rubber modified graft copolymers.

4.2 Experimental

4.2.1 Materials

The material studied is homopolymer poly(D,L-lactide) [PDLLA] synthesized by the procedure described in Chapter 2. Homopolymer PDLLA will be designated as PDLLA-Xk, where X is the M_n of the polymer (¹H NMR) in kg/mol. The physical properties of the various PDLLAs studied are given in Table 4-1.

Table 4-1 Physical properties of poly(D,L-lactide) [PDLLA] studied

Sample	M_n¹ (kg/mol)	\bar{D}²	T_g³ (°C)	Notebook ID
PDLLA-58k	58.1	2.4	54.7	GCT2106a
PDLLA-59k	59.4	1.9	55.3	GCT2007a
PDLLA-75k	74.7	2.4	56.0	GCT2113

1)Determined by ¹H NMR, 2)SEC in CHCl₃ at 35 °C, PS stds.,
3)DSC 2nd heating at 10°Cmin⁻¹

4.2.2 Compression molding of tensile bars

For the homopolymer PDLLA, approximately 4 g of as-dried polymer was compression molded into a film of nominally 0.55 mm thickness at 150 °C for 5 minutes,

with a maximum pressure of 0.7 MPa and subsequently quenched to room temperature in 5–8 minutes using water circulated through the platens of a Wabash MPI heated hydraulic press. From this film, small dogbone shapes were scored on the film with a diamond scribe and cut out using scissors. The preforms were then compression molded using a custom, stainless steel, non-ASTM standard dogbone tensile bar mold and the same conditions as above. The flash from all compression molded samples was removed using an Exacto knife. Using a light box and circular polarizers (one polarizer, one analyzer), the bars were examined for dust and defects. Samples containing dust and defects in the gage region were not tested.

4.2.3 Ambient conditioning of compression molded tensile bars per ASTM D882

In an attempt to adhere to ASTM D882, *Standard Test Method for Tensile Properties of Thin Plastic Sheeting*, compression molded samples were conditioned for about 48 hours on the lab bench top in re-sealable polyethylene bags. The samples were bagged and placed on the bench top within a few hours of compression molding. The average temperature of the laboratory, measured over a 16 h period using a data logger (Easy Log USB, Lascar Electronics) was found to be 24 ± 1 °C with an average relative humidity of 51 ± 4 %RH. The measured average values are close to the conditions prescribed in ASTM D882: 23 ± 2 °C and 50 ± 5 % RH for at least 40 hours prior to tensile testing. Tensile testing was performed at room temperature and ambient humidity (~ 23 °C , ~ 50 % RH)

4.2.4 Controlled physical aging of compression molded tensile bars

To observe the influence of variable conditioning temperatures and time, compression molded tensile bar samples were placed in re-sealable polyethylene bags and stored in a glass drying chamber (Chemglass) under dynamic vacuum (20–30 mtorr) within a few hours of compression molding. The drying chamber was then immersed into a thermostatted oil bath set to either 25 or 40 °C. A portable digital data logger (Easy Log USB, Lascar Electronics), placed inside the chamber, was used to confirm the temperature, humidity and stability of the conditions. The average oil bath temperatures were 25 ± 1 °C and 40 ± 2 °C respectively. The average relative humidity (RH) in both cases was $\leq 2\%$ RH. Samples were aged for times ranging from 1 to 4 days. Data for the unaged condition was obtained from samples stored in ambient laboratory conditions (see above) and tested within 2 hours of compression molding. After aging for the required amount of time, the samples were removed from the oil bath and brought to room temperature. Tensile testing was performed at room temperature and ambient laboratory humidity (~ 23 °C, $\sim 50\%$ RH) within 1 to 2 hours of removal of the sample from the oil bath.

4.2.5 Quantitative tensile testing

Tensile testing of compression molded non-ASTM standard dogbone samples (12 mm gage length, 0.5 mm gage thickness, 3 mm gage width) was conducted on a Rheometrics Scientific Minimat Instrument at a cross-head extension rate of 10 mm/min. Reported values are arithmetic averages of engineering stress and engineering strain with standard deviations of at least four samples without any toe correction (i.e., mathematical

correction of curvature in the beginning of the stress-strain data due to settling of the sample in the grips). Samples failing at visually observed defects (such as dust particles) or by tear failure were excluded from the data set per ASTM D882. Young's modulus (E) was measured as the slope of the linear portion of the stress-strain curve in the small-strain region before yield and after the toe region.

4.2.6 In-situ small-angle x-ray scattering and tensile testing

In-situ small-angle x-ray scattering and tensile testing were performed at the Advanced Photon Source at Argonne National labs 5ID-D beamline. SAXS data were collected on a circular marCCD camera (162 mm, Mar USA, Inc.) using exposures of 0.5 seconds. At least three exposures of the undeformed sample in the tensile apparatus were collected before starting the tensile test at which point, exposures were automatically collected every 5 seconds until tensile failure was observed. A vertical position was recorded for each scan allowing for calculation of a displacement relative to the beginning of the tensile test. The broken sample, still in the tensile apparatus, was then moved out of the x-ray beam path to obtain the background scattering data. The in-situ tests were conducted at both 9 and 17 keV with a constant sample-to-detector-distance of 4577 mm. The x-ray beam was off-set 30 mm in the vertical direction below the center of the circular detector. Samples were compression molded in the same manner as described above, but using the sample geometry shown in Figure 4-5a. The nominal thickness of the samples was 0.5 mm. The custom sample geometry was used to ensure that the deformation began first at the center of the sample where the stress was concentrated due to the semi-circular notches and which could be targeted with the x-ray beam. Tensile

testing was performed using a customized servo-hydraulic Instron Materials testing system which recorded load and position of the upper grip. The compression molded sample was placed in the hydraulic tensile grips (Instron servo-hydraulic testing system, model 8500) which were both controlled by actuators so that the center of the sample remained in the x-ray beam during entirety of the tensile test. Thus, displacement was calculated from the position data of the upper grip and multiplied by 2. The hydraulic tensile grips were operated using a PID controller at a cross-head extension rate of 0.125 mm/min. At the beginning of the experiment, the parameters of the PID controller were refined using the on-board software program. No additional attempts were made to further optimize the parameters. Thus, the resulting tensile data contains a periodic vibration. The in-situ tests were first performed using 17 keV and then repeated using 9 keV. Unfortunately, the PID parameters became less optimized for the later tests (at the 9 keV energy) causing the periodic vibration to change from an initially relatively high frequency to a lower frequency. Ultimately, the 17 keV scattering data proved most useful and will be analyzed below. In general, the results were the same at both energy levels. Due to the noise in the load data, the tensile data were smoothed using the smooth function in MATLAB R2013 with a Savitsky-Golay filter. The span was generally chosen to be about 5% of the total number of data points and the degree was adjusted manually to reduce the amplitude of periodicity while maintaining the original position of the yield point. A representative example of the original data compared with the smoothed data is shown in Figure 4-5b. Engineering stress was calculated from the measured load and the initial cross-sectional area of the gage at the narrowest point

(nominally 3 mm × 0.5 mm). The smoothed data retained the general shape of the stress-displacement curves and were used for qualitative analysis. Additionally, optical photos of the tensile bar during deformation were manually captured with the cameras used for initial positioning the sample in the tensile grips.

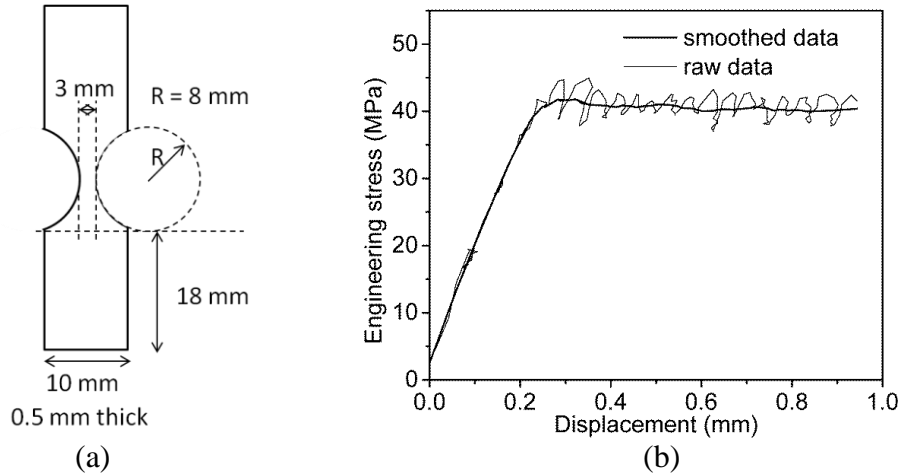


Figure 4-5 (a) A non-standard tensile bar geometry was utilized for the in-situ SAXS/tensile experiment. (b) A representative plot of engineering stress versus displacement for data obtained during the in-situ tensile/small-angle x-ray scattering experiment. The original data contained a periodic vibration due to sub-optimal PID control parameters. The data was smoothed to emphasize the qualitative shape of the stress-displacement curve.

4.3 Results

4.3.1 Quantitative tensile properties

A survey of literature regarding the tensile behavior of PLA reveals that the conditioning of samples, if mentioned at all, is usually said to be performed per ASTM D882 (or similar standard) which specifies storage of the samples at 23 ± 2 °C and 50 ± 5 % RH for at least 40 hours (h) prior to tensile testing. In this work, we study the effect of physical aging on the tensile behavior and tensile deformation mechanisms of PDLLA. We begin with quantitative tensile tests of PDLLA aged under various conditions. Due to

practical considerations, the shortest time achievable between compression molding and tensile testing was approximately 2 h. Consequently, we choose these samples to represent the “unaged” condition. The samples were exposed to ambient laboratory conditions (24 °C, 51% RH). Samples were also aged for 48 h in ambient laboratory conditions as prescribed by ASTM D882. Finally, for additional comparison, samples were aged in an evacuated chamber submerged in an oil bath set to 25 °C for 2 days (d) and 4 d, and at 40 °C for 1 d. The conditions are summarized in Table 4-2. Plasticization of PLA by water has been observed in the literature.^{51,52} However, the aging conditions used this study are relatively mild and thus, we expect little to no effect on mechanical properties due to the differences in relative humidity.

Table 4-2 Physical aging conditions

	Aging Temperature (°C)	Relative Humidity (%)	Aging time (h)
Unaged	24 ± 1	51 ± 4	2
Per ASTM D882	24 ± 1	51 ± 4	48
Controlled 25 °C	25 ± 1	≤ 2	48, 96
Controlled 40 °C	40 ± 2	≤ 2	24

Representative engineering stress-strain curves are shown in Figure 4-6a for poly(DL-lactide) with M_n of 75 kg/mol (PDLLA-75k) in the unaged and aged conditions. The samples were tested at 25 °C. All of the aged samples exhibited the brittle tensile behavior typically reported for PDLLA in literature.^{17,19} After an apparent linear elastic region at small strain, the brittle samples reached a maximum stress at the yield point (σ_y), plastically deformed and then failed catastrophically. Although only nominal stress and strain was computed rather than true stress-strain, the geometry of the sample after σ_y qualitatively appeared unchanged indicating that the post-yield stress decrease (PYSD)

likely resulted from strain softening and not from a geometric artifact that would be absent in the true stress-strain curve. All the samples were initially transparent due to the amorphous nature of the polymer. Thus, during the tensile test, some stress whitening in the gage region could be observed before brittle fracture in the stress whitened area occurred. A photograph of a brittle tensile bar after failure is shown in Figure 4-6b represented by the sample aged at 24 °C, 51% RH, 2 d. After failure, the width and thickness of the gage appeared the same as before testing. The black lines are wax-pencil guidelines added before the test to assist in positioning the sample in the grips. The spacing between the two outermost lines is approximately 12 mm with the middle line approximately positioned at the center point of the gage.

In contrast, relatively ductile tensile behavior was observed for the unaged samples (24 °C, 51% RH, 2 h). As seen in Figure 4-6a, after a linear elastic region, the ductile sample also exhibited a yield point followed by small decrease in stress. As before, the sample geometry appeared unchanged during the first stress drop. However, after some plastic deformation and stress whitening, a neck was initiated in the gage region resulting in an artificial stress drop. The neck was propagated through the entire gage section by cold-drawing at constant stress. As the neck was propagated into the transition region between the gage and the grips, the tensile stress appeared to increase. Failure occurred in the cold-drawn gage region. The final thickness and width of the gage was smaller than that of the initial sample as illustrated in Figure 4-6b by the sample aged at 24 °C, 2 h after failure compared with the sample aged at 24 °C, 2 d after failure.

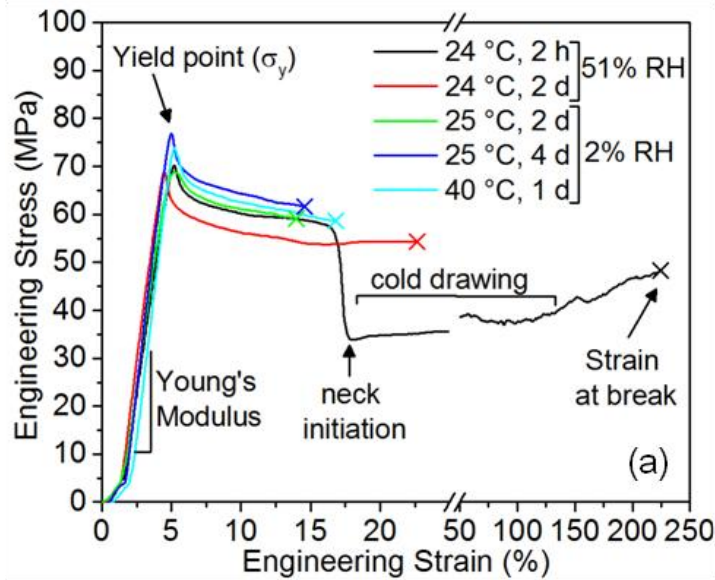


Figure 4-6 (a) Representative engineering tensile stress-strain curves of poly(D,L-lactide) with M_n of 75 kg/mol [PDLLA-75k]. The compression molded tensile samples were aged under various conditions before tensile testing at 25 °C and an extension rate of 10 mm/min for a nominal gage of 10 mm × 3 mm × 0.5 mm. The failure point is denoted by an 'x'. (b) The photograph of representative tensile bars after failure that were aged at 24 °C for 2 h and for 2 days illustrates both ductile and brittle behavior, respectively.

The average and standard deviation values of E , σ_y , ϵ_b , and tensile toughness from the tensile tests are shown in Figure 4-7. In general, the average values for the brittle samples are consistent with the values usually cited in literature. The values obtained for the unaged sample (aged at 24 °C, 2 h) are consistent with data reported by Pan et al. for amorphous PLLA aged at 25 °C for ~3 h.¹⁹ Ideally, the average values should be plotted against the extent of physical aging which is non-linearly dependent on aging time and

temperature as well as thermal history prior to aging. In this experiment, the primary variable was aging time at 25°C since all the samples were treated similarly prior to aging. Considering only the samples aged at 24 and 25°C, the measured Young's modulus (Figure 4-7a) shows the expected increasing trend with increasing aging time. The trend is less apparent in the yield strength data (Figure 4-7b) with the samples aged at 24 °C, 2 days having a slightly lower value than the unaged samples. Based on the average values of the modulus and yield strength for the samples aged at 40 °C for 1 d, the extent of physical aging is likely intermediate between samples aged at 25 °C for 2 d and for 4 d. A substantial difference in strain at break is seen for the unaged sample relative to all the aged samples (Figure 4-7c). All of the aged samples have an average strain at break that is less than 25%, which is 10× smaller than that for the unaged sample. Furthermore, the sample aged for 2 days in ambient laboratory conditions (24 °C, 51% RH) has a larger ϵ_b relative to its oil bath analog (25 °C, 2% RH). The increased ϵ_b and slightly lower σ_y may indicate a plasticization effect of water that may have been absorbed by the PLA sample in the ambient laboratory conditions. The experiment conducted by Pan et al. revealed that the strain at break began to decrease slightly even after only 3 h of physical aging at 25 °C and reached a relatively constant value (~ 6 %) after about 24 h of aging.¹⁹ Our values of strain at break are slightly larger, possibly due to the tensile testing frame utilized.¹⁷ As mentioned before, the post-yield stress drop (PYSD) may indicate strain softening of the material and was seen to increase with physical aging. Typically, the PYSD is calculated from the upper and lower yield points of the true stress-true strain curve. In this case, PYSD was approximated as the difference

between σ_y and the stress at break (or stress just before neck initiation in the case of the ductile sample). No trend is apparent from Figure 4-7d. Overall, the quantitative tensile data confirms that embrittlement of PLA due to physical aging at 25 °C is rapid, occurring within two days during our study and even faster according to Pan et al.¹⁹

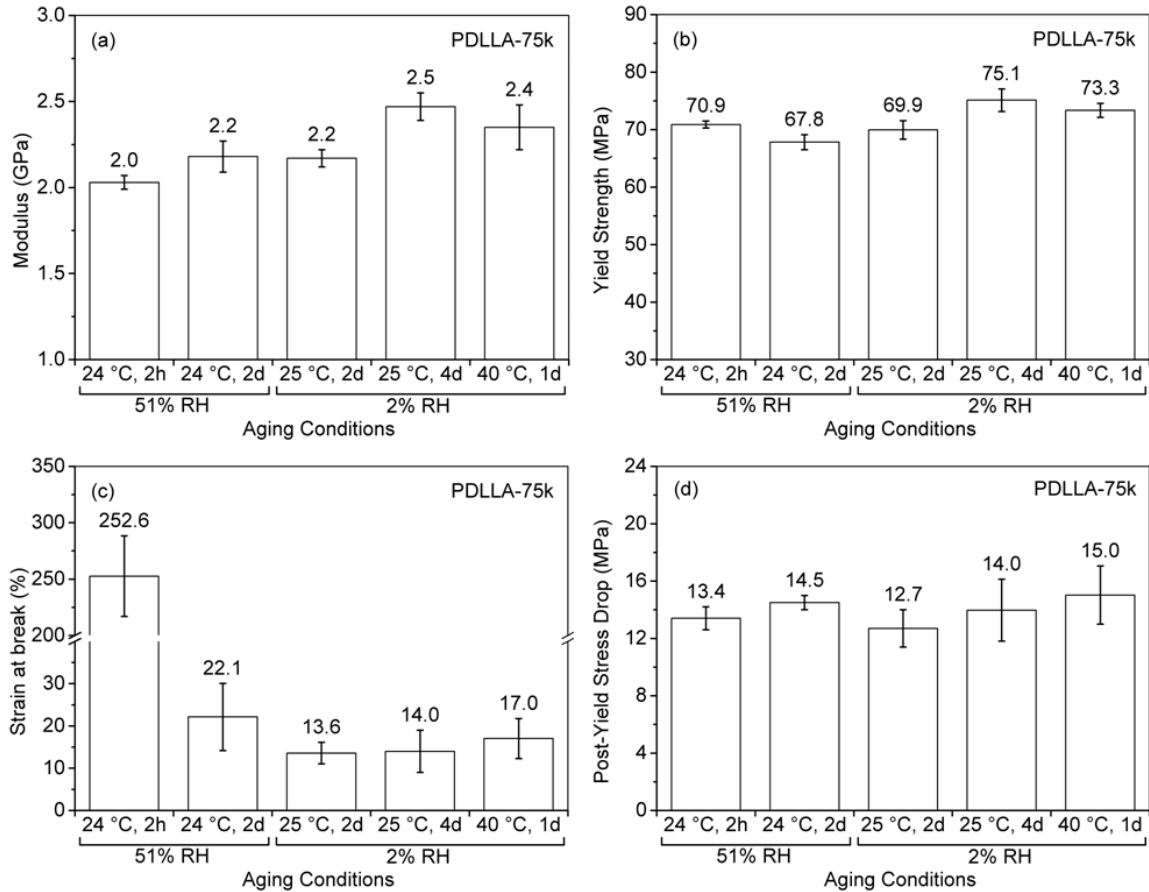


Figure 4-7 The average and standard deviation of (a) Young's modulus, (b) yield strength, (c) strain at break, and (d) post-yield stress drop for PDLLA-75k after physical aging on the laboratory bench top (51% RH) at 24 °C for 2 h and for 2 days, and aging in an oil bath (2% RH) at 25 °C for 2 and 4 days, and at 40 °C for 1 day. A minimum of four valid tests were used to obtain the average and standard deviation. The average value is listed above the error bar.

As previously described, the unaged sample was able to initiate and propagate a neck resulting in a large tensile strain at break (Figure 4-7c). The brittle samples only exhibited stress whitening before fracture. Thus, the deformation mechanisms are

different in the aged and unaged samples. The observed stress whitening in the samples is likely associated with the formation of crazes due to the change in refractive index of the material when voids are introduced. Scanning electron-microscopy on a tensile bar of PDLLA-50k that was aged at 24°C for 2 days in 51% RH after failure confirmed the presence of crazes (Figure 4-8) in the whitened regions. Although Pan et al. also observed the ductile tensile behavior of unaged PLA, the study focused on the kinetics of physical aging and not on the micromechanical deformation mechanism. However, the initiation and propagation of a macroscopic neck is known to result from a shear yielding mechanism¹³ which is consistent with the prediction made in the introduction that, based on the analysis of entanglement density, polylactide in the unaged state may exhibit both shear yielding and crazing as deformation mechanisms. Therefore, as a result of physical aging, the tensile deformation mechanism of PLA was seen to change from that of crazing followed by shear yielding to a mechanism of only crazing. It is unknown whether “perfectly unaged” PLA would exhibit only shear yielding.

The interaction and relationship between crazing and shear yielding is not straightforward with various studies concluding that crazes can be initiated or terminated by shear bands.^{53,54} Another study concluded that shear bands may be initiated at craze tips.⁵⁵ In order to obtain more detailed information about the micromechanical deformation mechanisms occurring during tensile testing, small-angle x-ray scattering and tensile testing were simultaneously conducted on PDLLA-58k, under two aging conditions. Although PDLLA-58k is of a lower molar mass than PDLLA-75k, they are

both well-entangled. Thus, we expect the tensile and aging behavior of PDLLA-58k to be essentially the same as PDLLA-75k.

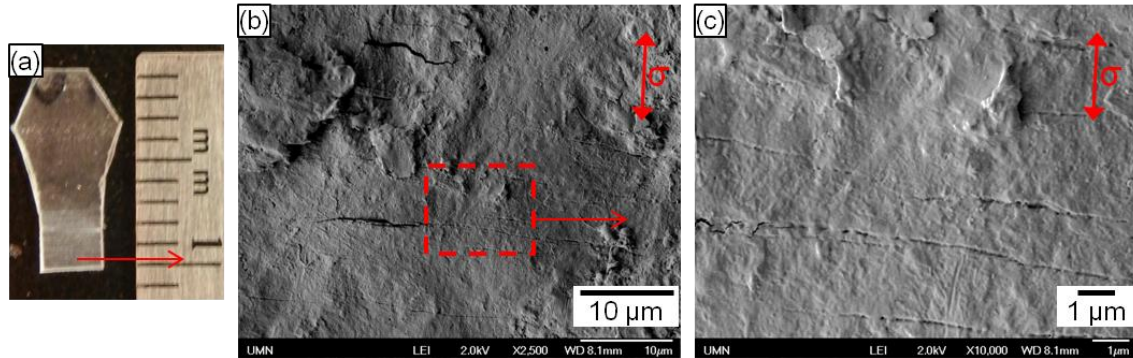


Figure 4-8 Collapsed crazes are observed by scanning electron microscopy of brittle PDLLA-59k aged at 24°C for 2 days in 51% RH, after tensile testing. (a) The sample was examined in the whitened gage region near the fracture surface as shown in the photograph. Collapsed crazes can be seen both at (b) 2500× magnification and (c) 10,000× magnification as approximately horizontal lines. The dashed rectangle highlights the magnified region shown in (c). The double headed arrow denotes the tensile axis.

4.3.2 Simultaneous small-angle x-ray scattering and tensile testing

The “unaged” condition was represented by samples that were placed in cold storage within a few hours of compression molding and remained there until 5 min before tensile testing resulting in a total aging time of ~66 h. The cold storage had an average temperature of -12 ± 9 °C and humidity of $29 \pm 2\%$ RH. The unaged samples were at room temperature for < 3h total before testing. The samples representing the aged condition were stored in ambient laboratory conditions (~23 °C, ~50% RH) until testing, resulting in an average conditioning time of 66 ± 3 h. A cross-head extension rate of $0.5 \text{ mm}\cdot\text{min}^{-1}$ was utilized to allow for enough time resolution to capture the tensile deformation phenomena. Assuming a 5 mm gage length, the initial strain rate was 0.002 s^{-1} . The hydraulic tensile grips moved in opposite directions (vertically) at the same rate

($0.25 \text{ mm}\cdot\text{min}^{-1}$) ensuring that the same sample area remained in the beamline throughout the duration of the tensile test. Due to the non-standard geometry of the sample, engineering tensile strain could not be calculated and instead the extension is reported as displacement. The same sample geometry was utilized for each material so relative comparisons can be made.

As described in the experimental section, the engineering stress data was smoothed due to periodic cycling of the cross-head actuators and cannot be compared quantitatively to a normal tensile test. The samples were additionally monitored visually during the test with two live-feed cameras used for sample alignment (horizontal and vertical) with the x-ray beam. The cameras were positioned at two different angles relative to the sample as illustrated schematically in Figure 4-9.

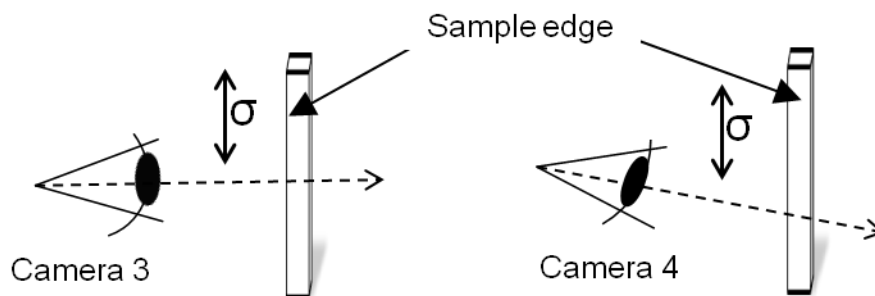


Figure 4-9 Schematic illustration of the general viewpoints of the sample shown by camera 3 and camera 4.

Time-stamped screen-shot images of the samples were manually captured throughout the duration of the test and can be associated with tensile displacement through the time-stamp. The photos of the sample shown with the 2D SAXS pattern were either taken at the same time or within a few seconds of when the SAXS pattern was acquired.

4.3.2.1 Results for aged PDLLA-58k

Representative in-situ tensile results for aged PDLLA-58k are shown in Figure 4-10. The stress at the beginning of the tensile test is non-zero because the load cells were zeroed before the sample was clamped. The clamping procedure applied a slight tensile force on the sample, but did not exceed the linear elastic limit. The sample failed in a brittle manner as expected with only a small amount of deformation (< 1 mm) as shown by the tensile stress vs. displacement curve (Figure 4-10i). Based on the optical photos, the engineering strain is estimated to be $\sim 12\%$. In general, the shape of the stress vs. displacement curve is consistent with the tensile behavior observed in the quantitative tests for aged PDLLA-75k. The two cameras that were used for initial sample alignment viewed the sample from different angles (Figure 4-9). Camera 3 shows the sample as if the viewer is approximately parallel to the tensile axis while camera 4 shows the sample from a slightly angled viewpoint. The black lines on the sample are reference marks that were applied using a wax crayon and spaced approximately 5 mm apart. As seen in Figure 4-10ii, through camera 3 the transparent sample initially appears homogeneous without any whitening in the gage. As discussed previously, visual observation of whitening of the gage implies that the refractive index of the material in the whitened area has changed relative to the undeformed material. A change in refractive index may result from a number of phenomena including void formation, crazing, or molecular alignment. As the sample is deformed, whitening in the gage is first noticeable by camera 3 at the yield point (Figure 4-10ii, point d). The whitened area is localized to a narrow rectangular strip in the middle of the sample and spanning the width of the gage. With

further tensile deformation, the whitened strip increased in intensity (more white) and increased along the tensile direction while still spanning the width of the gage. After failure, the whitened areas seen through camera 3 remained the same as just before failure (point f). The observations of the sample through camera 3 are consistent with the visual observations of brittle PLA during the quantitative tensile tests.

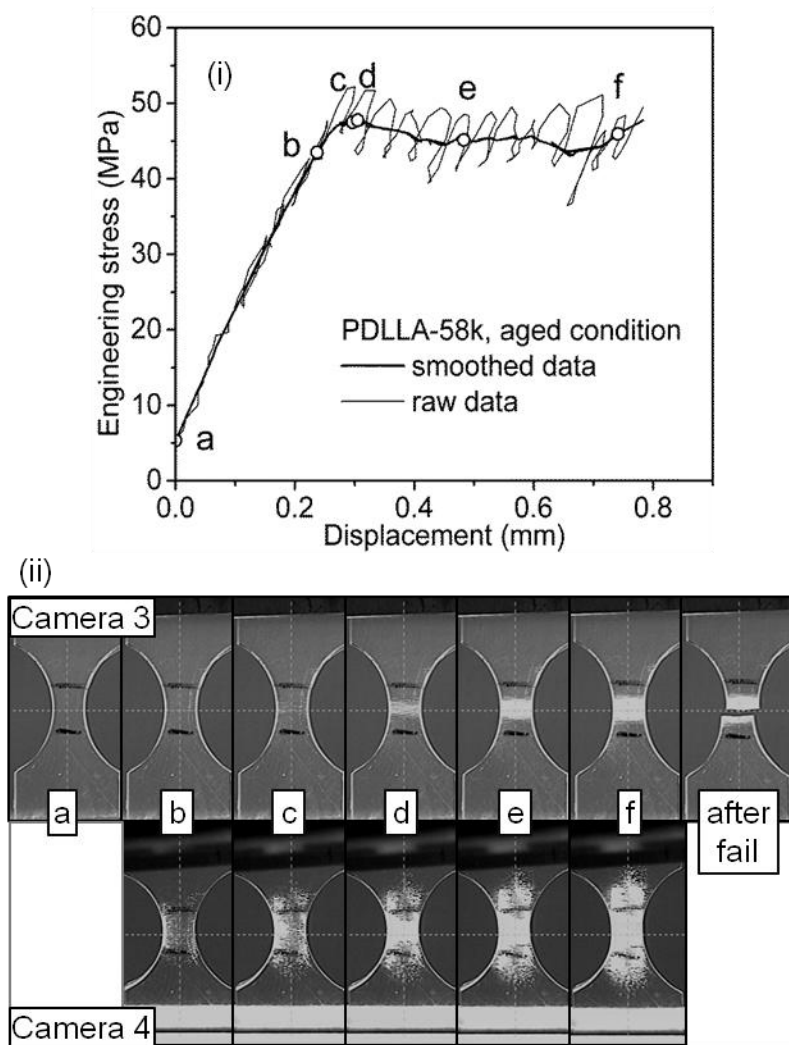


Figure 4-10 In-situ tensile data for PDLLA-58k in the aged condition (~ 25 °C for 66 h). Specific displacements are highlighted by the alphabetical points on the (i) engineering stress vs. displacement curve. The (ii) photographs from camera 3 and camera 4 correspond with the labeled points on the stress-displacement curve.

Interestingly, the progression of mechanical deformation, as implied by whitening of the gage, is different when observed from the angle of camera 4. A photo of the as-clamped sample from camera 4 was not captured; however, the sample appeared homogeneous as was seen by camera 3 (seen in other samples as well). In the seemingly linear region of the stress-displacement curve (Figure 4-10ii, point b), a slight whitening of the entire gage section is detected only by camera 4. The sample continued to whiten with increasing deformation. Both the intensity of the whitening and the amount of whitened area increased (up into the transition region of the sample) with greater deformation. A photo taken using camera 4 of the sample after failure was not captured. However, photos of aged PDLLA-58k, probed using the 9 keV energy, immediately before and after failure taken within an 8 second time span (Figure 4-11), show that some of the whitening seen through camera 4 before failure, dissipated after failure. Thus, the disappearance of some of the whitening after failure is also expected for the aged PDLLA probed using the 17 keV energy. By comparing the photos obtained by camera 3 and camera 4, it is evident that camera 4 captured both the deformation observed by camera 3 in addition to another, different deformation mechanism. The primary difference between camera 3 and camera 4 is the viewing angle relative to the surface of the sample. Thus, the visual observations suggest that the unknown deformation phenomenon possesses an anisotropic optical property. However, more precise experiments with polarized light must be conducted to determine if the unknown deformation phenomenon is birefringent. Stress-induced birefringence has been shown to occur in polymers during deformation.⁵⁶⁻

⁵⁸ Often stress-induced birefringence is attributed to rotation and orientation of the

polymer chains which may contribute to elastic deformation; however, shear bands and crazes are also known to be birefringent.^{59,60} In the latter case, the birefringence remains even in the unloaded condition due to the plastic nature of the deformation.

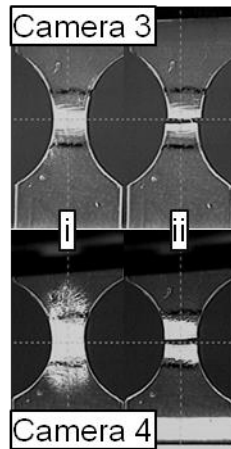


Figure 4-11 Optical photos of aged PDLLA-58k probed with an x-ray beam of 9 keV energy (i) before and (ii) immediately after tensile failure.

The 2D x-ray scattering patterns of aged PDLLA are shown in Figure 4-12. Initially, the scattering from the “as clamped” aged PDLLA-58k sample is negligible as expected (Figure 4-12, point a). As the sample is deformed elastically (Figure 4-12, point b), azimuthally narrow streaks emanating from the beam stop are observed in the 2D scattering pattern. There are two sets of approximately orthogonal streaks which are symmetric about the beam stop. One streak of each pair is located on either side of the equator, while the corresponding streaks are on either side of the meridian. Notably, the appearance of the narrow streaks coincides with the emergence of the optically anisotropic deformation phenomenon observed by camera 4. We shall refer to these features as “pre-yield streaks” and discuss them in greater detail later. At the yield point (point d), the characteristic craze scattering pattern is observed. The diffuse equatorial

lobes (perpendicular to the tensile axis) are due to scattering from between the craze fibrils akin to a nematic liquid crystal⁶¹ as shown schematically in Figure 4-3. The extremely intense meridional streak (parallel to the tensile axis) is due to scattering from the faces of the craze and total internal reflection from the craze faces³⁵. Thus, the whitening observed by camera 3, which started at the yield point, is due to crazing as expected. The characteristic craze pattern is maintained until failure.

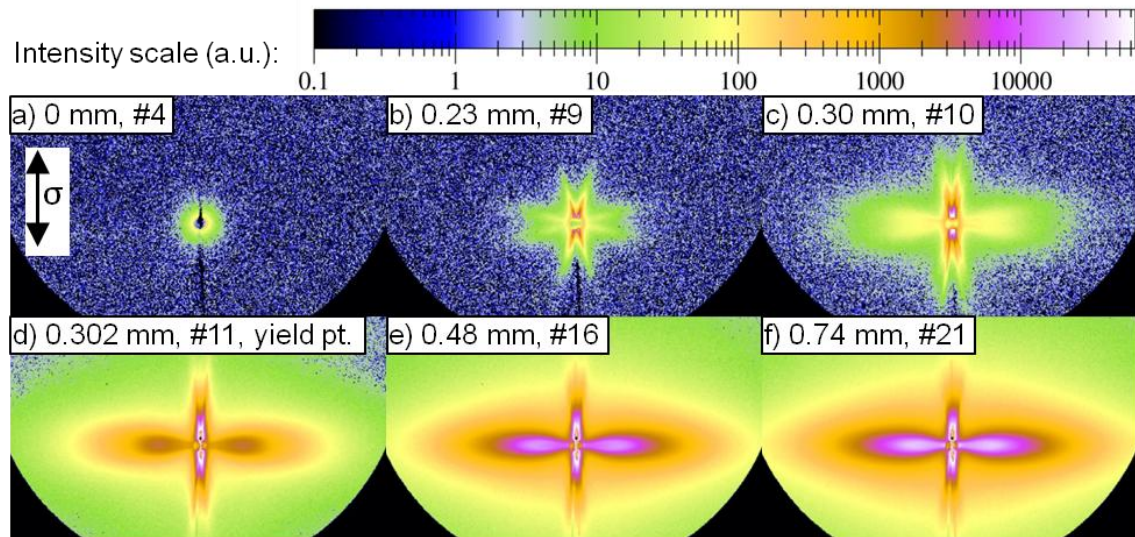


Figure 4-12 In-situ SAXS data for PDLLA-58k in the aged condition ($\sim 25^\circ\text{C}$ for 66 h) as it is deformed in tension. The tensile axis is vertical and denoted by the arrows. The 2D SAXS patterns correspond with the alphabetically labeled points on the engineering stress displacement curve shown in Figure 4-10. The 2D SAXS patterns are labeled with the displacement and file number. The scattered intensity scale of each SAXS image is the same for all the displacements shown.

The 2D SAXS images were then azimuthally integrated using 2 different azimuthal ranges shown in Figure 4-13. The accessible q -range in the equatorial direction was smaller than that of the meridional range because the x-ray beam was offset vertically from the center of the circular detector. In the q -range investigated, the scattering from the sample in the equatorial direction (Figure 4-14i) is relatively small

until point c, which occurred 5 s before the characteristic craze scattering pattern was observed at the tensile yield point (point d). At the yield point, a small peak with a maximum located 0.31 nm^{-1} developed. The peak results from the principal interfibril interference and has been observed for fresh crazes in polystyrene films⁶², polycarbonate crazes⁶³ and in polylactide crazes⁶⁴. Thus, the principal fibril-fibril spacing is approximately 20 nm. In addition, there is a large increase in overall scattered intensity relative to point c. With further tensile deformation (point e and f), the shape of the curve remains similar, but the overall intensity continues to increase. The peak maximum shifts towards somewhat lower q-values (0.29 and 0.28 nm^{-1} for point e and f respectively) so that the fibril-fibril spacing increases to 22 nm at point f. The increased intensity with little change of the shape of the curve is consistent with an increase in craze density. The intense scattering in the meridional range (Figure 4-14ii) results from the craze faces. As the sample is plastically deformed to failure, the meridional scattering at the low q-values increased to a level where the detector became saturated resulting in the intensity plateaus observed in the curves (starting at point d). The saturated intensity plateau broadened in q-range with additional deformation.

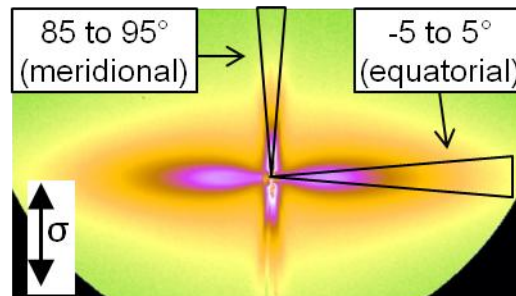


Figure 4-13 The azimuthal ranges used for integration of the 2D scattered intensity patterns are schematically illustrated.

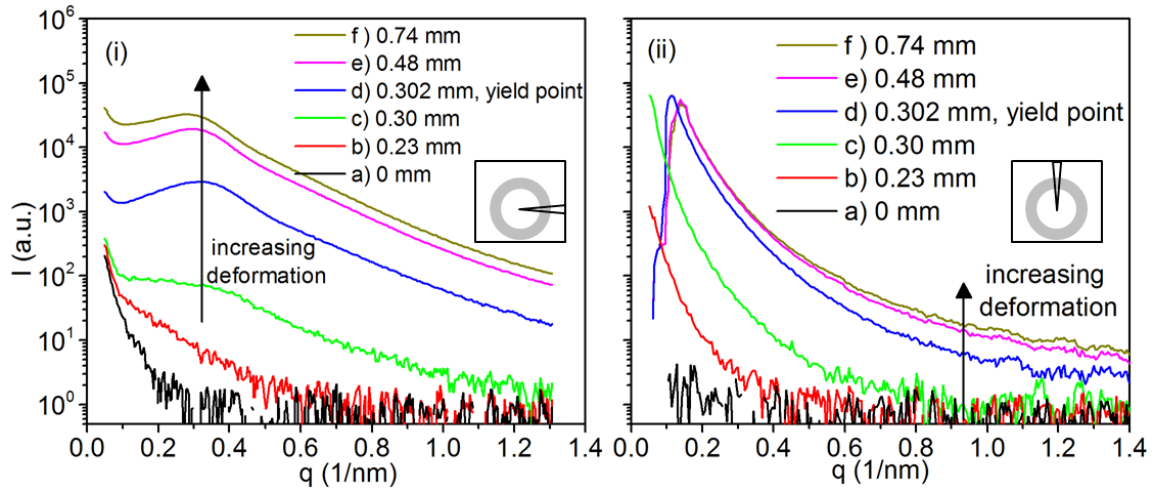


Figure 4-14 Curves of scattered intensity (I) versus wavevector (q) for aged PDLLA-58k were obtained by azimuthal integration in four ranges: (i) -5 to 5° , and (ii) 85 to 95° .

Based on the information obtained through the SAXS patterns, stress vs. displacement curve, and visual observations, we propose the following mechanism for aged PLA:

- 1) An optically anisotropic, possibly elastic, deformation mechanism becomes activated in the linear viscoelastic regime prior to the general yield point. The pre-yield streaks observed in the SAXS patterns are attributed to this unknown deformation mechanism and their origin will be discussed later.
- 2) At the general yield point, the typical craze scattering pattern was observed and the overall scattered intensity increased likely due to the rapid initiation of many crazes. The decrease in observed stress at the yield point may be due to intrinsic strain softening of PLA since no obvious geometric contraction was observed by the cameras. Additionally, the craze features have become large enough to scatter visible

light resulting in stress-whitening of a small portion of the gage, seen with both camera 3 and camera 4.

- 3) With additional tensile deformation, the overall scattered intensity of the integrated SAXS curve increases with no change of shape signifying an increase in craze density, likely through craze growth in both length and thickness as well as increase in the number of crazes. The apparent stress remains approximately constant as the micro-necking process of craze fibril formation occurs. Eventually, the craze density saturates and additional tensile strain results in microscopic extension (not craze thickening) and strain hardening of the previously formed craze fibrils instead of the formation of new crazed material. Extension of existing fibrils may decrease the fibril width which may explain the slight increase in the fibril-fibril spacing given by the interference peak just before failure. Also, the slight increase in apparent stress before failure may result from the strain hardening of the craze fibrils. The stress in the craze fibrils then reaches the critical value for chain scission resulting in crack initiation, propagation and brittle failure.

4.3.2.2 Results for unaged PDLLA-58k

Representative in-situ tensile data for PDLLA-58K in the unaged condition is shown in Figure 4-15. Although the aging of the sample (~ 66 h at -10°C and < 2 h at 25 °C) was different than the conditions used for the quantitative tensile experiments (~2 h at 24 °C), similar ductile tensile behavior was observed (Figure 4-15i). As shown by camera 3 (Figure 4-15ii) and consistent with the visual observations from the quantitative tensile tests, the sample whitened a small amount at the yield point (point d) and then

immediately formed a neck (point e) which propagated until failure occurred in the cold drawn gage. At point f and continuing through point h, the neck appears inclined at $\sim 76^\circ$ relative to the tensile axis. Additional cold drawing (point j) results in the neck becoming perpendicular to the tensile axis. As before, the stress-induced optical anisotropy is revealed by camera 4 prior to the yield point and progresses in a similar manner as in aged PDLLA-58k. The dissipation of some of the optically anisotropic area after the load is removed (failure) is also seen for unaged PDLLA-58k through camera 4 just before and just after failure.

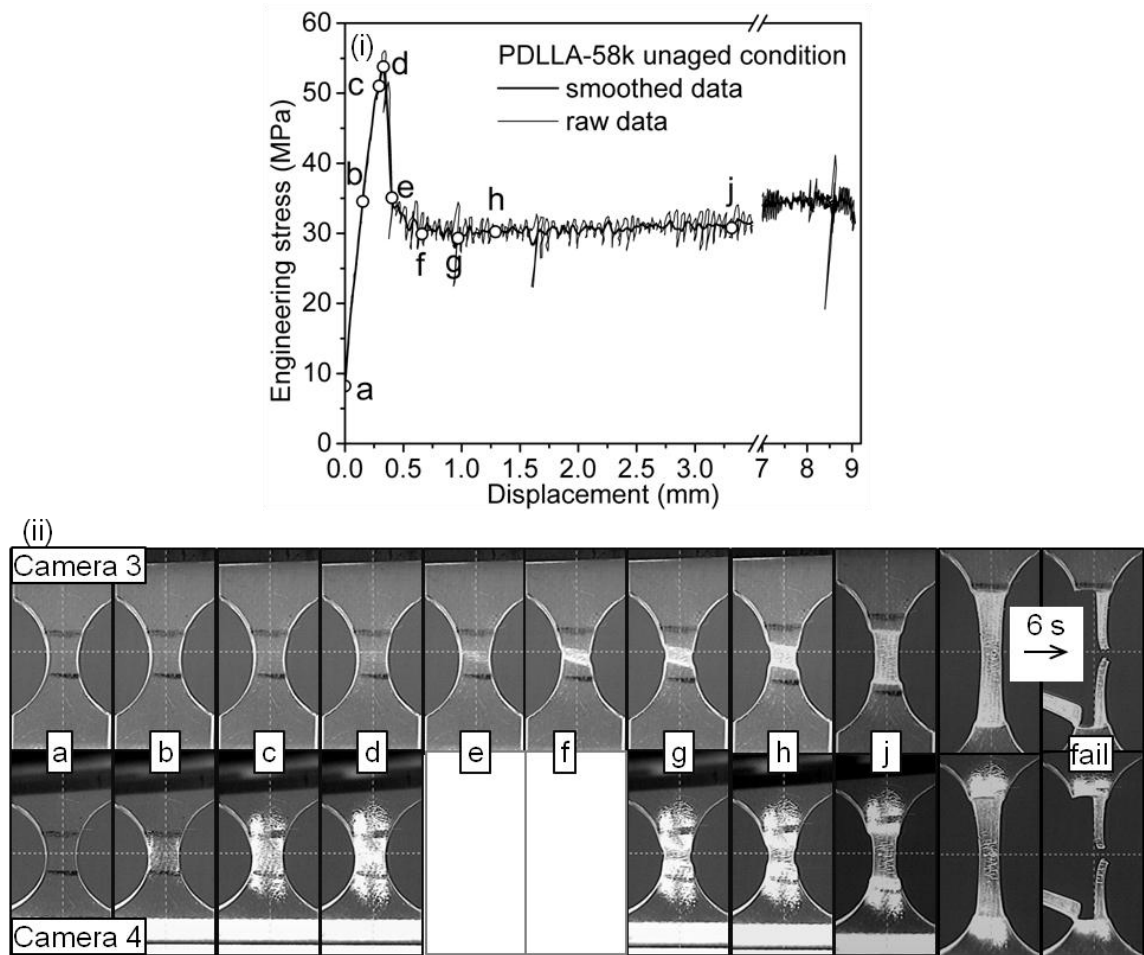


Figure 4-15 In-situ tensile data for PDLLA-58k in the aged condition (~ 25 °C for 66 h). Specific displacements are highlighted by the alphabetical points on the (i) engineering stress vs. displacement curve. The (ii) photographs from camera 3 and camera 4 correspond with the labeled points on the stress-displacement curve.

Relative to aged PDLLA-58k, the 2D SAXS patterns (Figure 4-16) for unaged PDLLA-58k are similar up until neck initiation (point e). The pre-yield streaks (seen at point b) are observed during the linear portion of the tensile curve. At the yield point (point d), the characteristic craze scattering pattern is seen. Thus, despite the lack of a crazing plateau in the stress-displacement curve, the SAXS data confirms that the crazing mechanism is also operative in unaged PDLLA-58k. The result highlights that the tensile

stress-strain data alone cannot be used to determine deformation mechanism. However, when the neck is initiated (point e), the characteristic craze pattern becomes slightly rotated. No additional features are observed in the 2D SAXS pattern. With further deformation (point f), the craze scattering becomes rotated slightly in the opposite direction while maintaining the same angle ($\sim 90^\circ$) between the equatorial and meridional streaks. Starting at point f, the meridional streak appears to be approaching the beamstop with increasing tensile strain, consistent with increasing spacing between the craze faces.

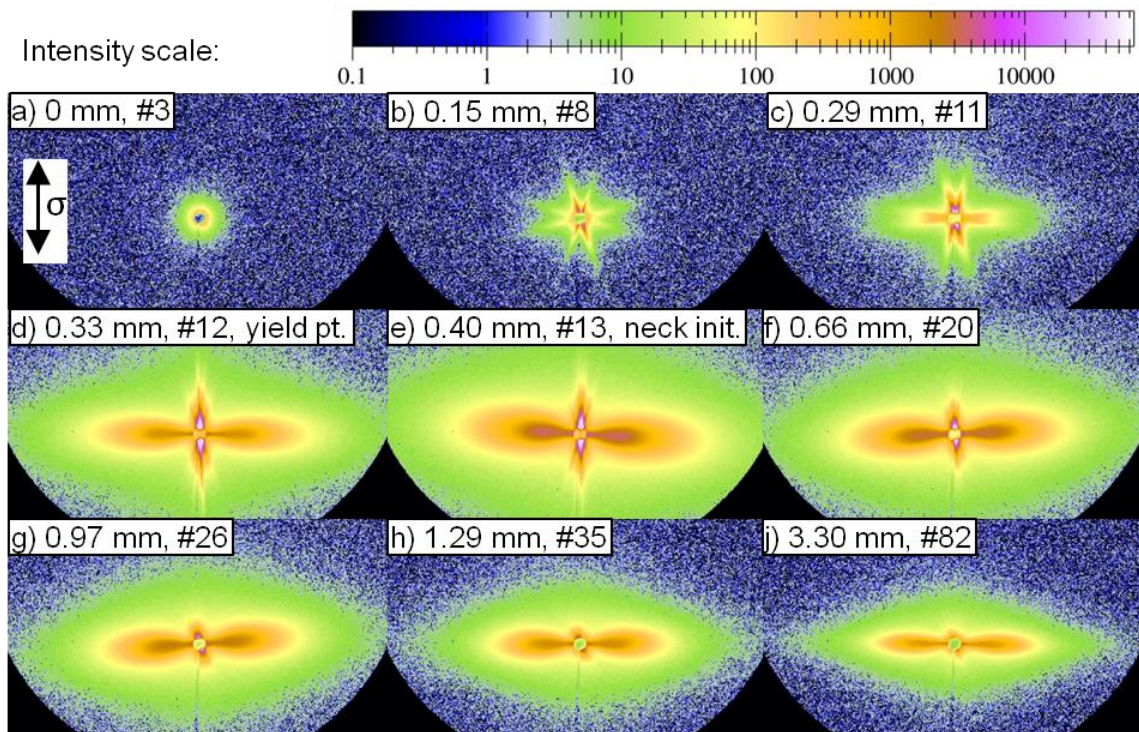


Figure 4-16 In-situ SAXS data for PDLLA-58k in the unaged condition as it is deformed in tension. The tensile axis is vertical and denoted by the arrows. The 2D SAXS patterns correspond with the alphabetically labeled points on the engineering stress displacement curve shown in Figure 4-15. The 2D SAXS patterns are labeled with the displacement and file number. The scattered intensity scale of each SAXS image is the same for all the displacements shown

The 2D SAXS patterns for unaged PDLA-58k were azimuthally integrated and shown for the equatorial (Figure 4-17) and meridional (Figure 4-18) ranges before and after neck initiation. In the equatorial range (Figure 4-17), the curves of integrated intensity as a function of wavevector (q), appear similar to that for aged PDLA-58k before the yield point (Figure 4-14). However, at the yield point (Figure 4-17i, point d), a distinct interparticle interference peak is not discernible. At neck initiation (Figure 4-17i, point e), a peak centered at 0.28 nm^{-1} develops, but it is less defined than in the curves for the aged PDLA-58k. The overall intensity of the scattering curve at point e is slightly lower than that of the aged sample at its yield point possibly indicating that the craze density in the unaged sample is slightly lower than in the aged sample.

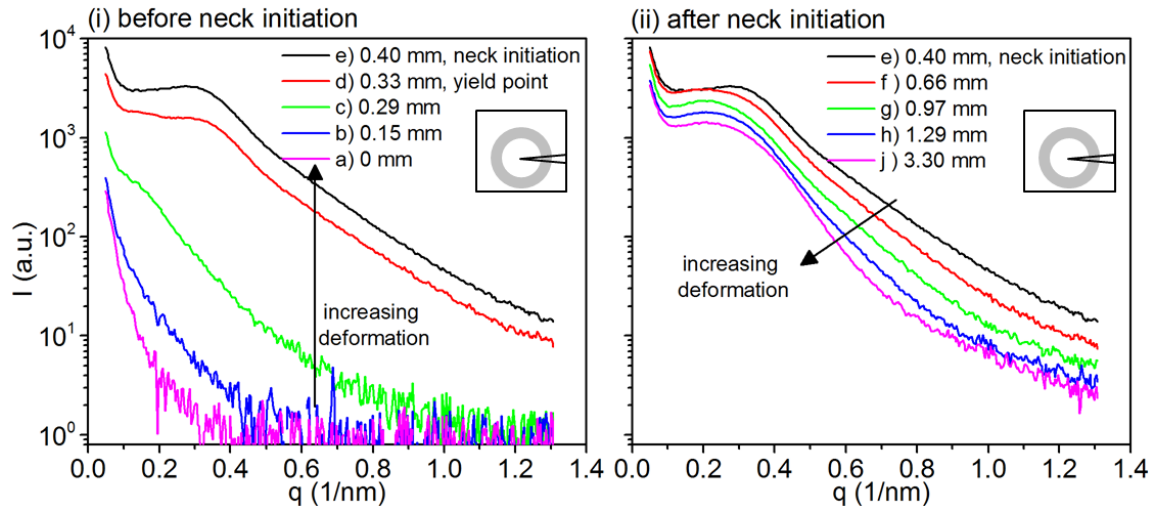


Figure 4-17 The 1D SAXS curves of scattered intensity (I) versus wavevector (q) for unaged PDLA-58k were obtained by azimuthal integration in the equatorial range (-5 to 5°) of the 2D-scattering patterns (i) before and (ii) after neck initiation at each highlighted displacement.

After neck initiation (Figure 4-17ii), starting at point f during the cold-drawing of the gage, the shape of the curve changes and the interference peak becomes broader.

However, a peak maximum can be found at 0.19 nm^{-1} . Additionally, the overall scattering

curve decreases in intensity, and shifts towards lower q -values which is indicative of increasing feature sizes. The decrease in intensity is consistent with a thinning of the sample as a result of cold-drawing. With further deformation, the overall intensity continues to decrease and the scattering continues to shift to lower q -values. The peak maximum remains centered around 0.19 nm^{-1} . The scattering curves in the remaining azimuthal ranges are similar to that for the aged sample before neck initiation. After neck initiation, the same trends of decreasing overall intensity and decreasing q -values were maintained. The curves obtained for the meridional direction (Figure 4-18) are similar to those of aged PDLA-58k. Before neck initiation, the general shift of the curves to greater overall intensity is consistent with the development of crazes. After neck initiation, the same trends observed in the equatorial direction are seen for the meridional direction.

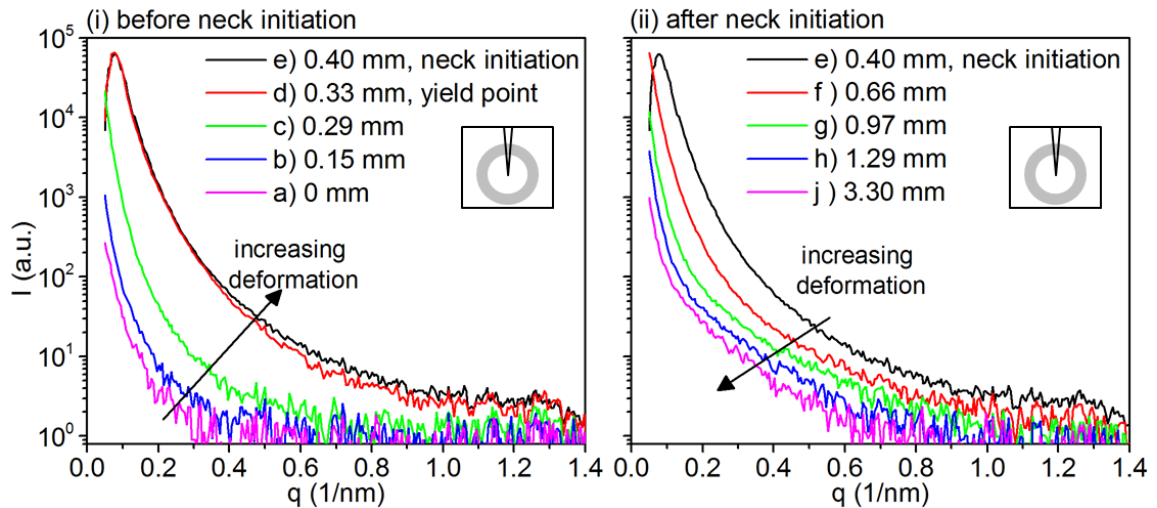


Figure 4-18 The 1D SAXS curves of scattered intensity (I) versus wavevector (q) for unaged PDLA-58k were obtained by azimuthal integration in the meridional (85° – 95°) range of the 2D-scattering patterns (i) before and (ii) after neck initiation at each highlighted displacement.

The data presented above suggest the following deformation mechanism for unaged PLA:

- 1) As seen in aged PLA, an optically anisotropic deformation mechanism becomes activated in the linear viscoelastic regime. The pre-yield streaks are also observed in the 2D SAXS pattern prior to the yield point for the unaged sample and will be discussed later.
- 2) At the yield point, crazes were initiated evidenced by the characteristic craze scattering pattern. Relative to aged PDLA, only a small amount of stress-whitening in the unaged sample was visually observed.
- 3) Neck initiation occurred immediately after the yield point. The 2D SAXS pattern reflected a more developed craze pattern of slightly higher overall intensity. The photograph of the sample from camera 3 revealed a shear band inclined at $\sim 76^\circ$ relative to the tensile axis. However, no new scattering features attributable to the shear yielding mechanism are observed by SAXS.
- 4) Cold-drawing of the lightly crazed gage can be identified in SAXS data by the increasing domain spacing between the craze faces (meridional streak approaches beam stop) as well as a change to the shape of the integrated intensity in the equatorial direction. Additionally, the overall intensity begins to decrease due to sample thinning. The slight rotation of the characteristic craze pattern is indicative of the shear deformation affecting the crazes.
- 5) As the neck is propagated through the sample, the general shape of the characteristic craze pattern is maintained. However, the meridional streak continues to approach the beamstop, the thickness of the equatorial streak decreases and the overall intensity

decreases with increasing tensile elongation. Thus, although the interface between the cold-drawn and undeformed sample is far from the x-ray beam, the crazes initially observed at the center of the sample are still being deformed. The craze faces separate further, the craze fibril alignment is almost perfectly parallel with the tensile direction (denoted by the narrow azimuthal width of the equatorial streak) and the sample continues to thin until failure occurs.

4.3.3 Analysis of pre-yield streaks

Now let us return to the unknown deformation mechanism(s) observed in both aged and unaged PLA prior to the yield point. Recall that an optically anisotropic phenomenon was qualitatively seen by comparison of the photographs from camera 3 and camera 4, while images of azimuthally narrow streaks that we termed “pre-yield streaks” were collected in the SAXS data. In order to quantify the azimuthal shift of the pre-yield streaks, the 2D SAXS images were radially integrated from 0–0.90 nm⁻¹ through an azimuthal range of 355°. The resulting curves of scattered intensity vs. azimuthal angle are shown in Figure 4-19 for both the aged and unaged PDLA-58k up to the yield point. Each curve is identified by scan number and displacement. The pre-yield streaks seen in the 2D images appear as peaks in Figure 4-19. Since the streaks are symmetric about the beamstop, only the evolution of the peaks located near 0° and 90° need to be monitored. For both the aged and unaged case (Figure 4-19, i and ii) a small meridional peak can be observed starting at scan 6. A second meridional peak appears in the following scan, scan 7. The two peaks are labeled as mer1 and mer2. Vertical lines were placed at the peak position of each meridional streak at scan 7 to serve as a visual guide. At scan 8, two

lower intensity equatorial peaks (eq1 and eq2) become well defined. In both the aged and unaged case, with additional deformation, the overall scattered intensity increases indicating that more scatterers are being initiated. Simultaneously, the peak positions for the equatorial and meridional streaks approach 0° and 90° , respectively signifying that the dominant orientation of the scatterers approaches either the equator or the meridian.

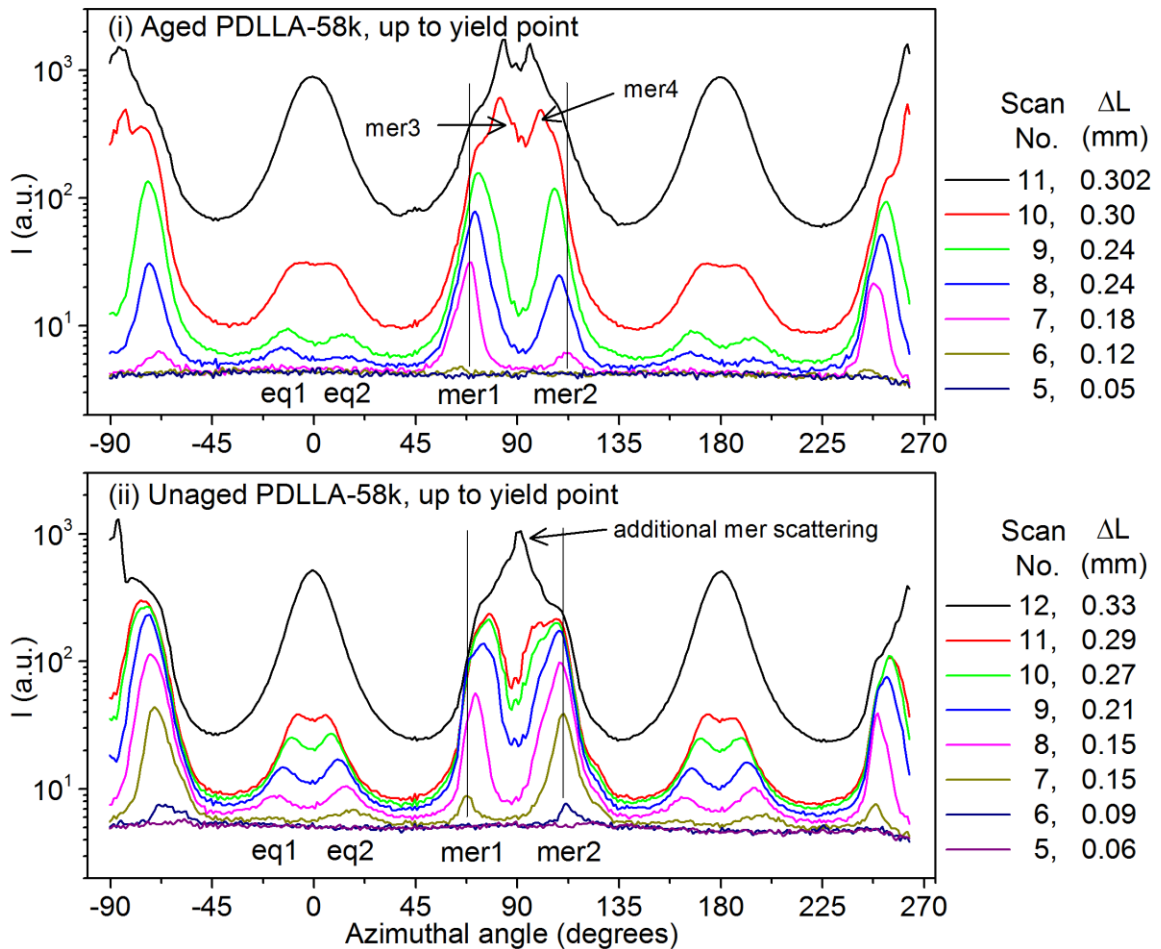


Figure 4-19 Radial integration of the 2D SAXS images of (i) aged PDLLA-58k, (ii) unaged PDLLA-58k up to the yield point from 0 to 0.90 nm^{-1} resulted in plots of intensity vs. azimuthal angle for each highlighted displacement. No vertical translations were applied to the intensity values. The vertical lines serve as a visual guide of mer1 and mer2 peak position.

Up to just before the yield point, eq1 and mer1 are separated by $84^{\circ} \pm 1^{\circ}$ on average, while the second pair is separated by 94° for the aged sample. Similar values were found for the unaged case. Thus, we believe that the 2D SAXS pattern consists of two sets of approximately orthogonal scattering streaks which are mirror images. The streaks are illustrated schematically in Figure 4-20c using the average angle between the equatorial or meridional streak and the tensile axis from scan 8 ($74^{\circ} \pm 2^{\circ}$, $20^{\circ} \pm 1^{\circ}$, respectively). The cross-like, pre-yield streaks resemble scattering from a craze in that the meridional component is of higher intensity than the equatorial streak, and the two streaks remain approximately orthogonal. Assuming the scatterers are crazes, the peak positions imply that the crazes are tilted with respect to the tensile axis, while the azimuthally narrow nature of the streaks indicates a small distribution of orientations of either the fibrils in the case of the equatorial streak, or of the craze faces in the case of the meridional streak (illustrated schematically in Figure 4-20d).

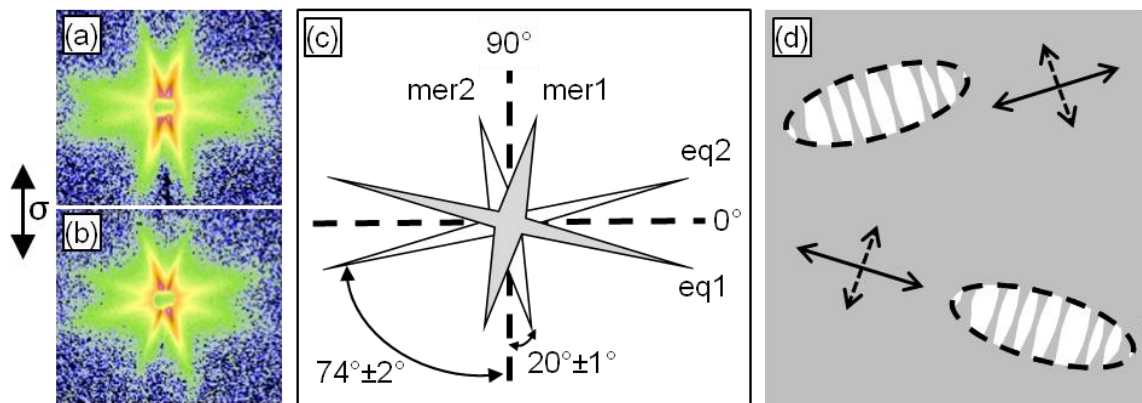


Figure 4-20 The streaks in the 2D SAXS patterns for (a) aged PDLA-58k and (b) unaged PDLA-58k at scan 8 are composed of (c) two cross-like streaks shown schematically. (d) The streaks are consistent with x-ray scattering from tilted crazes with narrow domain size distributions. The tensile direction is vertical.

Tilted crazes have been previously documented in literature through optical photographs, SEM and TEM and attributed to the influence of chain orientation on the principal strain direction which dictates the craze growth direction^{23,53}. Chau and co-workers observed shear-crazes by SEM in polystyrene film after a tensile stress was applied to pre-existing shear bands (Figure 4-20 a). Donald and Kramer strained films of a 90:10 v/v blend of PS and poly(xylene ether).⁵³ Using TEM, they found tilted crazes within the shear bands. A schematic based upon their micrographs is shown in Figure 4-21 b. The craze faces in the shear band were oriented at $\sim 75^\circ$ to the tensile axis, while the craze fibrils remained orthogonal to the craze faces. Termed “shear crazes” in the literature, Stoclet and co-workers⁶⁴ concluded the same result from streaks in 2D SAXS data that were similar to our pre-yield streaks for the uniaxial drawing of poly(L-lactide) at 50°C. However, to our knowledge, there are no other reports of shear crazes observed by SAXS.

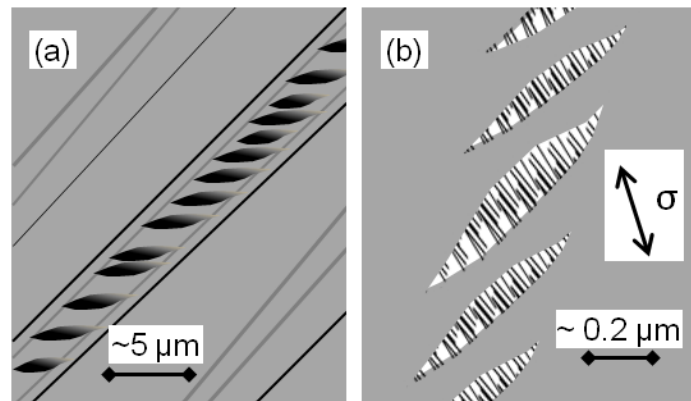


Figure 4-21 (a) A drawing based off of an SEM micrograph of tilted crazes in a shear band formed in polystyrene [PS]. The shear crazes were produced by applying tension to a pre-existing shear band visible on the surface of the polymer as straight lines.⁶⁵ (b) A drawing based off of a TEM micrograph of tilted crazes in a shear band. The micrograph was of a strained film of a 90:10 v/v blend of PS and poly(xylene ether). The arrow indicates the approximate tensile axis as determined from the text of the paper.⁵³

Returning to the azimuthal scan of the pre-yield streaks (Figure 4-19), just before the yield point (scan 10 for aged PDLLA, scan 11 for unaged PDLLA), eq1 and 2 appear to merge almost forming one broad peak, while the shape of the meridional peaks changes more significantly. In the aged case, there are two intense maxima at 82.5° and 100.5° , and two less intense, shoulders at $\sim 73.5^\circ$ and 104.5° close to the previous positions of mer1 and mer2 at scan 9. As the aged sample is deformed to the yield point (scan 11), the same general shape of the meridional peaks is preserved and actually enhanced supporting the idea that two additional meridional peaks (streaks in 2D SAXS pattern) appeared just before yield (labeled mer 3 and 4 in Figure 4-19i). In the unaged case, the presence of additional meridional scattering can also be seen at the yield point (scan 12). Due to the overlap of the equatorial streaks at the yield point, we are unable to determine if there is additional equatorial scattering associated with the newly formed meridional peaks. The final detail to note is the large jump in overall scattered intensity at the yield point apparent in Figure 4-20 for both the aged and unaged cases. The intensity increase may be due to a large change in electron density between the scatterers and the matrix, such as between polymer and voids; or due to a rapid proliferation of the number of scatterers in the illuminated sample volume. Considering that the characteristic craze scattering pattern appeared at the yield point, the additional meridional streaks likely result from the typically observed crazes which grow perpendicular to the tensile direction. The sizeable intensity increase at the yield point also suggests that a relatively large number of the typical crazes are initiated.

Ultimately, we believe the optically anisotropic deformation phenomenon likely occurred simultaneously or before the pre-yield scattering was observed by SAXS and results from both the elastic response of the polymer chains and from the formation of discrete shear bands, also known as micro-shear bands.¹³ The strain inside the bands is known to be much higher than in the undeformed polymer. Thus, an elevated stress state also resides within the band. Craze initiation within the shear band may occur at stresses below the general yield point because of the increased true stress and the effect of chain orientation on craze stress. The 2D SAXS data is consistent with scattering from a few “shear crazes” or crazes initiated within shear bands. Instead of growing perpendicular to the tensile axis, shear crazes grow in a direction which is oblique to both the tensile axis and the shear band orientation which may result from the alignment of the chains in the shear bands. From the 2D SAXS data, as the tensile strain is increased, the dominant orientation of the tilted crazes shifts towards that of the typical craze (craze growth normal to the tensile axis). Unfortunately, direct characterization of the shear bands is not possible using SAXS and other experimental techniques are necessary to confirm and elucidate the mechanism of the tilted craze rotation.

Although the overall tensile behavior of unaged PDLA-58k is very different from aged PDLA-58k, the collected in-situ SAXS data reveals that the operative deformation mechanisms prior to the yield point are generally the same for both samples. In both cases, azimuthally narrow streaks were observed during the linear portion of the load-displacement curve. The orientation of the pre-yield streaks approached that of the typical craze pattern until the characteristic craze pattern was observed at the respective

yield points. Based on the integrated scattering curves of intensity vs. q , the overall scattering intensity for both cases were essentially the same at the yield point (Figure 4-22, point d), indicative of similar craze densities. However, the interference peak in the equatorial scattering curve at the yield point was more prominent for the aged sample implying that the aged sample developed more short-range order of the fibrils relative to the unaged case. While the aged sample continued to form additional crazes as evidenced by the increasing overall intensity with little change to the shape of the scattering curve (Figure 4-22), the unaged sample underwent neck initiation which slightly rotated the craze structure relative to the tensile axis and decreased the overall scattering intensity due to thinning of the sample. Cold drawing of the unaged PDLA-58k also caused the craze structures to increase in size along the tensile axis as shown by the shifting of the scattering curves (Figure 4-17ii and Figure 4-18ii) towards smaller q -values signifying generally larger domain spacings. The fibril-fibril spacing remained at about 22 nm for the aged case; while in the unaged case, the spacing began at 22 nm then increased to 33 nm after cold drawing.

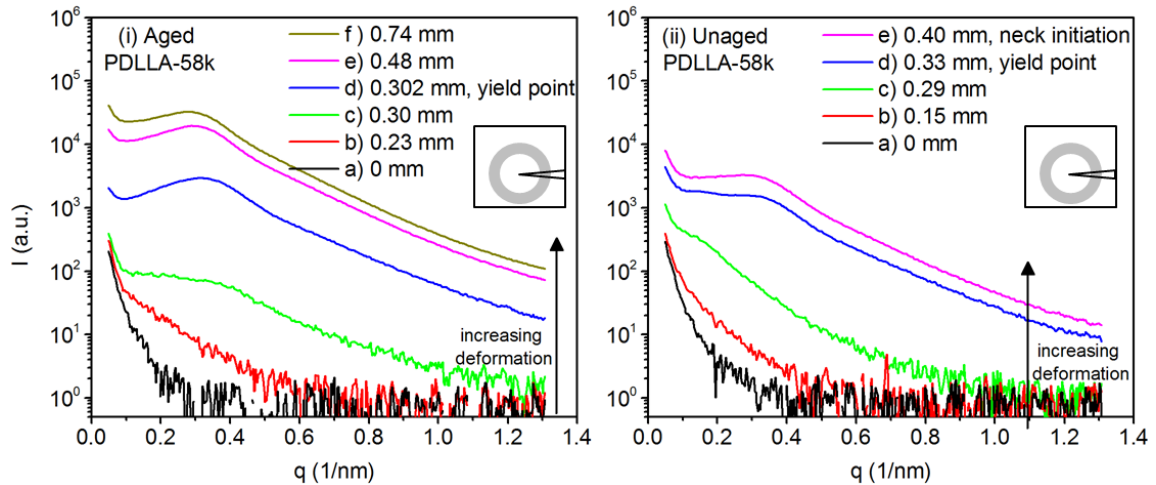


Figure 4-22 The integrated intensity curves in the equatorial direction is shown for (i) aged PDLA-58k in comparison to the curves for (ii) unaged PDLA-58k up to neck initiation, as a function of displacement.

Our observations are somewhat consistent with those of Stoclet et al. who studied the tensile deformation behavior of poly(L-lactide) blown films ($M_n = 116$ kg/mol by SEC, nominal thickness of $200\mu\text{m}$) at 25°C and 50°C using in-situ synchrotron small-angle x-ray scattering.⁶⁴ At 25°C , they observed brittle behavior and found SAXS evidence for crazing. An intense meridional streak was first seen at about 5% strain and relatively low-intensity equatorial streak was observed starting at about 9% strain. The intensity of the equatorial scattering increased with additional tensile elongation until brittle fracture at $> 16.5\%$ nominal strain. They did not observe any streaks prior to the meridional scattering. The sample tested at 50°C exhibited ductile tensile behavior with neck initiation and propagation. The in-situ SAXS revealed streaks in the 2D SAXS pattern before the yield point, similar to the pre-yield streaks observed in this study. They also observed the shift of the intense meridional streaks towards the tensile axis with increasing deformation. The characteristic craze pattern was observed just after neck

initiation. The researchers proposed that the streaks seen prior to neck initiation were consistent with scattering from “shear crazes” while the SAXS pattern observed after neck initiation was representative of “standard crazes”. Optical microscopy of a sample after failure revealed crazes with discrete shear bands emanating from the tips of the crazes. Based on the collective data, they speculated that shear bands formed early in the deformation and under the effect of the tensile stress, shear crazes were initiated in the shear bands. As the deformation increased, the “shear crazes” and shear bands would become more aligned towards the tensile axis, propagate, grow and then intersect. The intersections would 1) stop the propagation of the shear crazes by stabilizing them and 2) nucleate “standard” crazes. Additionally, since the shear crazes were stabilized, the primary deformation mechanism would switch to standard crazing in the matrix and at the intersections of the “shear band crazes”. Finally, because the characteristic craze pattern was only observed after neck initiation and during cold drawing, they claimed that crazing was active during neck propagation.

The absence of the pre-yield streaks in their 25°C test may result from the particular experimental set-up. In our study, the intensity of the pre-yield streaks was generally an order of magnitude or more lower than the craze fibril scattering seen at the yield point, thus requiring the intensity scale to span almost six orders of magnitude. In their publication, the intensity scale of the presented 2D SAXS images only spans 3 orders of magnitude. It is possible that the streaks exist in their data, but cannot be detected due to the chosen intensity scale. Furthermore, in the ductile case, our data shows that after the formation of a macroscopic neck, crazing does not continue but the

preexisting craze features simply become larger in size. Unfortunately, no information about the transition from crazing to shear yielding was obtained through the SAXS experiments. Researchers have observed the formation of shear bands, inclined at $\sim 35^\circ$ relative to the craze plane, at the tips of crazes through the use of in-situ optical microscopy or in-situ TEM.^{9,66-69} The shear bands are believed to arrest further craze growth by reducing the triaxial stress at the craze tip resulting in crazes that are relatively short.⁶⁶ Thus, a macroscopic shear band could hypothetically develop if the micro shear bands coalesced with one another. In fact, Mills and Walker also observed shear bands growing from craze tips and connecting individual crazes.⁶⁶ Similarly, Liu observed sequentially: craze initiation and growth, micro shear band formation at the craze tips and macroscopic shear band formation in films of poly(phenyl quinoxaline).⁶⁸ Thus, in the case of unaged PDLA, the transition from crazing to shear yielding may be due to the formation of micro shear bands at the craze tips which coalesced into a macroscopic neck. Furthermore, Donald and Kramer discovered that physical aging inhibited the formation of the shear bands in thin films of poly(styrene-acrylonitrile), poly(styrene-*ran*-methyl methacrylate) and a blend of PS and poly(2,6-dimethyl-1,4-phenylene oxide).⁹ As a direct result of physical aging, it is probable that the critical stress for shear was increased such that micro shear bands could not form at the craze tips in aged PDLA. Additional experiments, such as in-situ optical/tensile measurements on would be required to determine if micro shear bands are initiated at the craze tips in unaged PDLA and not initiated in aged PDLA.

4.4 Summary

The physical aging embrittlement of well-entangled PDLLA was found to be very rapid, occurring within 2 days of aging at 25°C. Slight increases to the Young's modulus and yield strength due to physical aging were observed. However, no trend with respect to the post-yield stress drop could be discerned. Simultaneous SAXS and tensile testing revealed that both aged and unaged PDLLA-58k experience some inelastic deformation, possibly shear crazing, prior to the general yield point. The phenomenon was optically anisotropic and possessed a characteristic SAXS patterns consisting of two pairs of approximately orthogonal streaks. Based on the available data, we speculate that the phenomenon may be the initiation of micro shear bands and shear band crazes, followed by the rotation of the shear band crazes towards the standard craze alignment with respect to the applied stress. At the yield point, both aged and unaged PDLLA-58k initiated new crazes with the standard alignment (fibrils parallel to the applied stress). However, while aged PDLLA-58k continued to craze additional undeformed material (increase in craze density), unaged PDLLA-58k initiated a macroscopic neck that was propagated by cold-drawing. Likely, neck initiation resulted from coalescence of shear bands that we hypothesized to be formed at the tips of the newly initiated crazes in the unaged sample, but not in the aged sample. Unfortunately, no features in the scattering data could be directly attributed to the hypothesized shear bands. The effect of cold-drawing was primarily to increase the spacing between the pre-existing craze faces. The obtained SAXS data will serve as a basis for comparison to the graft copolymer materials in the following chapter.

4.5 Acknowledgements

Thanks to the DND-CAT staff especially Dr. Steven Weigand and Dr. Mike Guise. Thanks to Dr. Carmelo Declet-Perez for assistance in performing the in-situ SAXS experiments. Portions of this work were performed at the DuPont-Northwestern-Dow Collaborative Access Team (DND-CAT) located at Sector 5 of the Advanced Photon Source (APS). DND-CAT is supported by E.I. DuPont de Nemours & Co., The Dow Chemical Company and Northwestern University. Use of the APS, an Office of Science User Facility operated for the U.S. Department of Energy (DOE) Office of Science by Argonne National Laboratory, was supported by the U.S. DOE under Contract No. DE-AC02-06CH11357.

4.6 References

- ¹ Drumright, R. E.; Gruber, P. R.; Henton, D. E. *Adv Mater* **2000**, *12*, 1841-1846
- ² Grijpma, D.; Penning, J.; Pennings, A. *Colloid Polym. Sci.* **1994**, *272*, 1068-1081
- ³ Perego, G.; Cella, G. D.; Bastioli, C. *J Appl Polym Sci* **1996**, *59*, 37-43
- ⁴ Anderson, K. S.; Schreck, K. M.; Hillmyer, M. A. *Polymer Reviews* **2008**, *48*, 85-108
- ⁵ Södergård, A.; Stolt, M. *Progress in Polymer Science* **2002**, *27*, 1123-1163
- ⁶ Dorgan, J. R.; Lehermeier, H. J.; Palade, L.; Cicero, J. *Macromol. Symp.* **2001**, *175*, 55-66
- ⁷ O'Connell, P. A.; McKenna, G. B. In *Yield and Crazing in Polymers*; Encyclopedia of Polymer Science and Technology; John Wiley & Sons, Inc.: 2002;
- ⁸ Aanand L.; Spitzig, W. *Acta Metallurgica* **1982**, *30*, 553-561
- ⁹ Donald, A. M.; Kramer, E. J. *J. Mater. Sci.* **1982**, *17*, 1871-1879

-
- ¹⁰ Bowden, P. B.; Raha, S. *Philosophical Magazine* **1970**, *22*, 463-482
- ¹¹ Haward, R. N.; Young, R. J., Eds.; In *The Physics of Glassy Polymers*; Chapman & Hall: London, 1997; pp 176-180.
- ¹² Haward, R. N.; Young, R. J., Eds.; In *The Physics of Glassy Polymers*; Chapman & Hall: London, 1997;
- ¹³ Lu, J.; Ravi-Chandar, K. *Int. J. Solids Structures* **1999**, *36*, 391-425
- ¹⁴ Argon, A. S.; Andrews, R. D.; Godrick, J. A.; Whitney, W. *J. Appl. Phys.* **1968**, *39*, 1899-1906
- ¹⁵ Meijer, H. E. H.; Govaert, L. E. *Macromolecular Chemistry and Physics* **2003**, *204*, 274-288.
- ¹⁶ Stokes, V. k.; Bushko, W. C *Polym. Eng. Sci.* **1995**, *35*,291.
- ¹⁷ Renouf-Glauser, A. C.; Rose, J.; Farrar, D. F.; Cameron, R. E. *Biomaterials* **2005**, *26*, 5771-5782.
- ¹⁸ Kulinski, Z.; Piorkowska, E. *Polymer* **2005**, *46*, 10290-10300
- ¹⁹ Pan, P.; Zhu, B.; Inoue, Y. *Macromolecules* **2007**, *40*, 9664-9671
- ²⁰ Kramer, E.; Berger, L. In *Fundamental processes of craze growth and fracture*; Kausch, H. -, Ed.; Springer Berlin Heidelberg: 1990; Vol. 91/92, pp 1-68
- ²¹ Michler, G. In *Crazing in amorphous polymers—formation of fibrillated crazes near the glass transition temperature*; Deformation and Fracture Behaviour of Polymers; Springer: 2001; pp 193-208.
- ²² Deblieck, R. A. C.; van Beek, D. J. M.; Remerie, K.; Ward, I. M. *Polymer* **2011**, *52*, 2979-2990
- ²³ Beardmore, P.; Rabinowitz, S. *J. Mater. Sci.* **1975**, *10*, 1763-1770
- ²⁴ Lee, J. Y.; Crosby, A. J. *Macromolecules* **2005**, *38*, 9711-9717.
- ²⁵ Ishikawa, M.; Takahashi, H. *J. Mater. Sci.* **1991**, *26*, 1295-1300
- ²⁶ Kambour, R. P. *Journal of Polymer Science: Macromolecular Reviews* **1973**, *7*, 1-154

-
- ²⁷ Collyer, A. A., Ed.; In *Rubber Toughened Engineering Plastics*; Chapman and Hall: London, UK, 1994; , pp 366
- ²⁸ McCrum, N. G.; Buckley, C. P.; Bucknall, C. B. In *Principles of Polymer Engineering*; Oxford University Press: New York, 1997;
- ²⁹ Argon, A. S. *Polymer* **2011**, *52*, 2319-2327
- ³⁰ Bucknall, C. B. *Polymer* **2007**, *48*, 1030-1041
- ³¹ Henkee, C. S.; Kramer, E. J. *J. Mater. Sci.* **1986**, *21*, 1398-1404
- ³² Brown, H.; Kramer, E. *Journal of Macromolecular Science-Physics* **1981**, *B19*, 487-522
- ³³ Salomons, G. J.; Singh, M. A.; Bardouille, T.; Foran, W. A.; Capel, M. S. *Journal of Applied Crystallography* **1999**, *32*, 71– 81.
- ³⁴ Leferink Op Reinink, A. B. G. M.; Belli, S.; van Roij, R.; Dijkstra, M.; Petukhov, A. V.; Vroege, G. J. *Soft Matter* **2014**, *10*, 446-456
- ³⁵ Berger, L.; Buckley, D.; Kramer, E.; Brown, H.; Bubeck, R. *Journal of Polymer Science Part B-Polymer Physics* **1987**, *25*, 1679-1697
- ³⁶ Kulinski, Z.; Piorkowska, E. *Polymer* **2005**, *46*, 10290-10300
- ³⁷ van Melick, H. G. H.; Govaert, L. E.; Meijer, H. E. H. *Polymer* **2003**, *44*, 3579-3591
- ³⁸ Henkee, C. S.; Kramer, E. J. *Journal of Polymer Science Part B-Polymer Physics* **1984**, *22*, 721-737
- ³⁹ Dorgan, J. R.; Janzen, J.; Knauss, D. M.; Hait, S. B.; Limoges, B. R.; Hutchinson, M. H. *Journal of Polymer Science Part B: Polymer Physics* **2005**, *43*, 3100-3111
- ⁴⁰ Hodge, I. J. *Non Cryst. Solids* **1994**, *169*, 211-266
- ⁴¹ Ren, J.; Urakawa, O.; Adachi, K. *Macromolecules* **2003**, *36*, 210-219
- ⁴² Ruokolainen, J.; Fredrickson, G. H.; Kramer, E. J.; Ryu, C. Y.; Hahn, S. F.; Magonov, S. N. *Macromolecules* **2002**, *35*, 9391-9402
- ⁴³ Meijer, H.; Govaert, L. *Prog. Polym. Sci.* **2005**, *30*, 915-938.

-
- ⁴⁴ Hill, A.; Heater, K.; Agrawal, C. *Journal of Polymer Science Part B-Polymer Physics* **1990**, *28*, 387-405
- ⁴⁵ Bubeck, R.; Bales, S.; Lee, H. *Polym. Eng. Sci.* **1984**, *24*, 1142-1148
- ⁴⁶ Senden, D. J. A.; van Dommelen, J. A. W.; Govaert, L. E. *Journal of Polymer Science Part B-Polymer Physics* **2012**, *50*
- ⁴⁷ Brady, J. *Polymer* **1992**, *33*, 2981-2988
- ⁴⁸ Biddlestone, F.; Harris, A.; Hay, J.; Hammond, T. *Polym. Int.* **1996**, *39*, 221-229
- ⁴⁹ Tan, Z. Y.; Sun, S. L.; Xu, X. F.; Zhou, C.; Ao, Y. H.; Zhang, H. X. *Journal of Polymer Science Part B-Polymer Physics* **2005**, *43*, 2715-2724
- ⁵⁰ Cheng, T.; Keskkula, H.; Paul, D. *J Appl Polym Sci* **1992**, *45*, 531-551
- ⁵¹ Holm, V. K.; Ndoni, S.; Risbo, J. *J. Food Sci.* **2006**, *71*, E40-E44.
- ⁵² Wu, L.; Zhang, J.; Jing, D.; Ding, J. *Journal of Biomedical Materials Research Part A* **2006**, *76A*, 264-271.
- ⁵³ Donald, A. M.; Kramer, E. J.; Kambour, R. P. *J. Mater. Sci.* **1982**, *17*, 1739-1744
- ⁵⁴ Chau, C. C.; Li, J. C. M. *J. Mater. Sci.* **1979**, *14*, 2172-2182
- ⁵⁵ Kowalczyk, M.; Piorowska, E. *J Appl Polym Sci* **2012**, *124*, 4579-4589
- ⁵⁶ Osaki, K.; Inoue, T.; Hwang, E. J.; Okamoto, H.; Takiguchi, O. *J. Non Cryst. Solids* **1994**, *172*, 838-849
- ⁵⁷ Osaki, K.; Okamoto, H.; Inoue, T.; Hwang, E. J. *Macromolecules* **1995**, *28*, 3625-3630
- ⁵⁸ Mulligan, J.; Cakmak, M. *Macromolecules* **2005**, *38*, 2333-2344
- ⁵⁹ Argon, A. S.; Andrews, R. D.; Godrick, J. A.; Whitney, W. *J. Appl. Phys.* **1968**, *39*, 1899-1906
- ⁶⁰ Bucknall, C. B.; Smith, R. R. *Polymer* **1965**, *6*, 437-446.
- ⁶¹ Leferink Op Reinink, A. B. G. M.; Belli, S.; van Roij, R.; Dijkstra, M.; Petukhov, A. V.; Vroege, G. J. *Soft Matter* **2014**, *10*, 446-456

-
- ⁶² Yang, A.; Kramer, E. *Journal of Polymer Science Part B-Polymer Physics* **1985**, *23*, 1353-1367
- ⁶³ Hristov, H.; Yee, A.; Xie, L.; Gidley, D. *Polymer* **1994**, *35*, 4287-4292
- ⁶⁴ Stoclet, G.; Lefebvre, J. M.; Seguela, R.; Vanmansart, C. *Polymer* **2014**, *55*, 1817-1828
- ⁶⁵ Chau, C.; Li, J. *J. Mater. Sci.* **1981**, *16*, 1858-1873
- ⁶⁶ Mills, N. J.; Walker, N. *J. Mater. Sci.* **1980**, *15*, 1832-1840
- ⁶⁷ Dalal, V.; Moet, A. *Polym. Eng. Sci.* **1988**, *28*, 544-549
- ⁶⁸ Liu, W.; Shen, J.; Wang, Z.; Lu, F.; Xu, M. *Polymer* **2001**, *42*, 7461-7464
- ⁶⁹ Brûlé, B.; Kausch, H. H.; Monnerie, L.; Plummer, C. J. G.; Halary, J. L. *Polymer* **2003**, *44*, 1181-1192

Chapter 5: Tensile deformation and physical aging of poly(1,5-cyclooctadiene-co-5-norbornene-2- methanol-graft-DL -lactide)s

5.1 Background

As discussed in Chapter one, rubber toughening is a well-studied approach for increasing the mechanical robustness of glassy polymers.¹ Methods for creating a rubber-toughened polymer include melt blending rubbery polymers and/or discrete rubbery particles into the glassy matrix as well as block copolymerization with the glassy polymer.² Rubber toughening of polylactide through melt blending and copolymerization have been recently reviewed.^{3,4}

In general, the rubber domain is found to have different roles in the various deformation processes depending on its specific morphology and interfacial strength with the matrix.⁵⁻⁸ For example, Jansen and co-workers found that an 80/20 w/w blend of PMMA and cross-linked epoxy rubber nominally resulted in a material with increased ductility relative to PMMA.⁹ Neat PMMA deforms by crazing in tension before failure but, in the 80/20 PMMA/epoxy blend, the rubber epoxy domains (domain size ~ 20 nm) cavitated before homogeneous PMMA crazes were initiated. The cavitation of the epoxy particles was found to alleviate the local triaxial stresses in the PMMA matrix thereby suppressing craze initiation. In another example, Declet-Perez and co-workers toughened cross-linked epoxies by mixing in small amts. (< 6 wt%) of a linear diblock copolymer of poly(ethylene-oxide) with either poly(ethylene-alt-propylene) [PEO-PEP] or polystyrene [PEO-PS].¹⁰ The diblock copolymers formed spherical micelles with 20 nm diameters having either a PEP core or a PS core and a PEO corona in a matrix of epoxy. Notably,

epoxy samples containing the glassy PS core micelles showed improved critical energy release rate (G_{IC}) relative to unmodified epoxy. However, the samples containing the rubbery PEO core micelles increased the G_{IC} even more relative to the glassy-core modified epoxies. Using in-situ small-angle x-ray scattering and tensile testing, the researchers determined that in the epoxy samples containing PEO-PS, the glassy PS core did not cavitate during tensile deformation.¹¹ However, for the epoxy samples containing PEO-PEP, the rubbery PEP cores increased nearly 6× in volume allowing for much greater rubber toughening efficiency. Similarly, Schwier and co-workers investigated the tensile deformation behavior of sphere and cylinder forming PS-polybutadiene (PB) diblocks and diblock/homopolymer PS blends in the composition range of 3 to 30 vol% PB.^{12,13} Transmission electron microscopy of crazed and subsequently stained polymer films revealed a new form of craze morphology as seen schematically in Figure 5-1a where the network structure resulted from repeated cavitation of the rubber domains and drawing of the surrounding polymer to form the fibrils. Similar craze morphology was observed in sphere forming diblock copolymers and blends of PS/diblock Figure 5-1b); however, the crazes were generally only one domain thick. The researchers monitored the craze growth kinetics (increase in craze length at constant stress) and found the data to fit well to the hetero-phase cavitation model vs. the homogeneous crazing model seen in homopolymers (meniscus instability mechanism) for diblock compositions > 11 vol% PB. For diblock compositions in the range of 6 – 11 vol% PB, craze growth velocities were intermediate between the two mechanisms; thus, it is possible that both were operative.

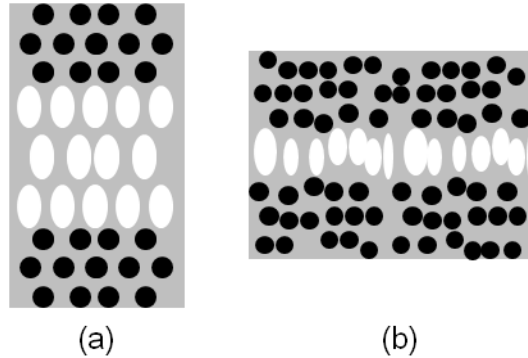


Figure 5-1 (a) A cartoon drawing based off a transmission electron micrograph of crazing in polystyrene-*block*-polybutadiene [PB] having 23 wt.% PB and exhibiting hexagonally close-packed cylindrical PB morphology.¹⁴ (b) A cartoon schematic based off a transmission electron micrograph of a craze in a sphere forming blend of diblock with PS containing 11 vol.% PB.¹² Both samples were stained with osmium prior to sectioning. The black circles represent uncavitated PB domains. The white ovals represent cavitated and elongated rubber domains.

The influence of physical aging on rubber-modified polymers is an active area of research. However, there are limited studies and a lack of consensus on the effect of copolymerization and chain architecture on the kinetics of physical aging. Over two decades ago, DiCorleto and Cohen studied the effect of physical aging on the toughness of poly(styrene)-*block*-poly(butadiene) copolymers and their blends with polystyrene.¹⁵ They observed physical aging of the materials by dynamic mechanical spectroscopy (DMS) after slow cooling and isothermally annealing the samples. However, relative to the unaged samples, they did not observe significant differences in the resulting craze growth rates and tensile behavior. In contrast, Inoue et al. recently reported that blends of PC and poly(styrene)-*block*-poly(ethylene-co-butylene)-*block*-poly(styrene) copolymers [SEBS], containing more than 5 wt% SEBS, exhibited a resistance to physical aging embrittlement.¹⁶ Although physical aging of the PC matrix in the blends was observed by DSC, the impact strength of the blends did not decrease with increased aging time and

remained near the value of the unaged material. The authors attributed the results to the development of negative pressure in the SEBS domains due to the thermal expansion difference between PC and SEBS. They postulated that the negative pressure caused dilational stress fields in the matrix to form, thereby promoting additional local segmental motion of the matrix during deformation. Furthermore, they speculated that a minimum concentration of SEBS particles was necessary to create a percolating network of stress fields that would allow the dilational stress fields to effectively enhance the local segmental motion.

In this chapter, we will investigate the effect of physical aging on the tensile behavior and deformation mechanisms of polylactide graft copolymers through small-angle x-ray scattering and tensile testing. We will then compare the results with the knowledge gained from our examination of well-entangled polylactide in Chapter 4.

5.2 Experimental

5.2.1 Materials

The materials studied include various PCNL graft copolymers described in detail in Chapters 2 and 3. As before the PCNL graft copolymers will be labeled as PCNL-X-Y-Z, where the X is the N_n of 1,5-cyclooctadiene in the backbone, the Y is the average number of grafts per chain, and the Z is the weight percentage of PDLLA in the graft copolymer.

5.2.2 Compression molding of tensile bars

Samples of PCNL were prepared in the same manner as was homopolymer PDLLA detailed in Chapter 4. The flash from all compression molded samples was

removed using an Exacto knife. Using a light box and circular polarizers (one polarizer, one analyzer), the bars were examined for dust, defects, and crystallinity in the gage section.

5.2.3 Conditioning of compression molded tensile bars

The PCNLs were conditioned and physically aged in the same manner as homopolymer PDLA detailed in Chapter 4. For reference, the aging conditions are listed in Table 5-1 below.

Table 5-1 Physical Aging Conditions

	Aging Temperature (°C)	Relative Humidity (%)	Aging time (h)
Unaged	24 ± 1	51 ± 4	2
Controlled 25 °C	25 ± 1	≤ 2	48, 96
Controlled 40 °C	40 ± 2	≤ 2	24

5.2.4 Quantitative tensile testing

The PCNLs were tested in the same manner as homopolymer PDLA detailed in Chapter 4.

5.2.5 In-situ small-angle x-ray scattering and tensile testing

The PCNLs were physical aged and tested in the same manner as homopolymer PDLA detailed in Chapter 4. In this case, the unaged condition refers to samples aged at ~ -10°C for 66 hours before testing. Aged samples were conditioned at 25°C for ~ 66 hours before testing.

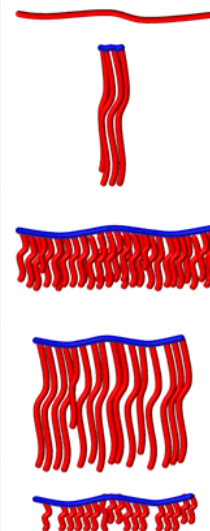
5.3 Results

5.3.1 The effect of physical aging on tensile properties of PCNLs

The tensile properties of a select number of PCNLs were quantitatively measured following physical aging under several conditions. Table 5-2 summarizes the characteristics of the graft copolymers examined in more detail. A cartoon schematic is shown next to each polymer where red represents polylactide and blue represents the PCN backbone.

Table 5-2 Characteristics of the materials in the physical aging study

Sample	wt % PLA	M_n^a (kg/mol)	\bar{D}^b	$M_{n,eff}^c$ (kg/mol)	$T_{g,PLA}^d$ (°C)
PDLLA-75k	100	75	2.4	n/a	56
PCNL-92-4-96	96	211	2.8	2.8	55
Macroinitiator		10.4	2.5		
PLA Grafts ^e		50	2.3		
PCNL-594-90-95	95	1283	5.6	0.7	52
Macroinitiator		74.2	2.8		
PLA Grafts ^e		15	1.9		
PCNL-495-19-95	95	835	5.3	2.8	55
Macroinitiator		55.8	2.8		
PLA Grafts ^e		45	2.2		
PCNL-495-19-81	81	284	4.9	2.8	51
PLA Grafts ^e		12	1.6		



^a Determined by ¹H NMR spectroscopy

^b Determined by size exclusion chromatography in CHCl₃ at 35°C (PS stds.)

^c $M_{n,eff}$ is the M_n of the rubbery backbone divided by the average number of grafts per chain.

^d Determined by the half-height method on the second heating run of an as-molded sample at 10°C/min

^e Determined by ¹H NMR of the metathesis degradation product of PCNL¹⁷

Two of the graft copolymers, PCNL-594-90-95 and PCNL-495-19-80, have PLA grafts that are below the critical entanglement molar mass of PLA (~ 18 kg/mol)¹⁸ while the other two PCNLs have well entangled PLA grafts. This particular set of graft copolymers was chosen to examine the effect of total backbone molar mass (compare PCNL-92-4-96 and PCNL-495-19-95), graft density (compare PCNL-495-19-95 and PCNL-594-90-95), and composition (compare PCNL-495-19-95 and PCNL-495-19-80). The materials studied were physically aged and then extended to failure in tension. The average and standard deviation values of E , σ_y and ϵ_b from the tensile tests are shown in Figure 5-10a and b, and Figure 5-11. The expected increase in modulus with aging is observed for PDLLA-75k. For the rubber-modified materials, it is difficult to discern a significant trend in modulus with aging time. This may be due to a small sampling window with respect to aging time. Inspecting the reported data¹⁹ of Pan et al. for PLLA aged at 25 °C, the increase in E from unaged to four days was only about 0.15 MPa, which is similar to the change seen in some of the rubber-modified materials.

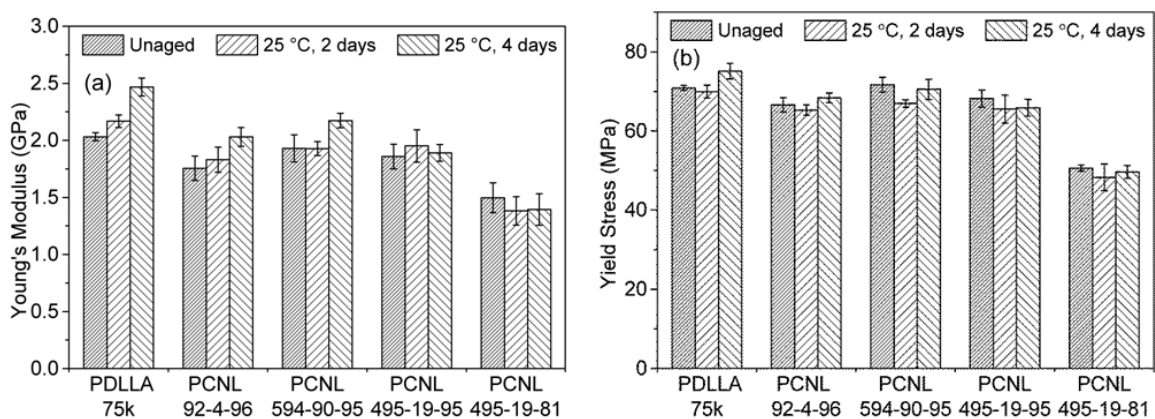


Figure 5-2 Average (a) Young's modulus and (b) yield strength of tensile samples in the unaged and aged conditions. Error bars represent one standard deviation about the mean.

The yield stress values shown in Figure 5-10b follow a similar trend as tensile modulus with respect to rubber composition. Interestingly, although PCNL-594-90-95 has un-entangled PLA grafts, it has σ_y values that are similar to the entangled graft copolymers and the PLA control. A slight increase in yield stress is observed for the PLA control, while trends in the rubber-modified PLA materials could not be conclusively determined. In the work of Pan et al. the yield stress for PLLA increased by only about 4 MPa over 4 days at 25 °C.⁹ Similarly, in the work of Senden and co-workers, the increase in yield stress for polycarbonate aged at $T_g - T_a = 25$ °C was only about 3 MPa over 4 days.²⁰ There was no significant influence of physical aging based on modulus and yield strength over the short aging time period for the graft copolymers utilized in this study.

As discussed in Chapter 4, unaged PDLA-75k exhibits ductile tensile behavior and elongates to an average $252 \pm 35\%$ strain at break, consistent with data reported by Pan et al. However, after aging at 25 °C for 2 days, ϵ_b for PDLA-75k is reduced to a relatively constant value of $13.6 \pm 2.5\%$ which is closer to typically reported ϵ_b values for entangled PLA. Similar behavior was observed for PCNL-92-4-96 and PCNL-594-90-95. The PCNL-495-19-95 sample also appears to embrittle as a result of physical aging, but at a slower rate. After aging for 4 days at 25 °C, the average ϵ_b for PCNL-495-19-95 is still larger than that for PDLA-75k. However, after aging for 1 day at 40 °C, the avg. ϵ_b for PCNL-495-19-95 has reached the same low value as PDLA-75k. A decrease in ϵ_b for PCNL-495-19-81 is not observed until it is aged for 4 days at 25 °C. Further, PCNL-495-19-81 appears to reach a steady-state average ϵ_b of $\sim 230\%$, which is much higher than that of PLA and the other graft copolymers.

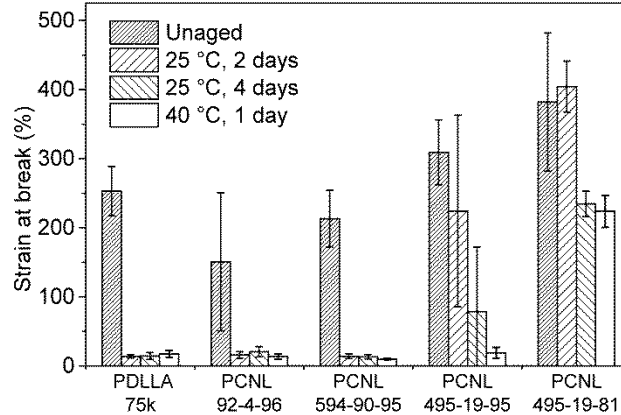


Figure 5-3 Average strain at break for tensile samples in the unaged and physically aged condition. Error bars represent one standard deviation about the mean.

The extreme decrease in ϵ_b with increased physical aging in these samples results from a change in deformation mechanism. Figure 5-4a shows representative stress-strain tensile curves for PDLLA-75k, PCNL-495-19-95, PCNL-495-19-81 in the unaged state (samples were tested within 2 h of compression molding and stored at room temperature during the interim). As established in Chapter 4, unaged PDLLA-75k deforms after the yield point by a small amount of crazing followed by neck initiation causing an artificial decrease in the engineering stress. The neck then stably propagates, at a constant flow stress, along the full length of the gage up to the grips until the sample fractures in a brittle manner in the drawn gage. Unaged PCNL-495-19-95 behaves in a similar manner as unaged PDLLA-75k except that neck initiation occurred at smaller strain in PCNL-495-19-95 relative to PDLLA-75k. In contrast, PCNL-495-19-81 almost immediately initiates a stable neck after the yield point. After neck initiation, the deformation mechanism proceeds in the same manner as with PDLLA-75k.

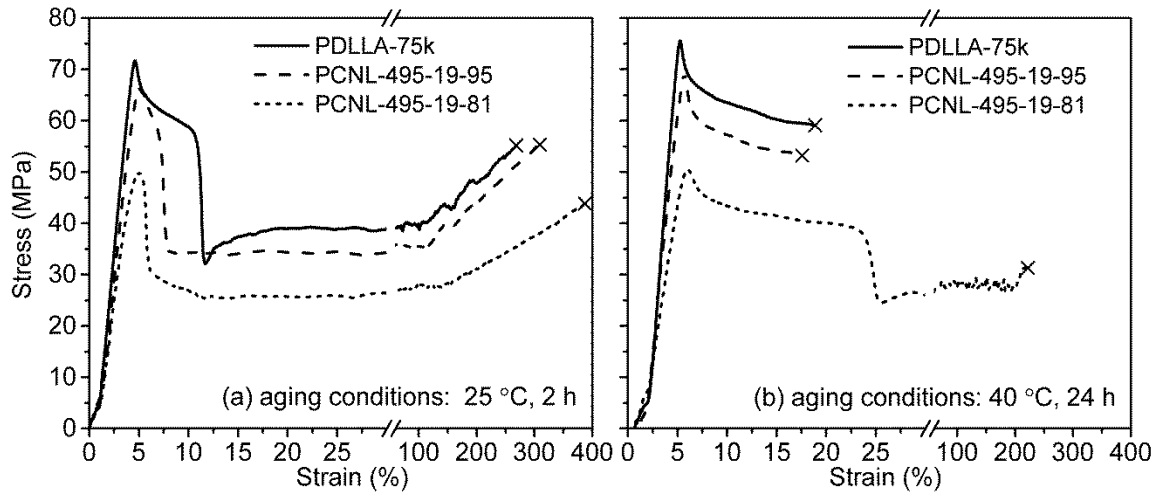


Figure 5-4 Representative engineering stress-strain curves for the control, PDLLA-75k, and some of the PCNLs in the (a) unaged condition soon after compression molding and (b) after aging at 40 °C for 24 h. Both plots are scaled to the same axes. In the relatively unaged state (a), only PDLLA-75k and PCNL-495-19-95 exhibit crazing before neck initiation followed by stable neck propagation. PCNL-495-19-81 initiates a neck almost immediately after the yield point followed by stable neck propagation. After aging at 40 °C for 24 h, PDLLA-75k and PCNL-495-19-95 exhibit crazing and brittle fracture before initiation of a neck, while PCNL-495-19-81 is still able to initiate and propagate a stable neck region. Notably, in the aged state, PCNL-495-19-81 exhibited a significant amount of crazing before neck initiation as manifested by the larger neck initiation strain.

The deformation mechanism clearly changes with physical aging as can be seen in the representative stress-strain curves for the same four materials after aging at 40 °C for 1 day (Figure 5-4b). Both PDLLA-75k and PCNL-495-19-95 fail after crazing and are unable to initiate a stable neck. Furthermore, the stress-strain curve of PCNL-495-19-81 after aging at 40 °C for 1 day (Figure 5-4b) resembles that of PDLLA-75k aged for 2 hours at 24 °C (Figure 5-4a) by exhibiting noticeable crazing after the yield point followed by neck initiation and cold-drawing. The strain at which neck initiation occurs (identified in Figure 4-6a) is plotted for each sample and aging condition in Figure 5-5. A trend of increasing neck initiation strain with increasing physical aging can be observed in

samples PCNL-495-19-95 and PCNL-495-19-81. This is indicative of an increasing amount of crazing before neck initiation due to physical aging.

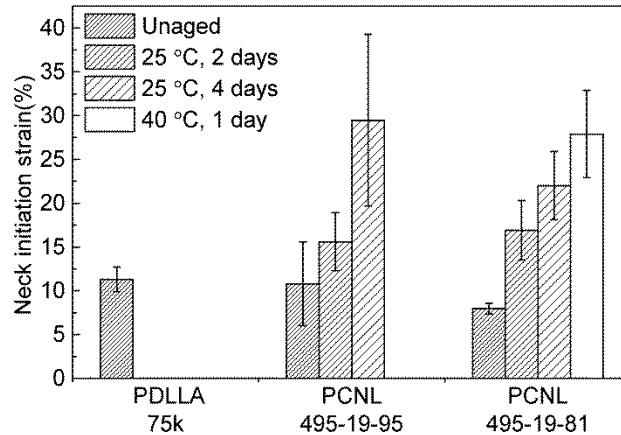


Figure 5-5 The average neck initiation strain for tensile samples in the unaged and physically aged condition. Error bars represent one standard deviation about the mean. The PDLLA-75k control only exhibited stable neck initiation in the unaged state. PCNL-495-19-95 did not exhibit stable neck initiation after aging at 40 °C for 1 day.

5.3.2 Simultaneous small-angle x-ray scattering and tensile testing

In order to obtain more detailed information about the micromechanical deformation mechanisms occurring during tensile testing, small-angle x-ray scattering and tensile testing were simultaneously conducted on two graft copolymers, PCNL-495-19-95 and PCNL-594-90-95, under two aging conditions. The graft copolymers selected for this study have similar PCN total molecular weight ($M_n \sim 50\text{--}60$ kg/mol) and PLA content (95 wt% PLA), but vary in $M_{n,\text{eff}}$ (backbone molecular weight between graft points) resulting in different domain sizes and spacing of the same morphology (poorly ordered spheres). The “unaged” condition was represented by samples that were placed in cold storage within a few hours of compression molding and remained there until 5 min before tensile testing (~ 70 h). The cold storage had an average temperature of -12 ± 9 °C and humidity of $29 \pm 2\%$ RH. In total, the unaged samples were at room temperature for

< 3h before testing. The samples representing the “aged” condition were stored in ambient conditions until testing, resulting in an average conditioning time of 66 ± 3 h.

5.3.2.1 Results for aged PCNL-594-90-95, $M_{n,eff} = 0.7$ kg/mol

Representative in-situ tensile data is shown for PCNL-594-90-95 aged at ~ 25 °C for ~ 66 h in Figure 5-6. Recall that in the previous quantitative tensile tests, PCNL-594-90-95 exhibited similar aging embrittlement behavior as PDLLA (Chapter 4) where the graft polymer is ductile ($\epsilon_b > 200\%$) within 2 h of compression molding, but significantly embrittled ($\epsilon_b \approx 10\%$) after aging at 25 °C for 48 h. In the in-situ SAXS/tensile experiment, aged PCNL-594-90-95 showed brittle tensile behavior (Figure 5-6) consistent with the quantitative aged tensile experiments. The photos of the sample during the test from cameras 3 and 4 (Appendix A, Figure A-1) indicate some optically anisotropic deformation that began prior to the yield point and stress whitening which initiated at the yield point, similar to that observed in PDLLA.

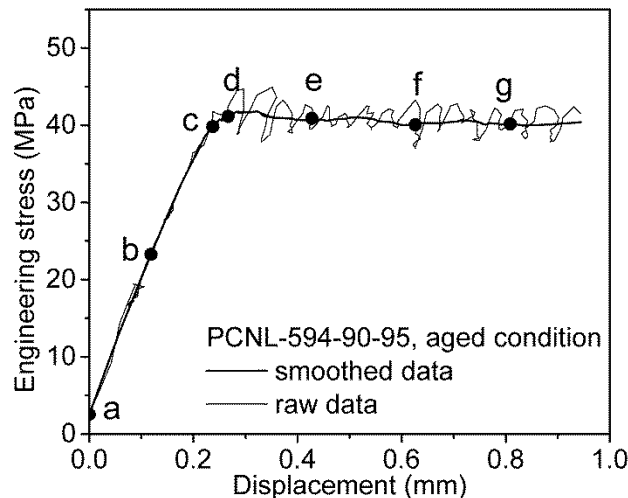


Figure 5-6 In-situ tensile data for PCNL-594-90-95 aged at 25 °C for 66 h. Specific displacements are highlighted by points on the (i) tensile stress-displacement curve.

From the 2D SAXS images (Figure 5-7), relatively isotropic block copolymer scattering is observed initially (point a) by the presence of a higher intensity ring. As the sample is deformed, pre-yield streaks, which were previously discussed in Chapter 4, appear near the beam stop (point b and c). Overall the azimuthal position and shifts of the pre-yield streaks are similar to that of the PDLA samples (Appendix A, Figure A-2). At the yield point, the characteristic craze scattering pattern is observed and remains until failure (point d to failure). After the yield point, the graft copolymer scattering becomes less discernible.

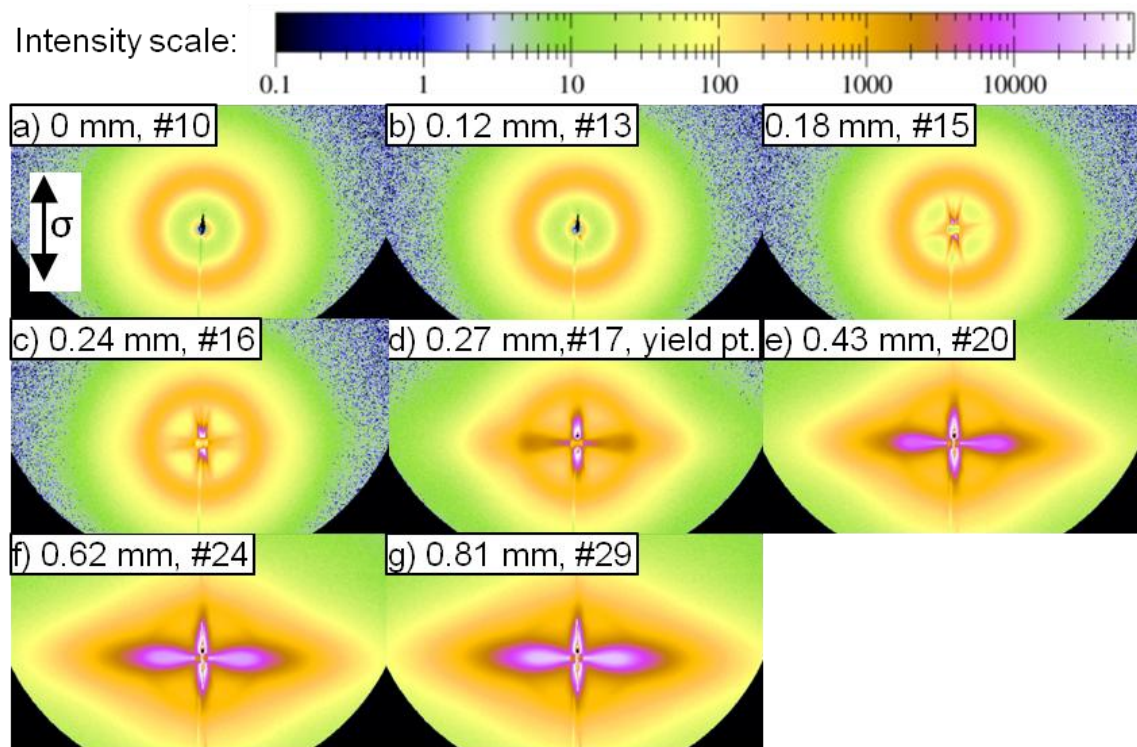


Figure 5-7 In-situ 2D SAXS patterns for PCNL-594-90-95 aged at 25 °C for 66 h. The 2D SAXS patterns are labeled with displacement and scan number. The scattered intensity scale of each SAXS image is the same.

Thus, the 2D SAXS patterns were azimuthally integrated in four different ranges: -5 to 5° (equatorial), 35 to 40° , 59 to 69° and 85 to 95° (meridional) to yield curves of intensity (I) versus scattering wavevector (q). The azimuthal ranges are illustrated in Figure 5-8 for point e with a logarithmic intensity scale that emphasizes the graft copolymer scattering. The scattering from the crazes overlaps the copolymer scattering in both the equatorial and meridional directions. Therefore, the 35 to 40° range was chosen in an attempt to examine the graft copolymer scattering near the equator with minimal overlap from the craze fibril scattering, while the 59 to 69° range was chosen for the same reasons, but applied to the meridional craze scattering.

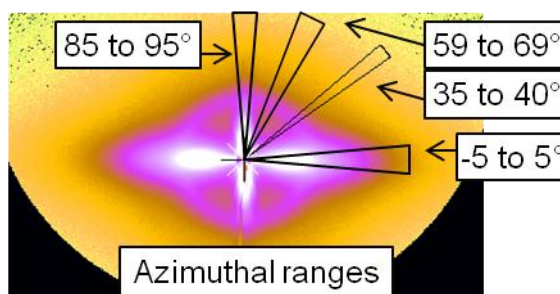


Figure 5-8 The azimuthal ranges used to obtain curves of intensity vs. wavevector are illustrated on the image for point e using a logarithmic intensity scale that emphasizes lower scattered intensities and thus, reveals the scattering from the graft copolymer more distinctly.

In the equatorial direction (Figure 5-9i), only the primary peak due to the graft copolymer morphology is observed initially with an intensity maximum located at 0.39 nm^{-1} . The 1D SAXS curve is consistent with the data shown in Chapter 3 where the SAXS curve for annealed PCNL-594-90-95 was fit using the Percus-Yevick model for hard spheres. From the in-situ data, the rubbery core radius was found to be 4.6 nm with an interparticle domain spacing of 16.7 nm . However, as the sample is deformed, the

scattering curve appears to become a superposition of the block copolymer scattering and scattering from the developing crazes (Figure 5-9i, point c). At the yield point (point d), a large increase ($\sim 10\times$, measured at the primary peak) in the overall scattered intensity is observed, consistent with the development of craze fibril scattering seen in PDLLA (Chapter 4). The peak maximum has shifted to 0.34 nm^{-1} . For comparison, the equatorial SAXS curve for aged PDLLA-58k at the yield point (Figure 5-9i, dashed line) is also shown. Although the curve of aged PDLLA-58k exhibits a peak maximum at 0.31 nm^{-1} , the shape of the curve at point d suggests that the superposition of craze scattering and block copolymer scattering is still occurring. The scattered intensity is proportional to the electron density contrast and number of scatterers.²¹ If the primary peak is a result of the superposition of craze scattering and graft copolymer scattering, it follows that the scattered intensity of the graft copolymer morphology must have also increased in order for the peak to remain visible. Since the number of graft copolymer domain scatterers is constant (constant sample volume), the larger intensity must result from an increase in electron density contrast, most likely due to cavitation of the rubber domains. Unfortunately, the graft copolymer scattering profile from the deformed sample cannot be fit to a form factor scattering model to determine the deformed size and shape of the rubber domains due to the limited q -range and the interference of scattering from the crazes. As the tensile deformation increases, the overall scattering intensity continues to increase and the peak maximum becomes less evident.

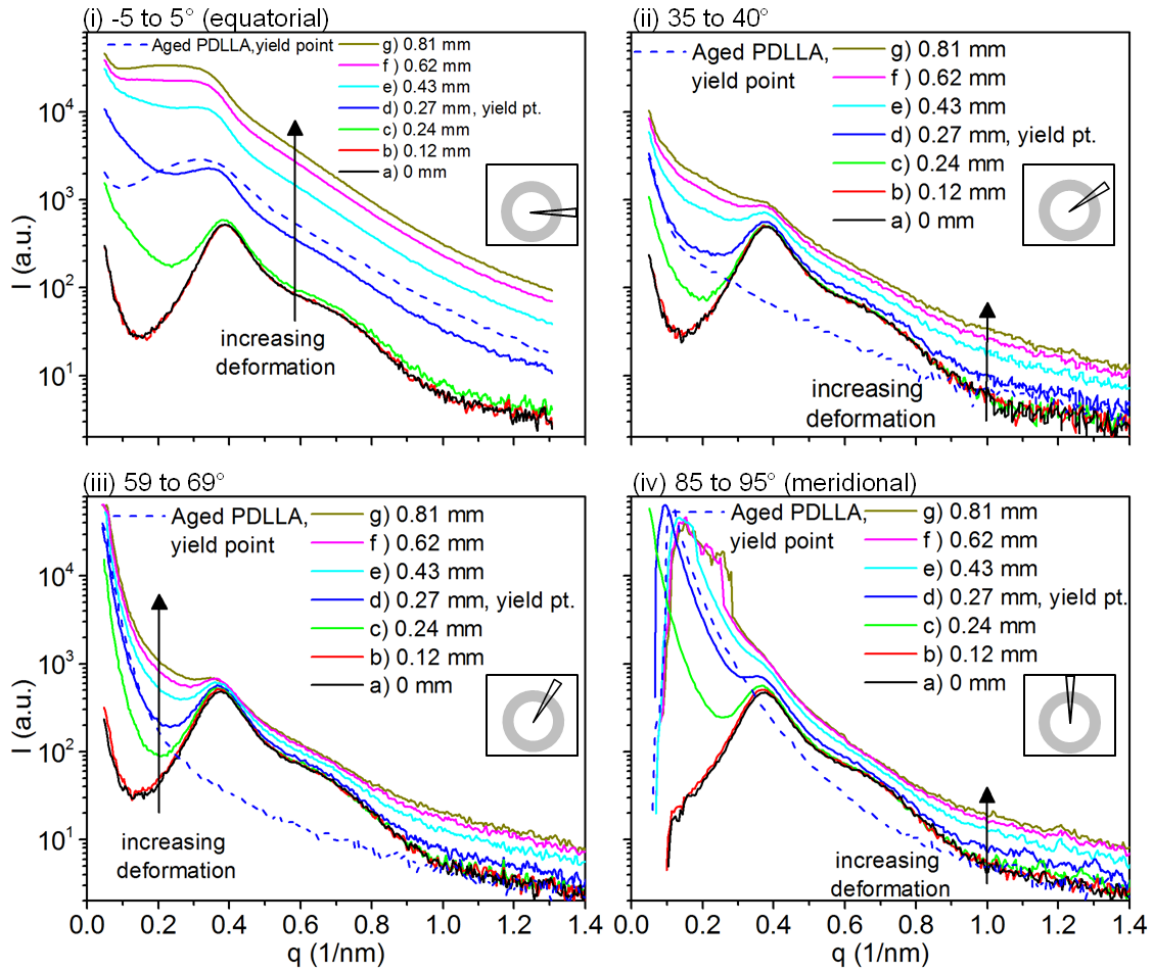


Figure 5-9 The SAXS curves of integrated scattering intensity (I) versus wavevector (q) for aged PCNL-594-90-95 at various tensile displacements are shown for the following azimuthal ranges: (i) -5 to 5° , (ii) 35 to 40° , (iii) 59 to 69° and (iv) 85 to 95° (meridional). For comparison, the SAXS curve for aged PDLLA-58k at the yield point (Ch. 4) is shown with a dashed line.

In the 35 to 40° , 59 to 69° , and meridional directions (Figure 5-9ii, iii, and iv respectively), the same graft copolymer scattering as in the equatorial direction is observed initially. In contrast to the equatorial result, at the yield point (point d), only a very small increase in overall intensity is observed. With increasing deformation, the peak from the block copolymer becomes less discernible. Aged PDLLA-58k at the yield point (denoted by the dashed lines in Figure 5-9) also exhibits some scattering in the 35

to 40° and 59 to 69° azimuthal ranges. Thus, it is likely that the scattering curves in the 35 to 40°, 59 to 69°, and meridional directions for aged PCNL-594-90-95 result from a simple overlap of the as-molded graft copolymer scattering and craze-fibril scattering in those respective directions. Specifically, for the 35 to 40° and 59 to 69° ranges (Figure 5-9ii and iii respectively), where the craze scattering is less dominant, the primary peak remains discernible throughout the entire deformation with no shift in q^* . The slight increases in intensity and broadening of the graft copolymer primary peak with greater tensile displacement are likely due to the increasing intensity of the craze scattering. In the meridional range, the primary peak is discernible until point e and remains at the same value of q^* . After point e, the extremely intense scattering from the craze faces overlaps the graft copolymer scattering so that only traces of the block copolymer primary peak may be identified by the slight change in slope at wavevector value of $\sim 0.38 \text{ nm}^{-1}$.

Ultimately, aged PCNL-594-90-95 deforms by crazing similar to aged PDLA. As with aged PDLA, the optically anisotropic deformation phenomenon and the pre-yield SAXS streaks were observed in the graft copolymer implying the formation of shear bands and shear crazes, in addition to shear craze rotation. At the yield point, the characteristic craze pattern was seen. However, the increase in electron density contrast for the graft copolymer morphology at the yield point suggests that the rubbery domains in the craze plane (equatorial direction) may also cavitate to form craze-like dilatation bands as discussed previously in Chapter 5. Thus, the deformation mechanism of aged PCNL-594-90-95 is probably a combination of both homogeneous and heterogeneous

crazing as predicted by the work of Schwier and Argon.¹⁴ The existence or lack of micro shear bands at the craze tips could not be determined by SAXS.

5.3.2.2 Results for unaged PCNL-594-90-95

Representative in-situ tensile data is shown for PCNL-594-90-95 in the “unaged” condition (-10°C for ~66 h). Unaged PCNL-594-90-95 exhibited ductile tensile behavior (Figure 5-10i) with the initiation of a neck and cold drawing of the gage consistent with the quantitative tensile results. Similar to the other samples, an optically anisotropic deformation mechanism was observed by camera 4 before the yield point (Appendix A, Figure A-3). Stress whitening was not observed by camera 3 until point e, just after the yield point and coincident with neck initiation. From the 2D scattering images, the morphology of unaged PCNL-594-90-95, as clamped, appeared to be isotropic (Figure 5-10ii, point a). As before, pre-yield streaks attributed to shear crazes are seen in the 2D SAXS pattern up to the yield point (Figure 5-10ii, points b – d). When the neck is initiated at point e, the equatorial streaks increased in intensity and extended towards smaller domain sizes (larger q-values). However, unlike all the previously discussed samples, no change in the meridional streaks could be seen. Additionally, the isotropic scattering ring from the graft copolymer begins to elongate in the equatorial direction. As the neck is propagated, the 2D SAXS pattern of the graft copolymer scattering becomes more anisotropic, forming an ellipse that is extended in the equatorial direction (Figure 5-10ii, points f – j). Meanwhile, the azimuthal width of the equatorial streaks from the shear craze fibrils decreases while the meridional streak approaches and then moves behind the beam stop.

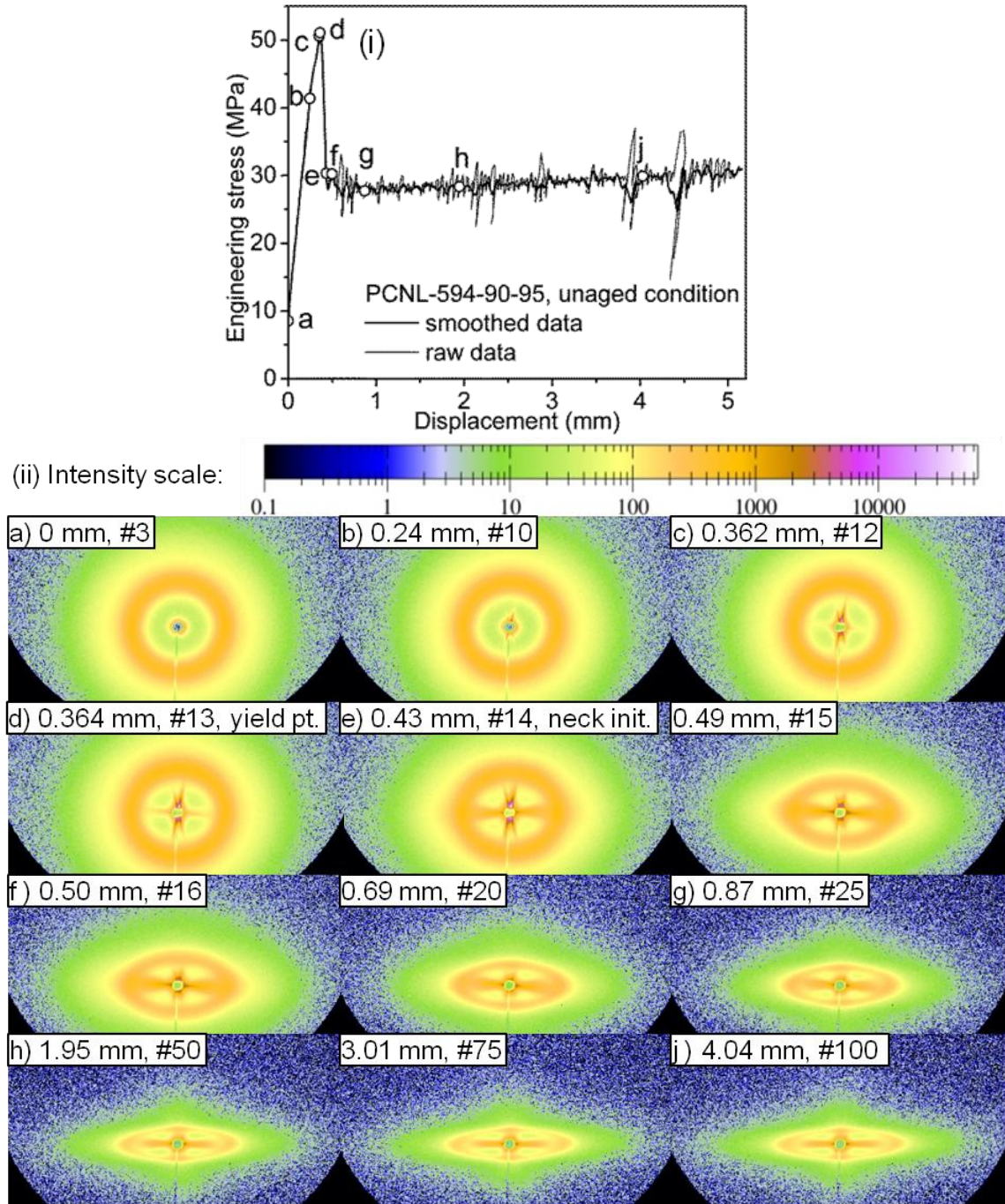


Figure 5-10 (i) In-situ tensile stress vs. displacement for unaged PCNL-594-90-95. The labeled points on the curve correspond with the 2D SAXS patterns. (ii) The in-situ 2D SAXS patterns for unaged PCNL-594-90-95 are labeled with tensile displacement and scan number. The scattered intensity scale of each SAXS image is the same.

The azimuthally integrated scattering curves of intensity (I) versus wavevector (q) in the equatorial ranges are shown in Figure 5-11i, both before and after neck initiation. The scattering curves for the equatorial range are generally similar to that of the aged graft copolymer up until the yield point (point d) of the unaged graft copolymer. As before, a small amount of low- q scattering, due to the craze formation process, is visible starting at point c. The craze scattering also appears to overlap the block copolymer scattering, however; to a lesser extent than in the aged case. At the yield point, there is not an obvious increase in overall intensity as there was in the aged case. It is not until point e, neck initiation, where a small increase in overall intensity is observed. However, the intensity increase between point d, just before the fibril scattering appears, and point e is only about 3 \times , smaller than the 10 \times increase observed for aged PCNL-594-90-95. The smaller value of the increase in intensity suggests that the craze or fibril density may be less in the unaged sample relative to the aged sample. After neck initiation, the shape of the curve remains similar to that at point e; however, the peak maximum shifts to larger values of q with increasing deformation. Additionally, the overall intensity decreases with increasing displacement due to thinning of the sample.

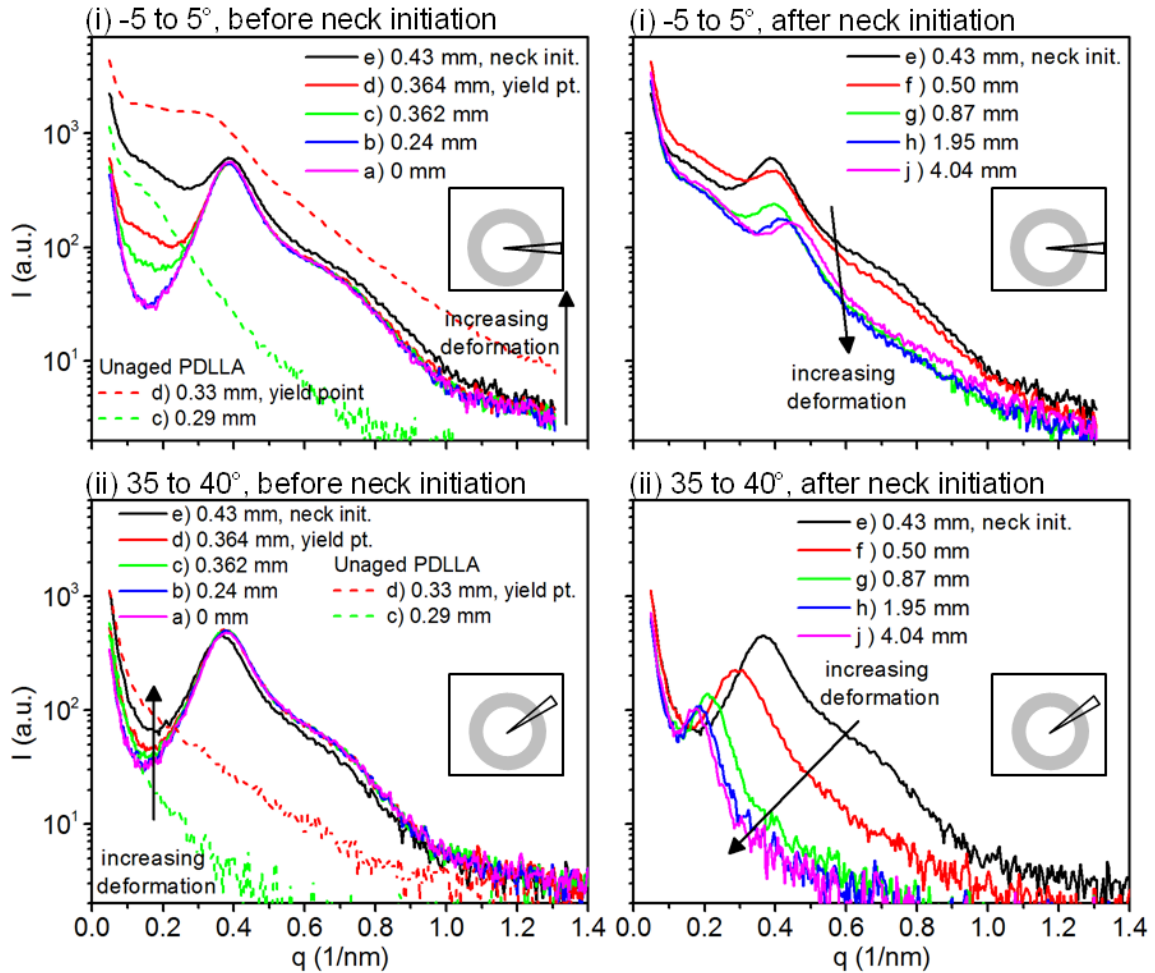


Figure 5-11 The 1D SAXS curves of scattered intensity (I) versus wavevector (q) for unaged PCNL-594-90-95 were obtained by azimuthal integration in the (i) equatorial range and the (ii) 35° – 40° range of the 2D-scattering patterns at each highlighted displacement. The progression of the scattered intensity is shown before and after neck initiation for each azimuthal range.

In the 35° – 40° azimuthal range (Figure 5-11ii), the shape of the scattering curve is relatively constant until neck initiation at point e which is in contrast to the aged sample where overlapping craze scattering was observed at lower q -values. At point e, there is a slight decrease in overall intensity and shift in q^* towards smaller q -values. After neck initiation, the same trends, with respect to intensity and q^* , continue. The scattering curves of intensity versus wavevector are shown in Figure 5-12i and ii for the

59°–69° and the meridional azimuthal ranges respectively. In the 59°–69° direction, the peak broadens slightly until the yield point. The intensity of the curve in the low- q region ($\sim 0\text{--}0.4\text{ nm}^{-1}$) also increases slightly. At neck initiation, the curve is translated towards lower q while the intensity decreases a small amount. Curves for aged PCNL-594-90-95 at the yield point and just before failure were also plotted using the dashed lines. Interestingly, the intensity of the low q -scattering, which increases from the yield point to 0.81 mm in the aged case, is not observed in the unaged graft copolymer. As the unaged sample is cold drawn (points f–j), the same trend of decreasing intensity and decreasing q^* that was seen for the 35°–40° range is observed for the 59°–69° range. Additionally, there is minimal overlapping craze scattering, unlike in the aged case. Qualitatively, the scattering curves for the meridional range are very similar to that for the 59°–69° range. Once again in contrast to the aged case, the meridional scattering from the crazes does not overlap the graft copolymer scattering significantly. Thus, the same trends of diminishing intensity and q^* with increased neck propagation are seen for the meridional range as well. The lack of overlapping craze scattering suggests that crazes were not initiated at the yield point in the unaged case.

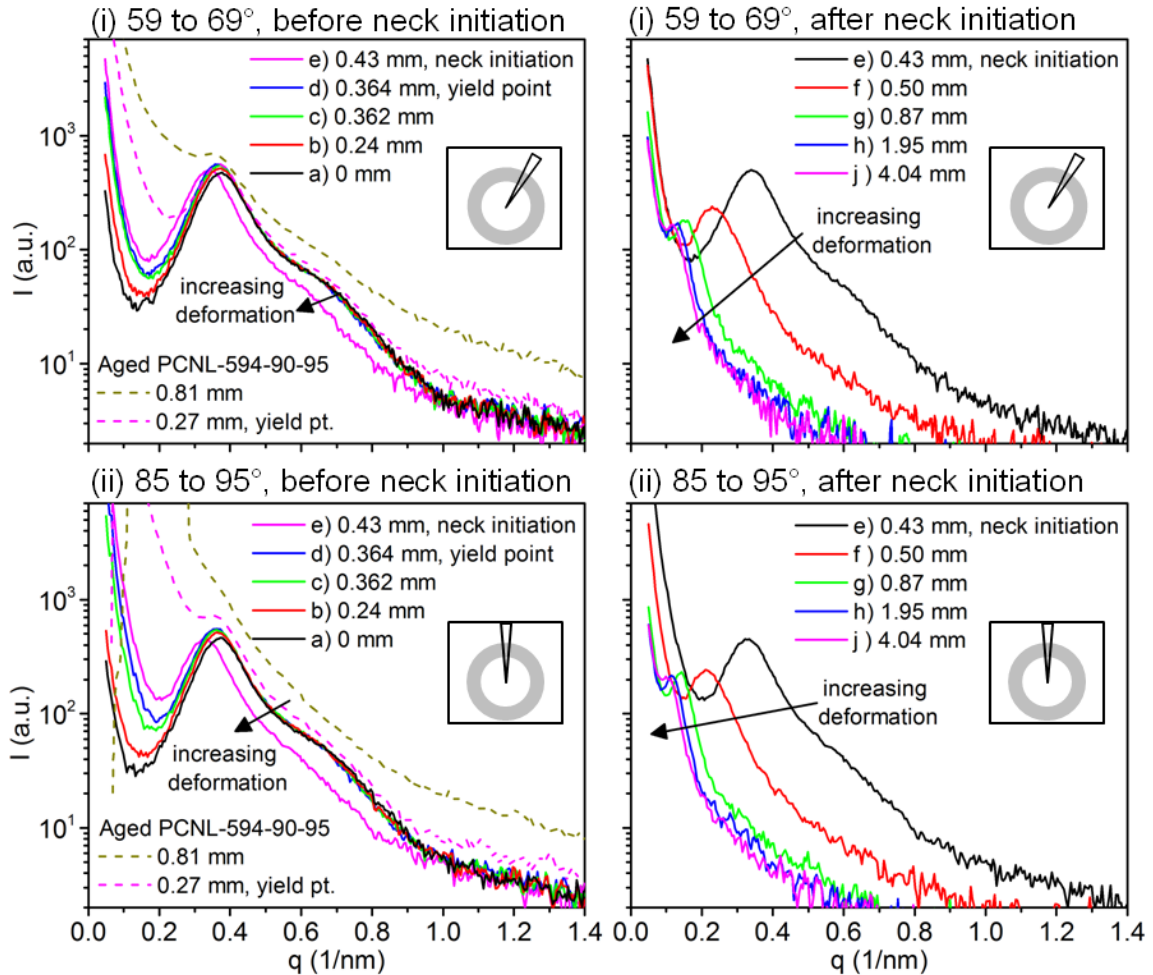


Figure 5-12 The 1D SAXS curves of scattered intensity (I) versus wavevector (q) for unaged PCNL-594-90-95 were obtained by azimuthal integration in the (i) 59° – 69° range and the (ii) meridional range (85° – 95°) of the 2D-scattering patterns at each highlighted displacement. The progression of the scattered intensity is shown before and after neck initiation for each azimuthal range.

The interparticle domain spacing (d^*) was calculated from the peak maximum (q^*) of the integrated scattered intensity (I) vs. wavevector (q) curves for all azimuthal ranges using the following equation, $d^* = 2\pi/q^*$. Figure 5-13i shows both domain spacing and engineering stress plotted as a function of tensile displacement for PCNL-594-90-95 in the aged and unaged conditions. Initially, the average and standard deviation of domain spacing (over the 4 azimuthal ranges) for the aged and unaged graft copolymers

were 16.6 ± 0.3 nm. Unlike the aged case, the unaged graft copolymer scattering peak remained visible throughout the tensile test for all azimuthal ranges. The domain spacing in all ranges did not change until neck initiation. For the 35 to 40°, 59 to 69° and meridional ranges, a rapid increase in d^* starts at neck initiation. The domain spacing then reaches a relatively steady state value as the rest of the gage undergoes cold-drawing. In contrast, d^* for the equatorial range decreases slightly at neck initiation and then continues to decrease to 14 nm as the gage is further cold drawn.

Overall, the tensile deformation behavior of unaged PCNL-594-90-95 begins similarly to all the previously examined materials with evidence for the formation and rotation of shear crazes (and implied micro shear bands) prior to the yield point (Appendix A, Figure A-4). However, the characteristic craze scattering pattern was never observed. At neck initiation, the overall scattering intensity in the equatorial direction increased only slightly while the intensity of the meridional streak remained relatively constant. Thus, some growth of the shear crazes occurred, but new crazes do not seem to have been initiated. The tensile deformation then proceeded by shear yielding of the PLA matrix resulting in widening of the craze faces, further alignment of the craze fibrils in the tensile direction and shear deformation of the rubber domains. The change in domain spacings of the unaged graft copolymer coupled with the shape of the SAXS curves suggests that the rubber domains became elongated in the tensile direction as shown in Figure 5-13ii. No increase in scattering intensity was observed to suggest rubber domain cavitation. However, fitting the data to the appropriate form factor would be necessary to confirm if the deformation was distortional, dilatational or a combination of both.

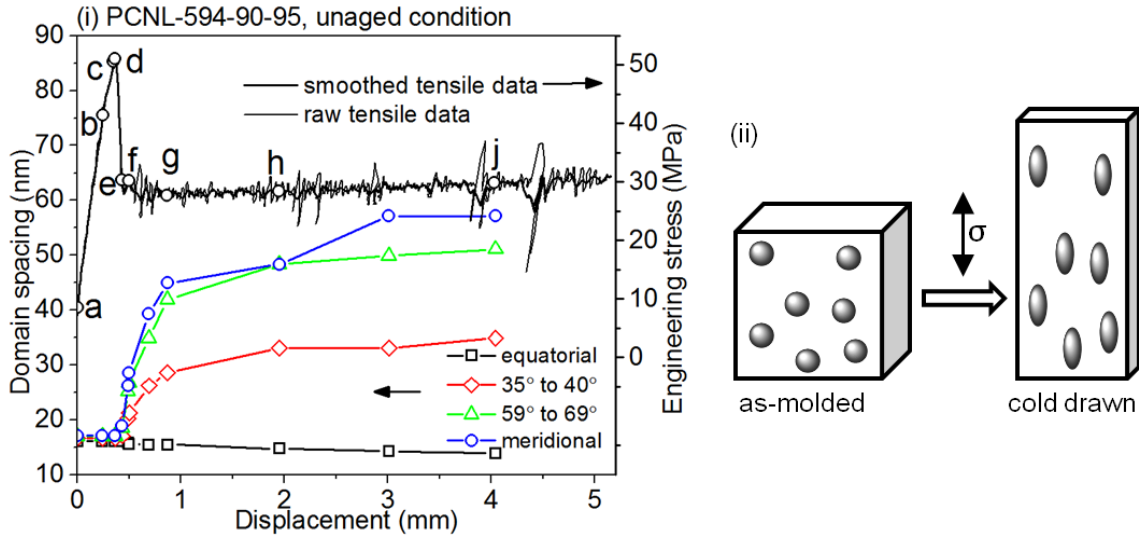


Figure 5-13 (i) The domain spacing determined from the peak of the integrated SAXS curves is plotted as a function of spacing on the left axis while the engineering stress plotted on the right axis for unaged PCNL594-90-95. (ii) Idealized schematic of rubber domains in a PDLA matrix transitioning from the as-molded morphology of isotropically distributed spheres to elongated elliptical domains that are spaced farther apart in the tensile direction, but closer in the other two orthogonal axes as a result of cold drawing.

5.3.2.3 Results for PCNL-495-19-95, $M_{n,eff} = 2.8 \text{ kg/mol}$

Both aged and unaged PCNL-495-19-95 deformed as expected from the results of the quantitative tensile tests. PCNL-495-19-95 aged for ~66h at 25°C exhibited crazing followed by neck initiation and cold drawing, while unaged PCNL-495-19-95 (~66 h at -10°) only crazed slightly before neck initiation and propagation as seen in the tensile stress vs. displacement curve (Figure 5-14). Overall, the deformation mechanisms were the similar in both the aged and unaged case. Thus, the deformation mechanism will be illustrated using only the data from the unaged case. All the in-situ tensile/SAXS data for aged PCNL-495-19-95 can be found in Appendix A, Figure A-6 to A-9.

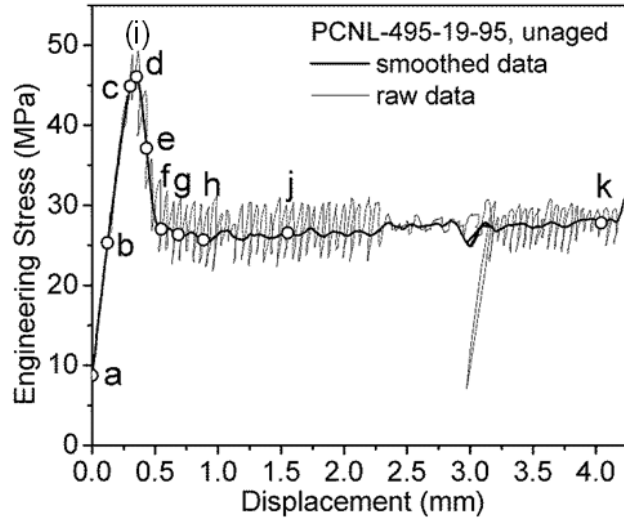


Figure 5-14 In-situ tensile data for unaged PCNL-495-19-95. Specific displacements are highlighted by points on the (i) tensile stress-displacement curve.

The initial morphology of “unaged” PCNL-495-19-95 is similar to that of the aged specimen by exhibiting a slight anisotropic texture in the scattering pattern. The 2D SAXS pattern at 0 mm displacement (Figure 5-15, point a) shows a slightly elongated ring with the long axis oriented approximately 45° from the vertical. Thus, either the rubber domains may be slightly elongated away from a spherical shape, or there is a slight (not completely random) ordering of the rubber domains in the PLA matrix resulting from the compression molding procedure. After a linear elastic deformation region, during which no change to the scattering pattern is observed, an intense meridional streak appears near the beamstop before the yield point (Figure 5-15, point c). The characteristic craze pattern (Figure 5-15 ii, point d) is then observed in the next acquisition at point d (5 seconds from when point c was acquired). A neck is then initiated (points e and f) and the sample is subsequently cold drawn. The equatorial

scattering starting after craze initiation (point d), is composed of an equatorial streak as well as a lobed feature that is located at lower q -values (closer to the beam stop).

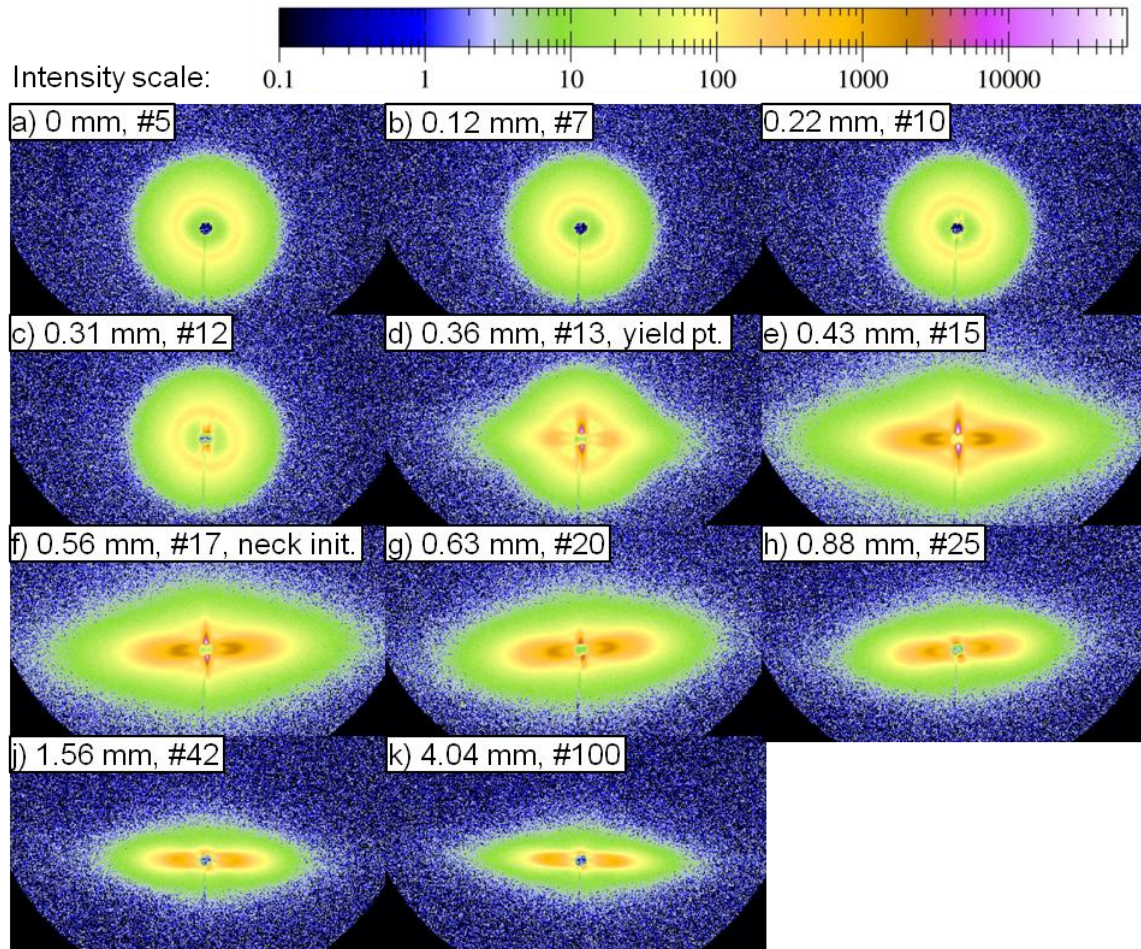


Figure 5-15 In-situ 2D SAXS patterns for unaged PCNL-495-19-95. The 2D SAXS patterns are labeled with displacement and scan number. The scattered intensity scale of each SAXS image is the same.

The SAXS curves for the equatorial and 35° – 40° ranges are shown in Figure 5-16. Initially (point a, 0 mm), the scattering in the equatorial direction (Figure 5-16i, before neck initiation) from the graft copolymer yields a broad interparticle interference peak resulting in a domain spacing of 30.4 nm, which is slightly larger than d^* of the

annealed graft copolymer (26.5 nm) discussed in Chapter 3. The curve could not be fit to the Percus-Yevick model, possibly due to the morphological texture introduced during sample preparation. However, a spherical form factor was fit to the curve using the first minimum located near 0.65 nm^{-1} resulting in a rubber domain radius of 7.1 nm, which is similar to the value obtained in Chapter 3 for the annealed graft copolymer (7.2 nm). No change in the scattering curve is observed until the yield point (point d). At point d, the overall intensity increases dramatically which signals the onset of craze formation. Additionally, the graft copolymer primary peak appears to shift to lower q -values while a shoulder (near 0.4 nm^{-1}) also appears. Similar to the scattering curve for aged PCNL-594-90-95, the shoulder feature can be attributed to craze fibril scattering. The position and overall intensity of the shoulder feature is similar to the shape of the 1D scattering curve for unaged PDLA-58k at its yield point (from Chapter 3) which is also shown in Figure 5-16i using a dashed line. As the graft copolymer begins neck initiation (point e), only the overall intensity increases while the shape of the curve remains the same. At neck initiation (Figure 5-16i, after neck initiation, point f), the scattering curve maintains approximately the same shape but the primary peak shifts position and the overall intensity decreases as the sample is deformed (points g-k). The change of domain spacing with displacement will be discussed later.

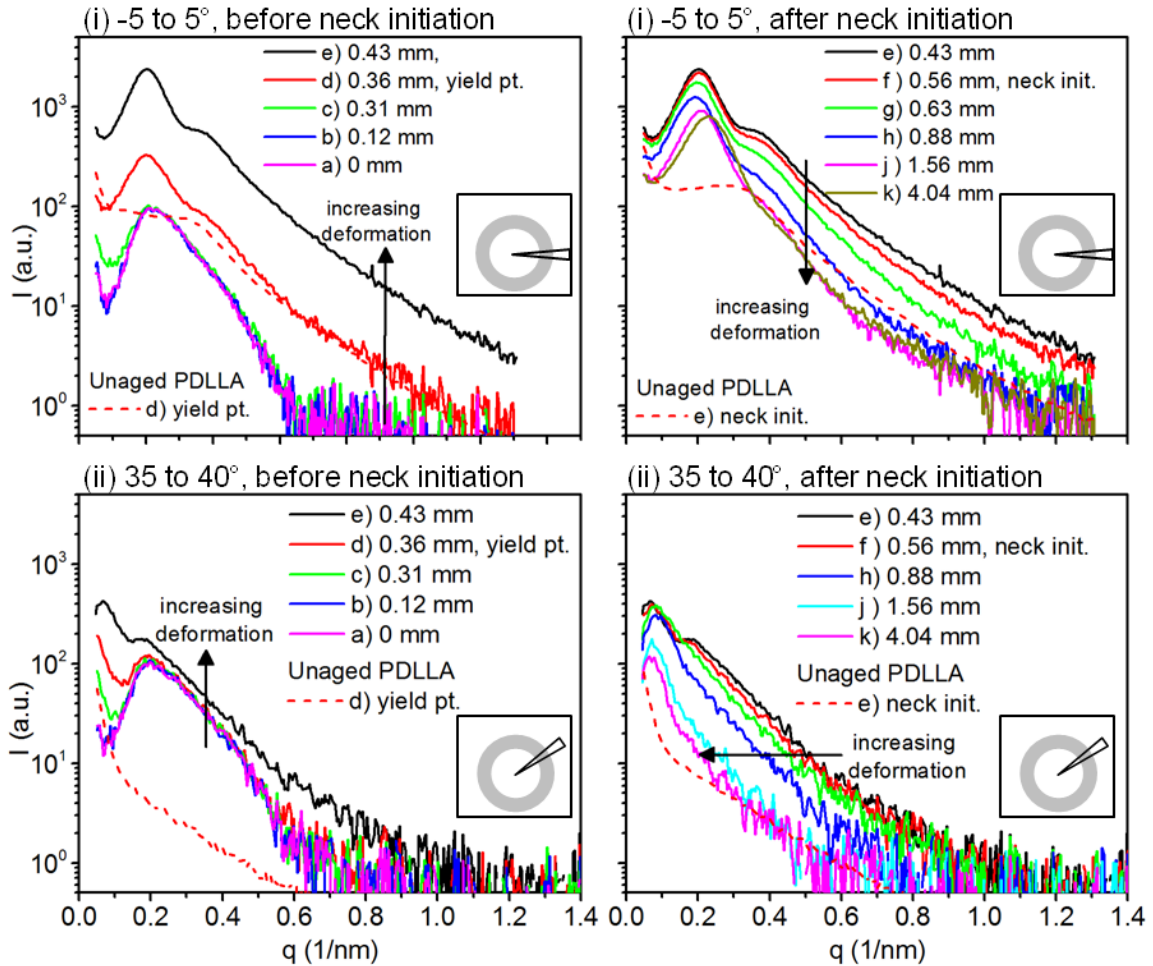


Figure 5-16 1D SAXS curves of scattered intensity (I) versus wavevector (q) for unaged PCNL-495-19-95 were obtained by azimuthal integration in the (i) $-5 - 5^\circ$ [equatorial range] and the (ii) $35^\circ - 40^\circ$ range of the 2D-scattering patterns at each highlighted displacement. The progression of the scattered intensity is shown before and after neck initiation.

In contrast to the scattering curve from the equatorial range, the scattering curve for the $35^\circ - 40^\circ$ range shows little change before neck initiation (Figure 5-16ii, before neck initiation). The shape of the curve and the position of the primary peak remain the same during the initial deformation with only a very small increase in overall intensity at the yield point (point d) and additional scattering in the low q region ($\sim 0.1 - 0.15 \text{ nm}^{-1}$) preceding the primary peak that can be attributed to the crazes. At the beginning of neck

initiation, at point e, a larger increase in overall intensity is observed likely associated with increased craze density. As cold drawing begins (Figure 5-16ii, after neck initiation, point f), the primary peak position appears to shift to lower q -value and there is even more scattering in the low q -region ahead of the primary peak forming a small apparent peak at 0.07 nm^{-1} . With additional deformation, the primary peak of the graft copolymer shifts further towards lower q -values and becomes overlapped by the other peak at point g. Beyond point g, although the two peaks cannot be resolved, it is clear that the entire scattering curve is shifting towards lower q -values (i.e. larger domain spacing).

The SAXS curves for the 59° – 69° and meridional (85° – 95°) ranges are shown in Figure 5-17i and ii, respectively. The progression of the scattering curve within the 59° – 69° range with displacement is similar to that observed in the 35° – 40° range. Before neck initiation, the intensity increases slightly with deformation, while the primary peak apparently shifts a small amount towards lower q -values without a notable change in the peak shape. Additionally, as before, the low q scattering preceding the primary peak also increases with increasing tensile displacement. At neck initiation (Figure 5-17i, after neck initiation, point f) the primary peak shifts further towards low q . As cold drawing ensues, the primary peak continues to shift to lower q -values until it can no longer be discerned (point h) due to overlap from the low q scattering. Also, the entire curve appears to shift towards smaller q -values with increasing tensile displacement.

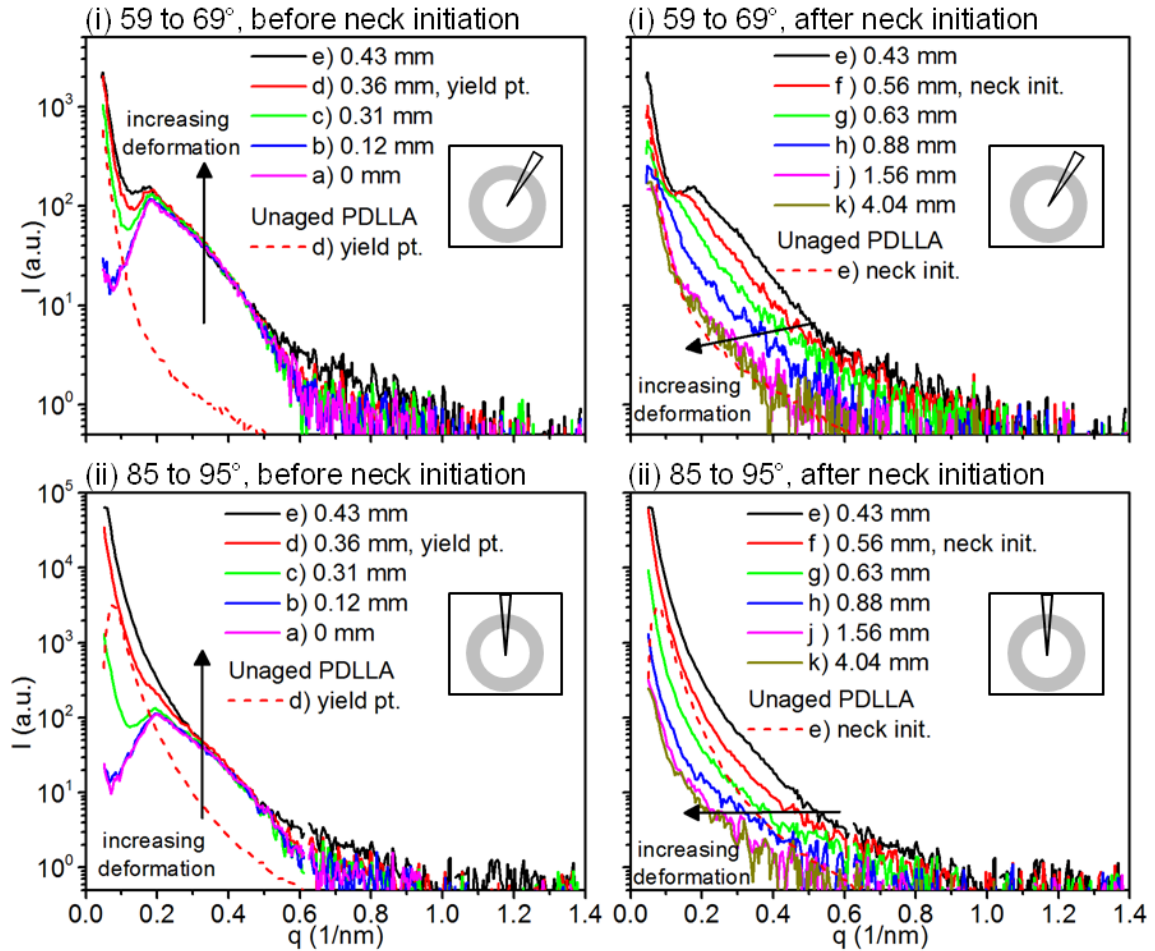


Figure 5-17 The 1D SAXS curves of scattered intensity (I) versus wavevector (q) for unaged PCNL-495-19-95 were obtained by azimuthal integration in the (i) 59° – 69° range and the (ii) meridional range (85° – 95°) of the 2D-scattering patterns at each highlighted displacement. The progression of the scattered intensity is shown before and after neck initiation.

In the meridional direction (Figure 5-17ii, before neck initiation), the primary peak from the graft copolymer becomes almost completely overlapped by the craze scattering at the yield point (point d). Beyond the yield point, the scattering from the graft copolymer cannot be discerned due to the intense meridional scattering from the craze faces. Just after the yield point, once again, the entire scattering curve can be observed

shifting towards lower q -values with increased tensile displacement (Figure 5-17ii, after neck initiation, points e–k).

The combined data indicate that prior to the yield point, PCNL-495-19-95 likely exhibited micro shear banding and the beginning of shear crazing as evidenced by the optical anisotropy and the pre-yield meridional streak. At the yield point, new crazes were initiated and propagated. The large increase in overall intensity and preservation of the shape of the graft copolymer scattering curve in the equatorial direction suggests that the rubber domains in the plane of the craze cavitated. Additionally, the 2D SAXS pattern of the craze at the yield point has a lobed feature along the equatorial axis that was not seen in PDLLA or PCNL-594-19-95. Similar scattering patterns have been observed previously and attributed to slight misalignment of the primary craze fibrils due to the presence of cross-tie fibrils.²² The presence of cross-tie fibrils is consistent with a mechanism of hetero-phase cavitation induced crazing and craze thickening as illustrated previously in Figure 5-1b. The graft copolymer domain spacing was calculated as a function of displacement and plotted with the stress-displacement curves in Figure 5-18. During crazing, the equatorial domain spacing remains relatively constant. The meridional craze scattering obscured the determination of d^* in the meridional direction for the graft copolymer. However, the large increase in d^* observed for the 59° - 69° direction suggests the domain spacing in the meridional direction also increased, consistent with the hetero-phase cavitation mechanism.

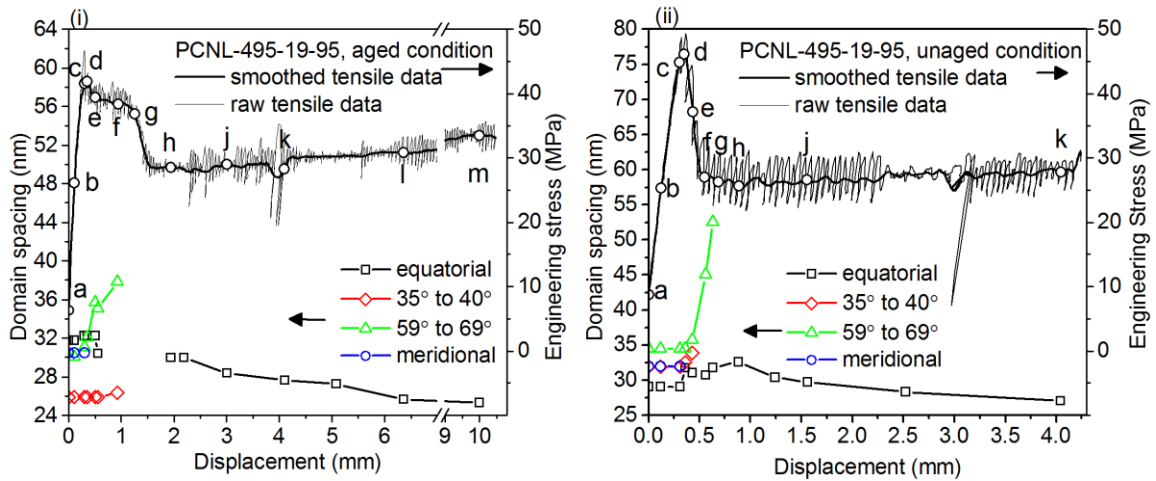


Figure 5-18 The domain spacing obtained from the position of the primary peak is plotted as a function of displacement and compared to the tensile behavior for the four different azimuthal ranges: -5° – 5° (equatorial), 35° – 40° , 59° – 69° , and 85° – 95° (meridional scattering) for the (i) aged and (ii) unaged conditions of PCNL-495-19-95.

5.4 Summary

In summary, all the graft copolymers exhibited some SAXS evidence of shear crazing prior to the yield point independent of aging condition. Unaged PCNL-594-90-95 deformed after the yield point only by shear yielding; possibly as a result of the coalescence of micro shear bands which initiated before the yield point and before the initiation of new crazes. However, only indirect evidence for micro shear bands was found from the SAXS experiment. Physical aging of PCNL-594-90-95 appeared to inhibit the coalescence of the micro shear bands and some hetero-phase cavitation induced crazes were initiated instead. Evidence for homogeneous crazing was also observed. Similar to aged PDLA-58k, brittle fracture in aged PCNL-594-90-95 resulted from craze failure. By increasing the rubber domain size, as in the case of PCNL-495-19-95, a unique craze scattering pattern was observed independent of aging conditions. Unaged PCNL-495-19-95 exhibited slight crazing and neck initiation at the yield point.

The data suggests that the hetero-phase cavitation mechanism was also occurring in this case. The lobed craze scattering pattern suggests that the craze morphology possesses cross-tie fibrils that were not seen for PDLLA or PCNL-594-90-95. The primary effect of physical aging on PCNL-495-19-95 was to increase the amount of deformation resulting from crazing before neck initiation. Since both aged and unaged PCNL-495-19-95 were able to initiate macroscopic necks, we can speculate that shear bands may have formed at the tips of the propagating crazes. Perhaps the crazes in aged PCNL-495-19-95 may have needed to grow longer before the shear bands could interact and coalesce.

Ultimately, the addition of the rubber phase did alter the deformation mechanism of the graft copolymers relative to PDLLA. In spite of the small rubbery core in PCNL-594-90-95, hetero-phase cavitation induced crazing took place in the aged case in addition to homogeneous crazing. However, as the rubbery core radius increased from ~ 4 nm in PCNL-594-90-95 to ~ 7 nm in PCNL-495-19-95, the relative amount of hetero-phase cavitation induced crazing increased and facilitated a craze morphology containing cross-tie fibrils. As mentioned in Chapter 4, cross-tie fibrils help to transfer the deformation stress laterally, which promotes craze tip advance. Thus, the crazes in PCNL-495-19-95 are more prone to delocalization of the tensile deformation through craze propagation relative to the crazes of PDLLA or PCNL-594-90-95. In addition to enabling additional deformation mechanisms, the graft copolymer architecture still may have changed the physical aging kinetics of the PLA matrix. Thus, the physical aging kinetics of the graft copolymers and homopolymer PLA will be investigated in Chapter 6 by differential scanning calorimetry.

5.5 References

- ¹ Haward, R. N.; Young, R. J., Eds.; In *The Physics of Glassy Polymers*; Chapman & Hall: London, 1997; , pp 508
- ² Arends, C. B., Ed.; In *Polymer Toughening*; Hudgin, D. E., Ed.; *Plastics Engineering*; Marcel Dekker, Inc.: New York, NY, 1996; Vol. 30.
- ³ Anderson, K. S.; Schreck, K. M.; Hillmyer, M. A. *Polymer Reviews* **2008**, 85-108.
- ⁴ Liu, H.; Zhang, J. *Journal of Polymer Science Part B-Polymer Physics* **2011**, 15, 1051-1083.
- ⁵ Bucknall, C. B. *Journal of Polymer Science Part B: Polymer Physics* **2007**, 45, 1399-1409.
- ⁶ Sferrazza, M.; Crawshaw, J.; Donald, A. M.; Narayanan, T. *Macromolecules* **2001**, 34, 6708-6718.
- ⁷ Dompas, D.; Groeninckx, G.; Isogawa, M.; Hasegawa, T.; Kadokura, M. *Polymer* **1994**, 35, 4760-4765.
- ⁸ Liu, J.; Sue, H.; Thompson, Z. J.; Bates, F. S.; Dettloff, M.; Jacob, G.; Verghese, N.; Pham, H. *Macromolecules* **2008**, 41, 7616-7624.
- ⁹ Jansen, B. J. P.; Rastogi, S.; Meijer, H. E. H.; Lemstra, P. J. *Macromolecules* **2001**, 12, 4007-4018.
- ¹⁰ Declet-Perez, C.; Redline, E. M.; Francis, L. F.; Bates, F. S. *ACS Macro Lett.* **2012**, 2, 338-342.
- ¹¹ Declet-Perez, C.; Francis, L. F.; Bates, F. S. *ACS Macro Lett.* **2013**, 10, 939-943.
- ¹² Schwier, C.; Argon, A.; Cohen, R. *Philos. Mag. A-Phys. Condens. Matter Struct. Defect Mech. Prop.* **1985**, 5, 581-603.
- ¹³ Schwier, C. E.; Argon, A. S.; Cohen, R. E. *Polymer* **1985**, 13, 1985-1993.
- ¹⁴ Argon, A. S.; Cohen, R. E.; Gebizlioglu, O. S.; Schwier, C. E. *Crazing in block copolymers and blends*. In Kausch, H. H., Ed.; Springer Berlin Heidelberg: 1983; Vol. 52-53, pp 275-335.
- ¹⁵ Dicorleto, J.; Cohen, R. *Polymer* 1988, 29, 1245-1254.

-
- ¹⁶ Suzuki, S.; Nishitsuji, S.; Inoue, T. *Polym. Eng. Sci.* 2012, 52, 1958-1963.
- ¹⁷ Mahanthappa, M.; Bates, F.; Hillmyer, M. *Macromolecules* **2005**, 19, 7890-7894.
- ¹⁸ Dorgan, J. R.; Janzen, J.; Knauss, D. M.; Hait, S. B.; Limoges, B. R.; Hutchinson, M. H. *Journal of Polymer Science Part B: Polymer Physics* 2005, 43, 3100-3111.
- ¹⁹ Pan, P.; Zhu, B.; Inoue, Y. *Macromolecules* 2007, 40, 9664-9671.
- ²⁰ Senden, D. J. A.; van Dommelen, J. A. W.; Govaert, L. E. *Journal of Polymer Science Part B-Polymer Physics* 2012, 50.
- ²¹ Kinning, D. J.; Thomas, E. L. *Macromolecules* **1984**, 9, 1712-1718.
- ²² Berger, L. L. *Macromolecules* **1989**, 7, 3162-3167.

Chapter 6: Physical aging kinetics of polylactide graft copolymers

6.1 Background

Physical aging, also termed structural relaxation, is the phenomenon by which glassy polymers approach, often slowly, thermodynamic equilibrium when annealed below their glass transition temperature (T_g) by way of local segmental chain motion.¹ The exact mechanisms responsible for physical aging are still under investigation, but it is well established that both the specific volume and enthalpy of the material decrease due to physical aging. Material properties, such as elastic modulus and ductility, also change with physical aging as a result of the change in structure and was experimentally demonstrated in Chapters 4 and 5.

A schematic representing the change in enthalpy of a non-crystallizable polymeric material as it is cooled from the liquid state is illustrated in Figure 6-1. As the polymer is cooled below T_g , it becomes kinetically trapped in a metastable solid state. The anticipated equilibrium enthalpy of the glassy polymer solid is given by extrapolation of the liquid enthalpy curve to temperatures below T_g . Although large-scale chain motion is absent below T_g , sub- T_g secondary relaxations may still occur. For PLA in particular, a β relaxation attributed to a small amplitude twisting motion of the chain was identified through dielectric relaxation spectroscopy studies below the T_g .² When a polymer glass is isothermally annealed at $T < T_g$ (e.g., T_a in) for some time (t), the structure changes through such local secondary motions to reduce its enthalpy (and Gibbs free energy) as the equilibrium state at a given temperature T_a [indicated by $H_\infty(T_a)$ in Figure 6-1 is approached.

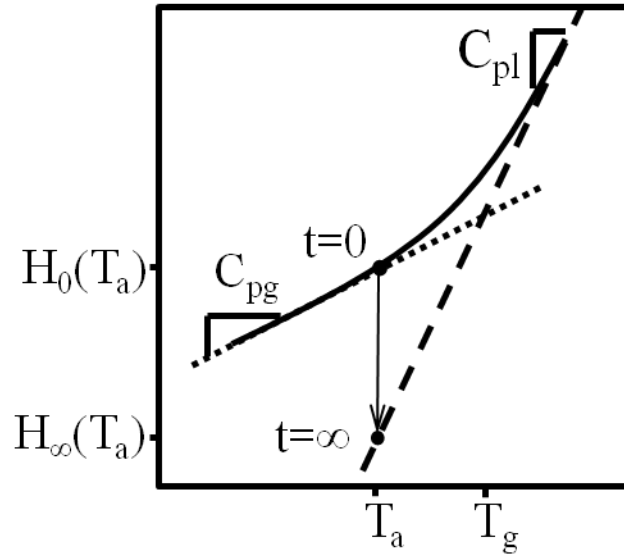


Figure 6-1 Schematic of the enthalpy of a glassy polymer as it is cooled through its glass transition temperature and then physically aged at temperature T_a . Initially ($t=0$), the material has an enthalpy of H_0 that approaches equilibrium (H_∞) with increasing time. The slope of the line above T_g is the heat capacity of the liquid (C_{pl}) while below T_g , the slope changes to the value of the heat capacity of the glassy solid (C_{pg}).

Reheating an aged glass through T_g results in a recovery of the enthalpy lost during aging, and in a differential scanning calorimetry (DSC) experiment, the recovered enthalpy is observed during heating as an endothermic peak around the glass transition (sometimes referred to as an “enthalpy overshoot” or “excess enthalpy”) as shown in Figure 6-2. The enthalpy overshoot is akin to a melting of a crystalline structure wherein heating results in elimination of the stabilizing intermolecular interactions in the crystal. The longer the material is aged below T_g , the larger the enthalpy overshoot, until the $H_\infty(T_a)$ is reached (which could be impractically long).

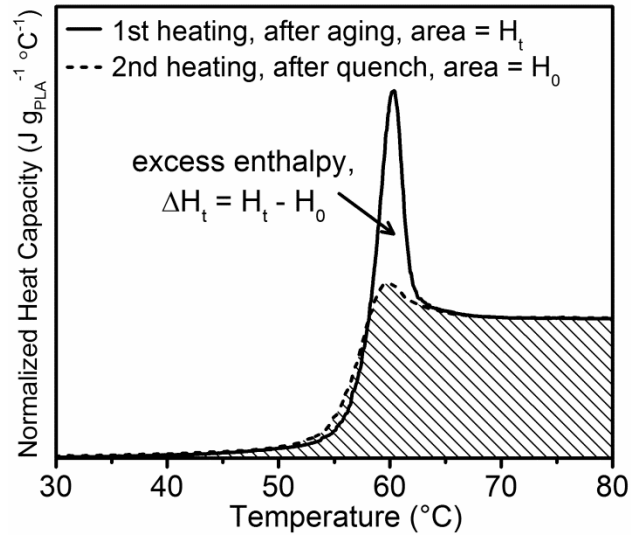


Figure 6-2 Differential scanning calorimetry (DSC) curves upon heating of a physically aged glassy polymer (—) and quenched glassy polymer (- - -) i.e., the state of polymer at aging time = 0. The large peak seen near T_g in the aged glassy polymer is due to the structural relaxation towards equilibrium during the physical aging process. The difference between the area under the aged and quenched DSC heat capacity curves yields the enthalpy change (ΔH_t) due to physical aging.

We and others are interested in the affect of chain topology on physical aging kinetics given the dependence of physical aging on segmental motion. In a recent paper, Frieberg et al. studied the aging kinetics of films (0.4–2 μm thickness) of anionically synthesized polystyrene star polymers by monitoring the change in film thickness (a measure of specific volume) with aging time.³ They determined that the aging rate, in units of specific volume change per logarithm of aging time, of the star polymers to be slower than that of their linear analogs and decreased with increasing junction point functionality. They speculated that the observed trends could be attributed to an increasing entropic penalty for the conformational rearrangements required for segmental relaxation. They cited simulations which indicated a monomer density gradient exists in star polymers which radiates outward from the core. Thus, segments near the core, due to

the imposed architecture (junction functionality), have less available conformations which would increase the overall rigidity of the chains.

As discussed in Chapter 5, a reduction in ductility as a result of physical aging was observed for all graft copolymers that were tested. Therefore, in this study, we examine the effects of composition and architecture on the kinetics of physical aging in an effort to further elucidate the variables that influence physical aging embrittlement.

6.2 Experimental

6.2.1 Materials

The materials studied include homopolymer poly(D,L-lactide) [PDLLA] and a series of PCNL graft copolymers listed in Table 6-1.

Table 6-1 Molecular characteristics of the graft copolymers studied

Graft Copolymer	vol % PLA	$M_{n,eff}$ (kg/mol)	$M_{n, PLA}$ (kg/mol)
PCNL-92-4-96	94	2.8	40.2
PCNL-495-19-95	93	2.8	48.0
PCNL-594-90-95	93	0.7	14.2
PCNL-495-19-81	66	2.8	12.0

The synthesis and morphology of the graft copolymers was discussed in Chapters 2 and 3 respectively. The graft copolymers exhibited spheroidal nanoscopic rubber domains in a matrix of polylactide with relatively poor long-range order. The glass transition temperature (T_g) was determined by differential scanning calorimetry (DSC) on a TA Discovery DSC utilizing an indium standard for temperature calibration and a sapphire standard for heat capacity calibration. At least 3 mg of sample contained in a

crimped T-zero aluminum pan was analyzed under N_2 . The half-height midpoint of the transition after erasing thermal history (at $150\text{ }^\circ\text{C}$) was defined as T_g .

6.2.1 Physical aging calorimetry procedure

The physical aging kinetics were measured using up-jump calorimetry experiments. Samples for DSC were cut from as-molded tensile bars using a razor blade. Sample dimensions were nominally $0.5\text{ mm} \times 3\text{ mm} \times 2\text{ mm}$ ($H \times W \times L$) with a nominal mass of 5 mg . The flat sample piece was crimped into a standard T-zero pan to ensure good thermal contact between the pan and sample. The thermal cycles used for the up-jump experiment are illustrated in Figure 6-3.

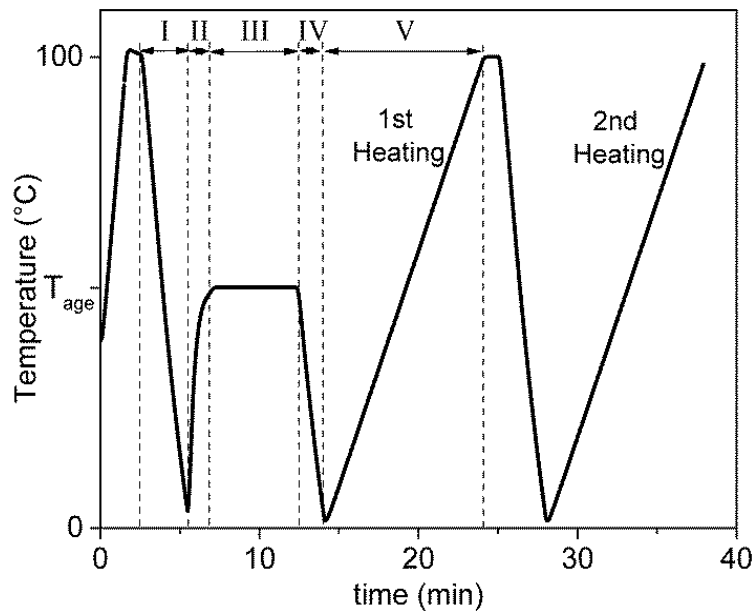


Figure 6-3 Heating/cooling protocol used for calorimetric study of the physical aging kinetics

After annealing at $100\text{ }^\circ\text{C}$ ($\sim T_g + 50\text{ }^\circ\text{C}$) for one minute to erase thermal history, the sample was quenched to $3\text{ }^\circ\text{C}$ at an average rate of $40\text{ }^\circ\text{C min}^{-1}$ shown in Figure 6-3, segment I. The sample was then ramped up to the aging temperature (T_a) at an average

rate of $30\text{ }^{\circ}\text{C min}^{-1}$ (Figure 6-3, II). Then the sample was held isothermally at T_a for various aging times ranging from 2 min to 24 hours (Figure 6-3, III - ~5 min of aging is depicted). The sample was then quenched at an average rate of $40\text{ }^{\circ}\text{C min}^{-1}$ to $0\text{ }^{\circ}\text{C}$ (Figure 6-3, IV). The aged sample was then heated at a rate of $10\text{ }^{\circ}\text{C min}^{-1}$ up to $100\text{ }^{\circ}\text{C}$ (Figure 6-3, V), held isothermally for one minute before quenching at $40\text{ }^{\circ}\text{C min}^{-1}$ to $0\text{ }^{\circ}\text{C}$ and then reheating up to $100\text{ }^{\circ}\text{C}$ at $10\text{ }^{\circ}\text{C min}^{-1}$. One aging trial consisted of one sample pan aged at one temperature for a series of aging times. The fidelity of the sample after the various aging times was confirmed by the T_g from the 2nd heating and SEC at the end of the series. Three to four aging temperatures ($T_g - T_a \approx 4, 5, 6$ and $7\text{ }^{\circ}\text{C}$) were used for each material studied and at least two trials were performed for every combination of material and temperature.

Heat flow data was divided by the programmed heating rate to yield heat capacity normalized to the mass of PLA in the material. Enthalpy was determined by integrating the heat capacity vs. temperature data from 30 to $80\text{ }^{\circ}\text{C}$. The enthalpy change (observed as excess enthalpy during the heating cycle immediately after aging) due to physical aging (ΔH_t , see Figure 6-2) was determined from subtraction of the enthalpy of the quenched sample (Figure 6-2, 2nd Heating) from that of the aged sample (Figure 6-2, 1st Heating). For at least two of the three aging temperatures, the aging times were extended until ΔH_t became relatively constant. Then the experimentally determined long time enthalpy (ΔH_{∞}) was defined as the average of the 2 to 3 long-time data points where the measured excess enthalpy was relatively constant with respect to time.

6.2.2 Modeling of physical aging kinetics

Modeling of physical aging kinetics is an area of active research, and the reader is directed to a number of recent reviews.^{40,4} In this study, we used the Tool-Narayanswamy-Moynihan (TNM) model, a commonly employed phenomenological model. It is well established that the relationship between excess enthalpy (ΔH_t) and aging time is neither linear nor exponential. Instead, the data is often fit to a stretched-exponential of the form shown in Equation 6-1 yielding a plot schematically represented in Figure 6-4 where β is the non-exponentiality parameter, and τ_0 is a characteristic relaxation time. The non-exponentiality parameter ($1 \leq \beta \leq 0$) is a measure of the distribution of relaxation times of the material and results from the variety of thermodynamic microstates relaxing at various rates. A value of $\beta = 1$, indicates a homogeneous system, whereas values approaching 0 suggest a wider distribution of relaxation times for the material.

$$\Delta H_t = \Delta H_\infty \left\{ 1 - \exp \left[- \left(\frac{t}{\tau_0} \right)^\beta \right] \right\} \quad \text{Equation 6-1}$$

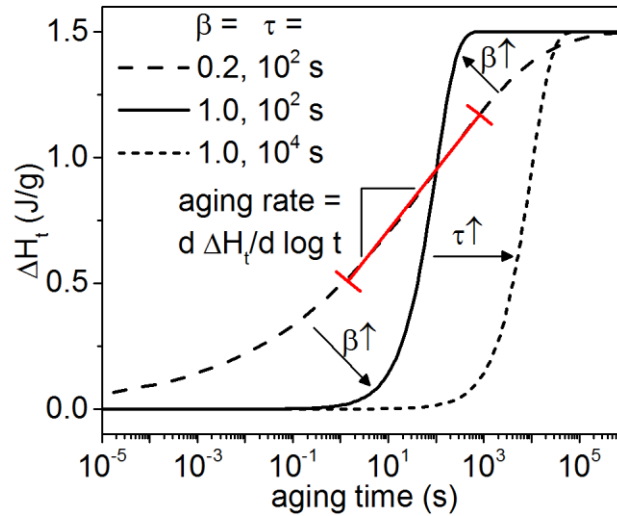


Figure 6-4 A schematic of excess enthalpy due to physical aging as a function of aging time on a logarithmic scale. The aging rate is defined as the slope of the linear portion of the curve. Increasing the non-exponentiality parameter (β) while holding the characteristic relaxation time (τ) constant increases aging rate. Increasing τ , while holding β constant, translates the curve on the time axis towards increasing time. $\Delta H_{\infty} = 1.5 \text{ J/g}$

To account for the non-linearity of the aging kinetics, τ_0 must be a function of time as well as the instantaneous glassy structure. In the TNM model, the glassy structure is mathematically represented by the Tool fictive temperature (T_f) at which the equilibrium enthalpy equals the enthalpy at a given aging time and temperature (Equation 6-2a). Assuming the dependence of C_p is small enough to be considered constant, integration and rearrangement of Equation 6-2a yields a simplified definition for T_f (Equation 6-2b) where ΔC_p is the change in heat capacity at the glass transition.

$$H_t(T_a) = H_{\infty}(T_{f,t}) - \int_{T_a}^{T_{f,t}} C_p dT \quad \text{Equation 6-2a}$$

$$T_f = T_a + \frac{\Delta H_{\infty} - \Delta H_t}{\Delta C_p} \quad \text{Equation 6-2b}$$

τ_0 is given by Equation 6-3a in the TNM model, where T is the temperature of the system which is a function of time, T_f is the fictive temperature, $\ln(A)$ is a material constant, Δh^*

is an apparent activation energy, and x is the non-linearity parameter ($0 \leq x \leq 1$) which partitions the dependence of the characteristic relaxation time on the aging temperature (2nd term of Equation 6-3a) and the structure of the system represented by fictive temperature (3rd term of Equation 6-3a) component. Within the relatively small temperature range of the glass transition, β , Δh^* , and x are considered independent of aging temperature.⁵

$$\tau_0(T, T_f) = \exp \left[\ln(A) + \frac{x\Delta h^*}{RT} + \frac{(1-x)\Delta h^*}{RT_f} \right] \quad \text{Equation 6-3a}$$

$$\tau_{0,k}(T_k, T_{f,k}) = \exp \left[\ln(A) + \frac{x\Delta h^*}{RT_k} + \frac{(1-x)\Delta h^*}{RT_{f,k-1}} \right] \quad \text{Equation 6-3b}$$

The dependence of T_f on time is also non-linear because the relaxation depends on the aging temperature, T_a , as well as the instantaneous structure of the glass (quantified by T_f). As a result, the appropriate model accounts for a series of characteristic relaxation times, $\tau_{0,t}$, which change as T_f changes. Since the relaxation behavior is recursive, the entire thermal history of system beginning at equilibrium, must be taken into account, resulting in a definition for τ_0 that depends on the current temperature T_k and the state of the system at the previous time step, $T_{f,k-1}$ (Equation 6-3b). Ultimately, the TNM model combines equations 6-1 and 6-3 and linearizes the time steps with a reduced time integral to define T_f in terms of thermal history and time (Equation 6-6), where T_0 is a temperature above T_g where the material is in equilibrium and Q is a heating or cooling rate. Equation 6-6 must be solved numerically due to the recursive dependence of τ_0 . Each portion of the thermal history is written in the form of Equation 6-7 and solved numerically using a program written in Matlab R2012b. $T_{f,0}$ and ΔC_p were found for

each material from fitting ΔH_∞ vs. T_a to Equation 6-2b solved at equilibrium. The experimentally determined excess enthalpy values (ΔH_t) were converted to fictive temperatures using Equation 6-2 where ΔC_p is the change in heat capacity at T_g .

$$T_f(T) = T_0 + \int_{T_0}^{T'} dT' \left\{ 1 - \exp \left[- \left(\int_{T'}^T \frac{dT''}{Q \tau_0} \right)^\beta \right] \right\} \quad \text{Equation 6-6}$$

$$T_{f,n} = T_0 + \sum_{j=1}^n \Delta T_j \left\{ 1 - \exp \left[- \left(\sum_{k=j}^n \frac{\Delta T_k}{Q_k \tau_{0,k}} \right)^\beta \right] \right\} \quad \text{Equation 6-7}$$

The apparent activation energy for physical aging was determined from the Arrhenius relationship between ΔH_∞ and T_a . With the activation energy held constant, a global fit (multiple aging temperatures) of the experimental fictive temperature vs. aging time data to the three-parameter TNM model was performed for each material using the MATLAB built-in *fmincon* function. The squared error between the experimental fictive temperature and the predicted fictive temperature was minimized iteratively to get the best fit values of the TNM parameters: $\ln(A)$, β , and x .

6.3 Results

Samples of all the materials in this study were physically aged in a differential scanning calorimeter at various levels of ΔT ($T_g - T_a$) for aging times ranging from 100 s to ~20 h (72,000 s). The error of the average enthalpy change is given as the range of the data from two trials. Only one trial was run for some of the long time (~20 h) data points. When plotted versus the logarithm of aging time, all materials exhibit the expected S-shape curves (Figure 6-5) with similar values of ΔH_t for similar values of ΔT . An experimental logarithmic aging rate was determined for all materials (at $\Delta T = 7$ °C) as the slope of the best-fit line in the intermediate region of the plot where the ΔH_t values

appear to be linear with the logarithm of aging time. The values of the logarithmic aging rate, shown in Table 6-2 are similar for all the materials studied and comparable to the enthalpic aging rate reported for other polymers, such as polystyrene ($0.6 \text{ J} \cdot \text{g}^{-1}$ per decade of time).⁶ Also for $\Delta T = 7 \text{ }^\circ\text{C}$, the logarithm of the time to equilibrium (t_∞) was calculated as the time at which the ΔH_t is 99% of ΔH_∞ (Table 6-2). Although the aging rates were found to be rather similar, the value of t_∞ for PDLLA-75k was the largest of all the materials studied by nearly a decade in time (at the most). The values of t_∞ for the rubber modified materials were lower than PDLLA-75k and similar to one another, but no trend with molar mass or architecture was discernible. The apparent activation energy (Δh^*), required for model fitting, was determined by assuming an Arrhenius dependence of t_∞ on aging temperature. The assumption of Arrhenius temperature dependence has been shown in literature to be acceptable provided that the range of aging temperatures is relatively small.^{7,8} The value of Δh^* ($987 \pm 32 \text{ kJ/mol}$) determined for the control, PDLLA-75k, is similar to the that reported in literature for PDLLA (870^9 – 1123^{10} kJ/mol), which supports the validity of the Arrhenius assumption for this study. The rubber modified materials have Δh^* values which are lower than the control. However, a trend of increasing Δh^* with increasing PLA M_n was observed as shown in Figure 6-6.

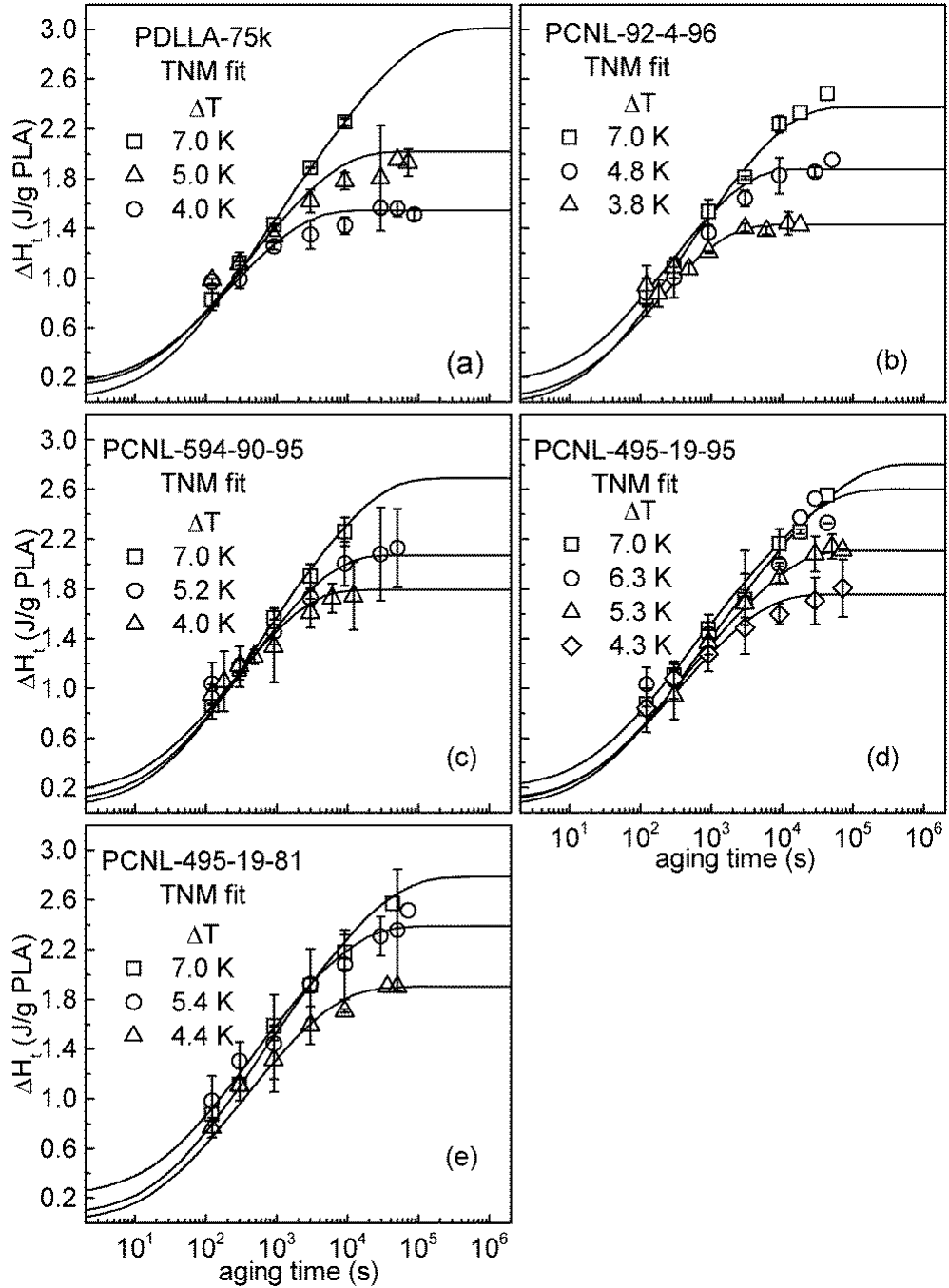


Figure 6-5 Enthalpy change due to physical aging at various degrees of $\Delta T = T_g - T_a$ for (a) Poly(DL-lactide) $M_n = 75\text{kDa}$, (b) PCNL-92-4-96, (c) PCNL-594-90-95, (d) PCNL-495-19-95, (e) PCNL-495-19-81. The solid lines represent the fits to the Tool-Narayanaswamy-Moynihan model with parameters given in Table 6-3

Table 6-2 The enthalpic aging rate and time to equilibrium measured for $T_g - T_a = 7\text{ }^\circ\text{C}$ with standard error listed in parentheses.

Material	aging rate ($\text{J}\cdot\text{g}^{-1}$ per decade)	$\log(t_\infty [\text{h}])$
PDLLA-75k	0.76 (0.02)	2.5 (0.3)
PCNL-92-4-96	0.74 (0.04)	1.6 (0.2)
PCNL-594-90-95	0.74 (0.02)	1.5 (0.3)
PCNL-495-19-95	0.65 (0.03)	1.9 (0.2)
PCNL-495-19-81	0.72 (0.04)	1.8 (0.2)

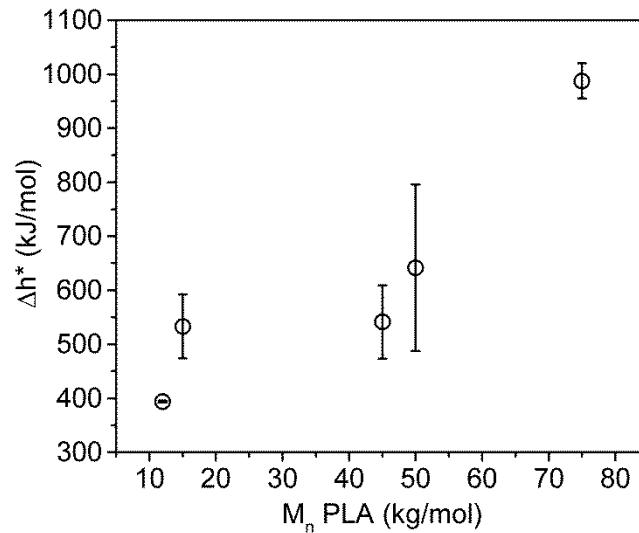


Figure 6-6 The apparent activation energy, Δh^* , as determined from the Arrhenius dependence of time to equilibrium on aging temperature, appears to be correlated with increasing polylactide molar mass. Error bars represent the 95% confidence interval estimated from the standard error resulting from the linear regression of $\ln(t_\infty)$ vs. T_a^{-1} .

The average values of Δh^* found above were used to perform a 3-parameter (β , x , $\ln A$) fit of the experimental average enthalpy change, ΔH_t (normalized to the mass of PLA in the sample), to the TNM model. Qualitatively, the fit of the data to the model (solid lines shown in Figure 6-5) appears satisfactory for all materials. For the purposes of estimating error in the TNM fitting parameters, the regression analysis for each material was also

performed using the average $\Delta h^* \pm$ one standard deviation about the mean. The resulting average values and standard deviation for the TNM parameters are reported in Table 6-3.

Table 6-3 Apparent activation energy used in the Tool-Narayanaswamy-Moynihan fit and the resulting fitted parameters

Material	Δh^* (kJ/mol) ^a	β^b	x^b	$\text{Ln}(A)^b$
PDLLA-75k	987 (32)	0.33 (0.01)	0.76 (0.04)	-359 (23)
PCNL-92-4-96	642 (154)	0.60 (0.36)	0.58 (0.38)	-230 (110)
PCNL-594-90-95	534 (59)	0.43 (0.18)	0.69 (0.32)	-192 (42)
PCNL-495-19-95	547 (75)	0.4 (0.05)	0.37 (0.12)	-192 (49)
PCNL-495-19-81	394 (2)	0.40 (0.00)	0.24 (0.01)	-139 (1)

^a Determined from assumed Arrhenius dependence of t_∞ , standard error * 1.96 is given in parentheses

^b Determined from 3-parameter fit of experimental data to the Tool-Narayanaswamy-Moynihan Model, standard deviation of the results from three fits using Δh^* and its 95% confidence interval.

The non-exponentiality parameter (β) determined for the PLA control is comparable to the low end of the range of values reported in literature (0.35 to 0.51) for homopolymer PLA.⁷⁻⁹ A smaller value of β indicates a more heterogeneous system with a large distribution of relaxation times and a higher degree of inter-chain cooperativity required for segmental motion. All the rubber-modified materials have slightly larger values of β relative to the PLA control. This is a surprising result since it is expected that the graft architecture would allow for additional chain relaxation modes, such as arm-retraction previously observed in star and comb polymers.¹¹⁻¹⁴ More experimental work regarding the specific chain motions is required to understand the unexpected result. There is no discernible trend with molar mass or composition.

The PLA control has a large value of the non-linearity parameter (x) which is similar to higher end of the range of values for x found in literature for homopolymer

polylactide of various stereochemistry (0.10^8 to 0.63^7). The x values obtained for the rubber-modified materials span a wide range; however, considering PCNL-495-19-95 and PCNL-495-19-81, there may be a slight trend of decreasing x with increasing rubber content. The values of the material constant, reported as $\ln(A)$, are consistent with literature.

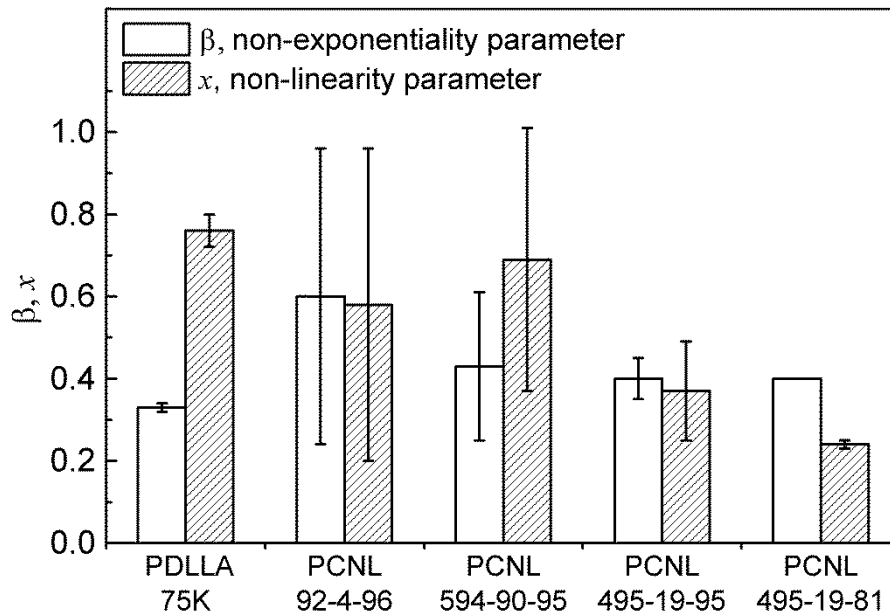


Figure 6-7 The average and standard deviation of the non-exponentiality (β) and non-linearity (x) parameters for each material obtained from fit of the Tool-Narayanaswamy-Moynihan model to experimental data with a constant activation energy given by the average value, the upper and the lower value of the 95% confidence interval of the activation energy.

The enthalpy change due to physical aging at 25 °C was predicted for all materials using TNM parameters found when using the experimentally calculated Δh^* and $\Delta h^* \pm$ the 95% confidence interval. The logarithmic aging rate and time to equilibrium (t_∞) was measured for each set of parameters and averaged (Table 6-4) with the standard deviation given as a measure of error. The aging rate obtained for the PLA control is similar to that

reported by Pan et al. (1.77 J/g per decade) for amorphous PLLA at $T_a = 40^\circ\text{C}$.⁹ Additionally, for the two graft copolymers with relatively small standard deviations, the aging rate is found to be nearly 2× slower than the control which is consistent with the findings of Frieberg et al.³ where polystyrene star polymers were found to age slower than linear polystyrene. The predicted t_∞ values indicate that the PLA control requires the most time to reach enthalpic equilibrium, while PCNL-495-19-81 requires the least time.

Table 6-4 Enthalpic aging rate and time to equilibrium of simulated data where $T_a = 25^\circ\text{C}$ (standard errors are listed in parentheses)

Material	aging rate (J g ⁻¹ per decade)	log(t_∞ [h])
PDLLA-75k	2.0 (0.2)	16.2 (1.0)
PCNL-92-4-96	1.7 (1.1)	10.3 (4.0)
PCNL-594-90-95	1.5 (0.5)	8.6 (1.3)
PCNL-495-19-95	1.1 (0.1)	9.6 (1.8)
PCNL-495-19-81	1.1 (0.0)	6.9 (0.0)

6.4 Summary and Discussion

The results of the calorimetry data indicate that physical aging occurs in all the materials studied. For $\Delta T = 7^\circ\text{C}$, the experimental aging rates in the linear portion of the aging curves ($d\Delta H/d\log t$) of the graft copolymers were found to be similar to that of the linear homopolymer PLA control (PDLLA-75k). However, the time to enthalpic equilibrium (t_∞) was longest for PDLLA-75k for the same value of ΔT . A correlation of increasing apparent activation energy (Δh^*) with increasing PLA M_n was observed which is consistent with the Adam-Gibbs theory of enthalpy relaxation in which the activation energy is an extensive property depending on the number of cooperatively rearranging regions (CRRs).¹⁵ The CRRs are composed of chain segments; thus, as the molar mass increases, if the size of the CRRs remain the same, then the number of CRRs should

increase resulting in a larger value of Δh^* . The average non-exponentiality parameters (β) for the rubber-modified materials are slightly larger than the PLA control, but within the range of values found in the literature for homopolymer PLA. Also considering the large estimates of error, the differences observed in β may not be significant. Thus, it appears that graft copolymerization only influences β slightly, if at all. The average non-linearity parameter (x) found for the PLA control was slightly greater than the largest of the values of x found in literature. However, a trend of decreasing x with increasing rubber content was observed indicating that the addition of the rubber, despite its immiscibility, lowers the sensitivity of the relaxation times to the aging temperature. The influence of specific graft copolymer parameters, such as $M_{n,eff}$ (molar mass between grafts) on x could not be deduced due to the large error bars.

6.5 Final Conclusions

Physical aging embrittlement (discussed in Chapter 4 and 5) was observed for all materials tested, but in contrast to the results from the calorimetry study, there was a conclusive difference in the rates of tensile embrittlement for all materials. The entangled PLA control embrittled quickly and exhibited the same quantitative tensile behavior as PCNL-92-4-96 and PCNL-594-90-95. Although aged PCNL-594-90-95 had a slightly different deformation mechanism of hetero-phase cavitation induced crazing in addition to homogeneous crazing, relative to PLA, the apparent rate of embrittlement was the same. In contrast, PCNL-495-19-95 exhibited an increased amount of hetero-phase cavitation induced crazing relative to homogeneous crazing and formed a new, likely more stable craze morphology resulting in the ductile to brittle transition occurring at a

slower rate. Although the error estimates for some of the materials are rather large, the average values of x were smallest for those materials that exhibited a different physical aging embrittlement behavior relative to the control, namely PCNL-495-19-95, PCNL-495-19-81. Unfortunately, the deformation mechanism of PCNL-495-19-81 was not determined; however, its cylindrical morphology would likely facilitate a deformation mechanism that is different from PCNL-495-19-95 or PLA. The TNM parameters allowed for the prediction of the logarithmic aging rate at 25 °C revealing that the aging rates for PCNL-495-19-95 and -81 are significantly slower than the control, consistent with the tensile embrittlement data. Unfortunately, the error estimates for the remaining graft copolymers materials are too large to form any additional concrete conclusions. Therefore, we conclude that in PCNLs having rather small rubber domains sizes and spacings, represented by PCNL-594-19-95, the physical aging kinetics appear unchanged relative to PLA. Furthermore, although, a new deformation mechanism was observed, hetero-phase cavitation induced crazing, the small rubber domain sizes still allowed homogeneous crazing to dominate, resulting in ultimately the same tensile behavior as PLA. On the other hand, graft copolymers with larger rubber domain sizes, exemplified by PCNL-495-19-95, may have some impact on the aging kinetics, possibly through the non-linearity parameter, x . Retardation of the physical aging kinetics may explain the ability of PCNL-495-19-95, aged for 2 days at 25 °C, to form a macroscopic neck after a significant amount of crazing occurred. Additionally, the hetero-phase cavitation induced crazing was more prevalent in PCNL-495-19-95 resulting in a more stable craze morphology. However, ultimately, the new mechanism could not overcome the physical

aging embrittlement of the matrix, as PCNL-495-19-95 returned to the brittle behavior of PLA after aging at 25°C, for four days.

6.6 Acknowledgements

This work was supported by the USDA and the U.S. DOE through Grant DE-PS36-06GO96002P. This work was also supported by the Center for Sustainable Polymers, an NSF-funded Center for Chemical Innovation at the University of Minnesota. Parts of this work were carried out in the Institute of Technology Characterization Facility, University of Minnesota, a member of the NSF-funded Materials Research Facilities Network. Parts of this work utilized computing resources from the University of Minnesota Supercomputing Institute.

6.7 References

- ¹ Hodge, I. *J. Non Cryst. Solids* **1994**, *169*, 211-266
- ² Ren, J.; Urakawa, O.; Adachi, K. *Macromolecules* **2003**, *36*, 210-219
- ³ Frieberg, B.; Glynos, E.; Sakellariou, G.; Green, P. F. *ACS Macro Letters* **2012**, *1*, 636-640
- ⁴ McKenna, G. B. In *Physical Aging in Glasses and Composites*; Pochiraju, KV Tandon, GP Schoeppner, GA, Ed.; Springer: New York; 233 Spring Street, New York, NY 10013, United States, 2012; , pp 309
- ⁵ Luthra, S. A.; Hodge, I. M.; Pikal, M. J. *J. Pharm. Sci.* **2008**, *97*, 3084-3099
- ⁶ Simon, S. L.; Sobieski, J. W.; Plazek, D. J. *Polymer* **2001**, *42*, 2555-2567
- ⁷ Li, Q.; Simon, S. L. *Polymer* **2006**, *47*, 4781-4788
- ⁸ Koh, Y. P.; Simon, S.L. *Macromolecules* **2013**,*46*, 5815-5821
- ⁹ Pan, P.; Zhu, B.; Inoue, Y. *Macromolecules* **2007**, *40*, 9664-9671

¹⁰ Aou, K.; Hsu, S. L.; Kleiner, L. W.; Tang, F. *J Phys Chem B* **2007**, *111*, 12322-12327

¹¹ Daniels, D.; McLeish, T.; Crosby, B.; Young, R.; Fernyhough, C. *Macromolecules* **2001**, *34*, 7025-7033.

¹² Chrissopoulou, K.; Harville, S.; Anastasiadis, S. H.; Fytas, G.; Mays, J. W.; Hadjichristidis, N. *Journal of Polymer Science Part B-Polymer Physics* **1999**, *37*, 3385-3391

¹³ Mijovic, J.; Sun, M. Y.; Pejanovic, S. *Macromolecules* **2003**, *36*, 7640-7651.

¹⁴ Miros, A.; Vlassopoulos, D. *J. Rheol.* **2003**, *47*, 163-176.

¹⁵ Hodge, I. M. *Macromolecules* **1987**, *20*, 2897-2908

Bibliography

Adhikari, R.; Lebek, W.; Godehardt, R.; Michler, G. H.; Cagliaio, M. E.; Calleja, F. J. B.; Knoll, K. *J Appl Polym Sci* **2006**, *101*, 998-1006.

Adhikari, R.; Michler, G. H. *Prog. Polym. Sci.* **2004**, *29*, 949-986.

Alonso-Villanueva, J.; Vilas, J. L.; Moreno, I.; Laza, J. M.; Rodriguez, M.; Leon, L. M. *Journal of Macromolecular Science Part A-Pure and Applied Chemistry* **2011**, *3*, 211-218.

American Chemistry Council December 2008 Resin Production and Sales Stats.
http://www.americanchemistry.com/s_acc/sec_news_article.asp?CID=206&DID=9277
(accessed 03/23, 2009).

Anand, L.; Spitzig, W. *Acta Metallurgica* **1982**, *30*, 553-561

Anderson, K. S.; Hillmyer, M. A. *Macromolecules* **2004**, *5*, 1857-1862.

Anderson, K. S.; Schreck, K. M.; Hillmyer, M. A. *Polymer Reviews* 2008, *48*, 85-108.

Aou, K.; Hsu, S. L.; Kleiner, L. W.; Tang, F. *J Phys Chem B* **2007**, *111*, 12322-12327

Arends, C. B. In *Polymer Toughening*. Hudgin, D. E., Ed.; *Plastics Engineering*; Marcel Dekker, Inc.: New York, NY, 1996; Vol. 30, pp 415.

Argon, A. S. *Polymer* **2011**, *52*, 2319-2327

Argon, A. S.; Andrews, R. D.; Godrick, J. A.; Whitney, W. *J. Appl. Phys.* **1968**, *39*, 1899-1906

Argon, A. S.; Cohen, R. E.; Gebizlioglu, O. S.; Schwier, C. E. *Crazing in block copolymers and blends*. In Kausch, H. H., Ed.; *Springer Berlin Heidelberg*: 1983; Vol. 52-53, pp 275-335.

Balagurusamy, V. S. K.; Ungar, G.; Percec, V.; Johansson, G. *J. Am. Chem. Soc.* **1997**, *119*, 1539-1555.

Balsamo, V.; von Gyldenfeldt, F.; Stadler, R. *Macromolecules* **1999**, *32*, 1226-1232
Barton, A. F. In *CRC handbook of solubility parameters and other cohesion parameters*; CRC press: 1991;

Bates, F. S.; Fredrickson, G. H. *Phys Today* **1999**, *2*, 32.

Beardmore, P.; Rabinowitz, S. *J. Mater. Sci.* **1975**, *10*, 1763-1770

- Berger, L. L. *Macromolecules* **1989**, *7*, 3162-3167.
- Berger, L.; Buckley, D.; Kramer, E.; Brown, H.; Bubeck, R. *Journal of Polymer Science Part B-Polymer Physics* **1987**, *25*, 1679-1697
- Beyer, F. L.; Gido, S. P.; Buschl, C.; Iatrou, H.; Uhrig, D.; Mays, J. W.; Chang, M. Y.; Garetz, B. A.; Balsara, N. P.; Tan, N. B.; Hadjichristidis, N. *Macromolecules* **2000**, *33*, 2039-2048.
- Biddlestone, F.; Harris, A.; Hay, J.; Hammond, T. *Polym. Int.* **1996**, *39*, 221-229
- Bielawski, C. W.; Grubbs, R. H. *Angew. Chem. Int. Ed.* **2000**, *39*, 2903-2906.
- Bowden, P. B.; Raha, S. *Philosophical Magazine* **1970**, *22*, 463-482
- Brady, J. *Polymer* **1992**, *33*, 2981-2988
- Brown, H.; Kramer, E. *Journal of Macromolecular Science-Physics* **1981**, *B19*, 487-522
- Brûlé, B.; Kausch, H. H.; Monnerie, L.; Plummer, C. J. G.; Halary, J. L. *Polymer* **2003**, *44*, 1181-1192
- Bubeck, R.; Bales, S.; Lee, H. *Polym. Eng. Sci.* **1984**, *24*, 1142-1148
- Bucknall, C. B. *Journal of Polymer Science Part B: Polymer Physics* **2007**, *45*, 1399-1409.
- Bucknall, C. B. *Polymer* **2007**, *48*, 1030-1041
- Bucknall, C. B.; Smith, R. R. *Polymer* **1965**, *6*, 437-446.
- Callister, W. D. In *Materials Science and Engineering An Introduction*; John Wiley & Sons, Inc.: Hoboken, NJ, 2003.
- Chau, C. C.; Li, J. C. M. *J. Mater. Sci.* **1979**, *14*, 2172-2182
- Chau, C.; Li, J. *J. Mater. Sci.* **1981**, *16*, 1858-1873
- Chen, L.; Qiu, X.; Deng, M.; Hong, Z.; Luo, R.; Chen, X.; Jing, X. *Polymer* **2005**, *46*, 5723-5729.
- Cheng, T.; Keskkula, H.; Paul, D. *J Appl Polym Sci* **1992**, *45*, 531-551
- Cho, B. K.; Jain, A.; Gruner, S. M.; Wiesner, U. *Science* **2004**, *305*, 1598-1601.

- Chrissoyoulou, K.; Harville, S.; Anastasiadis, S. H.; Fytas, G.; Mays, J. W.; Hadjichristidis, N. *Journal of Polymer Science Part B-Polymer Physics* **1999**, *37*, 3385-3391
- Cohn, D.; Hotovely-Salomon, A. *Polymer* **2005**, *46*, 2068–2075.
- Collyer, A. A. In *Rubber Toughened Engineering Plastics*. Chapman and Hall: London, UK, 1994; pp 366.
- Czelusniak, I.; Khosravi, E.; Kenwright, A. M.; Ansell, C. W. G. *Macromolecules* **2007**, *40*, 1444–1452.
- Dalal, V.; Moet, A. *Polym. Eng. Sci.* **1988**, *28*, 544-549.
- Daniels, D.; McLeish, T.; Crosby, B.; Young, R.; Fernyhough, C. *Macromolecules* **2001**, *34*, 7025-7033.
- Deblieck, R. A. C.; van Beek, D. J. M.; Remerie, K.; Ward, I. M. *Polymer* **2011**, *52*, 2979-2990.
- Dechy-Cabaret, O.; Martin-Vaca, B.; Bourissou, D. *Chem. Rev.* **2004**, *12*, 6147-6176.
- Declet-Perez, C.; Francis, L. F.; Bates, F. S. *ACS Macro Lett.* **2013**, *10*, 939-943.
- Declet-Perez, C.; Redline, E. M.; Francis, L. F.; Bates, F. S. *ACS Macro Lett.* **2012**, *2*, 338-342.
- Dicorleto, J.; Cohen, R. *Polymer* **1988**, *29*, 1245-1254.
- Dompas, D.; Groeninckx, G.; Isogawa, M.; Hasegawa, T.; Kadokura, M. *Polymer* **1994**, *35*, 4760-4765.
- Donald, A. M.; Kramer, E. J. *J. Mater. Sci.* **1982**, *17*, 1871-1879.
- Donald, A. M.; Kramer, E. J.; Kambour, R. P. *J. Mater. Sci.* **1982**, *17*, 1739-1744.
- Dorgan, J. R.; Janzen, J.; Knauss, D. M.; Hait, S. B.; Limoges, B. R.; Hutchinson, M. H. *Journal of Polymer Science Part B: Polymer Physics* **2005**, *43*, 3100-3111.
- Dorgan, J. R.; Lehermeier, H. J.; Palade, L.; Cicero, J. *Macromol. Symp.* **2001**, *175*, 55-66.
- Drumright, R. E.; Gruber, P. R.; Henton, D. E. *Adv Mater* **2000**, *12*, 1841-1846

Energy Information Administration EIA's Energy in Brief: How dependent are we on foreign oil? http://tonto.eia.doe.gov/energy_in_brief/foreign_oil_dependence.cfm (accessed 03/10, 2009).

Energy Information Administration U.S. Crude Oil Field Production. <http://tonto.eia.doe.gov/dnav/pet/hist/mcrfpus1m.htm> (accessed 03/10, 2009).

Fetters, L. J.; Lohse, D. J.; Richter, D.; Witten, T. A.; Zirkel, A. *Macromolecules* **1994**, *27*, 4639-4647.

Floudas, G.; Hadjichristidis, N.; Iatrou, H.; Avgeropoulos, A.; Pakula, T. *Macromolecules* **1998**, *31*, 6943-6950.

Floudas, G.; Hadjichristidis, N.; Tselikas, Y.; Erukhimovich, I. *Macromolecules* **1997**, *30*, 3090-3096.

Frick, E. M.; Zalusky, A. S.; Hillmyer, M. A. *Biomacromolecules* **2003**, *4*, 216-223.

Friberg, B.; Glynos, E.; Sakellariou, G.; Green, P. F. *ACS Macro Letters* **2012**, *1*, 636-640

Gido, S. P.; Lee, C.; Pochan, D. J.; Pispas, S.; Mays, J. W.; Hadjichristidis, N. *Macromolecules* **1996**, *29*, 7022-7028.

Gido, S. P.; Wang, Z. G. *Macromolecules* **1997**, *30*, 6771-6782.

Grijpma, D. W.; Joziase, C. A. P.; Pennings, A. J. *Makromol. Chem.-Rapid* **1993**, *14*, 155-161.

Grijpma, D. W.; Van Hofslot, R. D. A.; Super, H.; Nijenhuis, A. J.; Pennings, A. J. *Polymer Engineering & Science* **1994**, *34*, 1674-1684.

Grijpma, D.; Penning, J.; Pennings, A. *Colloid Polym. Sci.* **1994**, *272*, 1068-1081.

Hadjichristidis, N.; Iatrou, H.; Behal, S. K.; Chludzinski, J. J.; Disko, M. M.; Garner, R. T.; Liang, K. S.; Lohse, D. J.; Milner, S. T. *Macromolecules* **1993**, *26*, 5812-5815.

Hadjichristidis, N.; Pispas, S.; Pitsikalis, M.; Iatrou, H.; Vlahos, C. In *Asymmetric star polymers: synthesis and properties*; Branched polymers I; Springer: **1999**; pp 71-127.

Hashimoto, T.; Kawamura, T.; Harada, M.; Tanaka, H. *Macromolecules* **1994**, *27*, 3063-3072.

Haward, R. N.; Young, R. J. In *The Physics of Glassy Polymers*. Chapman & Hall: London, 1997.

Haward, R. N.; Young, R. J., Eds.; In *The Physics of Glassy Polymers*; Chapman & Hall: London, 1997; pp 176-180.

Henkee, C. S.; Kramer, E. J. *J. Mater. Sci.* **1986**, *21*, 1398-1404.

Henkee, C. S.; Kramer, E. J. *Journal of Polymer Science Part B-Polymer Physics* **1984**, *22*, 721-737.

Hill, A.; Heater, K.; Agrawal, C. *Journal of Polymer Science Part B-Polymer Physics* **1990**, *28*, 387-405.

Hillmyer, M. A.; Nguyen, S. T.; Grubbs, R. H. *Macromolecules* **1997**, *30*, 718-721.

Hodge, I. *J. Non Cryst. Solids* **1994**, *169*, 211-266.

Hodge, I. M. *Macromolecules* **1987**, *20*, 2897-2908.

Holm, V. K.; Ndoni, S.; Risbo, J. *J. Food Sci.* **2006**, *71*, E40-E44.

Hristov, H.; Yee, A.; Xie, L.; Gidley, D. *Polymer* **1994**, *35*, 4287-4292

Hudson, S. D.; Jung, H. T.; Percec, V.; Cho, W. D.; Johansson, G.; Ungar, G.; Balagurusamy, V. S. K. *Science* **1997**, *278*, 449-452.

Ishikawa, M.; Takahashi, H. *J. Mater. Sci.* **1991**, *26*, 1295-1300

Jansen, B. J. P.; Rastogi, S.; Meijer, H. E. H.; Lemstra, P. J. *Macromolecules* **2001**, *12*, 4007-4018.

Jha, S.; Dutta, S.; Bowden, N. B. *Macromolecules* **2004**, *37*, 4365-4374.

Ji, S.; Hoyer, T.; Macosko, C. *Macromolecules* **2004**, *37*, 5485-5489.

Jing, F.; Hillmyer, M. A. *J. Am. Chem. Soc.* **2008**, *130*, 13826-13827.

Joziase, C. A. P.; Veenstra, H.; Topp, M. D. C.; Grijpma, D. W.; Pennings, A. J. *Polymer* **1998**, *39*, 467-473.

Kambour, R. P. *Journal of Polymer Science: Macromolecular Reviews* **1973**, *7*, 1-154

Kiesewetter, M. K.; Shin, E. J.; Hedrick, J. L.; Waymouth, R. M. *Macromolecules* **2010**, *43*, 2093-2107.

Kinning, D. J.; Thomas, E. L. *Macromolecules* **1984**, *17*, 1712-1718.

Kinning, D. J.; Thomas, E. L.; Fetters, L. J. *J. Chem. Phys.* **1989**, *90*, 5806-5825.

- Koh, Y. P.; Simon, S.L. *Macromolecules* **2013**, *46*, 5815-5821
- Kowalczyk, M.; Piorkowska, E. *J Appl Polym Sci* **2012**, *124*, 4579-4589
- Kramer, E.; Berger, L. In *Fundamental processes of craze growth and fracture*; Kausch, H. -, Ed.; Springer Berlin Heidelberg: 1990; Vol. 91/92, pp 1-68.
- Kulinski, Z.; Piorkowska, E. *Polymer* **2005**, *46*, 10290-10300.
- Lee, C.; Gido, S. P.; Pitsikalis, M.; Mays, J. W.; Tan, N. B.; Trevino, S. F.; Hadjichristidis, N. *Macromolecules* **1997**, *30*, 3732-3738.
- Lee, C.; Gido, S. P.; Poulos, Y.; Hadjichristidis, N.; Tan, N. B.; Trevino, S. F.; Mays, J. W. *J. Chem. Phys.* **1997**, *107*, 6460-6469.
- Lee, C.; Gido, S. P.; Poulos, Y.; Hadjichristidis, N.; Tan, N. B.; Trevino, S. F.; Mays, J. W. *Polymer* **1998**, *39*, 4631-4638.
- Lee, I.; Panthani, T. R.; Bates, F. S. *Macromolecules* **2013**, *46*, 7387-7398.
- Lee, J. Y.; Crosby, A. J. *Macromolecules* **2005**, *38*, 9711-9717.
- Leferink Op Reinink, A. B. G. M.; Belli, S.; van Roij, R.; Dijkstra, M.; Petukhov, A. V.; Vroege, G. J. *Soft Matter* **2014**, *10*, 446-456.
- Lemmouchi, Y.; Perry, M. C.; Amass, A. J.; Chakraborty, K.; Schacht, E. *Journal of Polymer Science Part A: Polymer Chemistry* **2007**, *45*, 3966-3974.
- Li, Q.; Simon, S. L. *Polymer* **2006**, *47*, 4781-4788
- Liu, H.; Zhang, J. *Journal of Polymer Science Part B-Polymer Physics* **2011**, *15*, 1051-1083.
- Liu, J.; Sue, H.; Thompson, Z. J.; Bates, F. S.; Dettloff, M.; Jacob, G.; Verghese, N.; Pham, H. *Macromolecules* **2008**, *41*, 7616-7624.
- Liu, W.; Shen, J.; Wang, Z.; Lu, F.; Xu, M. *Polymer* **2001**, *42*, 7461-7464.
- Lohmeijer, B. G. G.; Pratt, R. C.; Leibfarth, F.; Logan, J. W.; Long, D. A.; Dove, A. P.; Nederberg, F.; Choi, J.; Wade, C.; Waymouth, R. M.; Hedrick, J. L. *Macromolecules* **2006**, *25*, 8574-8583.
- Lu, J.; Ravi-Chandar, K. *Int. J. Solids Structures* **1999**, *36*, 391-425.
- Luthra, S. A.; Hodge, I. M.; Pikal, M. J. *J. Pharm. Sci.* **2008**, *97*, 3084-3099.

- Mahanthappa, M.; Bates, F.; Hillmyer, M. *Macromolecules* **2005**, *19*, 7890-7894.
- Mark, J. E. In *Physical properties of polymers handbook*; Springer: 2007
- Matsen, M. W. *Macromolecules* **2012**, *45*, 2161-2165.
- Matsen, M. W.; Bates, F. S. *Macromolecules* **1996**, *29*, 1091-1098.
- Matsuo, M.; Ueno, T.; Horino, H.; Chujyo, S.; Asai, H. *Polymer* **1968**, *9*, 425-436.
- Mays, J. W.; Uhrig, D.; Gido, S.; Zhu, Y. Q.; Weidisch, R.; Iatrou, H.; Hadjichristidis, N.; Hong, K.; Beyer, F.; Lach, R.; Buschnakowski, M. *Macromolecular Symposia* **2004**, *215*, 111-126.
- McCrum, N. G.; Buckley, C. P.; Bucknall, C. B. In *Principles of Polymer Engineering*; Oxford University Press: New York, 1997;
- McKenna, G. B. In *Physical Aging in Glasses and Composites*; Pochiraju, KV Tandon, GP Schoeppner, GA, Ed.; SPRINGER: NEW YORK; 233 SPRING STREET, NEW YORK, NY 10013, UNITED STATES, 2012; , pp 309
- Meijer, H. E. H.; Govaert, L. E. *Macromolecular Chemistry and Physics* **2003**, *204*, 274-288.
- Meuler, A. J.; Hillmyer, M. A.; Bates, F. S. *Macromolecules* **2009**, *42*, 7221-7250.
- Michler, G. In *Crazing in amorphous polymers—formation of fibrillated crazes near the glass transition temperature*; Deformation and Fracture Behaviour of Polymers; Springer: 2001; pp 193-208.
- Mijovic, J.; Sun, M. Y.; Pejanovic, S. *Macromolecules* **2003**, *36*, 7640-7651.
- Mills, N. J.; Walker, N. *J. Mater. Sci.* **1980**, *15*, 1832-1840.
- Milner, S. T. *Macromolecules* **1994**, *27*, 2333-2335.
- Miros, A.; Vlassopoulos, D. *J. Rheol.* **2003**, *47*, 163-176.
- Mori, Y.; Lim, L. S.; Bates, F. S. *Macromolecules* **2003**, *26*, 9879-9888.
- Mulligan, J.; Cakmak, M. *Macromolecules* **2005**, *38*, 2333-2344
- O'Connell, P. A.; McKenna, G. B. In *Yield and Crazing in Polymers*; Encyclopedia of Polymer Science and Technology; John Wiley & Sons, Inc.: 2002;
- Oh, S.; Lee, J.; Theato, P.; Char, K. *Chem. Mater.* **2008**, *20*, 6974-6984.

- Osaki, K.; Inoue, T.; Hwang, E. J.; Okamoto, H.; Takiguchi, O. *J. Non Cryst. Solids* **1994**, *172*, 838-849.
- Osaki, K.; Okamoto, H.; Inoue, T.; Hwang, E. J. *Macromolecules* **1995**, *28*, 3625-3630.
- Osswald, T. A.; Menges, G., *Materials Science of Polymer for Engineers*; Hanser Publishers 2003.
- Pae, Y. *J. Appl. Polym. Sci.* **2006**, *99*, 300–308.
- Pan, P.; Zhu, B.; Inoue, Y. *Macromolecules* **2007**, *40*, 9664-9671.
- Percec, V.; Cho, W. D.; Ungar, G.; Yearley, D. J. P. *J. Am. Chem. Soc.* **2001**, *123*, 1302-1315.
- Perego, G.; Cella, G. D.; Bastioli, C. *J Appl Polym Sci* **1996**, *59*, 37-43.
- Pitet, L. M.; Hillmyer, M. A. *Macromolecules* **2009**, *42*, 3674–3680.
- Pitsikalis, M.; Pispas, S.; Mays, J. W.; Hadjichristidis, N. In *Nonlinear block copolymer architectures*; Blockcopolymers-Polyelectrolytes-Biodegradation; Springer: 1998; pp 1-137.
- Pochan, D. J.; Gido, S. P.; Pispas, S.; Mays, J. W. *Macromolecules* **1996**, *29*, 5099-5105.
- PURAC Lactic Acid- safe and natural. <http://www.lactic-acid.com/index.html> (accessed 03/02, 2009).
- Qiao, L.; Leibig, C.; Hahn, S. F.; Winey, K. I. *Ind Eng Chem Res* **2006**, *45*, 5598-5602.
- Ren, J.; Urakawa, O.; Adachi, K. *Macromolecules* **2003**, *36*, 210-219.
- Renouf-Glauser, A. C.; Rose, J.; Farrar, D. F.; Cameron, R. E. *Biomaterials* **2005**, *26*, 5771-5782.
- Runge, M. B.; Dutta, S.; Bowden, N. B. *Macromolecules* **2006**, *39*, 498–508.
- Ruokolainen, J.; Fredrickson, G. H.; Kramer, E. J.; Ryu, C. Y.; Hahn, S. F.; Magonov, S. N. *Macromolecules* **2002**, *35*, 9391-9402
- Salomons, G. J.; Singh, M. A.; Bardouille, T.; Foran, W. A.; Capel, M. S. *Journal of Applied Crystallography* **1999**, *32*, 71– 81.
- Schmidt, S. C.; Hillmyer, M. A. *Journal of Polymer Science Part B: Polymer Physics* **2002**, *40*, 2364-2376.

- Schwier, C. E.; Argon, A. S.; Cohen, R. E. *Polymer* **1985**, *13*, 1985-1993.
- Schwier, C.; Argon, A.; Cohen, R. *Philos. Mag. A-Phys. Condens. Matter Struct. Defect Mech. Prop.* **1985**, *5*, 581-603.
- Senden, D. J. A.; van Dommelen, J. A. W.; Govaert, L. E. *Journal of Polymer Science Part B-Polymer Physics* **2012**, *50*.
- Sferrazza, M.; Crawshaw, J.; Donald, A. M.; Narayanan, T. *Macromolecules* **2001**, *34*, 6708-6718.
- Simon, S. L.; Sobieski, J. W.; Plazek, D. J. *Polymer* **2001**, *42*, 2555-2567.
- Sioula, S.; Tselikas, Y.; Hadjichristidis, N. *Macromolecular Symposia* **1997**, *117*, 167-174.
- Södergård, A.; Stolt, M. *Progress in Polymer Science* **2002**, *27*, 1123-1163.
- Staudinger, U.; Weidisch, R.; Zhu, Y.; Gido, S. P.; Uhrig, D.; Mays, J. W.; Iatrou, H.; Hadjichristidis, N. *Macromolecular Symposia* **2006**, *233*, 42-50.
- Stoclet, G.; Lefebvre, J. M.; Seguela, R.; Vanmansart, C. *Polymer* **2014**, *55*, 1817-1828
- Stokes, V. k.; Bushko, W. C. *Polym. Eng. Sci.* **1995**, *35*, 291.
- Suzuki, S.; Nishitsuji, S.; Inoue, T. *Polym. Eng. Sci.* **2012**, *52*, 1958-1963.
- Tan, Z. Y.; Sun, S. L.; Xu, X. F.; Zhou, C.; Ao, Y. H.; Zhang, H. X. *Journal of Polymer Science Part B-Polymer Physics* **2005**, *43*, 2715-2724
- The Society of the Plastics Industry Plastics Fact Sheet. www.plasticsdatasource.org (accessed 03/23, 2009).
- Tselikas, Y.; Iatrou, H.; Hadjichristidis, N.; Liang, K. S.; Mohanty, K.; Lohse, D. J. *J. Chem. Phys.* **1996**, *105*, 2456-2462.
- U.S. Environmental Protection Agency Basic Information Climate Change. <http://www.epa.gov/climatechange/basicinfo.html> (accessed 03/10, 2009).
- U.S. Environmental Protection Agency Basic Information Sustainability. <http://www.epa.gov/sustainability/basicinfo.htm#sustainability> (accessed 03/10, 2009).
- U.S. Environmental Protection Agency Plastics Common Wastes and Materials. <http://www.epa.gov/epawaste/conserva/materials/plastics.htm> (accessed 03/10, 2009).
- van Melick, H. G. H.; Govaert, L. E.; Meijer, H. E. H. *Polymer* **2003**, *44*, 3579-3591

- Vink, E. T. H.; Rabago, K. R.; Glassner, D. A.; Springs, B.; O'Connor, R. P.; Kolstad, J.; Gruber, P. R. *Macromol. Biosci.* **2004**, *4*, 551-564.
- Wanamaker, C. L.; O'Leary, L. E.; Lynd, N. A.; Hillmyer, M. A.; Tolman, W. B. *Biomacromolecules* **2007**, *8*, 3634-3640.
- Wang, J.; Dong, C. *Macromolecular Chemistry and Physics* **2006**, *207*, 554-562.
- Wang, Y.; Noga, D. E.; Yoon, K.; Wojtowicz, A. M.; Lin, A. S. P.; Garcia, A. J.; Collard, D. M.; Weck, M. *Adv. Func. Mater.* **2008**, *18*, 3638-3644.
- Weidisch, R.; Ensslen, M.; Michler, G.; Fischer, H. *Macromolecules* **1999**, *32*, 5375-5382.
- Williams, C. K.; Hillmyer, M. A. *Polymer Reviews* **2008**, *48*, 1-10.
- World Commission on Environment and Development **1987**, *Annex to General Assembly document A/42/427*
- Wu, L.; Zhang, J.; Jing, D.; Ding, J. *Journal of Biomedical Materials Research Part A* **2006**, *76A*, 264-271.
- Xenidou, M.; Beyer, F. L.; Hadjichristidis, N.; Gido, S. P.; Tan, N. B. *Macromolecules* **1998**, *31*, 7659-7667.
- Yang, A.; Kramer, E. *Journal of Polymer Science Part B-Polymer Physics* **1985**, *23*, 1353-1367.
- Zhu, Y.; Burgaz, E.; Gido, S. P.; Staudinger, U.; Weidisch, R.; Uhrig, D.; Mays, J. W. *Macromolecules* **2006**, *39*, 4428-4436.

Appendix A

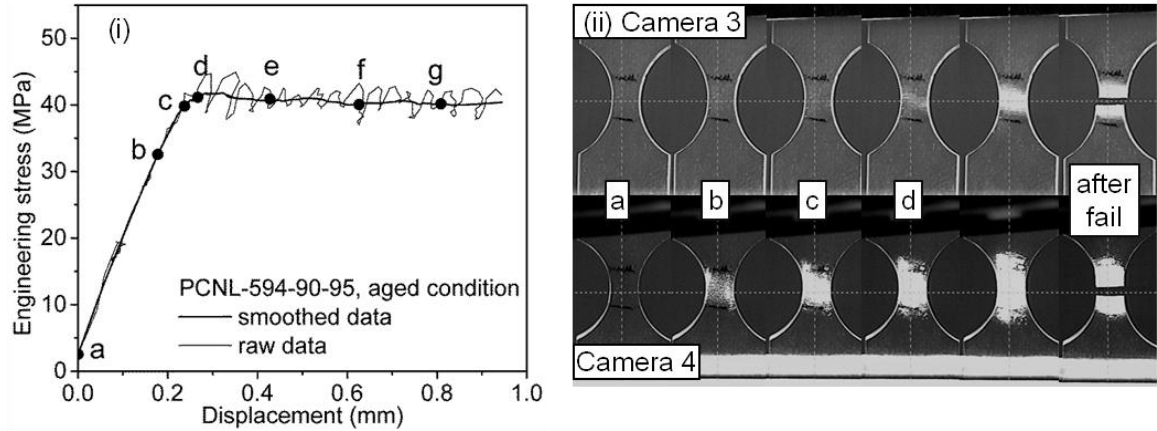


Figure A-1 In-situ tensile data for PCNL-594-90-95 aged at 25 °C for 66 h. Specific displacements are highlighted by points on the (i) tensile stress-displacement curve. The photographs (ii) correspond with the alphabetically labeled points.

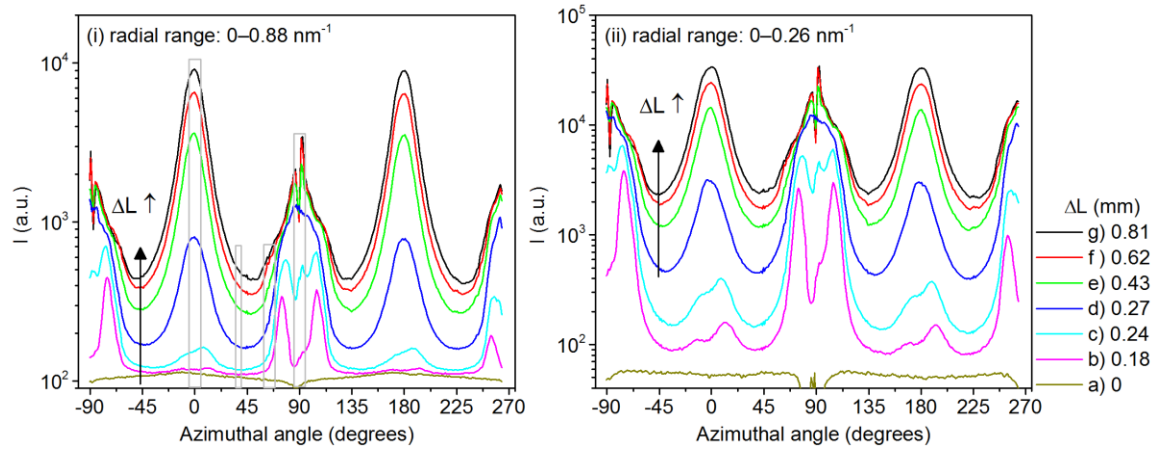


Figure A-2 Intensity versus azimuthal angle for aged PCNL-594-90-95 in two different radial ranges: (i) 0 – 0.88 nm⁻¹ and (ii) 0 – 0.26 nm⁻¹.

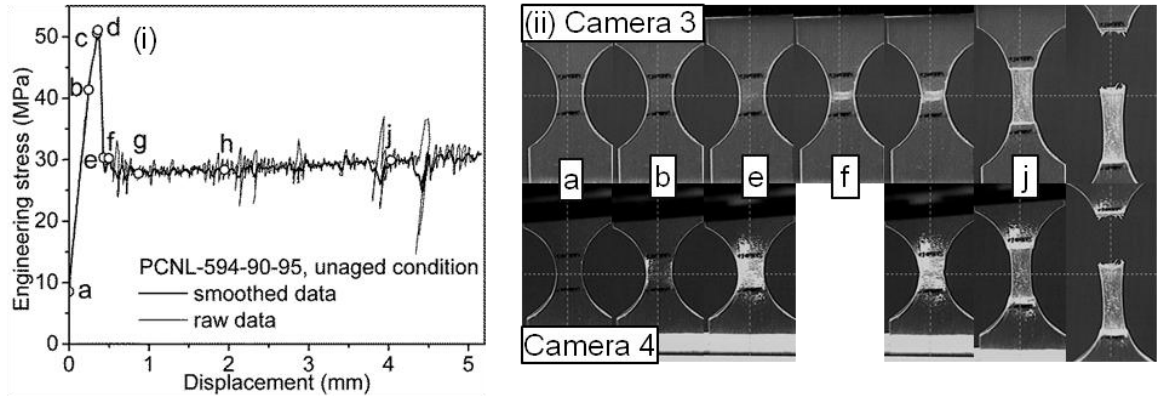


Figure A-3 In-situ tensile data for unaged PCNL-594-90-95 (-10 °C for 66 h). Specific displacements are highlighted by points on the (i) tensile stress-displacement curve. The photographs (ii) correspond with the alphabetically labeled points.

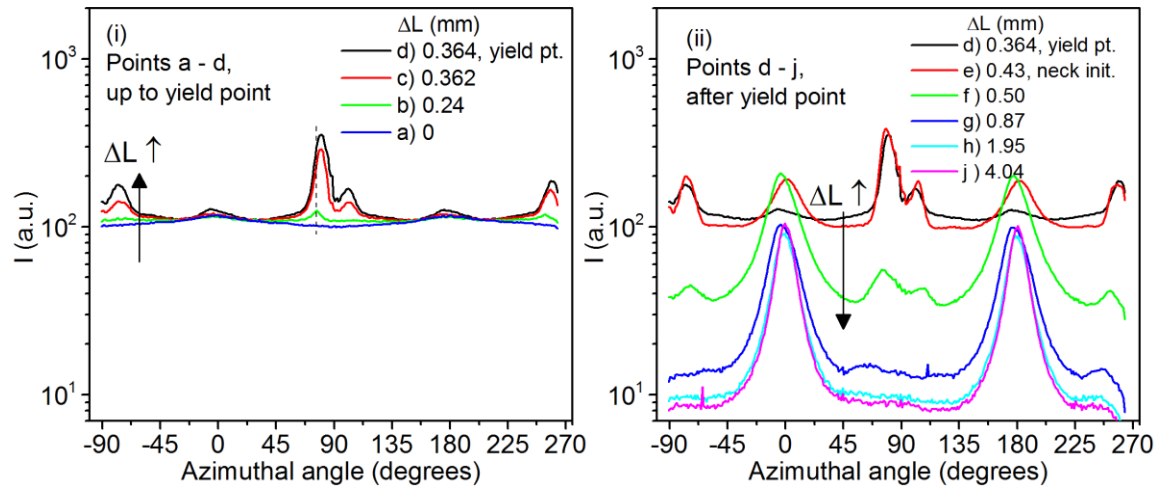


Figure A-4 Intensity versus azimuthal angle for unaged PCNL-594-19-95 in integrated from 0 to 0.88 nm^{-1} (i) before and (ii) after the yield point.

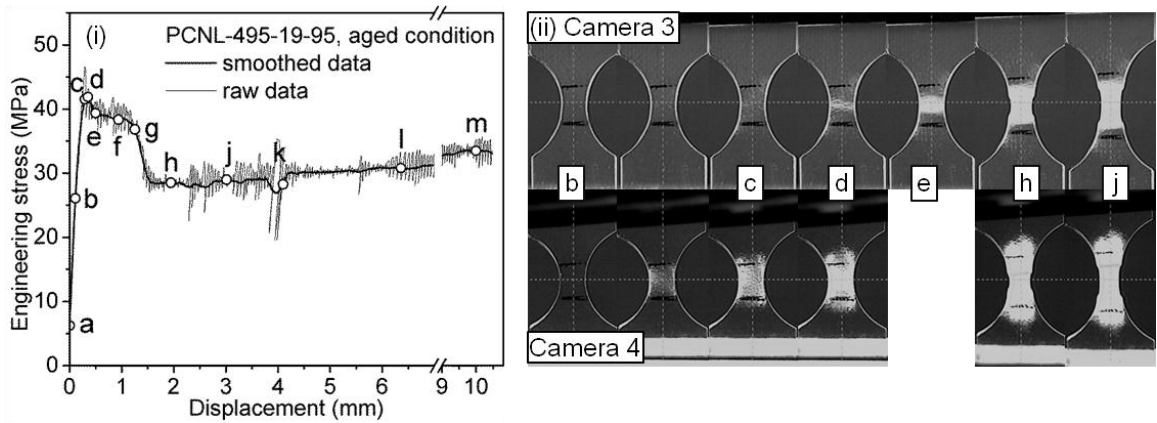


Figure A-5 (i) In-situ tensile stress vs. displacement for aged PCNL-495-19-95. The labeled points on the curve correspond with the (ii) photographs.

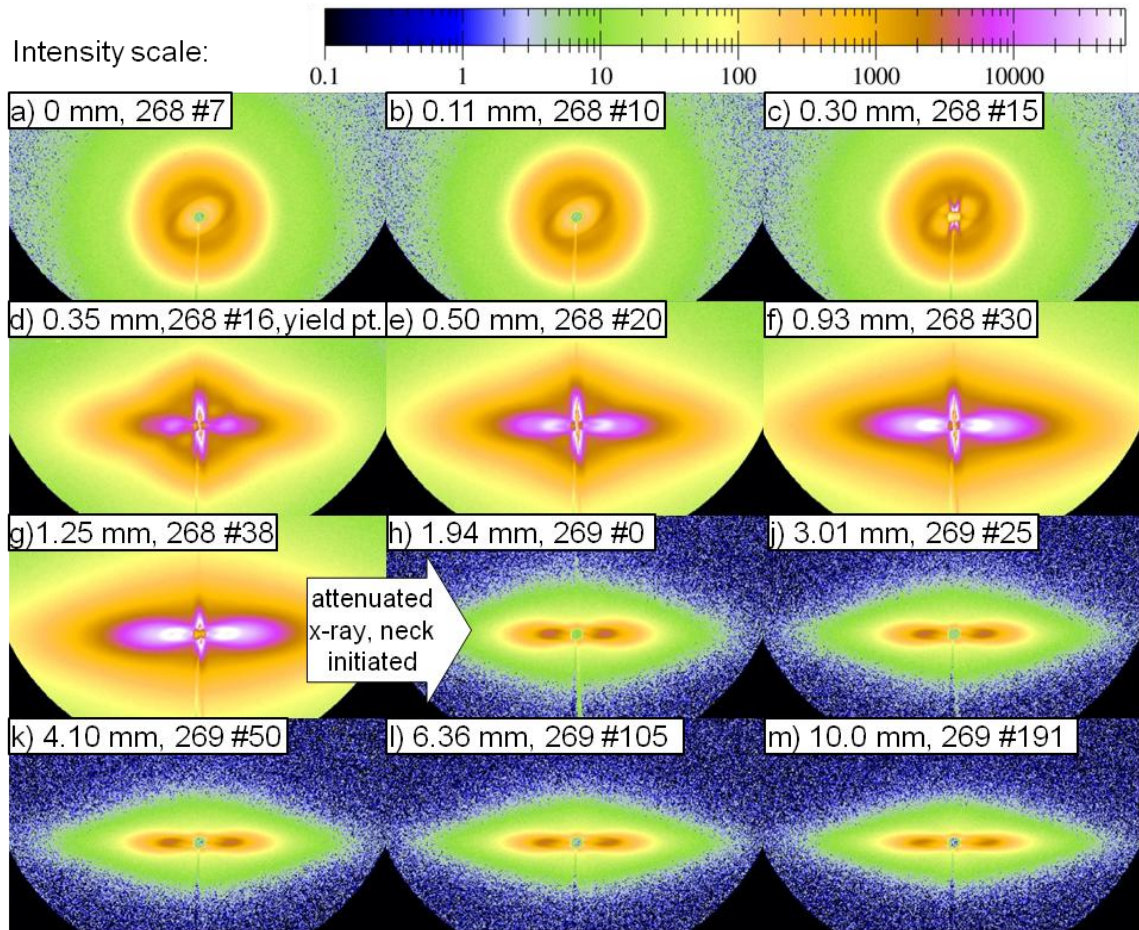


Figure A-6 The in-situ 2D SAXS patterns for aged PCNL-495-19-95 are labeled with tensile displacement and scan number. The scattered intensity scale of each SAXS image

is the same. Between points g and h, the x-ray beam was attenuated by 20 \times to avoid further saturation of the detector.

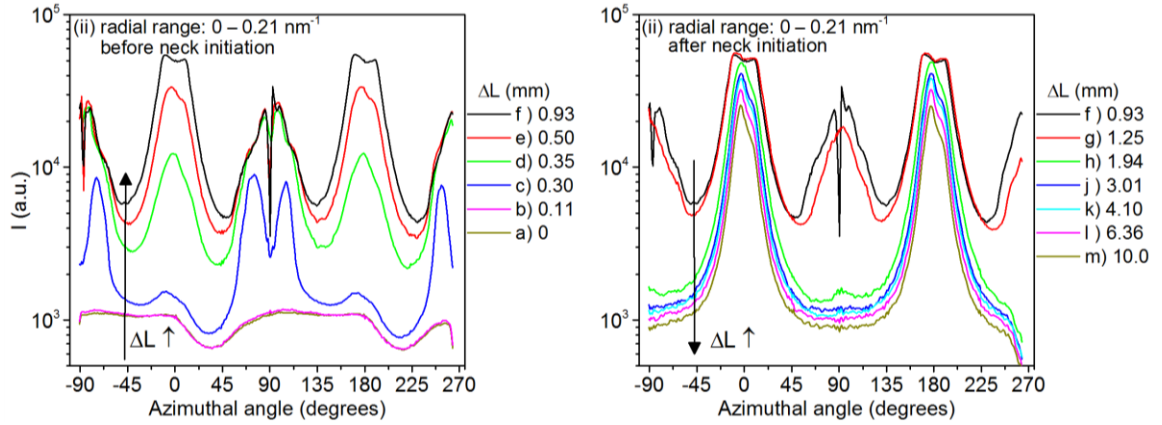


Figure A-7 Intensity versus azimuthal angle for aged PCNL-495-19-95 integrated in the radial range from 0 to 0.21 nm^{-1} .

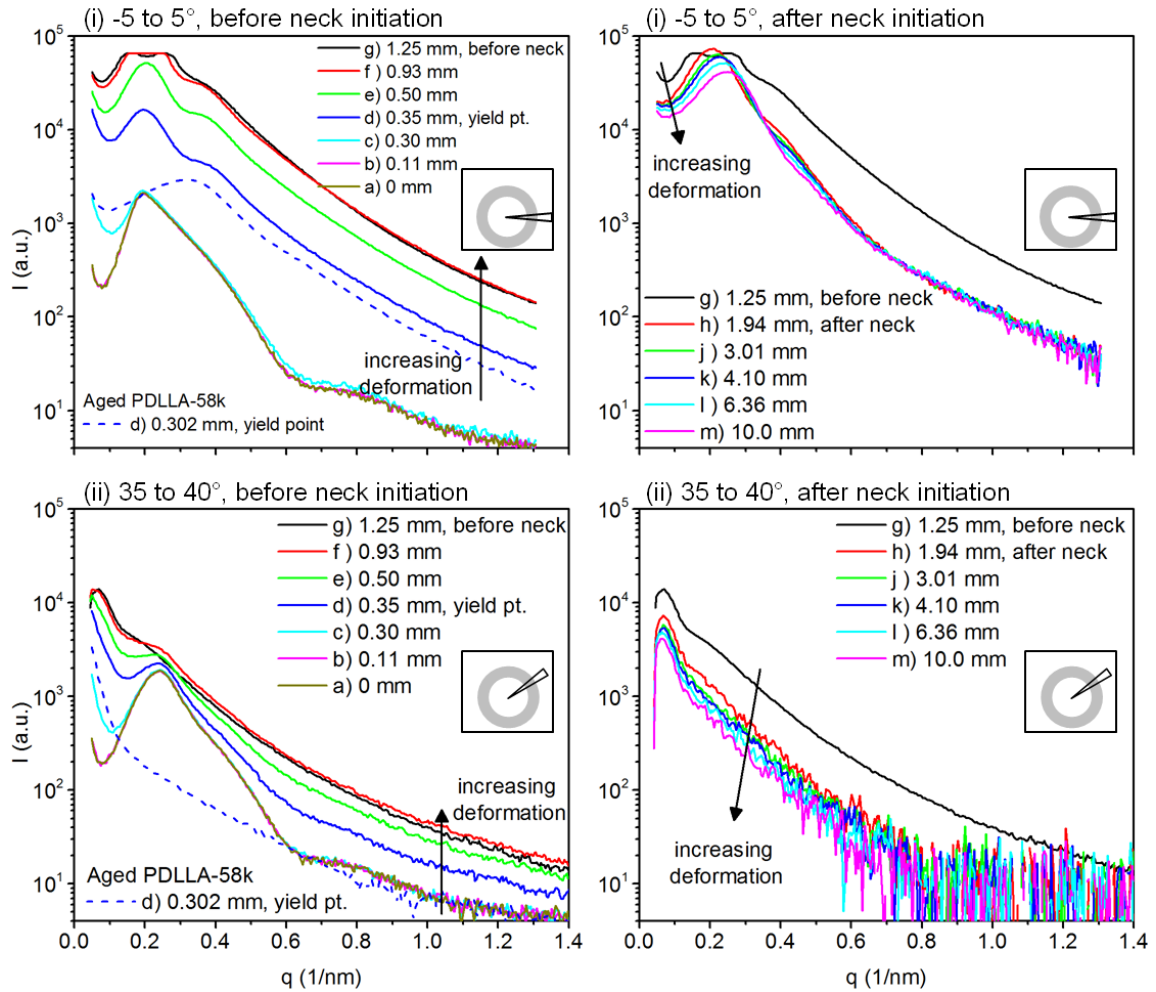


Figure A-8 The 1D SAXS curves of scattered intensity (I) versus wavevector (q) for aged PCNL-495-19-95 were obtained by azimuthal integration in the (i) equatorial range and the (ii) 35°–40° range of the 2D-scattering patterns at each highlighted displacement. The progression of the scattered intensity is shown before and after neck initiation for each azimuthal range.

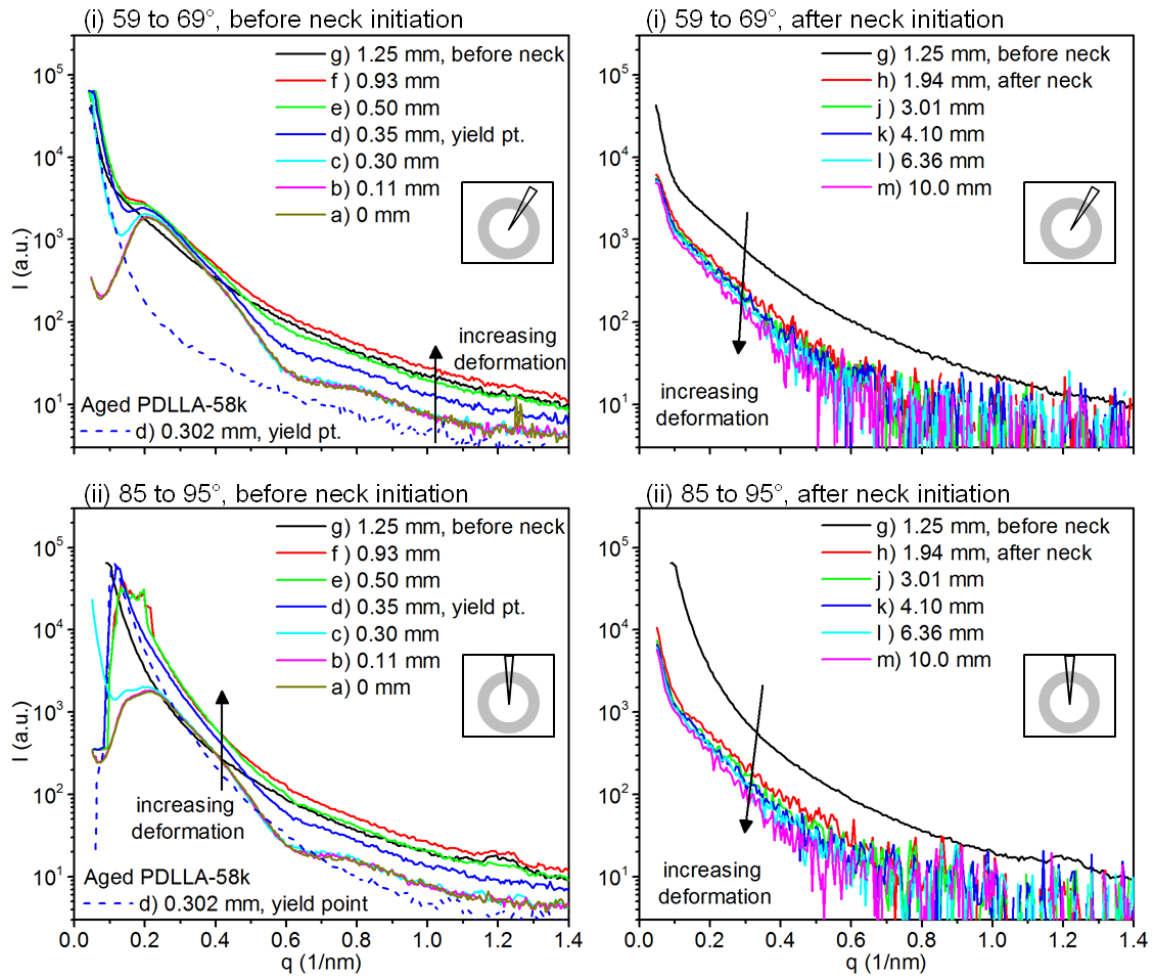


Figure A-9 The 1D SAXS curves of scattered intensity (I) versus wavevector (q) for aged PCNL-495-19-95 were obtained by azimuthal integration in the (i) 59 – 69° and (ii) 85 – 95° range of the 2D-scattering patterns at each highlighted displacement. The progression of the scattered intensity is shown before and after neck initiation for each azimuthal range.

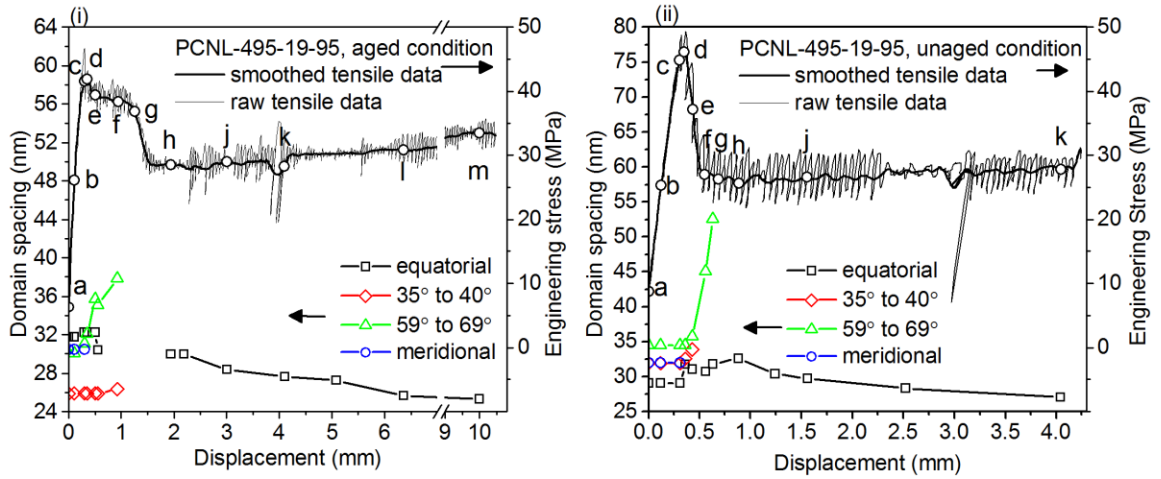


Figure A-10 When possible, the interparticle domain spacing of the graft copolymer was calculated from the position of the primary peak for each azimuthal range and plotted as a function of tensile displacement for (i) aged PCNL-495-19-95 and (ii) unaged PCNL-495-19-95.